

**DARPA BACKGROUND CLUTTER COLLECTION
EXPERIMENT EXCAVATION RESULTS
AT FIRING POINT 20**

Vivian George
Walcoff and Associates
1429 N. Quincy Street
Arlington, VA 22207
Telephone: (703) 351-8644

Thomas W. Altshuler and Erik M. Rosen
Institute for Defense Analyses
1801 N. Beauregard Street
Alexandria, VA 22311
Telephone: (703) 578-2715

Prepared for:

Regina E. Dugan
Defense Advanced Research Projects Agency
Arlington, VA

DIST A :

DISTRIBUTION STATEMENT A
Approved for Public Release
Distribution Unlimited

20011031 066

Clifton, Peggy

From: George, Vivian Ms PM-MCD [vivian.george@nvl.army.mil]
Sent: Friday, April 27, 2001 9:27 AM
To: 'Clifton, Peggy'
Subject: RE: Distribution on DARPA/Walcoff Documents & Data

All are approved for public distribution A, unlimited.

-----Original Message-----

From: Clifton, Peggy [mailto:pclifton@dtic.mil]
Sent: Wednesday, April 11, 2001 9:50 AM
To: 'Vivian George'
Subject: Distribution on DARPA/Walcoff Documents & Data

Vivian,

I am putting in the background clutter data documents and discs; some are marked "Approved for public release, distribution is unlimited," but others have no markings for distribution. Are they all unlimited distribution? If, not we will have to figure out what the distribution levels are for the unmarked documents. TIA,

Peg Clifton

Margaret Clifton
Nonprint Program Manager
Defense Technical Information Center
703.767.9085
pclifton@dtic.mil

"Civilization advances by extending the number
of important operations which we can perform without thinking about them."
-Alfred North Whitehead

ABSTRACT

Most technologies in use or proposed for use to detect landmines and unexploded ordnance (UXO) suffer from unacceptably high false-alarm rates, even at modest probabilities of detection. High false-alarm rates are a consequence of the inability to discriminate real UXO and landmines from man-made and naturally occurring clutter.

The goal of the Defense Advanced Research Projects Agency (DARPA)-sponsored Background Clutter Data Collection Experiment is to provide data which will support the development of techniques that are more adept at discriminating UXO from benign man-made objects. During the fall of 1996 high areal density site surveys were completed using the following sensor types: magnetometer, infrared, electromagnetic induction, and ground-penetrating radar. Preliminary analysis of the data has confirmed that a large number of anomalies evident in the sensor data are indistinguishable from anomalies that are a result of emplaced inert UXO or landmines. The Firing Point 20 site at Fort A.P. Hill exhibits the largest number of these ordnance-like anomalies.

To determine the source of a subset of these sensor response anomalies, a 1-week excavation effort was conducted. The analysis of the data to determine the candidate locations for excavation, the procedures used during the excavation, and the results of the digging are presented.

ACKNOWLEDGMENTS

DARPA and the authors would like to thank the following individuals and supporting organizations for their much needed help during the week allotted for digging: SGT Chandra M. Hartung and SGT Jason R. Harper, Army (EOD) out of Fort Belvoir, Virginia; John Fasulo, Fort A.P. Hill, Virginia; Tommy Berry, Waterways Experiment Station, Vicksburg, Mississippi; MSGT Dunkel, USMC (EOD) out of Quantico, Virginia; Leslie Sowers, Strategic Analysis, Inc., Arlington, Virginia; and Kelly Sherbondy and Christopher Drake, Night Vision and Electronic Sensors Directorate, Fort Belvoir, Virginia.

CONTENTS

I. INTRODUCTION.....	I-1
A. Objective	I-1
B. Site Selection.....	I-2
C. Data Visualization.....	I-2
II. SELECTION OF ANOMALIES AND THEIR EXCAVATION.....	II-1
A. Selection.....	II-1
B. Excavation Technique.....	II-2
III. DIGGING RESULTS.....	III-1
A. Excavation Results.....	III-1
B. Analysis Goals.....	III-9
C. Pre-Dig Surveys.....	III-10
D. Signature Comparisons	III-14
1. EM61 Analysis	III-21
2. Magnetometer Analysis.....	III-28
3. GEM-3 Analysis	III-30
E. Empty Holes.....	III-34
F. Post-Dig Site Maps	III-35
G. Linear Features	III-38
H. Location Accuracy.....	III-38
IV. DATA	IV-1
V. SUMMARY	V-1
REFERENCES	R-1
APPENDIX A—Data Image Catalog of the 10-m × 10-m Portions of the Site.....	A-1
APPENDIX B—Depth Estimation from Magnetic Data using Full-Width Half-Maximum Method	B-1
APPENDIX C—Parsons and Geometrics Location Data Analyses	C-1
APPENDIX D—Summary of Excavation and Object Information	D-1
APPENDIX E—Data Image Catalog of Pre-Dig Survey Data	E-1

FIGURES

1.	Image of Center Square at FP20 Using 0.5-m Vertical Stand-Off Geometrics G-858 Magnetometer Data.....	I-3
2.	Image of Center Square at FP20 Parsons EM61 Induction Coil Data	I-3
3.	Image of Center Square at FP20 Using the Amplitude Response as Computed from the Geophex 4-kHz Response Data.....	I-4
4.	Image of Center Square at FP20 Resulting from the Computation of the Geophex Phase Difference (12 kHz – 4 kHz).....	I-4
5.	Illustration of Method Used to Grid Sensor Data onto a 0.5-m × 0.5-m Uniform Grid.....	I-6
6.	Sensor Data from all Three Sensors for a 10-m × 10-m Region Centered on Registration Target 1	I-7
7.	Sensor Data from all Three Sensors for a 10-m × 10-m Region of the Site Centered on the Location 75.0 m East and 5.0 m North of the Origin.....	I-7
8.	Illustration Depicting the Location of the Three Linear Features Evident in All Three Sensor Data Sets	II-3
9.	Map Depicting Locations that Were Excavated on FP20.....	III-2
10.	OB50—An Example of the Most Common Object Found at the Site: Metal Banding	III-2
11.	OB49—An Example of an M12 Inert AT Landmine as it is Being Measured and Surveyed.....	III-3
12.	OB57—An Example of an Irregularly Shaped, Large Metal Plate.....	III-3
13.	OB68—An Example of a Uniform Disk-Like Metal Plate	III-4
14.	EX-63C—The White Cable Bundle Responsible for Linear Feature B.....	III-4
15.	OB105—The Fuel Tank Found on Site.....	III-5
16.	OB134—A Disk-Like Metal Plate that is Most Likely Composed of Nonferrous Metal.....	III-5
17.	OB107—A Piece of Foil.....	III-6
18.	OB155—An “M19 Danger” Minefield Warning Sign.....	III-7

19.	OB160—Photograph of the Straightest, Longest Piece of Metal Banding Found.....	III-7
20.	EX-172P—The 55-gallon Drum Found 1.0 m Deep with a Front-End Loader	III-8
21.	OB194—A Soda Can of Unknown Brand.....	III-8
22.	OB164—A Spent Round	III-9
23.	Data Image of Parsons EM61 Data	III-11
24.	Pre-Dig Survey Data Taken from Location EX-1; Compare to 10-m × 10-m Centered On [75E, 5N].....	III-13
25.	Pre-Dig Survey Data Taken from Location EX-116; Compare to 10-m × 10-m Centered on [50E, 90N].....	III-13
26.	Comparison of Parsons EM61 Response to M12 Inert Landmines and the Metal Plates Found on the Site	III-23
27.	Parsons EM61 Sensor Response Depicted in 6-m Slices to Objects in the “Tiny” Size Category	III-23
28.	Parsons EM61 Sensor Response Depicted in 6-m Slices to Objects in the “Medium” Size Category	III-24
29.	Parsons EM61 Sensor Response Depicted in 6-m Slices to Objects in the “Medium” Size Category	III-24
30.	Parsons EM61 Sensor Response Depicted in 6-m Slices to Registration Targets.....	III-25
31.	Histogram of Peak Voltage from Parsons EM61 for Object Classes.....	III-26
32.	Histogram of Peak Voltage from Geophex GEM-3 for Object Classes.....	III-26
33.	Histogram of Peak Phase Difference from GEM-3 for Object Classes.....	III-27
34.	Histogram of Peak Field from Geometrics Magnetometer for Object Classes.....	III-27
35.	Geometrics Magnetometer and Modeled Data for OB3.....	III-30
36.	Magnetic Color Plots and Contour Plots for (a) OB2 and (b) OB137	III-31
37.	Magnetic Signature of OB100	III-31
38.	Digitally Altered Image of Center Square at FP20 Using 0.5-m Vertical Stand-Off Geometrics G-858 Magnetometer Data after Anomalies Associated with the Excavated Objects Are Removed from the Data	III-36

- 39. Digitally Altered Image of Center Square at FP20: Parsons EM61 Induction Coil Data after Anomalies Associated with the Excavated Objects Are Removed from the Data..... III-36
- 40. Digitally Altered Image of Center Square at FP20 Using the Amplitude Response as Computed from the Geophex 4-kHz Response Data after Anomalies Associated with the Excavated Objects Are Removed from the Data III-37
- 41. Digitally Altered Image of Center Square at FP20 Resulting from the Computation of the Geophex Phase Difference after Anomalies Associated with the Excavated Objects Are Removed from the Data..... III-37

TABLES

1.	Comparison of Pre-dig 1.0-m EM61 Data with Parsons 0.5-m EM61 Data	III-12
2.	Comparison of Peak Signatures from the M12 Inert Mines	III-15
3.	Comparison of Peak Signatures from the Big Metal Plates.....	III-16
4.	Comparison of Peak Signatures from Objects Classified as Tiny	III-16
5.	Comparison of Peak Signatures from Objects Classified as Small.....	III-17
6.	Comparison of Peak Signatures from Objects Classified as Medium.....	III-19
7.	Comparison of Peak Signatures from Objects Classified as Large.....	III-21
8.	Objects with Outlier Sensor Responses.....	III-28
9.	Magnetic Characteristics of M12s.....	III-29
10.	Registration Object Locations.....	III-32
11.	Ferrous Registration Targets.....	III-33
12.	Aluminum Registration Targets.....	III-33
13.	Metallic Calibration Targets in Yellow Side Bar.....	III-33

I. INTRODUCTION

This report is the result of continued work in support of the DARPA-sponsored Background Clutter Data Collection Experiment, the objective of which is to advance the state of the art in UXO and landmine detection (Ref. 1). Data collection was completed during the fall of 1996 and consisted of high areal density¹ site surveys using the following sensor types: magnetometer, infrared (IR), electromagnetic induction (EMI), and ground-penetrating radar (GPR). Preliminary analyses of the data collected revealed a substantial number of sensor responses that appear to be similar to the response expected from buried UXO or landmines (see Figures 1–4). To determine the source of a subset of these sensor responses, a 1-week excavation effort was conducted.

A. OBJECTIVE

The purpose of digging at the Firing Point 20 (FP20) background site was to learn the following:

- What types of objects are the source of observed anomalies in the Background data set?
- Are the objects similar to UXO or landmines in characteristics (e.g., length to width ratio, composition, manufacturing process, etc.) or are they simply unrelated man-made objects (e.g., fence material, nails, engine parts, etc.)? Also, what constitutes similar and what can be exploited in the data to distinguish “similar” items from “nonsimilar” items to reduce the false-alarm rate?
- What digging procedure is necessary to determine the source of an anomaly?
- Is it possible to uncover the source of an anomaly? If not, is it because of the poor location accuracy of the data or because of difficulties locating the source? If so, are anomalies produced by anthropic objects or geological features?
- Does digging at anomaly locations reveal enough useful information to warrant future excavations?
- Is the selected site indeed free of UXO as stipulated in the original experiment design?

¹ The data is high areal density relative to standard survey data densities in 1996.

Because the criteria for site selection during the design of the Backgrounds experiment was that the site must be free of any UXO or related items, we expected that all of the anomaly sources selected for excavation were man-made objects unrelated to UXO. In particular, we assumed that we would not find training rounds, fragmentation debris, duds, and spent shells or landmines. The data collected from FP20 produced a large number of anomalies that exhibit the same characteristics as buried UXO and thus in a real-world scenario using current technology would have to be excavated.

B. SITE SELECTION

The FP20 site was selected for initial digging because it is the most cluttered of the four background sites, offering many interesting anomalies in the data sets. FP20 is also the most geologically altered of the four sites: early in the program it was necessary to fill large holes on the FP20 site to allow for uninterrupted survey by vehicle sensor systems; after the surveys were complete a gravel road was built that currently crosses the northwest corner of the site.

We determined candidate anomaly locations for excavation, placing emphasis on magnetometer and EMI sensor data sets because the GPR and IR data sets are far more complex and difficult to analyze. To support the selection of metallic anomalies, we considered the following data sets:

- Geometrics, Inc., G-858 magnetometer at a height of 0.5 m above the ground (“magnetometer”)
- Geophex, Inc. GEM-3 (“GEM-3”)
- Parsons Engineering Science 0.5-m Geonics EM61 using the response from the upper receive coil (“EM61”)

As a result, this excavation exercise provides information about metallic anomalies and the value of such a digging effort. If we learn a great deal from the metallic anomalies, additional analyses can be performed to identify uniquely GPR anomalies to support future excavation efforts.

C. DATA VISUALIZATION

Figures 1–4 show the sensor responses in the clutter portion of the site, the center square, for each of the sensors considered. These images were generated from sensor

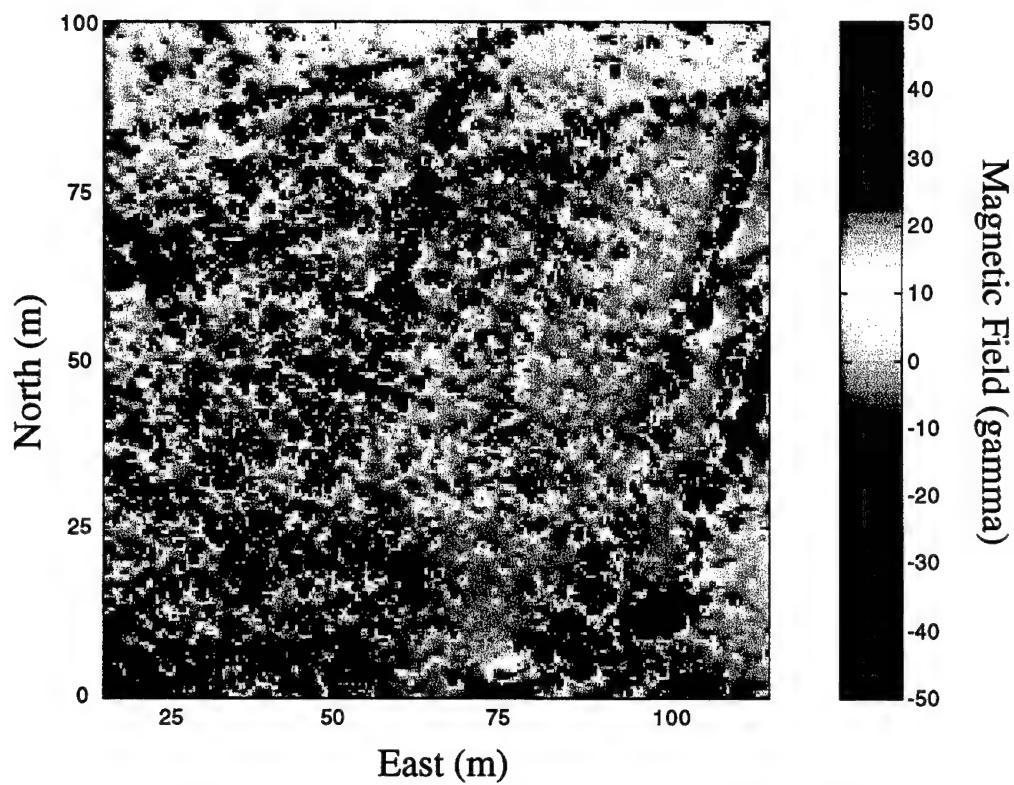


Figure 1. Image of Center Square at FP20 Using 0.5-m Vertical Stand-Off Geometrics G-858 Magnetometer Data

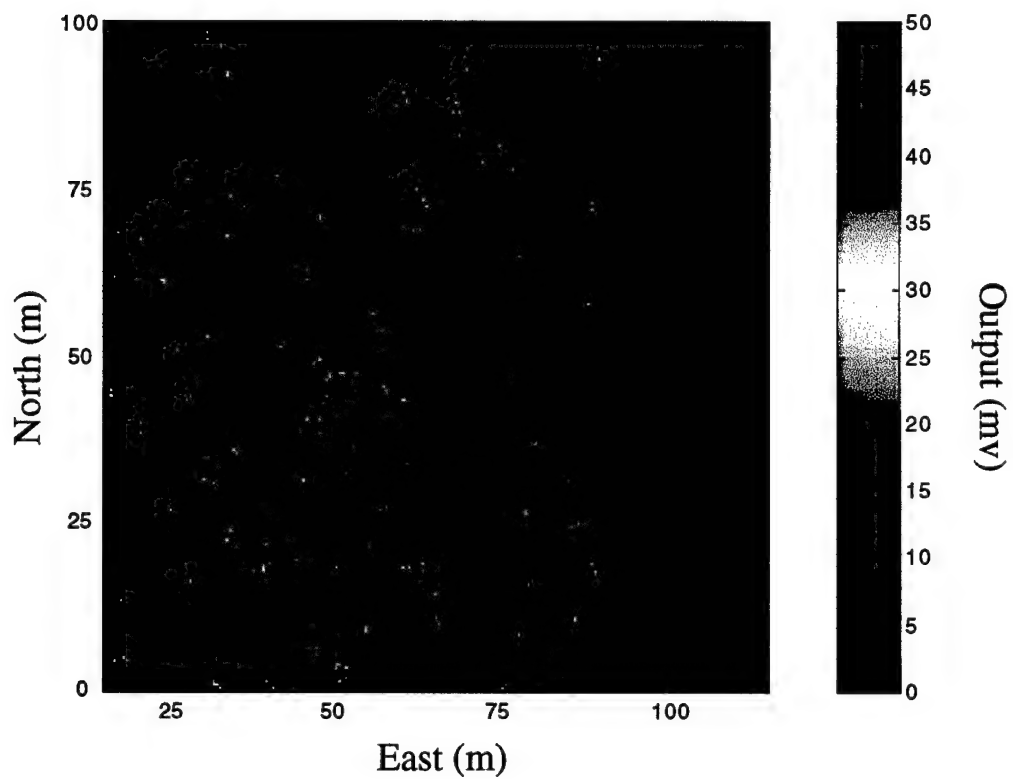


Figure 2. Image of Center Square at FP20 Parsons EM61 Induction Coil Data

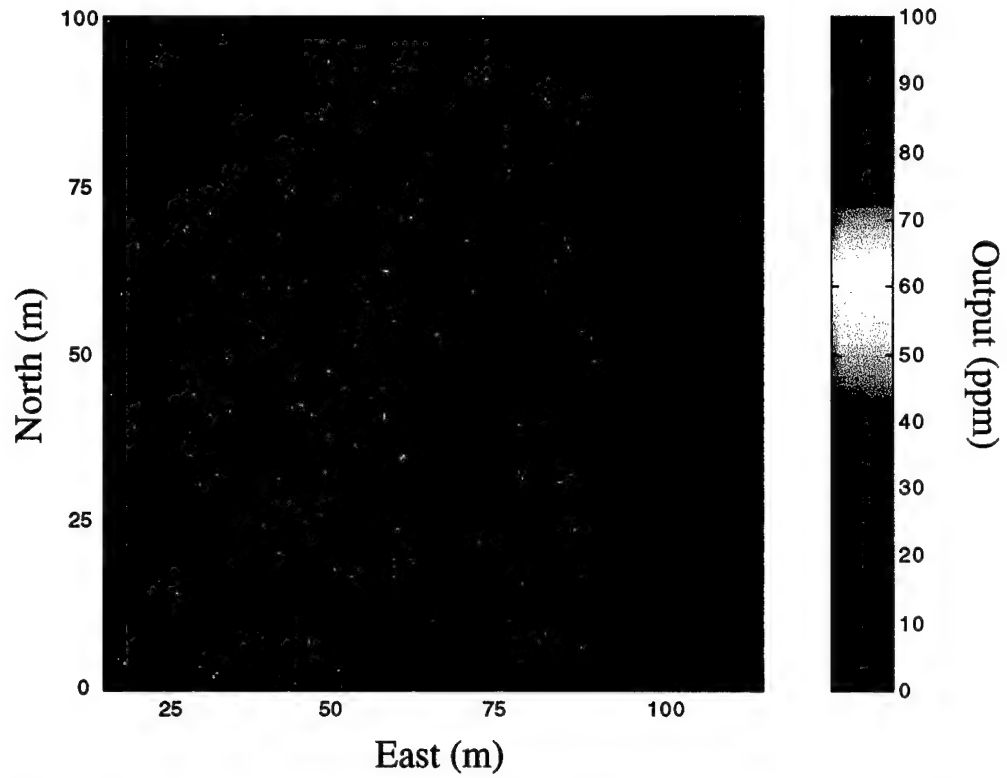


Figure 3. Image of Center Square at FP20 Using the Amplitude Response as Computed from the Geophex 4-kHz Response Data

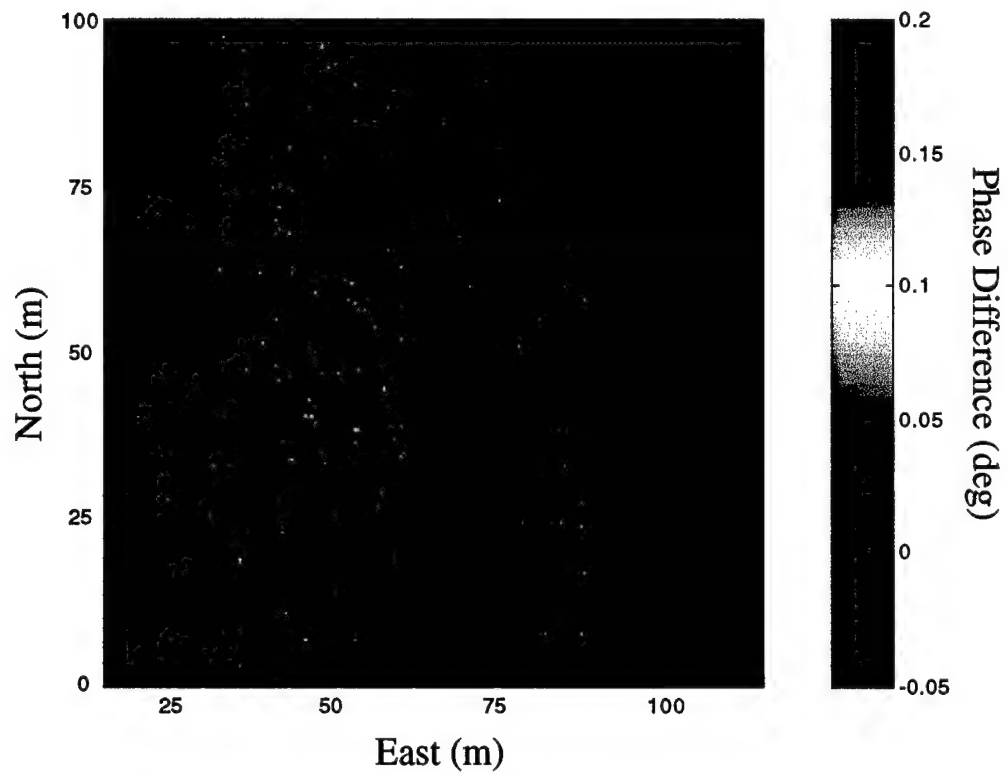


Figure 4. Image of Center Square at FP20 Resulting from the Computation of the Geophex Phase Difference (12 kHz – 4 kHz)

responses interpolated onto a 0.5×0.5 -m grid.² The along line (north or south direction) data spacing for all three sensors was less than 0.5 m, but the use of square pixels greatly simplified the analysis. Thus the pixels to be filled were linearly interpolated from the values of the two nearest values (see Figure 5).

All of the data was processed using the location data provided by each contractor. The magnetometer location data is the most accurate of the four data sets considered; the deviation from the actual is estimated to be less than ± 0.5 m. The 0.5-m EM61 data set is estimated to have positional inaccuracies ranging from 0.0 to 0.75 m. The GEM-3 data set location inaccuracies are on the order of 1.0 m but have been observed to deviate from the actual location by much more than that. The GEM-3 location data was provided using a pure dead-reckoning technique for each 100-m pass.

The magnetometer data came from a 6-element G-858 magnetometer array. The data considered was only that from the two sensors positioned 0.5 m above the ground.

The GEM-3 sensor provides data at two frequencies: approximately 4 kHz and 12 kHz. The 4-kHz data set was chosen as the representative peak signal amplitude A for the GEM-3 sensor. It should be noted that the results presented here would not differ significantly had we chosen the 12 kHz data set for the amplitude intensity comparisons. The amplitude response was computed for the GEM-3: $A = \sqrt{I^2 + Q^2}$, where I refers to the in-phase response and Q refers to the quadrature response. The in-phase and quadrature data supplied by the GEM-3 system are converted into a part-per-million (ppm) unit, defined as:

$$\text{ppm} = 10^6 * \frac{\text{secondary magnetic field at receiver coil}}{\text{primary magnetic field at receiver coil}} \text{ (Ref. 4).}$$

The GEM-3 phase-angle difference is computed as the difference in the measured phase between the 12-kHz and the 4-kHz data set. The phase-angle difference is computed to be $\beta - \alpha$, where β is the 12-kHz phase angle and α is the 4-kHz phase angle. It is expected that the phase response of the GEM-3 sensor will be dependent on the ferrous content (magnetic permeability) as well as the conductivity and size of the source

² For all sensors, the data density in the east direction (cross-track) is two per meter. The density in the north direction (along track) was between 5 and 10 per meter. The along-track data was interpolated, resulting in smoothing in that direction only.

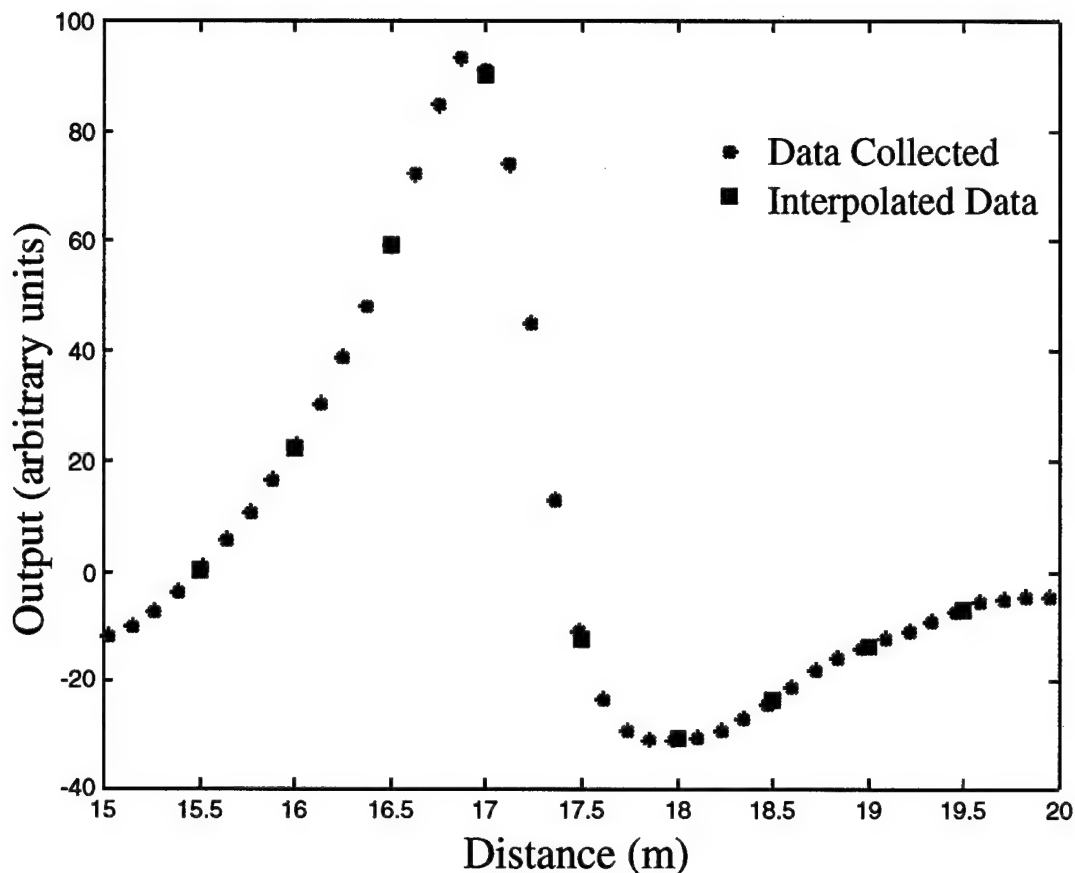


Figure 5. Illustration of Method Used to Grid Sensor Data onto a 0.5-m \times 0.5-m Uniform Grid

object. Using this phase-angle convention, a simple rule can be established: a negative phase-angle difference is indicative of a nonferrous material such as aluminum, and a positive phase-angle difference is indicative of ferrous items such as those containing iron.³ This can be seen in Figure 6, where the iron registration target appears in the GEM-3 data set as a positive phase-angle (red) anomaly, and the aluminum registration target appears as a negative phase-angle (blue) anomaly.

The anomaly selection process was aided by creating a color image of a 10-m \times 10-m area for each of the three sensors (see Figure 7). In addition, for many of these 10-m \times 10-m areas, a 3-D mesh plot was created to assist in the analysis of the sensor responses. These images were generated for all 10-m \times 10-m areas of the center square and are provided in Appendix A.

³ This is not always the case. The phase angle change is dependent on size, but this is ignored for this assessment because in general the sizes of the objects detected exhibit this aforementioned phase response.

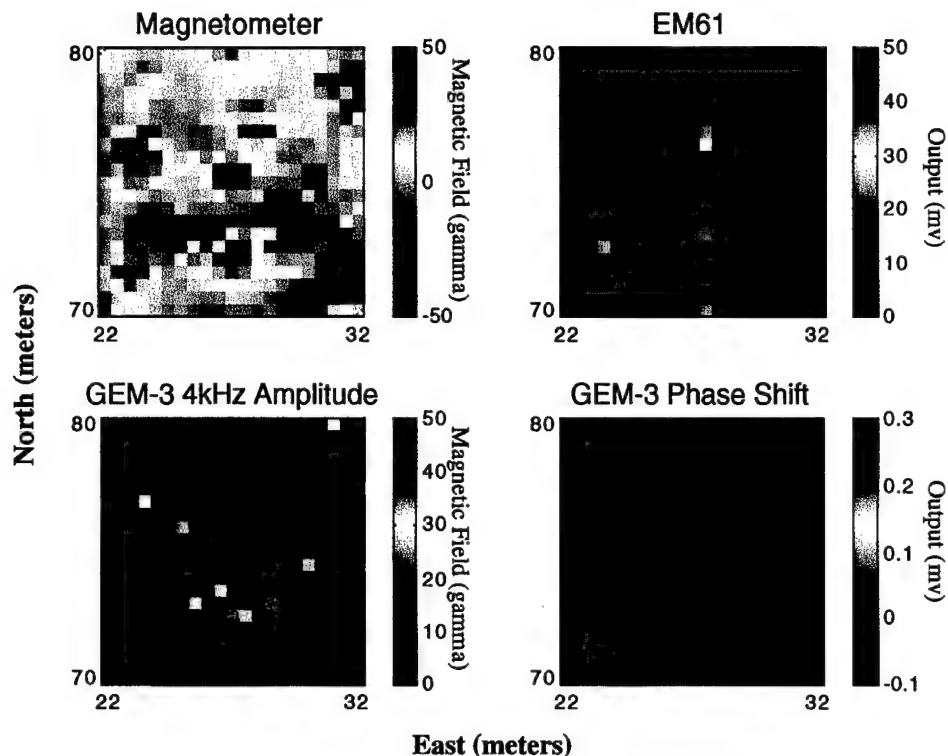


Figure 6. Sensor Data from all Three Sensors for a 10-m \times 10-m Region Centered on Registration Target 1

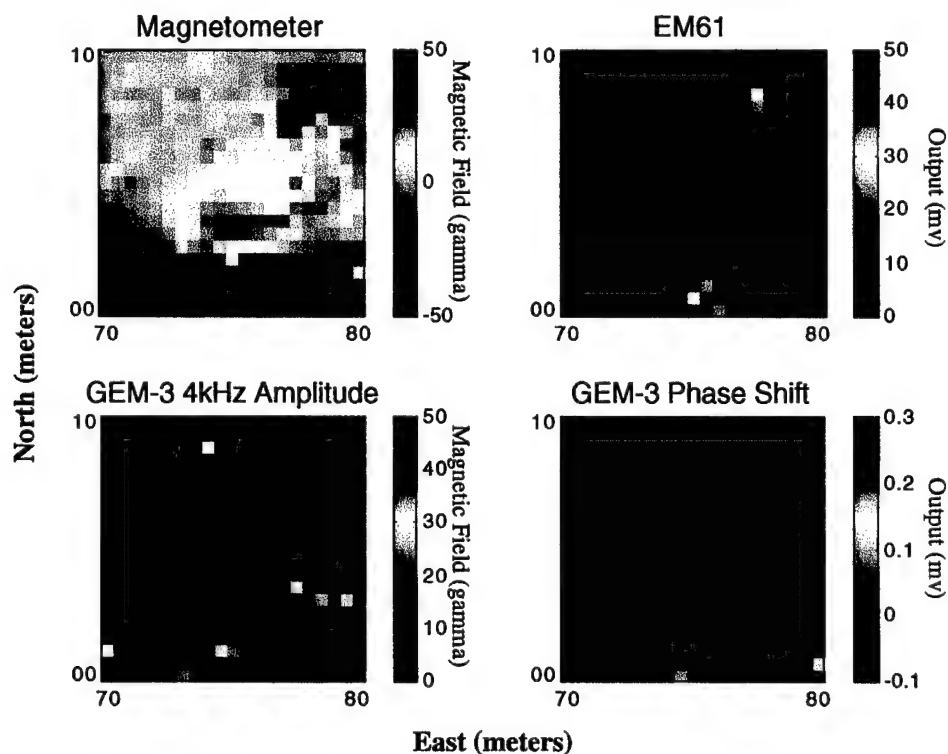


Figure 7. Sensor Data from all Three Sensors for a 10-m \times 10-m Region of the Site Centered on the Location 75.0 m East and 5.0 m North of the Origin

II. SELECTION OF ANOMALIES AND THEIR EXCAVATION

A. SELECTION

The process of selecting anomalies for excavation began by identifying large amplitude anomalies from the magnetometer data set. Of the large targets selected, we eliminated those that appeared to be due to a deep target, as estimated by the full-width, half-maximum (FWHM) location of the anomaly signature using the mesh plots. (Appendix B describes this method of depth estimation.) The depth estimation was intended to prevent the selection of targets greater than 1-m deep, since the excavation would be done by hand and holes deeper than a meter are difficult and time consuming to excavate with a shovel. In addition, most clutter experienced by landmine and UXO systems is present in the first meter of soil. In most cases, we required that a magnetometer anomaly be accompanied by a large signature in both the EM61 and GEM-3 data sets. In retrospect, we never experienced an exception to this rule—all large and shallow magnetometer responses that we investigated were accompanied by large EM61 and GEM-3 responses. In fact, the depth criteria is supported by the EM61 data: the magnetometer can “see” more deeply than the EM61, and those signatures that appeared to be from deeper objects in the magnetometer data set had reduced or nonexistent responses in the EM61 data set. The GEM-3 is expected to be more sensitive to shallow objects; thus, during the anomaly-selection phase, the GEM-3 data was used to confirm that an object was near surface. In addition, the phase response of the GEM-3 was used to estimate whether an object was ferrous.

After selecting large anomalies, the following additional types of anomalies were selected for excavation:

- Atypical magnetic dipole orientation. We typically observe the direction of the magnetization of UXO and mines to be such that its projection on the geomagnetic field is parallel to the geomagnetic field. We observe cases where clutter (and on rare occasions UXO/mines) have projections anti-parallel to the geomagnetic field.
- Large GEM-3 response with small responses from both the magnetometer and EM61 data set.

- GEM-3 strong negative phase response.
- GEM-3 strong positive phase response.
- Parts of all three of the linear features evident in all three data sets (see Figures 1–4).
- Very small isolated anomalies (where the anomaly can be small or nonexistent in any combination of the three sensors).
- Combinations of responses that do not seem to be intuitive; for example, a strong response from one of the three sensors and a small or nonexistent response from the other two sensors.
- Combinations of responses that seem to make sense; for example, a weak magnetic signature, a strong EM61 response, and a strong negative phase angle difference. The object would be expected to be a nonferrous object.
- Signatures that have features similar to those of targets in the Side Bars or Registration targets.
- Signatures that seemed to indicate small, shallow metallic debris on top of more deeply buried larger items. For example, a large extended magnetic dipole signature indicating a deeply buried large object accompanied by a sharp strong response in the GEM-3 data set.
- A few anomalies that were expected to be deeply buried.
- A number of M12 inert landmines were uncovered after digging commenced. New anomalies were excavated based on their similarity to the M12 signatures, as well as anomalies that seemed to be located in the pattern that might be expected if the M12 mines were laid out as a minefield.

B. EXCAVATION TECHNIQUE

The following method was used to excavate each selected anomaly:

1. The location of the anomaly was found using Real-Time Kinematic Differential Global Positioning System (RTK DGPS) and a plastic flag was placed within 5 cm of the location.
2. A Geonics EM61 EMI system with a 1-m coil size and a GEM Systems, Inc., GSM-19 proton precession magnetometer were used to collect sensor data on a 0.5-m grid from a 3-m x 3-m area immediately surrounding the flagged location.
3. To help guide the digging process, a Fisher model M-95 metal detector was used to find the location of metallic objects. In general, targets were no more than 20 cm from the flagged location. However, the use of the metal detector might have been misleading since it only detects very shallow (depending on

the amount of metal) objects. But it was psychologically satisfying to use this technique rather than digging at the flagged location given the expected 0.5-m inaccuracy in the location data. Furthermore, real-time assessments of the objects uncovered generally resulted in convincing agreement between the anomaly and the type of object discovered. The most satisfying agreement came with the discovery of a buried cable bundle along linear feature B (see Figure 8).

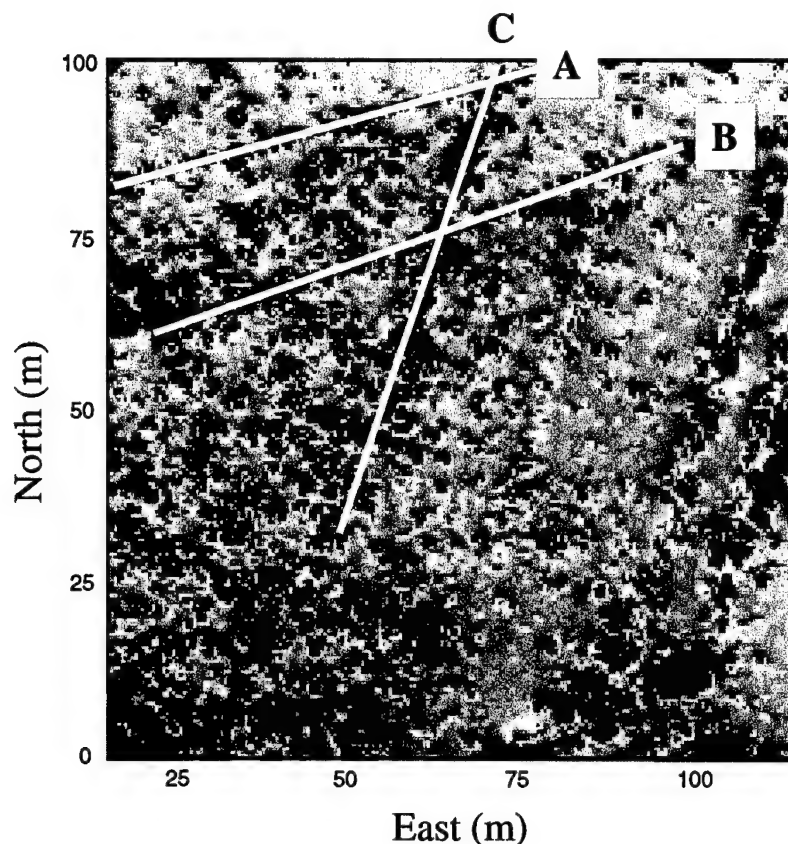


Figure 8. Illustration Depicting the Location of the Three Linear Features Evident in all Three Sensor Data Sets

4. After the presence of metal was confirmed with the hand-held metal detector, a shovel was used to remove dirt and vegetation until the item was found. In the case of large, shallow items this was a simple process. In the case of small items, repeated interrogation with the metal detector was necessary and in many cases small items (on the order of a 3-cm \times 1-cm piece of metal) were removed from the hole and later found in the pile of excavated dirt. This happened frequently if the metal was rusted and of irregular shape, making it difficult to distinguish from rocks and clumps of soil. Digging continued until the object was uncovered or a depth of 1 m had been reached. If the object uncovered was smaller than the data suggested, its position was

recorded, and the object was moved to determine if larger or additional objects remained underneath the extracted object. For deep objects, digging commenced at the flagged location, and the use of the metal detector was postponed until after a substantial hole was dug.

5. Some of the excavation work during the week was filmed using a hand-held video camera. All uncovered objects were given a unique identification number, recorded, and photographed. In addition, written description of the objects was recorded including object dimensions, hole dimensions, object depth, and physical description. Appendix C is a summary of the information collected for each object; the data are also available on CD-ROM as an Excel Worksheet. All of the object photographs are also provided on CD-ROM available from Walcoff and Associates upon request. Figures 10–22 are examples of the photographs. The pink survey tape (used to record the object identification numbers) shown in each image is 3-cm wide.
6. After all objects from each hole were uncovered, the location of each object was surveyed using RTK-DGPS with accuracy better than 1 cm. In the case of round or approximately square objects, the center of the object was surveyed. For extended objects or objects with elongated irregular shapes, the corners and ends were surveyed. Care was taken not to move the object during digging to ensure an accurate record of its location.
7. Most of the smaller objects were placed in plastic bags, taken off-site, and archived. The larger objects were taken off-site to an area in the woods for unsecured storage.
8. All of the dirt removed from the holes was placed on heavy-gage plastic placed next to the hole. After all the objects were removed from the holes, the holes were refilled and the plastic was removed from the site and properly disposed of at the Fort A.P. Hill plastic recycling repository.

III. DIGGING RESULTS

In total, 101 holes were dug and 203 objects uncovered. With the exception of the cable bundles, none of the discovered objects were left on the site. Of the 203 objects recovered, 14 were inert landmines; of those, 12 were identical M12 landmines.¹ Seven of the objects were minefield warning signs, one of which was in good enough condition to read the following: "M19 Danger." The M19 is a plastic AT mine; it is not possible to reliably detect that mine with current technology. Thus, there are two possible scenarios: there remains an M19 minefield at FP20, or the mine signs were used either out of error or necessity to flag the minefield of M12 mines.

A. EXCAVATION RESULTS

Figure 9 shows the locations that were excavated at the site. The red lines indicate linear features known to be buried wires. The locations of the M12 mines are shown as light blue circles. The two other mine types found on the site are shown as triangles in hot pink. The mystery hole, EX-128P, is shown as a hot pink square. The locations where old minefield warning signs were found are shown as green diamonds. Objects that are larger than a meter can be seen as connected dots.

The objects found at the site include metal banding, metal scrap, car parts, communications wire, training rounds, metal plates, two fence posts, one soda can, one piece of foil, one 55-gallon drum, and one fuel tank. In terms of number, the most abundant item (64 percent) discovered at the site was metal banding. A close second was the scrap category; in most cases these items were either too mangled or too small to be identified. The single items and other selected objects are shown in Figures 10–22. The 55-gallon drum was flattened. The soda can was not a recognizable brand, suggesting that it was quite old. The fuel tank was identified from the vapors released as it was uncovered.

¹ One of the inert M12s, OB168, was rusted to the extent that it was obvious that the mine was filled with sand rather than explosives.

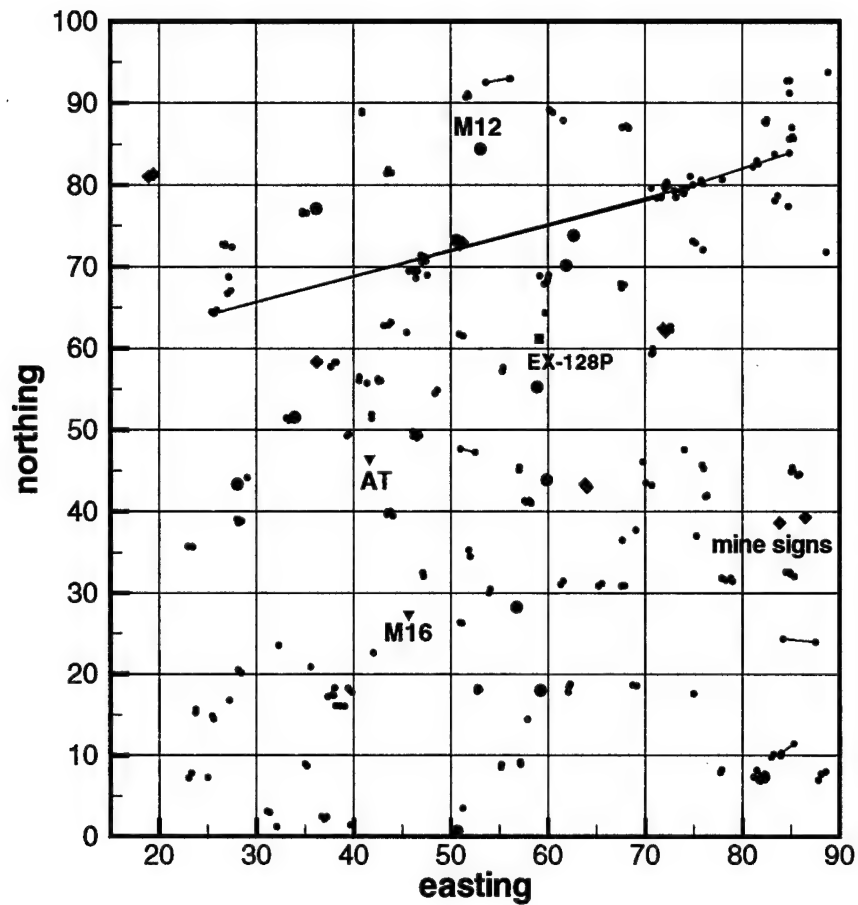


Figure 9. Map Depicting Locations that Were Excavated on FP20



Figure 10. OB50—An Example of the Most Common Object Found at the Site: Metal Banding

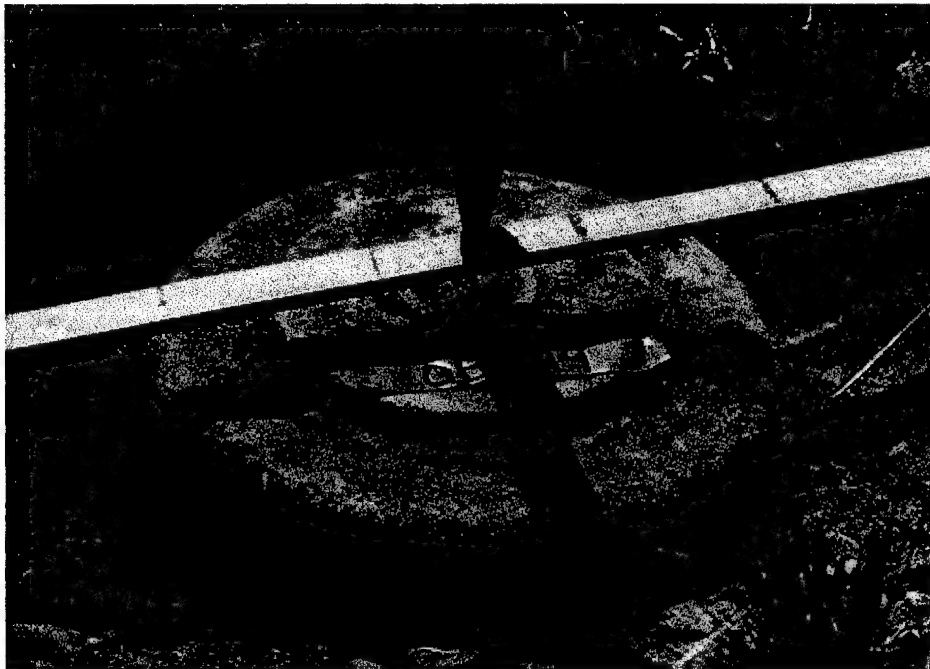


Figure 11. OB49—An Example of an M12 Inert AT Landmine as it is Being Measured and Surveyed



Figure 12. OB57—An Example of an Irregularly Shaped, Large Metal Plate



Figure 13. OB68—An Example of a Uniform Disk-Like Metal Plate



Figure 14. EX-63C—The White Cable Bundle Responsible for Linear Feature B



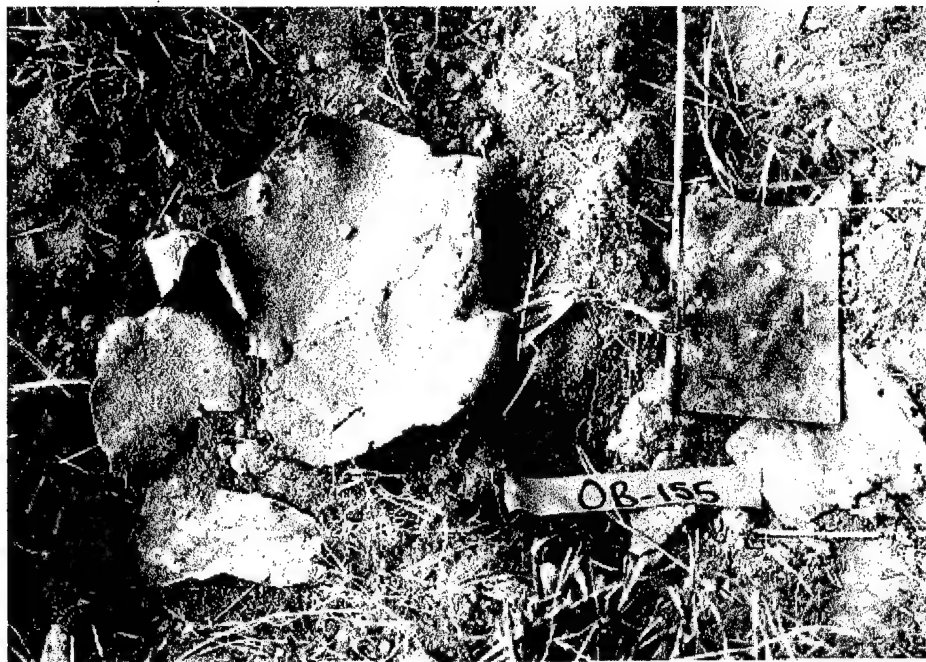
Figure 15. OB105—The Fuel Tank Found on Site



Figure 16. OB134—A Disk-Like Metal Plate that Is Most Likely Composed of Nonferrous Material



Figure 17. OB107—A Piece of Foil



**Figure 18. OB155—An “M19 Danger” Minefield Warning Sign.
This was the sign that was in the best condition of the seven found.**



**Figure 19. OB160—Photograph of the Straightest, Longest Piece of Metal Banding
Found. Used to estimate line-to-line location accuracy.**



Figure 20. EX-172P—The 55-gallon Drum Found 1.0 m Deep with a Front-End Loader



Figure 21. OB194—A Soda Can of Unknown Brand



Figure 22. OB164—A Spent Round

B. ANALYSIS GOALS

The digging data analysis addresses the following issues and questions:

- Do the GSM-19 magnetometer and EM61 data collected during the excavation show a good correlation to the sensor data used to determine which anomalies to dig?
- How similar are the M12 landmine signatures to each other in each of the three contractor data sets?
- How similar are the M12 landmine signatures to the large metal plates found at the site?
- Does the GEM-3 phase response predict the composition of the buried item?
- How does the signature data from clutter objects compared to buried targets in the Side Bars and the M12 landmines?
- Is there a correlation among object size, sensor response strength, and spatial extent?
- Are there any uncovered objects for which there is no reasonable explanation for the sensor response?
- Can a minimum detectable object size and depth be estimated for each of the sensors given this digging data set and does that estimate correlate well with the expected sensor performance?

- Can sensor response maps of the site be estimated by eliminating the target signatures that were excavated?
- Can additional information be gleaned from the data set regarding the location accuracy of the three data sets used?
- Are all linear features the result of buried wires or cables?

C. PRE-DIG SURVEYS

During the design of the digging experiment there was concern that the digging locations could not be located accurately enough to ensure that the object excavated was the source of the anomaly in the data. This concern arose from the observed location errors for the site registration targets. To address this concern, before digging selected excavation areas, an EM61 1-m EMI system² and GSM-19 proton precession magnetometer were used to survey a 3-m \times 3-m area centered on the flag that marked the planned digging location. This pre-dig survey data was compared to the contractor data, (collected in 1996 and used to select anomalies) to assure that we had located the same anomaly detected by the contractor. In addition, coverage maps from the laser tracker data set were used to assure that the contractors had indeed surveyed the area since the data image was interpolated and small coverage gaps will not be apparent. Figure 23 shows a coverage map for the Parsons EM61 survey overlaid with 3 m \times 3 m white squares centered on the excavation locations that were surveyed by the EM61 and GSM-19 just prior to excavation. Appendix E gives color images of the pre-dig data, which is also available on CD-ROM.

When comparing the pre-dig survey data set to the contractor data set it was usually necessary to shift the location of the anomaly as shown in Table 1. In most cases the general shape and signal intensity of the anomaly was comparable in both data sets. Figures 24 and 25 show examples of the pre-dig data (images on the left side of the figures) and can be compared to the contractor data shown in the images on the right hand side of the figures.

It should be noted that a one-to-one correspondence is not expected because of the different transmit fields, coil sizes, receive electronics, and the height of measurement relative to the optimal sensor height. When there were differences in the two data sets, the noted difference came in the form of a larger response in the pre-dig data set.

² We will refer to the 1-m EM61 data collected just prior to excavation as EM61 or the pre-dig data. This differs from the 1/2 m EM61 data collected by Parson in 1996.

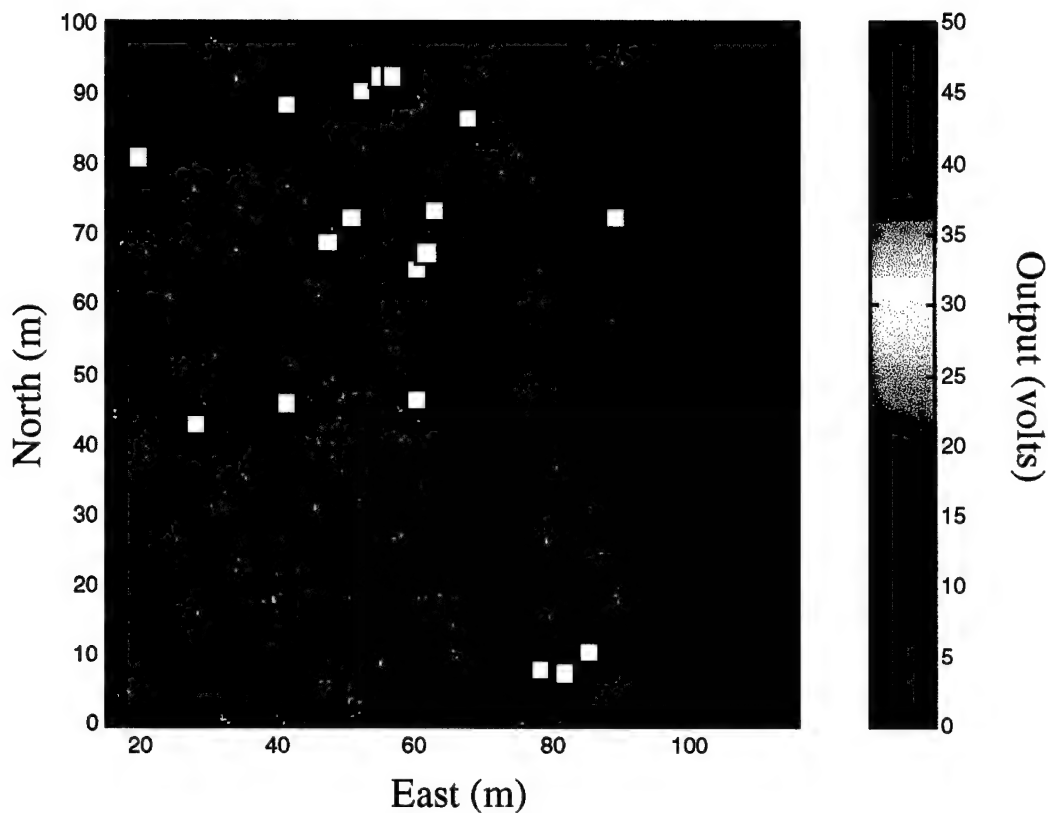


Figure 23. Data Image of Parsons EM61 Data. The white squares indicate the areas where pre-dig surveys were taken.

The most extreme example of location differences between the two data sets is EX-116 (Figure 25); Table 1 shows that a 50-mV reading was determined for each data set, but the 0.5-m EM61 data set was shifted by 1.5 m to obtain this match. The source of this location discrepancy is unknown.

The observed trend in signal differences may be explained by comparing the types of objects. The larger objects, which produce the larger signals, were most likely to exhibit differences in signal strength. Perhaps these differences can be explained by fundamental differences in the two sensors. The EM61 used for the pre-dig surveys was a full 1-m set of coils, but the EM61 used by Parsons was a modified EM61, using 0.5-m coils positioned at the same height as the 1.0-m EM61.

Despite the differences between the two EM61s, we feel that the survey method is the most significant source of the signal variations observed. The pre-dig EM61 surveys were more controlled; data were collected every 0.5 m using a grid painted on the site

Table 1. Comparison of Pre-dig 1.0-m EM61 Data with Parsons 0.5-m EM61 Data

Pre-Dig Excavation ID Number	Associated Object ID Numbers	Maximum 1.0-m EM61 response (mV)	Maximum 0.5-m EM61 response (mV)	Comments on 0.5-m EM61 Coverage	1.0-m EM61 Compared to 0.5-m EM61 Spatial Extent
EX-1	OB1	90	80		similar
EX-6	OB63-64 (M12)	700	400		similar
EX-7	OB3 (M12)	700	300	not complete	bigger
EX-8	OB58-60	20	20		similar
EX-16	OB112	800	275		similar
EX-17	OB11-16	100	450		similar
EX-18	OB8	500	360	not complete	bigger
EX-77	OB78	20	15		similar
EX-105	OB48 (M12)	600	270	not complete	similar
EX-107	OB47	20	30		bigger
EX-112	OB46	40	60		similar
EX-116	OB19	50	50	location inaccuracy	bigger
EX-117	OB20, OB21	1.5	13		similar
EX-118	OB22	0	0		similar
EX-121	OB50-52	15	30		similar
EX-125A	OB199	15	20		similar
EX-125B	-	60	-		similar
EX-126	OB81-82	15	8		bigger

before the survey.³ On the other hand, the 0.5-m EM61 was dragged across the site as part of a complete site survey using tapes and cones. Thus, it is likely that slight navigation inaccuracies could have caused small portions of the site to be missed or produce suboptimal positioning of the coils for detection of particular objects.⁴ This is apparently the case for holes EX-7, EX-18, and EX-105.

In contrast to the EMI data, comparison of the magnetometer data sets revealed a near-perfect match. In conclusion, it is clear that we were digging at the source of the anomaly observed in the original data sets.

³ Contactors were not permitted to use paint to aid in their site surveys.

⁴ It should be remembered that the induced signature from the object under ground is highly sensitive to the position of the transmit and the receive coils of the EMI system

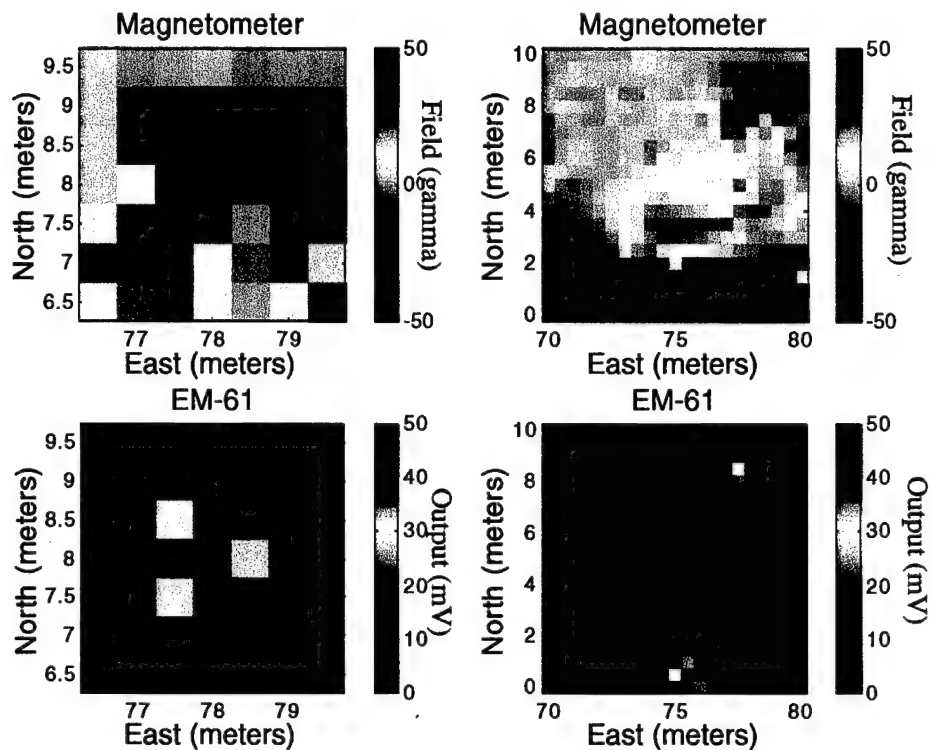


**Figure 24. Pre-Dig Survey Data Taken from Location EX-1;
Compare to 10 -m x 10-m Centered On [75E, 5N]**

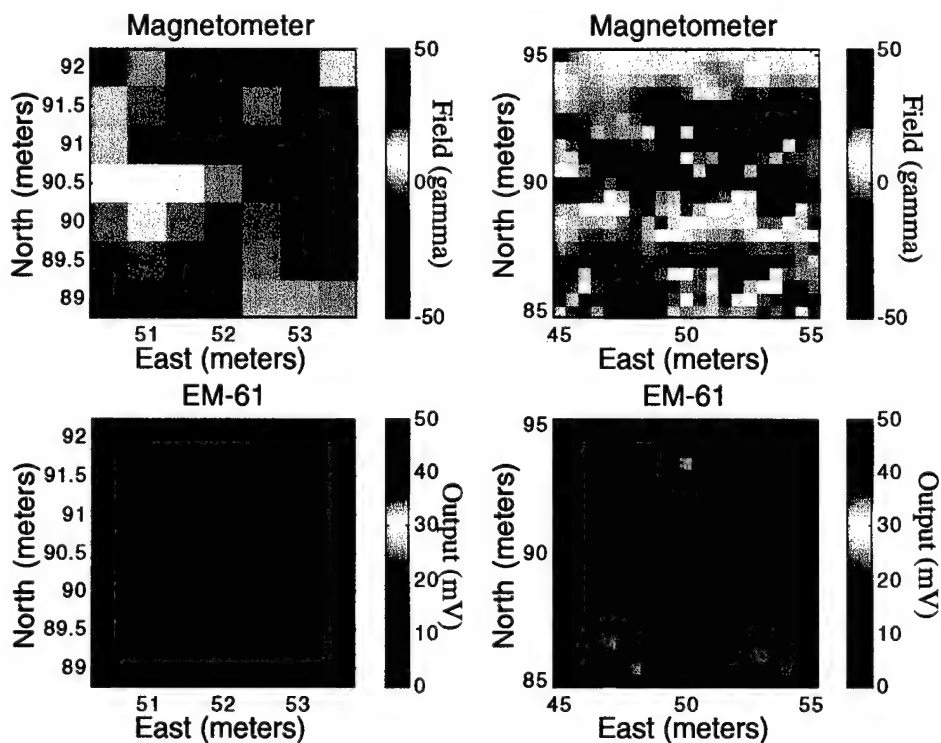


**Figure 25. Pre-Dig Survey Data Taken from Location EX-116;
Compare to 10 -m x 10-m Centered on [50E, 90N]**

D. SIGNATURE COMPARISONS

To compare signatures resulting from different objects, the features to be compared must be defined. The features chosen in this study were the simplest and most obvious: peak signal strength or phase-angle difference and spatial extent. These parameters were determined using the data from each set displayed in twelve 6-m traces along the survey direction (north-south) and twelve 6-m traces perpendicular to the survey direction (east-west). We call these traces 6-m data slices. In addition the general shape of the magnetic signature was also used as a feature. The search for reliable and sophisticated features that can be exploited for discrimination is the focus of other research efforts that are currently being conducted using this data set.

Tables 2 through 7 give peak (maximum) signal strengths for each of the four data sets for a number of different object categories. Object categories were determined empirically. The following list defines approximate object dimension ranges for each category used.

- Tiny —M16 round or less
- Small —fits in a 20 cm \times 20 cm square
- Medium —banding 40 cm–60 cm \times 4 cm or approximate equivalent amount of metal
- Small —fits in a 20 cm \times 20 cm square
- Large —1.0 m or longer banding, item larger than the big metal plates

Note that this categorization based on object size may be misleading as future successful discrimination algorithms may be based on other properties.

In the case of data sets that have both positive and negative peak values, the maximum is determined for the absolute value, but the sign is maintained in the table. The peak signals were determined by selecting the largest absolute value of the sensor data within 1.5 m of the given location. In some cases this resulted in the selection of a peak signal that was caused by a nearby anomaly with a larger signature amplitude. These signatures were eliminated and are marked TCTBO.⁵ Discussion of signature comparisons will be organized by the sensor type. Note that the magnetometer has a peak signature that ranges from a large positive value to a large negative value. The sign assigned to the peak signature is really a measure of the orientation of the dipole moment

⁵ TCTBO = Too Close To a Bigger Object. This indicates that objects in this table are smaller than an object they are very near to, with the signature being dominated by the larger object.

relative to the geomagnetic field. Thus, there is some utility to looking at the absolute value of the peak signature, which is also given in the tables. Figure 26 through 30 show us figures of the data presented in Tables 2-7. Figure 31 through 34 show histograms of each of the size categories as a function of sensor type.

Table 2. Comparison of Peak Signatures from the M12 Inert Mines

Identification Number	0.5-meter EM61 (mv)	GEM-3 Phase Δ (deg)	4-kHz GEM-3 (ppm)	Magnetometer ⁺ (gamma)
OB3	301.26	0.40	1,514.27	196.06
OB4	204.48	-0.16	973.05	241.03
OB48	269.36	0.15	392.63	-444.57
OB49	274.54	0.39	918.75	244.93
OB63	408.78	0.08	484.44	-151.35
OB77	370.89	0.23	874.30	216.41
OB104	389.55	-0.14	1,041.44	144.38
OB113	383.36	0.44	780.38	211.20
OB119	222.88	0.96	1,119.93	211.50
OB166	234.64	0.14	705.97	163.90
OB168	471.17	0.40	867.97	681.63
OB169	403.50	0.55	1,021.02	204.29
Average	327.87	0.29	891.18	159.95 (259.3)
Std. Dev.	87.10	0.31	293.70	262.90 (153.9)
Minimum	204.48	-0.16	392.63	-444.57 (144.8)
Maximum	471.17	0.96	1,514.27	681.63

+ The values in parentheses are determined taking the absolute value of the magnetic field.

Table 3. Comparison of Peak Signatures from the Big Metal Plates

Identification Number	0.5-m EM61 (mv)	GEM-3 Phase Δ (deg)	4-kHz GEM-3 (ppm)	Magnetometer* (gamma)
OB5	539.71	-0.09	1,008.36	218.54
OB57	207.04	0.21	884.71	-180.12
OB68	200.07	-0.08	537.65	-97.65
OB85	153.63	-0.12	728.90	175.82
OB130	83.15	0.08	514.97	114.39
OB134	58.07	-0.25	1,062.83	38.81
OB138	273.41	0.12	1,022.44	718.93
Average	216.44	-0.02	822.84	141.25 (220.61)
Std. Dev.	160.67	0.16	231.16	292.25 (227.8)
Minimum	58.07	-0.25	514.97	-180.12 (38.81)
Maximum	539.71	0.21	1062.83	718.93

* The values in parentheses are determined taking the absolute value of the magnetic field.

Table 4. Comparison of Peak Signatures from Objects Classified as Tiny

Identification Number	0.5-m EM61 (mv)	GEM-3 Phase Δ (deg)	4-kHz GEM-3 (ppm)	Magnetometer* (gamma)
OB148	6.14	0.03	27.26	- 43.35
OB162	- 4.23	0.01	25.90	15.66
OB167	9.01	0.04	37.58	- 56.27
OB173	12.23	0.09	77.14	26.00
OB175	12.23	0.02	27.99	26.00
OB176	12.23	0.09	77.14	26.00
OB180	31.36	0.06	53.37	77.17
OB199	19.79	0.11	94.68	132.01
OB200	17.10	0.10	99.61	56.47
OB201	6.12	0.04	95.96	412.14
Average	12.20	0.06	61.66	67.18 (87.11)
Std. Dev.	9.44	0.04	30.61	132.75 (119.20)
Minimum	- 4.23	0.01	25.90	- 56.27 (15.66)
Maximum	31.36	0.11	99.61	412.14

* The values in parentheses are determined taking the absolute value of the magnetic field.

Table 5. Comparison of Peak Signatures from Objects Classified as Small

Identification Number	0.5-m EM61 (mv)	GEM-3 Phase Δ (deg)	4-kHz GEM-3 (ppm)	Magnetometer ⁺ (gamma)
OB20	12.79	0.06	54.21	137.74
OB33	21.77	0.05	79.73	-92.34
OB38	13.54	0.06	58.39	-141.90
OB39	-3.00	0.01	18.00	-101.97
OB40A	-3.54	0.02	23.53	-101.97
OB41	-2.97	0.01	12.97	-101.97
OB42	14.11	0.30	191.07	57.64
OB44	14.00	0.30	191.07	57.64
OB53	29.01	0.06	48.41	109.44
OB59	19.54	0.36	211.46	-145.55
OB72	40.48	0.42	366.91	140.74
OB79	22.18	0.14	101.24	130.84
OB82	7.77	0.01	14.21	44.87
OB90	22.97	0.04	28.00	57.87
OB102	30.63	0.05	41.32	-33.89
OB103	30.63	0.05	41.32	-33.89
OB106A	9.76	0.26	165.53	-106.09
OB107	9.91	-0.06	343.75	65.28
OB108	25.91	0.09	62.82	65.28
OB114	11.10	0.06	48.41	109.44
OB116	26.74	0.75	366.13	-109.84
OB123	-4.24	0.05	57.83	43.60
OB124	-4.24	0.05	57.83	43.60
OB125	8.26	0.32	229.62	43.60
OB126A	8.26	0.04	40.79	38.56
OB129	19.43	0.09	93.95	143.25
OB131	83.15	0.35	514.97	-139.42
OB132	83.15	0.35	514.97	114.39
OB135	104.65	0.06	100.40	-393.46
OB142A	15.61	0.09	78.96	-72.94

(cont'd)

Table 5 (continued)

Identification Number	0.5-m EM61 (mv)	GEM-3 Phase Δ (deg)	4-kHz GEM-3 (ppm)	Magnetometer* (gamma)
OB145A	7.05	0.01	14.01	55.71
OB146	7.35	0.16	133.95	16.82
OB147A	4.74	0.02	16.66	43.20
OB149	15.28	0.07	85.75	22.55
OB151A	9.81	0.02	18.13	32.80
OB153A	9.35	0.05	38.58	15.55
OB158A	71.89	0.19	222.56	-76.69
OB159	15.31	0.05	47.86	62.37
OB161A	6.09	0.01	5.37	22.27
OB163	2.93	0.05	35.27	79.81
OB171	14.60	0.09	95.46	142.08
OB174	12.23	0.09	77.14	26.00
OB177	9.51	0.09	77.14	-44.20
OB179	31.36	0.06	53.37	77.17
OB181A	16.96	0.04	33.49	-124.69
OB183	20.36	0.07	60.31	8.79
OB184	-4.22	0.01	20.28	15.37
OB185A	-3.71	0.01	12.67	15.37
OB186	30.78	0.04	69.85	22.06
OB187	-33.77	0.04	69.85	43.98
OB188	-5.58	0.04	95.96	412.14
OB189	6.12	0.04	95.96	412.14
Average	17.53	0.11	106.49	21.33 (91.36)
Std. Dev.	23.71	0.14	119.97	126.37 (89.01)
Minimum	-33.77	-0.06	5.37	-393.46 (8.79)
Maximum	104.65	0.75	514.97	412.14

* The values in parentheses are determined taking the absolute value of the magnetic field.

Table 6. Comparison of Peak Signatures from Objects Classified as Medium

Identification Number	0.5-m EM61 (mv)	GEM-3 Phase Δ (deg)	4-kHz GEM-3 (ppm)	Magnetometer* (gamma)
EX-128P	14.38	0.07	61.42	324.52
OB1A	78.92	0.29	242.03	124.44
OB19B	48.95	0.10	75.58	137.74
OB23A	31.36	0.06	53.37	77.17
OB36	31.28	0.12	648.68	-141.90
OB37A	31.28	0.12	648.68	-141.90
OB46	58.63	0.22	335.26	-68.08
OB47A	30.45	0.07	67.05	80.59
OB50A	30.46	0.27	207.11	70.57
OB50B	30.46	0.27	207.11	70.57
OB51A	30.46	0.27	207.11	109.44
OB52A	10.67	0.06	48.41	109.44
OB56A	49.90	0.12	106.96	-63.91
OB58A	19.54	0.36	211.46	-145.55
OB60A	19.54	0.36	211.46	-145.55
OB61A	37.71	0.21	141.23	-124.60
OB62	51.47	0.12	96.21	102.28
OB65A	14.37	0.04	43.37	133.01
OB67A	24.06	0.05	42.45	90.41
OB69A	43.50	0.05	132.63	85.41
OB70	11.98	0.98	656.56	183.99
OB71A	55.98	0.92	517.56	178.91
OB76	80.76	0.42	366.91	174.85
OB80A	22.18	0.14	101.24	130.84
OB84A	50.23	0.33	287.27	-73.80
OB86A	153.63	-0.12	728.90	175.82
OB88A	22.97	0.04	28.00	-70.35
OB91A	12.88	0.04	34.01	-83.51
OB101A	13.68	-0.03	120.90	-96.22
OB110A	37.56	0.13	87.84	64.34
OB111A	34.18	0.10	79.71	-111.00
OB115A	38.53	0.75	366.13	-109.84
OB118A	18.76	0.11	85.75	76.38

(cont'd)

Table 6 (continued)

Identification Number	0.5-m EM61 (mv)	GEM-3 Phase Δ (deg)	4-kHz GEM-3 (ppm)	Magnetometer* (gamma)
OB120	222.88	0.96	1119.93	211.50
OB128A	19.43	0.03	27.04	143.25
OB133A	18.03	0.39	407.88	99.09
OB136A	104.65	0.06	318.05	-393.46
OB141	102.70	0.73	397.36	245.14
OB150A	19.03	0.03	27.33	77.36
OB155	20.64	0.19	162.71	137.44
OB156	71.89	0.19	183.69	-76.69
OB157A	71.89	0.19	222.56	-76.69
OB170A	14.60	0.09	95.46	142.08
OB172A	16.96	0.04	33.49	-124.69
OB178A	17.10	0.10	99.61	56.47
OB190A	21.77	0.06	54.94	-113.74
OB191A	21.77	0.08	72.51	-113.74
OB192A	19.48	0.05	47.99	-69.31
OB193A	17.81	0.22	154.70	133.97
OB194	31.58	0.12	99.59	-139.58
OB195A	25.06	0.12	99.59	-139.58
OB197A	38.80	0.14	122.89	-180.88
OB198A	38.80	0.13	102.53	-180.88
OB202A	14.09	0.25	159.96	79.80
Average	40.18	0.21	208.48	15.58 (126.15)
Std. Dev.	37.33	0.24	217.65	141.01 (62.59)
Minimum	10.67	-0.12	27.04	393.40 (56.47)
Maximum	212.98	0.98	1119.93	324.52 (393.46)

* The values in parentheses are determined taking the absolute value of the magnetic field.

Table 7. Comparison of Peak Signatures from Objects Classified as Large

Identification Number	0.5-m EM61 (mv)	GEM-3 Phase Δ (deg)	4-kHz GEM-3 (ppm)	Magnetometer* (gamma)
OB2	450.21	0.91	812.96	839.00
OB8A	268.56	0.36	501.47	-880.91
OB8B	268.56	0.36	501.47	-880.91
OB8C	361.10	0.36	501.47	827.84
OB16A	450.21	0.91	812.96	839.00
OB16B	450.21	0.91	812.96	839.00
OB16C	450.21	0.91	812.96	839.00
OB16D	450.21	0.91	812.96	839.00
OB117A	197.63	0.15	248.35	-995.10
OB117B	197.63	0.15	248.35	-1183.81
OB137A	148.70	0.13	135.66	718.93
OB137B	148.70	0.06	116.90	718.93
OB160A	99.19	0.27	199.72	-60.41
OB160B	95.25	0.26	188.83	133.59
Average	288.31	0.48	479.07	185.23 (756.82)
Std. Dev.	142.94	0.35	287.80	819.17 (301.91)
Minimum	95.25	0.06	116.90	-1183.81 (60.41)
Maximum	450.21	0.91	812.96	839.00 (1183.81)

* The values in parentheses are determined taking the absolute value of the magnetic field.

1. EM61 Analysis

The discovery of an M12 training minefield offers an unexpected opportunity to compare the signatures of these mines to some of the other objects discovered on the site, which include heavy metal disks similar in size to the M12 mines.⁶

One would expect the different sensors to have similar responses to the inert M12 mines; in particular, the EM61 and the GEM-3 are metal detectors and thus identical metallic objects, buried at the same depth, should offer an ideal situation to compare induced signals. Differences in soil characteristics surrounding the objects that affect the signature should be negligible compared to the similarities in the objects. If identical

⁶ The M12 is a metal-cased AT mine having a diameter of 30 cm and a height of 7 cm. The disks were so similar that there is some conjecture that the metal plates were placed on the site as a training aid for soldiers who were to detect the M12 mines.

mines have very different signatures, the development of discrimination algorithms for these sensors will be even more difficult.

The EM61 peak signal responses to each of the M12s, shown in Table 2, vary in in peak signal strength from 204.68 mV to 471.17 mV, a range of over 200 mV. This contrasts with the range of peak signal strengths observed for the medium-sized objects, about 258 mV, and for the small objects, about 137 mV. The differences in peak signal strength is comparable in all categories. Perhaps it is more enlightening to compare normalized standard deviation in peak signal response, computed by dividing the standard deviation by the average peak signal response for each category:

M12s	Big Metal Plates	Tiny	Small	Medium
27%	74%	77%	135%	109%

By this measure, the M12 mines are the most similar in signature. The similarity of the M12 mines is further illustrated in Figure 26, which shows the east-west and north-south 6-m slices of the data. By comparison, Figures 27–29 show the slices for the tiny, small, medium, and large object size categories, respectively. Much more spread in the slice shape is observed for all categories compared with the M12 mine slices. The observed variations in signals are not surprising, but they could have been exacerbated by the rough categorization that out of necessity included objects in the same category that were in some cases substantially different in size, although not different enough to be moved to a different category. But even a much finer categorization could not produce the limited variation as observed for the M12 mines, since there was not a large enough set of objects similar enough in size to constitute a category for comparison. It is expected that were such a set found, a tight group of peak signatures such as that observed for the M12s could be created. On the other hand, the result computed for the big metal plates does not conform to this argument.

The big-metal-plates category is by far the most homogenous of the four created categories. Within this set, OB68, OB130, and OB138 are nearly identical in appearance, but OB130 was found deeper than the other two. Table 3 shows the peak signal responses for the seven big metal plates. Figure 26, showing the comparison of the variation in peak signal responses and slice data, reveals that despite the physical similarities between the big metal plates and the M12s, the variation in signal strength is much greater for the big metal plates than the variation within the M12 set. This comparison is even more interesting given the similarity in shape and size between the big metal plates and the M12s. The variation in peak signal responses implies that the convolution of object

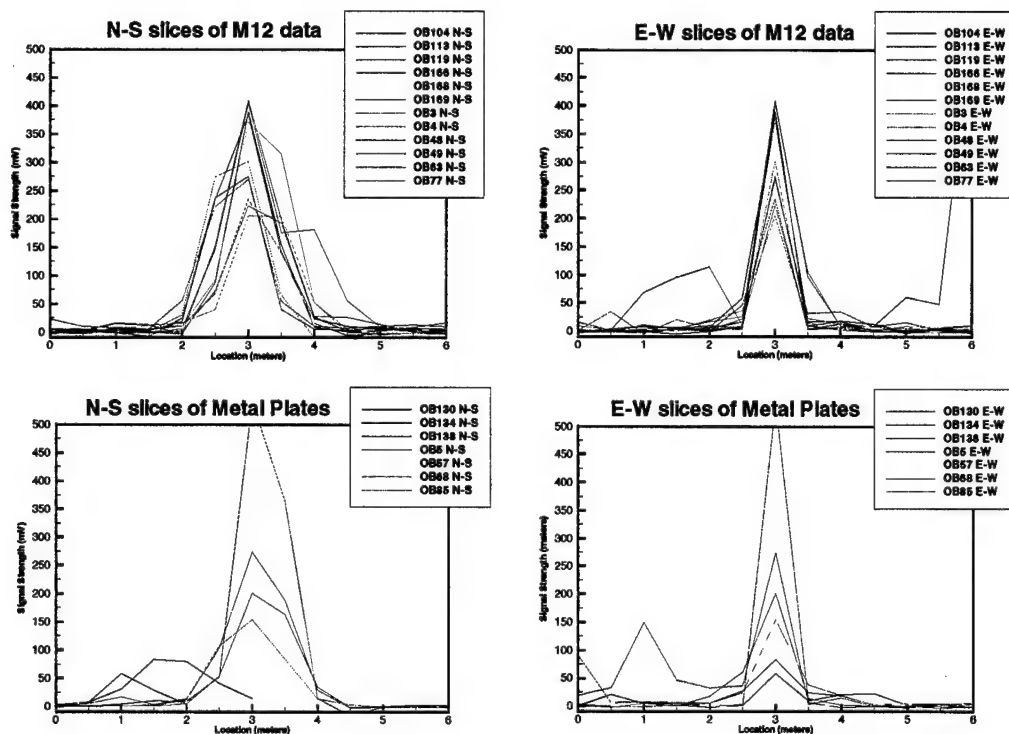


Figure 26. Comparison of Parsons EM61 Response to M12 Inert Landmines and the Metal Plates Found on the Site. OB134 is believed to be nonferrous.

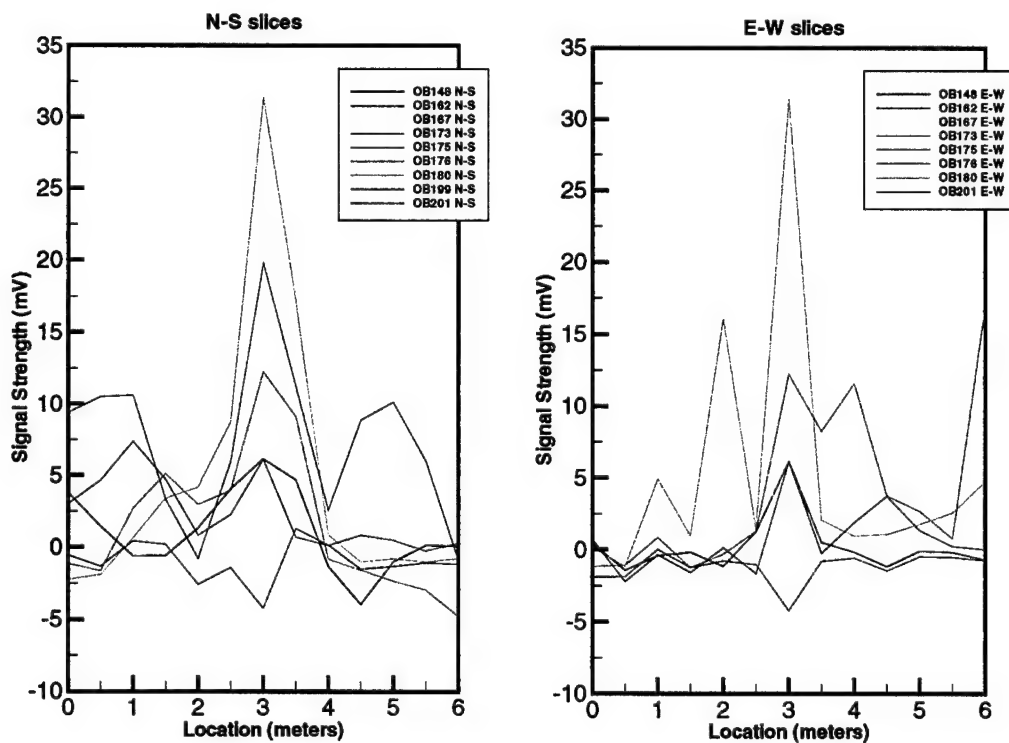


Figure 27. Parsons EM61 Sensor Response Depicted in 6-m Slices to Objects in the "Tiny" Size Category

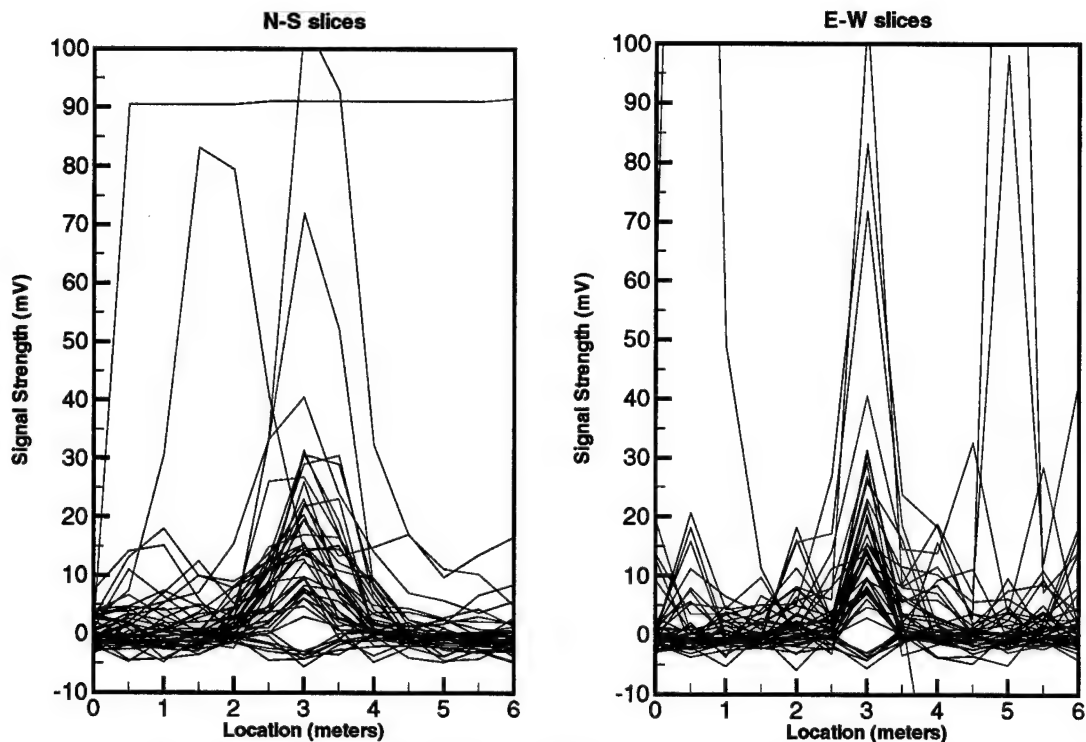


Figure 28. Parsons EM61 Sensor Response Depicted in 6-m Slices to Objects in the "Small" Size Category

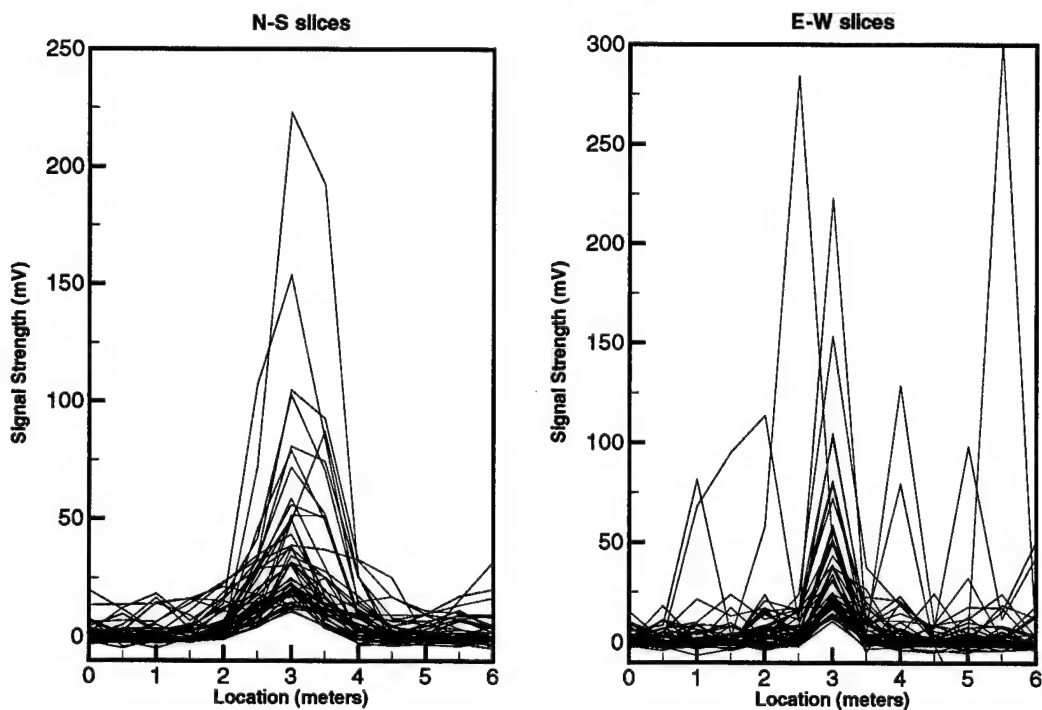


Figure 29. Parsons EM61 Sensor Response Depicted in 6-m Slices to Objects in the "Medium" Size Category

composition, size, and depth would lead one to confuse clutter objects with non-clutter objects even if the exact window of expected target signatures were known a priori. Of course, given different mine or UXO types and burial depths, the target signature space would quickly span the possible response space, in effect supplying no useful information for discrimination.

The robustness of the EM61-sensor-peak-magnitude responses is clearly demonstrated by the correlation between average peak signal strength and size category. Nonetheless, there are a few outliers; fortunately, a reasonable explanation exists for almost all of them. First, an entire set of outliers was tossed out and marked as TCTBO in the data provided in Appendix C. There are a few cases where a set of smaller objects in a cluster were all declared TCTBO, since the combined signature produced anomalous results. Thus, remaining in Tables 5–7 are only a few objects that require discussion; they are summarized in Table 8. Only one object out of 203 has a signature that is hard to explain, 0B86A, and even it does not have a signature that is vastly out of range for the category. Another similar data set is the response to the registration targets. Parsons EM61 response to registration targets is shown in Figure 30. All of the arguments presented lead to the conclusion that the EM61 signal responses correlate well with the uncovered objects.

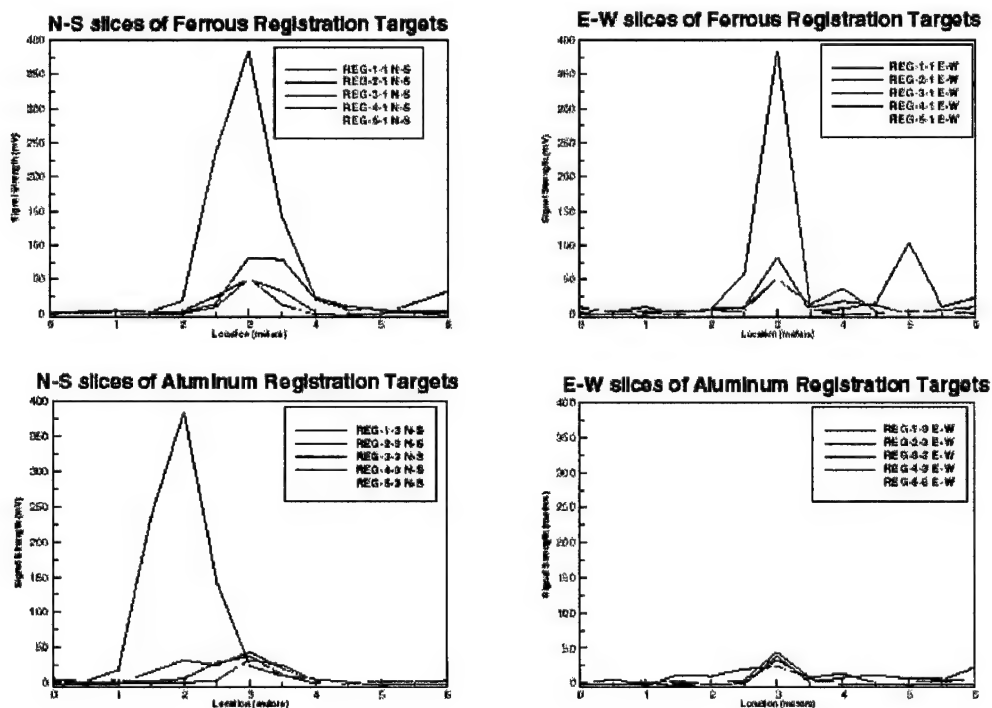


Figure 30. Parsons EM61 Sensor Response Depicted in 6-m Slices to Registration Targets

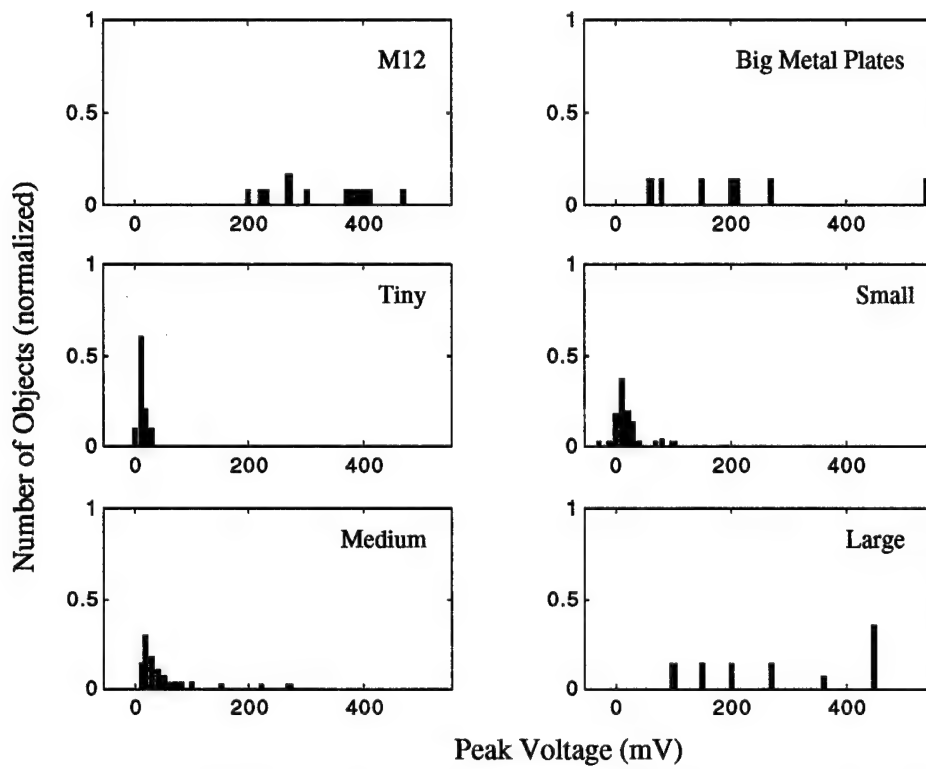


Figure 31. Histogram of Peak Voltage from Parsons EM61 for Object Classes

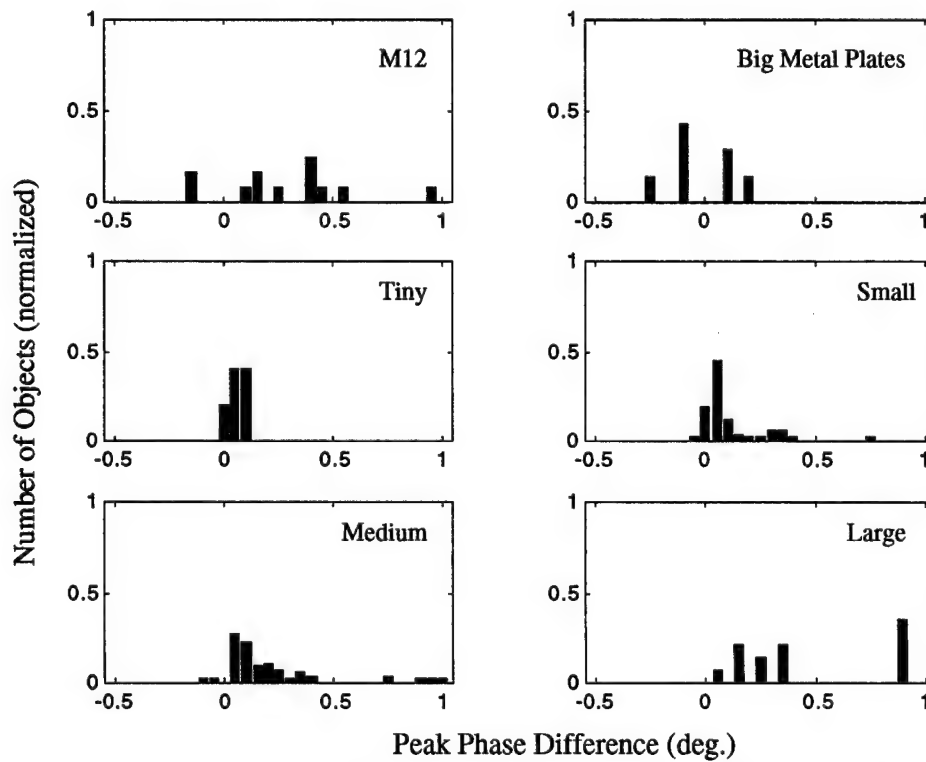


Figure 32. Histogram of Peak Voltage from Geophex GEM-3 for Object Classes

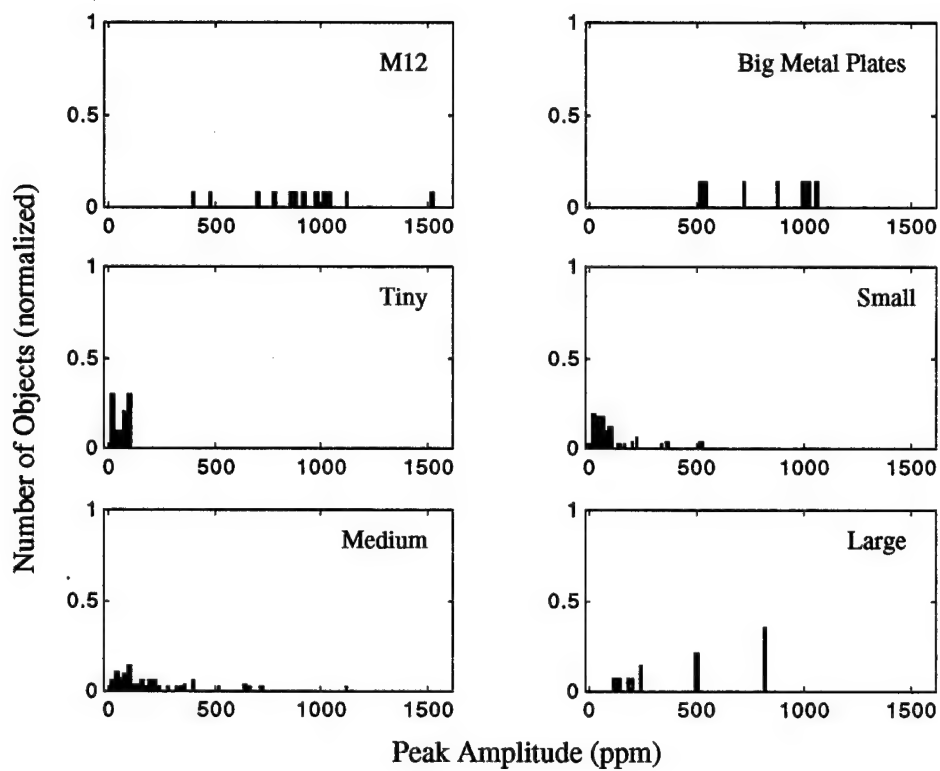


Figure 33. Histogram of Peak Phase Difference from GEM-3 for Object Classes

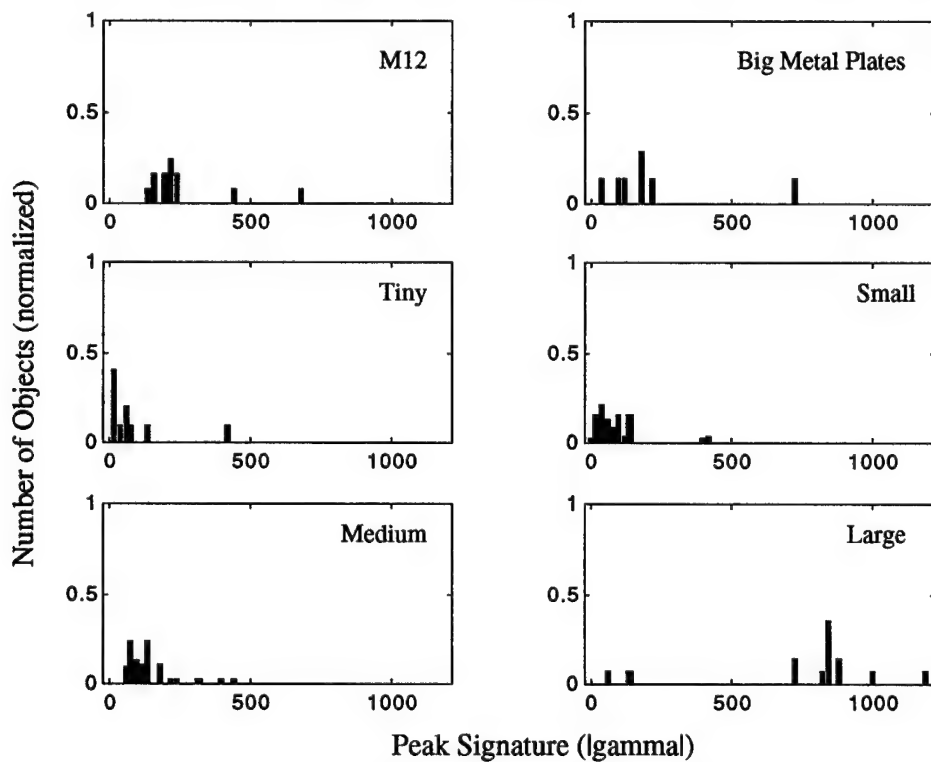


Figure 34. Histogram of Peak Field from Geometrics Magnetometer for Object Classes

Table 8. Objects with Outlier Sensor Responses

Object Identification Number	Table	Explanation
OB160A,B	7 (Large)	This is a long strip of banding. The sensor only sees a segment of it for each pass (see Figure C-1). Similar arguments can be made for each of the elongated items listed as large.
OB86A	6 (Medium)	None.
OB120	6 (Medium)	It is hard to determine the size or (more accurately) metal content from the photo. It is likely that this object is more akin to a metal plate.

2. Magnetometer Analysis

The magnetometer responses are more difficult to analyze, since it is not only the magnitude of the signal strength (typically the dipole field strength) that is important but the orientation of the dipole field and potentially the magnitude and orientation of higher moments. Furthermore, peak signal strength is associated with ferrous size or extent of the object and not total object size if the object contains nonferrous components. It is beyond the scope of this paper to determine the dipole orientation for each dipole signature in the data set, and then to make statistically sound conclusions based on the dipole orientations. However, several characteristic objects including the M12 practice mines were analyzed using this approach. Table 9 lists the magnetic fit parameters of eight of the M12s for which the dipole fitting routine could be implemented. The characteristics we choose to exploit for this paper are the ferrous size⁷ and the inclination of the magnetization. The ferrous size and inclination permits us to look at the consistency of the magnetic signature of the M12s. The M12s exhibit very consistent signatures. Note that the ratio of the standard deviation to the mean ferrous size is 16.5 percent which is better than the ratio the standard deviation of the peak signature to mean peak signature for the EM61 response from the same eight M12s. The inclination of the fit magnetic moments show more spread, but OB104 and OB63 appear to be outliers compared to the other six M12s. It should be noted that if one models the M12 as an oblate spheroid, the ferrous size is approximate 11 cm and the inclination is 25 degrees, consistent with the data collected by Geometrics.

⁷ The ferrous size is defined as the radius of a solid sphere which yields the same induced magnetic moment in the geomagnetic field at FP20,

Before the excavation phase of this project, we did perform a quasi-quantitative look at the “shape” of the sensor response, as shown in Figure 35. Figure 35a shows an image (interpolated to 5 cm × 5 cm pixel size) of the signature of a M12 mine (OB3). The mine has a very distinct spatial signature. Figure 35b is an image of the modeled signature of the M12 landmine. Note the general shape similarities. The spatial extent and overall appearance of the M12 landmines and large metal plate signatures (except OB134, which is nonferrous) are very similar. In fact, during the excavation process, this similarity was used to assist in the location of additional plates and mines. Our success using this crude analysis suggests that a magnetometer data set can become more enlightening during a real remediation effort, as “learning” takes places regarding the correlation between the types of ordnance found on the site and the induced signatures. The learning process has also been observed in real site survey and remediation by Dr. Jim McDonald of NRL (Ref. 2).

Table 9. Magnetic Characteristics of M12s

Object ID	Ferrous Size (cm)	Inclination (deg)
OB3	12.1	15.24
OB49	11.8	22.6
OB166	11.1	22.0
OB119	8.4	22.7
OB113	11.8	22.7
OB104	7.6	73.7
OB77	9.0	34.6
OB63	10.7	1.41
Mean	10.3	26.9
Standard Dev.	1.7	21.1
Ratio STD/mean	0.165	0.784

⁸ Post-excavation analysis has shown that there are subtle differences in the orientation of the magnetic moments of these two flat objects because the different demagnetization constants characteristic of the objects.

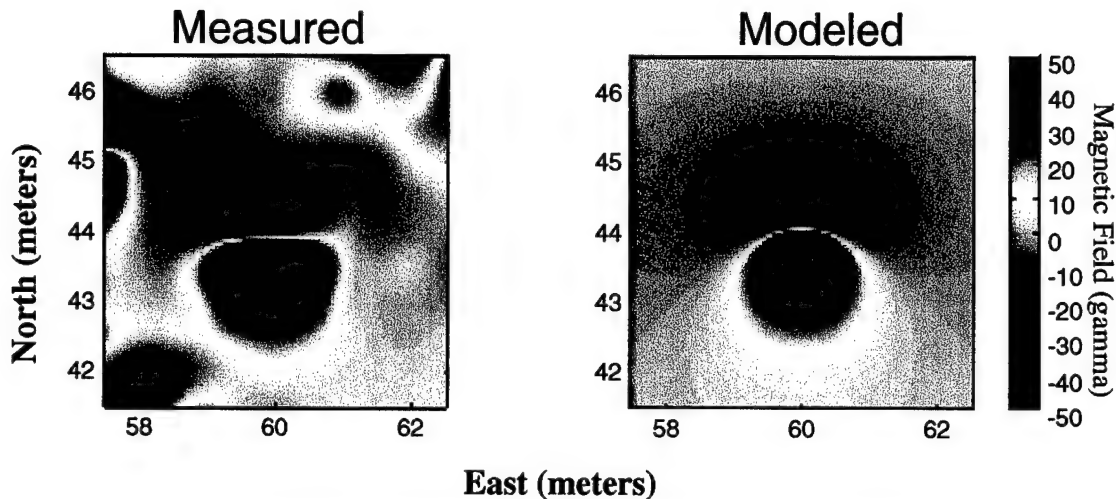


Figure 35. Geometrics Magnetometer Model and Modeled Data for OB3

We also used the magnetometer data set to estimate the depth of buried objects. In many cases, a cursory employment of the full-width, half-maximum estimate of depth was accurate enough to steer us to a 55-gallon drum at 1.0-m depth (EX-172P) and a big flat metal piece (OB100) at 77-cm depth. In some cases, however, we expected an object to be deeper than it was actually found. This happened because the cursory approach of our depth-estimation technique ignored the effect of higher magnetic moments for spatially extended magnetic signatures. For example, we expected OB2, a car part, and OB137, a fence post, to be deeply buried; however, both turned out to be large, elongated near-surface objects. Figure 36 shows the magnetic signature produced by these objects. If a robust dipole fitting model is used, the estimated depth is closer to the actual depth. This signature can be compared to the signature produced by OB100, Figure 37, or EX-172 (55-gallon drum), which was in fact a deep object. A more robust depth-estimation tool will be used in a separate paper to analyze the excavated objects.

3. GEM-3 Analysis

The analysis of the GEM-3 is frustrated by the highly contaminated nature of the site and the location inaccuracies inherent in the GEM-3 data set. The true source of the scattered responses shown in the full site map can not be determined due to the combined effect of location inaccuracies and substantial metallic clutter on the site. It is nearly impossible to separate the cause of spatial separation in GEM-3 signals; is it truly a result of the induced pattern of responses or is it an artifact of the location inaccuracies? Nonetheless, there are enough instances of signal separation to observe single-object-induced

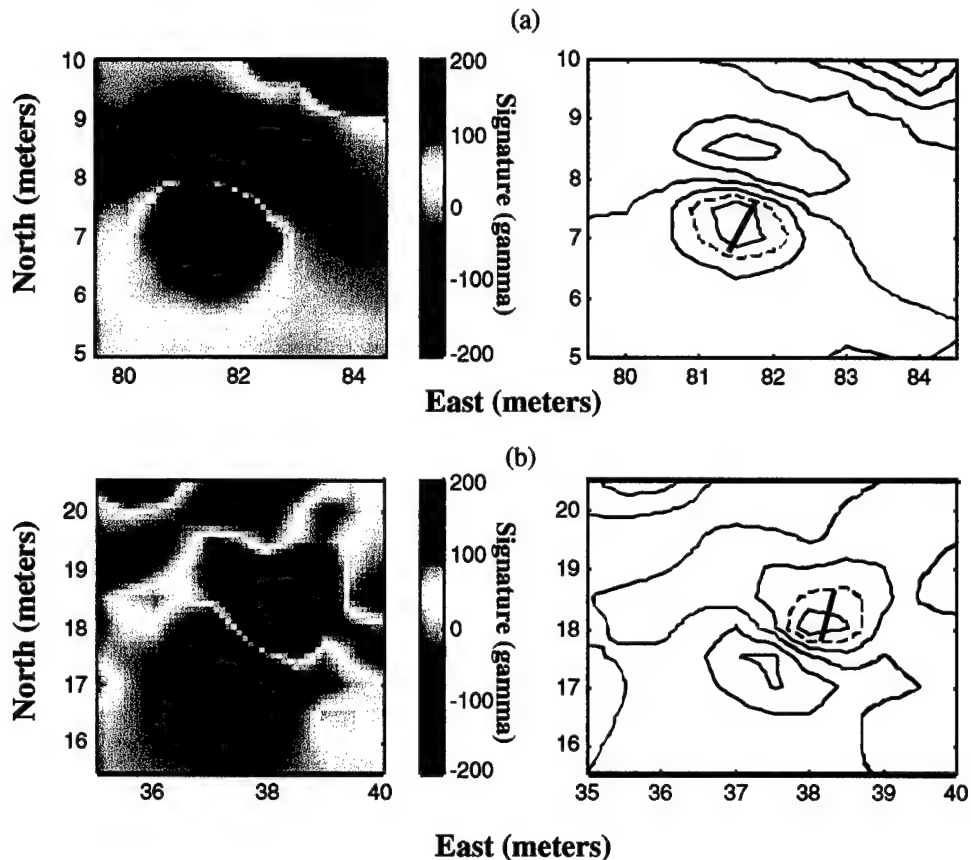


Figure 36. Magnetic Color Plots and Contour Plots for (a) OB2 and (b) OB137

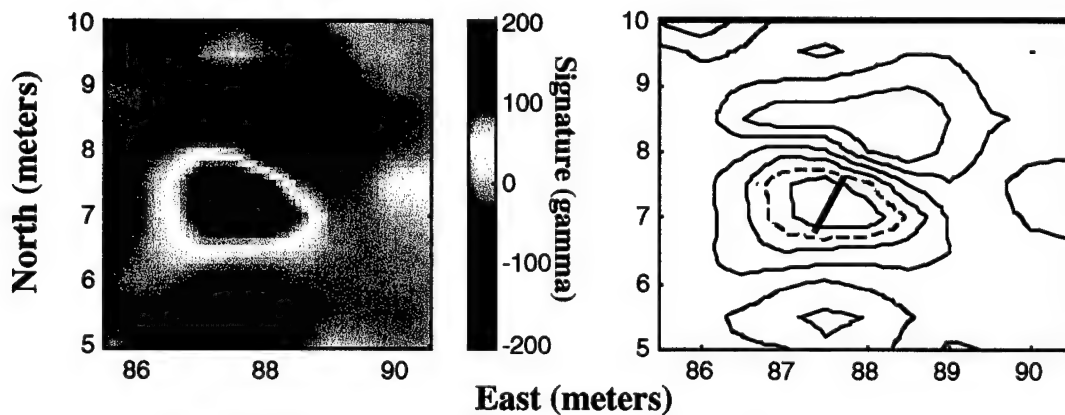


Figure 37. Magnetic Signature of OB100

responses to make inclusion of the GEM-3 data useful. It was hoped that the maximum difference in phase-angle response provided by the GEM-3 system would offer insights into the material composition of the object. In this data set, using our rough rule of thumb, a negative phase-angle difference should be indicative of a nonferrous object and a positive phase-angle difference indicative of a ferrous object. This expected response is observed in four of the five registration target sets; this data is illustrated in Appendix A.

Each registration target set includes an aluminum plate and an iron sphere separated in the north-south direction by 4 m. Table 10 gives the registration object locations.

Table 10. Registration Object Locations

Target	Easting	Northing
REG 1-1 (Iron Sphere)	27.432	73.156
REG 1-3 (Aluminum Plate)	27.422	77.134
REG 2-1 (Iron Sphere)	39.994	22.968
REG 2-3 (Aluminum Plate)	40.053	26.967
REG 3-1 (Iron Sphere)	52.548	85.499
REG 3-3 (Aluminum Plate)	52.540	89.401
REG 4-1 (Iron Sphere)	64.946	10.475
REG 5-3 (Aluminum Plate)	64.938	14.449
REG 5-1 (Iron Sphere)	77.526	60.474
REG 5-3 (Aluminum Plate)	77.538	64.466

(a) GEM-3 Phase

The phase differences computed for the registration target set indicate that the phase difference provides insight whether the target is ferrous or nonferrous. This is in contrast to the phase-difference responses provided for the set of M12 mines. It was expected that the phase difference would be approximately the same for each of the M12s. Since the location data for the GEM-3 is substantially inaccurate, the next step taken was to ensure that the “peak” phase difference was likely to be the result of the mine. In other words, could the observed differences in phase-angle differences be removed if different locations near the expected object location were selected? The answer is no, and in fact choosing different locations to determine sensor responses increased the observed variation in phase-angle differences. The phase-angle differences for each of the registration targets and the calibration targets in the yellow lane are provided in Tables 11-13. Since the phase-angle differences for the M12 targets vary from slightly negative to strongly positive, and since the iron registration target in the REG-2 set appears to have a negative phase-angle difference (blue), opposite to the rule of thumb response, further analysis of the GEM-3 phase response was abandoned. As stated earlier, permeability, conductivity and size can affect the phase angle difference. In addition, if the density of clutter is high near an object of interest, there is the potential that the phase-angle difference may be hard to classify by simple rules.

Table 11. Ferrous Registration Targets

Target	0.5-m EM61 (mV)	4-kHz GEM-3 (ppm)	GEM-3 Phase Δ (deg)	Magnetometer (gamma)
REG-1-1	155.36	290.73	0.328	60.95
REG-2-1	203.72	646.95	0.727	93.02
REG-3-1	164.40	787.99	0.439	35.19
REG-4-1	162.65	142.28	0.116	62.15
REG-5-1	165.53	224.32	0.229	58.78
Average	169.93	418.45	0.378	62.03
Std. Dev.	19.22	284.42	0.221	20.57
Minimum	155.76	142.28	0.166	35.19
Maximum	203.72	787.99	0.727	93.02

Table 12. Aluminum Registration Targets

Target	0.5-m EM61 (mv)	4-kHz GEM-3 (ppm)	GEM-3 Phase Δ (deg)
REG-1-3	43.52	437.76	-0.12
REG-2-3	37.59	1312.19	0.83
REG-3-3	23.50	748.16	-0.16
REG-4-3	32.71	648.29	-0.15
REG-5-3	27.05	872.09	-0.19
Average	32.87	803.70	0.04
Std. Dev.	8.02	325.73	0.44
Minimum	23.50	437.76	-0.19
Maximum	43.52	1312.19	0.83

Table 13. Metallic Calibration Targets in Yellow Side Bar

Target	0.5-m EM61 (mv)	4-kHz GEM-3 (ppm)	GEM-3 Phase Δ (deg)	Magnetometer (gamma)
YEL-5	55.86	985.05	-0.24	-142.82
YEL-6	62.46	988.37	-0.24	-40.64
YEL-9	30.15	8.25	0.01	-27.32

(b) GEM-3 Amplitude

Substantial deviation in the GEM-3 peak amplitude response is observed in the data. This variation is believed to be a result of the location inaccuracy of the GEM-3. It is also suspected that the GEM-3 does not have good measurement capability for deeper

(greater than 0.5 m) objects. Thus, a tiny piece of metal close to the surface can induce a sensor response greater than a deeper, larger object. Therefore, the observed deviations in sensor responses for each of the categories (M12, big metal plate, small, medium, and large)⁹ cannot be explained.

The GEM-3 is a very sensitive detector designed to detect tiny pieces of metal, such as might be found in a low-metallic landmine. Unfortunately, an analysis of the tiny pieces of metal is frustrated by the overwhelming number of bigger pieces of metal on the site. From this data set it seems that metallic clutter larger than the smallest piece of metal that can be detected will mask the responses from the smaller pieces, even if the smaller pieces are separated spatially. The smallest piece of metal that can be found in practice at FP20 cannot be determined, given the large location inaccuracies. An attempt to determine the minimum amount of metal detectable by the GEM-3 in the field might be made at one of the cleaner sites in Fort Carson.

E. EMPTY HOLES

One hole remains a mystery: EX-128P. This hole offered a large magnetic dipole signature and was selected for excavation for two reasons: (1) we surmised that a deeper object resided there, and (2) it formed a part of linear feature C, Figure 8. After digging to a depth of almost 1 m and having no success in steering the dig with the handheld metal detector, we decided to use the proton precession magnetometer to steer the dig. A number of times the magnetometer responses slightly altered the course of digging until finally a hole about 1.5×2.0 m in size and almost 1 m deep suddenly produced no magnetic signature whatsoever. Two pieces of scrap metal that would have ended up in the medium category had they not been 0.5 m deep, were all that was found in the hole. The amount of metal found certainly did not account for the signature in the data set or the response of the magnetometer during digging. The source of the anomaly remains a mystery, but it is not an unheard of event (Ref. 2). In contrast, OB100 revealed a big deep piece of metal, and EX-172P (the only hole dug with machinery) revealed a 55-gallon drum about 1 m deep (Figure 20).

1. A second empty hole is EX-157P. This was chosen for excavation because it was a very small, isolated magnetic anomaly with an atypical magnetic moment orientation, perhaps due to a nail. The hole was abandoned after no object could be found. The source of the magnetic anomaly remains a mystery.

⁹ Tiny category excluded because of locations inaccuracies

object could be found. The source of the magnetic anomaly remains a mystery.

2. EX-30P was selected for excavation since it was a large magnetic anomaly. After some initial digging concrete was found, so the digging was halted. Time constraints prevented the excavation team from returning to the hole and continuing the investigation.

F. POST-DIG SITE MAPS

We now consider what the clutter level on the site might look like now that we have removed 203 objects from the site. Rather than resurveying the site with the sensors in a field exercise, we present sensor response maps (Figures 38–41) where the sensor response local to each excavation site has been nulled to the background level. This is only an estimation, however, since this approach not only nulls out only the response caused by the excavated item, but also that of any other clutter nearby. To determine the spatial extent of the signature to be nulled, an image area above a defined threshold (less than -12.5γ , or greater than 12.5γ for the magnetometer, 4 mV for the Parsons EMI system, 4 ppm for the Geophex 4-kHz amplitude data, and less than -0.025 or greater than 0.1 for the Geophex phase difference) is selected using an eight-nearest-neighbor connected-component algorithm, i.e., all pixels near the excavation point with a threshold greater than a predetermined value are selected as long as they are one of the eight nearest neighbors of a previously selected pixel. To further localize the selected area, a limit to the spatial extent is established by convolving the selected pixels with a box filter surrounding the excavation point. For the EMI systems, the box filter is $2.5 \text{ m} \times 2.5 \text{ m}$. For the magnetometer, the box filter is $3.5 \text{ m} \times 3.5 \text{ m}$. The difference in box filter size accounts for the EMI system response being more localized than that of the magnetometers. The total filter is then applied to the original image. A more accurate approach for nulling only the sensor response is possible by using a signature model and nulling out the expected (or fit signature) consistent with the physical anomaly excavated, but doing so is beyond the scope of this report.

From the altered site maps, it is clear that many more anomalies remain on the site. Were this site to be “remediated” using current metal detection technologies and a threshold of 10 mV, approximately 350 more areas would have to be excavated.

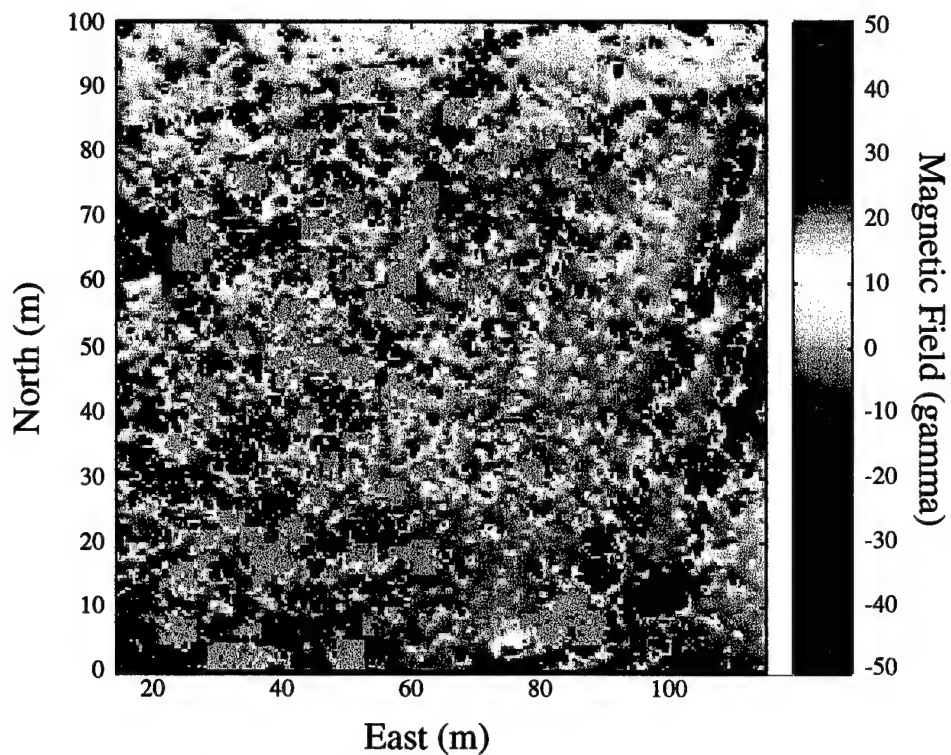


Figure 38. Digitally Altered Image of Center Square at FP20 Using 0.5-m Vertical Stand-Off Geometrics G-858 Magnetometer Data after Anomalies Associated with the Objects Are Removed from the Data

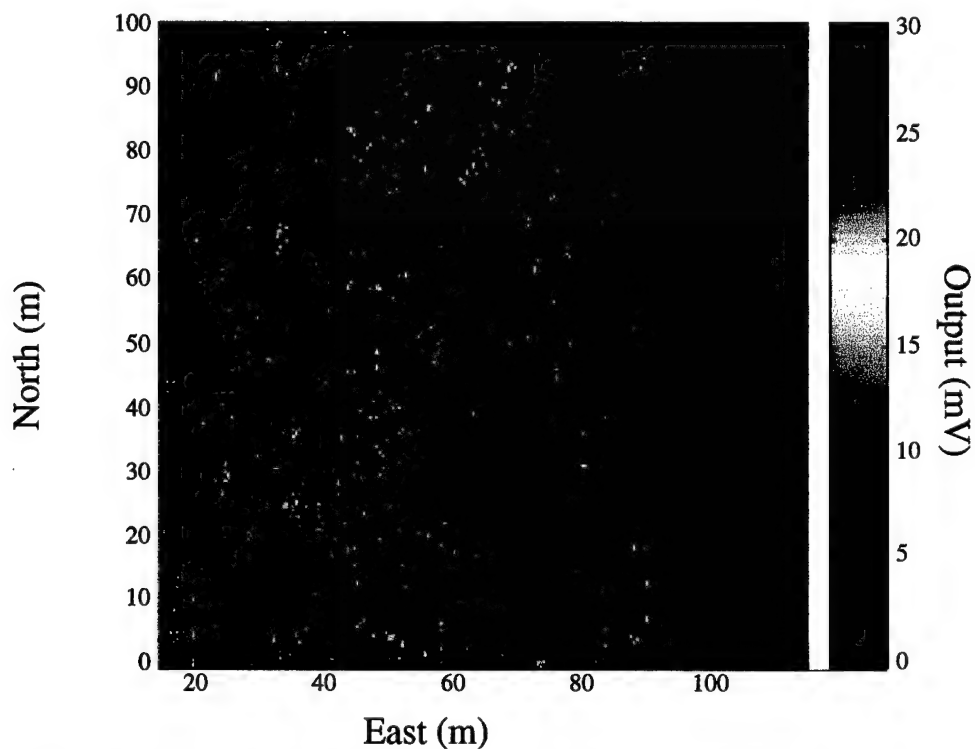


Figure 39. Digitally Altered Image of Center Square at FP20: Parsons EM61 Induction Coil Data after Anomalies Associated with the Objects Are Removed from the Data

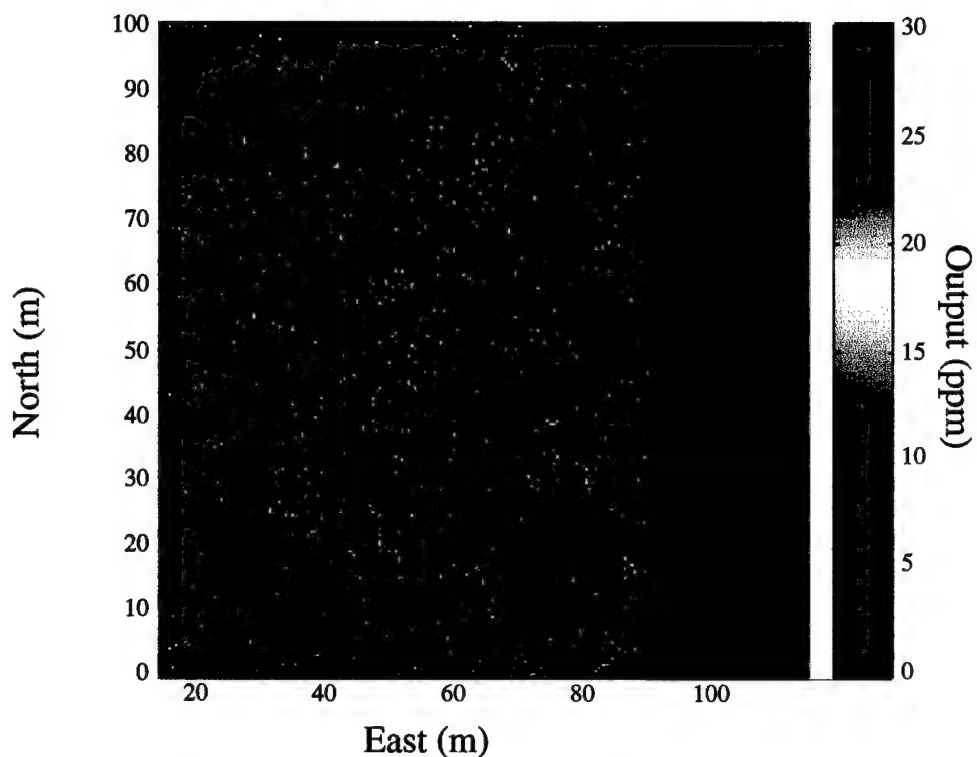


Figure 40. Digitally Altered Image of Center Square at FP20 Using the Amplitude Response as Computed from the Geophex 4-kHz Response Data after Anomalies Associated with the Excavated Objects Are Removed from the Data

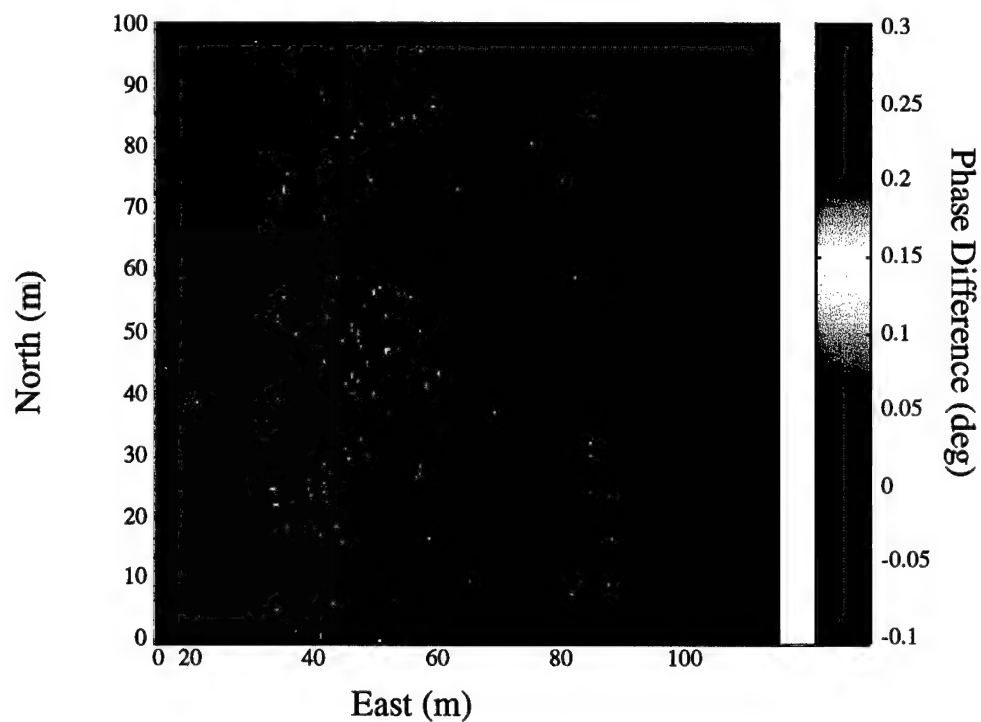


Figure 41. Digitally Altered Image of Center Square at FP20 Resulting from the Computation of the Geophex Phase Difference after Anomalies Associated with the Excavated Objects Are Removed from the Data

G. LINEAR FEATURES

Figure 8 shows three linear features visible in the magnetometer data for which there are also sensor data available from the other two sensors. The linear feature B was the result of a buried white cable bundle, pictured in Figure 14. The white cable bundles were found at the following locations: EX-109C, EX-118C, EX-124C, EX-63C, OB24-32, and OB34-35.

Linear feature A also appears to be the result of buried wire; however, the case is not as strong. The two places where buried wire was found on this feature are OB21 and OB22. In Figure 8, these two locations are plotted and connected by a line. At one of the locations, we found a single strand of white wire similar to wires that made up the 15-strand bundle that was the source of linear feature B. At the other location, we found several strands of a thinner gage black wire. No other locations along this feature were excavated, but it seems to be a logical conclusion that feature A is the result of buried wire.

Locations excavated along linear feature C did not reveal buried wire, except for location EX-128P, which was the mystery hole. Here, a set of six to seven strands of the same black wire found in OB22 was uncovered at about the same depth. The orientation of the wires would seem to indicate that linear feature C is likely the combined result of these black wires and other metallic debris lying on top or near to the wires. Other locations excavated along linear feature C that did not reveal buried wire are OB199, OB72-76.

H. LOCATION ACCURACY

Some of the uncovered objects offer a unique opportunity to better understand the limitations of location accuracy. OB160, a long straight piece of metal banding lying nearly parallel to the east-west axis, provides an opportunity to quantify the line-to-line location errors and to evaluate efforts to improve location accuracy. Appendix C gives a detailed analysis of the location accuracy for two of the contractor data sets, Parsons 0.5-m EM61 and Geometrics G-858 array, both at FP20. In summary, the estimated uncertainty for the Parson's 0.5-m EM61 data set is from +2 cm to +95 cm. The estimated uncertainty for the Geometrics data set at FP20 is ± 25 cm. Location data analyses and efforts to produce a modified data set with increased location accuracy were pursued rigorously at IDA.

It is doubtful that the laser tracker data will improve the location accuracy already associated with the Geometrics data set. Therefore, no substantial effort was ever made to improve that particular data set. However, a significant effort was made to improve the location accuracy associated with the Parsons EM-61 0.5-m data set. Some success was achieved with this Parson's data set. Two of the methods that IDA has pursued to aid in the creation of an improved location accuracy data set are described in detail in Appendix C. In addition, a more complete report on the subject is forthcoming.

IV. DATA

All of the digging data is available on CD-ROM as part of the DARPA Backgrounds Clutter Data Collection Experiment data set. The data has been included on CD-ROM CLUT-11 Rev. 2 in the directory "fp20dig." The data contained in the directory "fp20dig" is described here:

- The Excel file "fp20dig.xls" lists each object identification number, excavation identification number, easting and northing location in the local coordinate system, and a description of the hole and object. An ASCII tab-delimited version of this file is available as "fp20dig.txt."
- There are three subdirectories under fp20. The "photos" directory contains a ".pcx" file for each of the objects. The ".pcx" files are the result of 3×5 photographs scanned in using an HP ScanJet 4c image scanner. The "photos" directory contains 184 files. A few object photographs are missing.
- The pre-dig magnetometer and EMI data can be found in the directories "predgmag" and "predigem." For selected holes, these two sensors were used before excavation to provide a 3-m \times 3-m sensor response map using a 50-cm grid to guide the data collection. The purpose of these data sets was to verify that the sensor response was similar to the contractor data collected a year earlier and was used to select sites for excavation. There are a total of 37 files (18 magnetometer, 19 EMI). The files are named using the excavation identification number. The format of the data files is described here:
 - EMI: 4 columns and 49 rows. A data point was taken every half meter on a 3-m \times 3-m square resulting in a 7×7 matrix of entries. Column 1 is easting $\times 10$ in meters (e.g., 650 = 65.0 m). Column 2 is northing $\times 10$ in meters. The third column is the response from the lower coil. The fourth column is the response from the upper coil.
 - Magnetometer: 5 columns by 49 rows. The first and second columns are the same as the EMI data file. The third column is the measured magnetic field (γ) for the magnetometer located 0.5 m above the ground. The fourth column is the gradient [bottom magnetometer -top magnetometer (at 1.0 m)]. The fifth column is measurement confidence.

V. SUMMARY

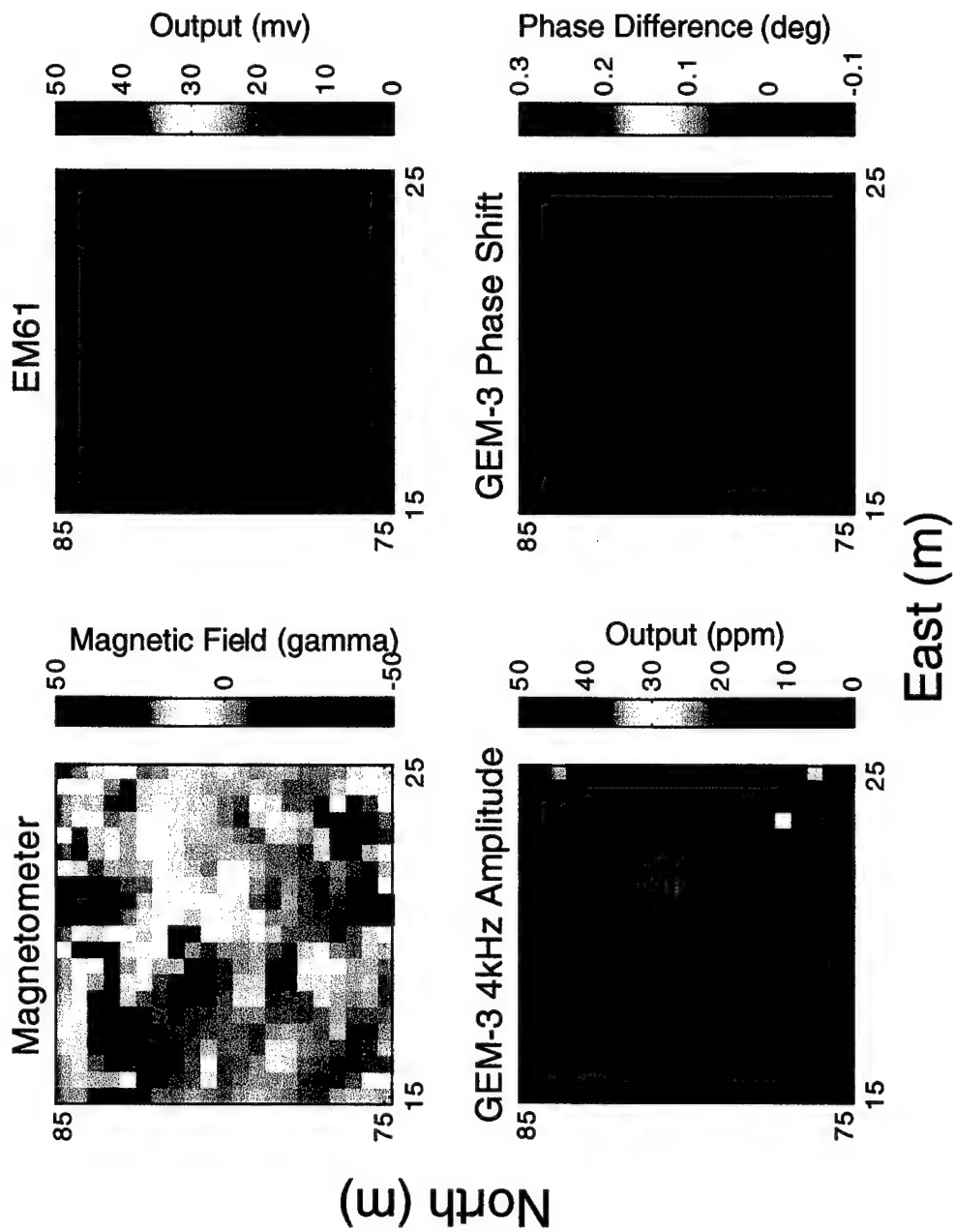
For two reasons, additional digging at each of the four sites is recommended. First, the object-location data has proved useful for improving the location accuracy in the Parsons data set. It is likely that similar improvements can be made to the GEM-3 data set and perhaps to the GPR data sets. To support location accuracy improvements, the criteria for selecting anomalies to dig will have to be modified to include anomalies at key locations in addition to anomalies with particular sensor response characteristics. Second, the discovery of an M12 minefield at FP20 is evidence that our premise of a completely landmine- and UXO-free Center Square area is no longer valid. To support discrimination algorithm development, the location of all valid targets must be known so that all other anomalies can be declared to be clutter objects. Since FP22 is less than 300 m distant from FP20, digging at FP22 is necessary to determine whether the Center Square at FP22 is also contaminated with additional target signatures. At the very least, additional digging at FP20 is necessary to fill in gaps in known object locations to complete an improved location accuracy map for Parsons.

REFERENCES

1. George, Vivian, and Thomas Altshuler, "Design of the DARPA Background Clutter Data Collection Experiment," UXO Forum 1996, May 28–30, 1997, Nashville, Tennessee.
2. Communication with Dr. Jim MacDonald of the Naval Research Laboratories (NRL) during the Institute for Defense Analyses (IDA) Clutter Workshop, October 29 and 30, 1997.
3. Altshuler, Thomas, "Shape and Orientation Effects on Magnetic Signature Prediction for Unexploded Ordnance," UXO Forum 1996, March 26–28, 1996 (pp. 282–291), Williamsburg, Virginia.
4. Won, I.J., Dean Keiswetter, and David Hanson, "GEM-3: A Monostatic Broadband Electromagnetic Induction Sensor," *JEEG*, Vol. 2, Issue 1, March 1997, p. 53–64.

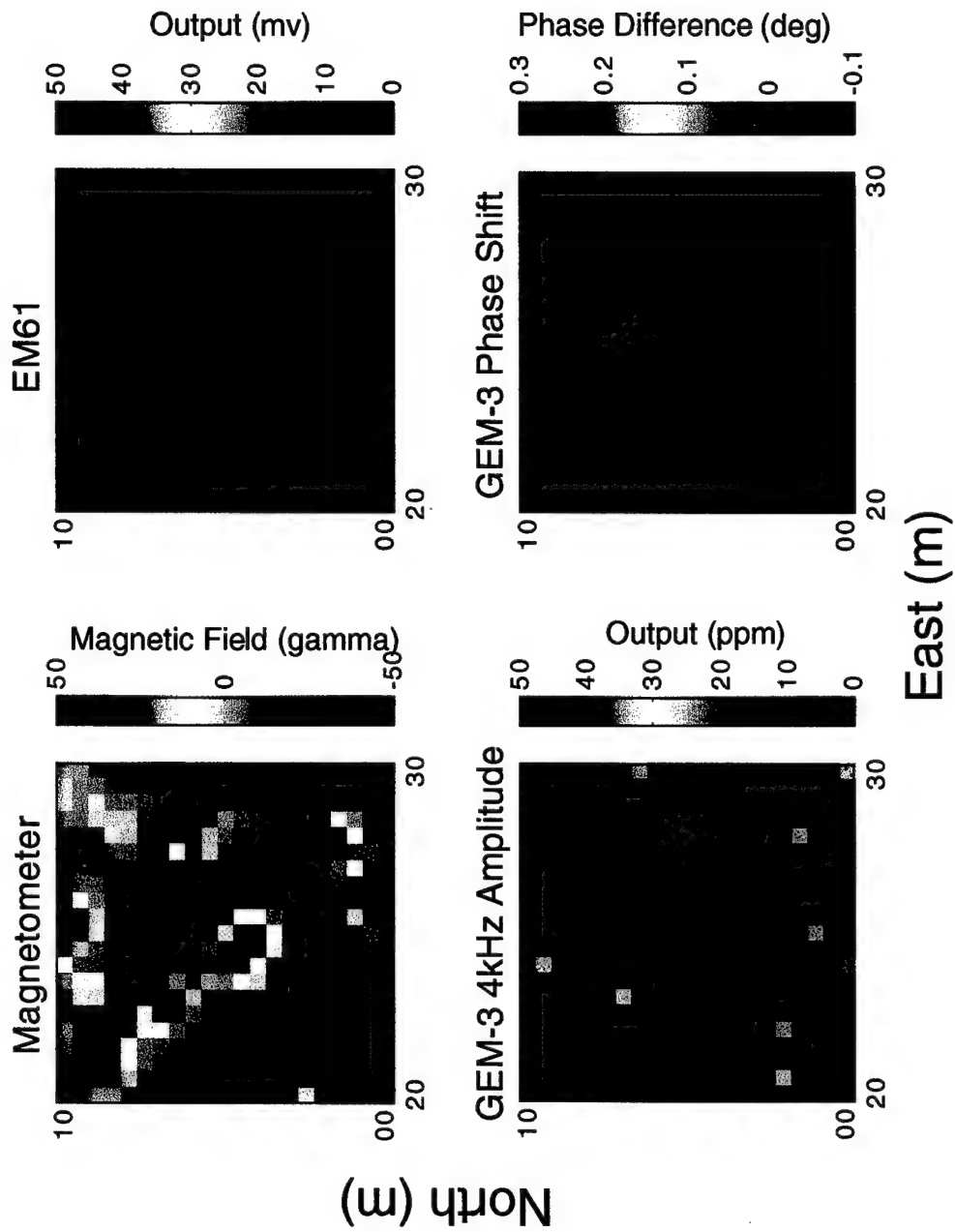
APPENDIX A

DATA IMAGE CATALOG OF THE 10-m \times 10-m PORTIONS OF THE SITE



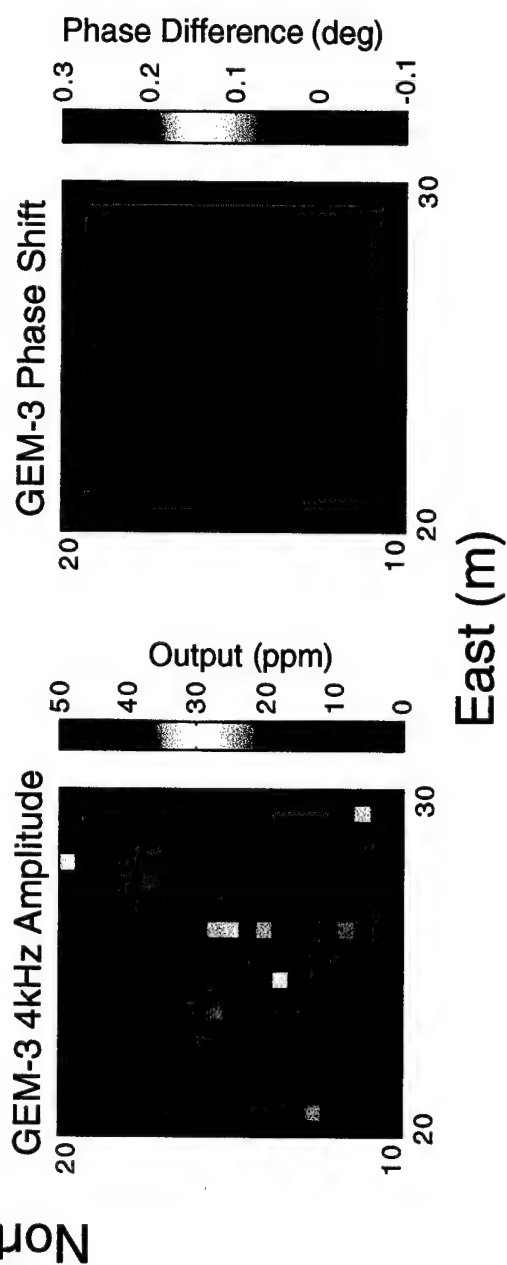
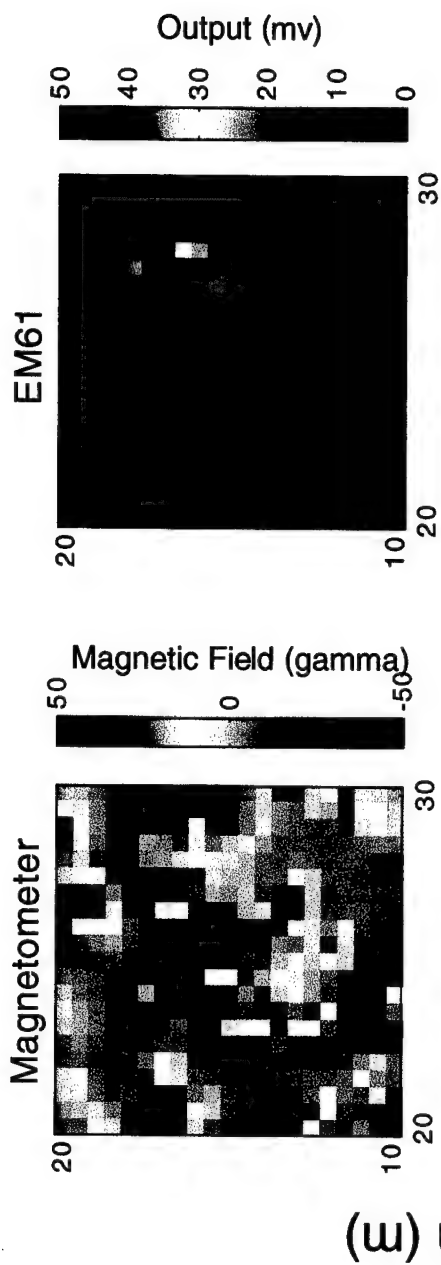
[20E, 80N]

A-3



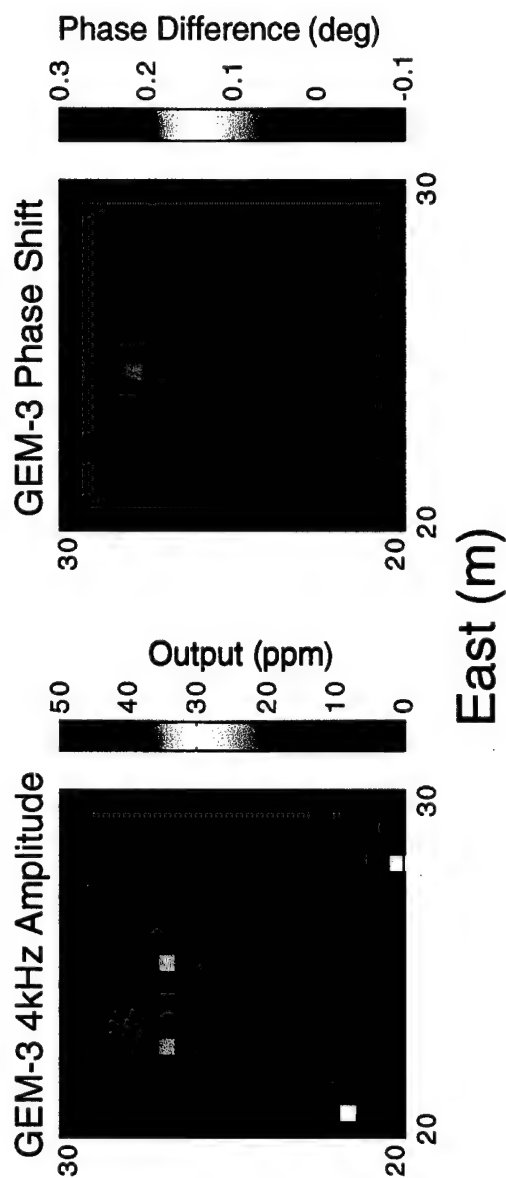
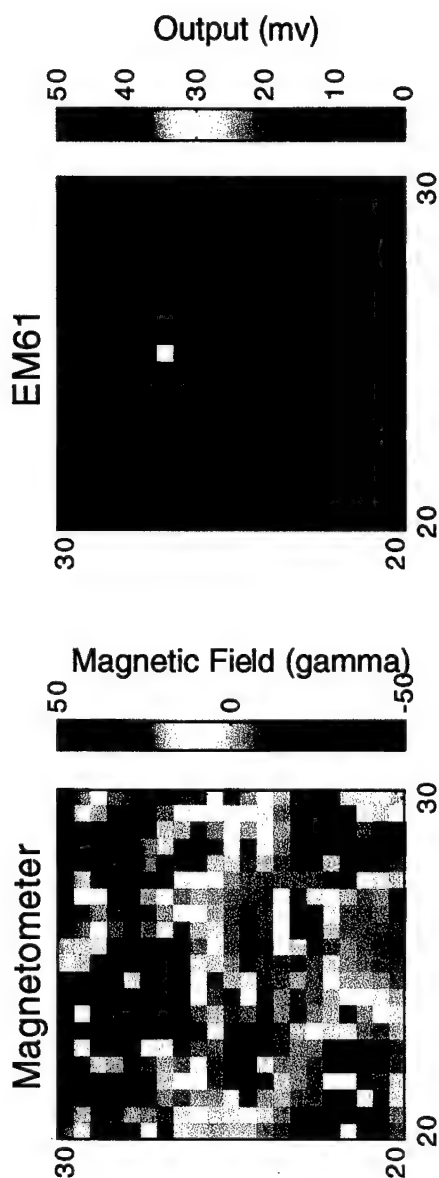
[25E,5N]

A-4



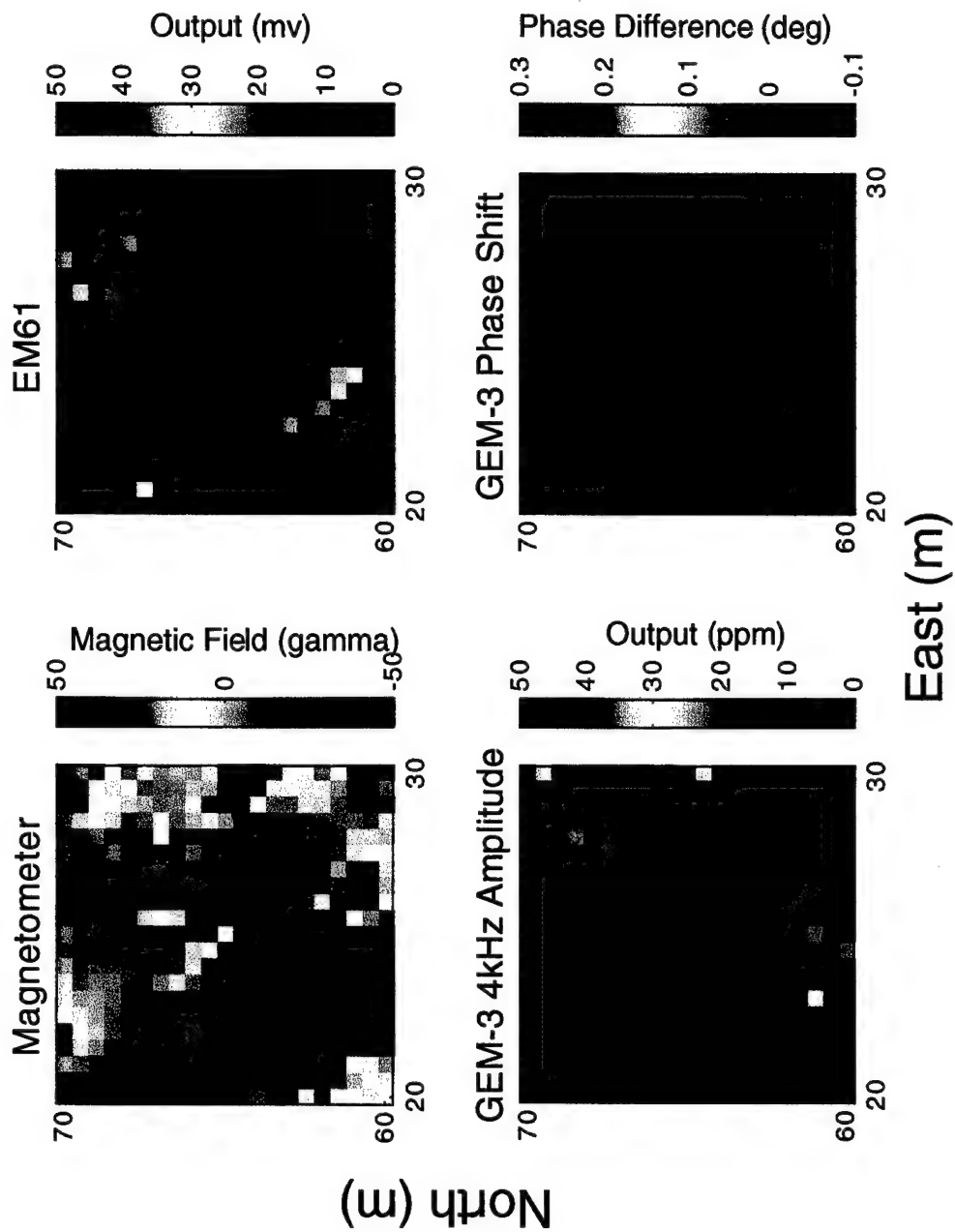
[25E, 15N]

A-5



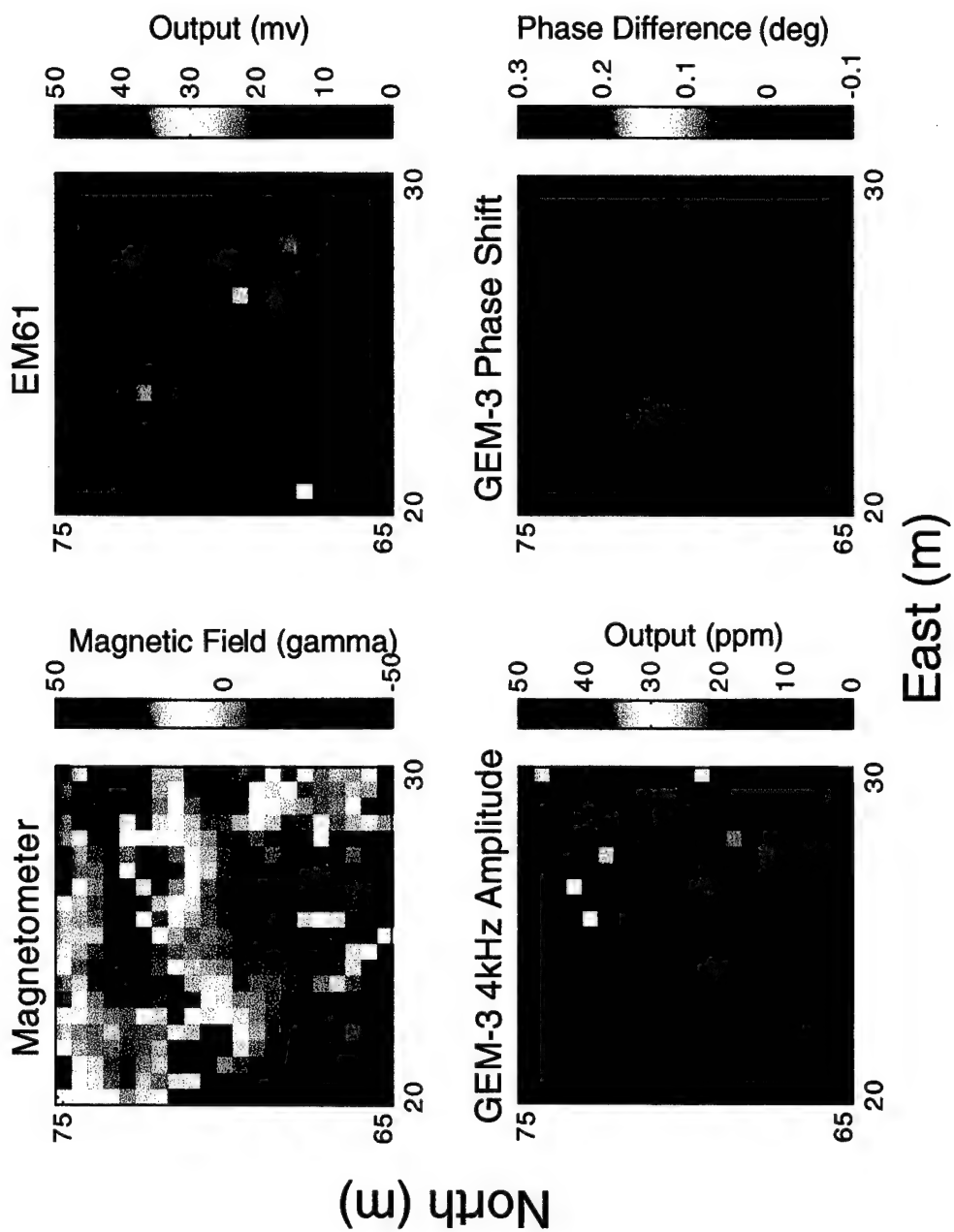
[25E,25N]

A-6



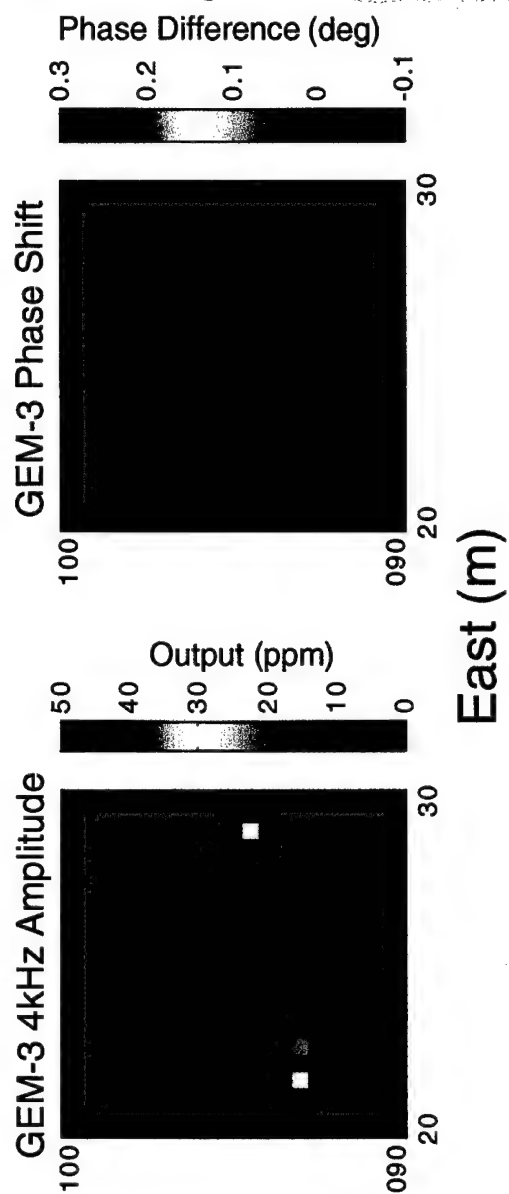
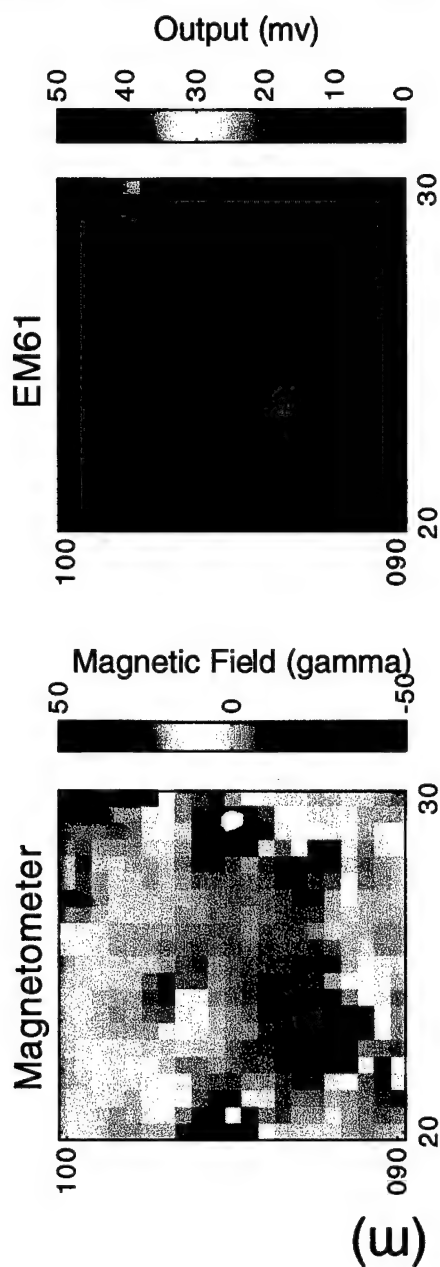
[25E,65N]

A-9



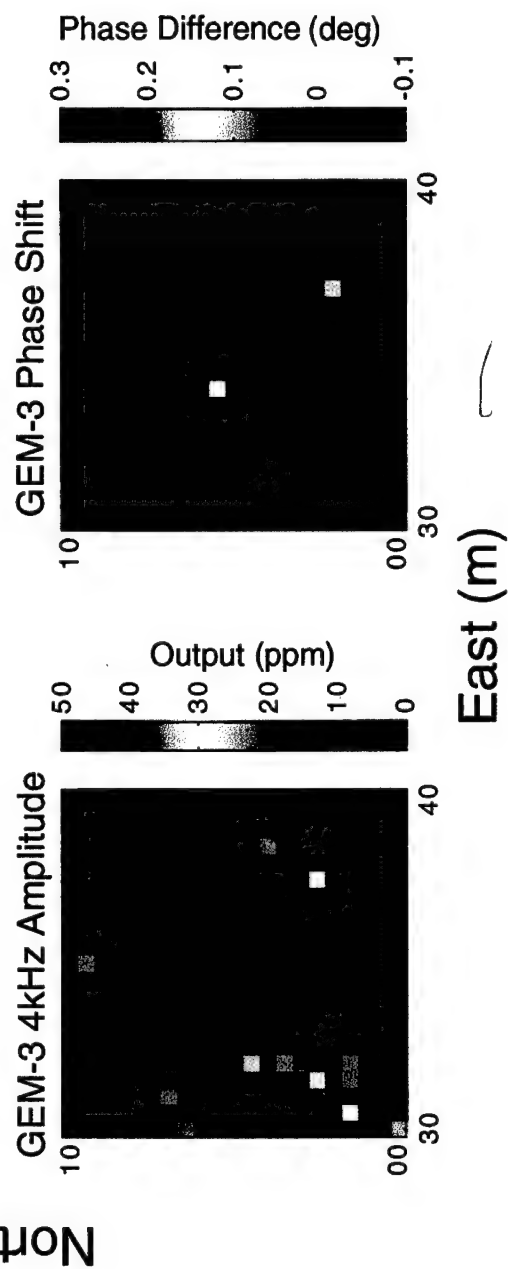
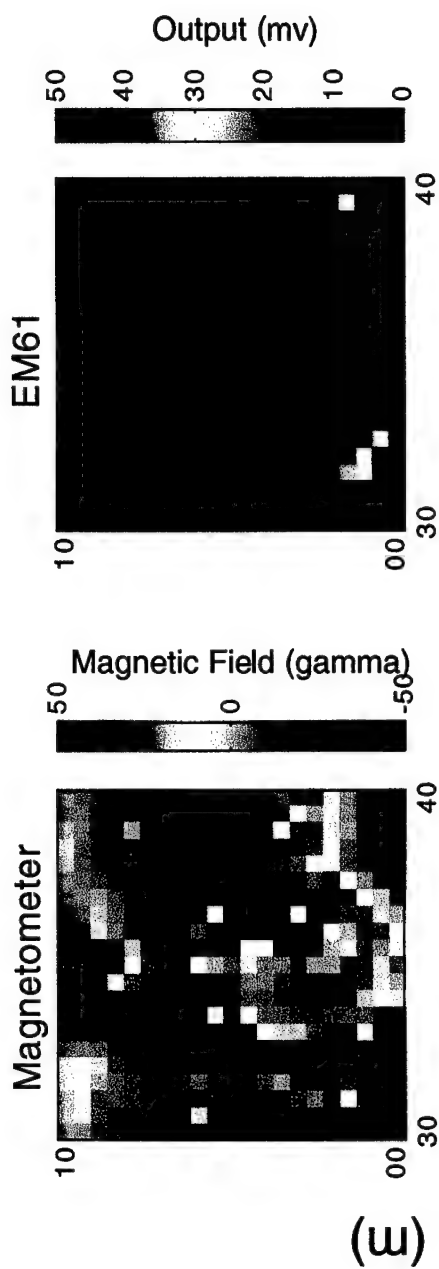
[25E,70N]

A-10



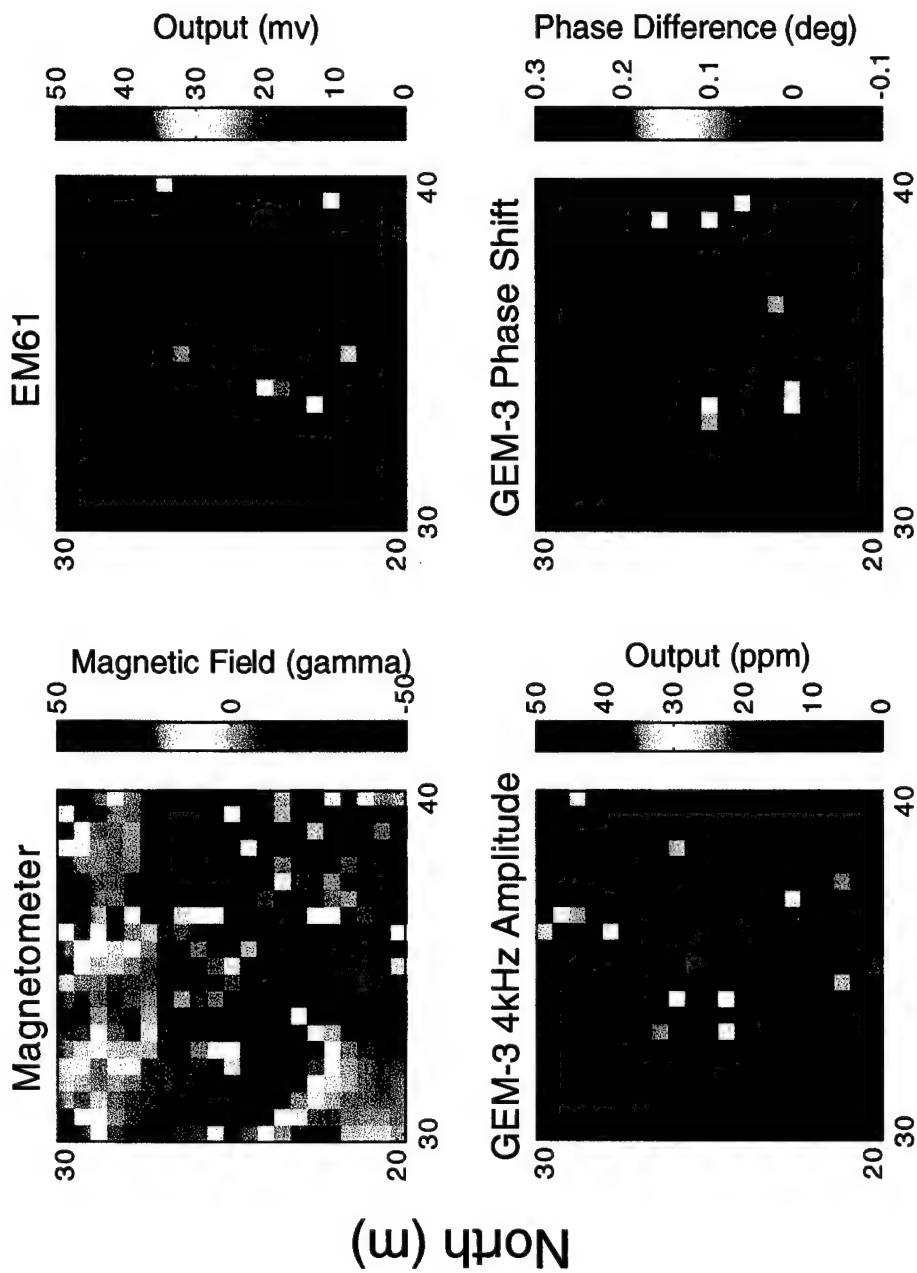
[25E,85N]

A-11



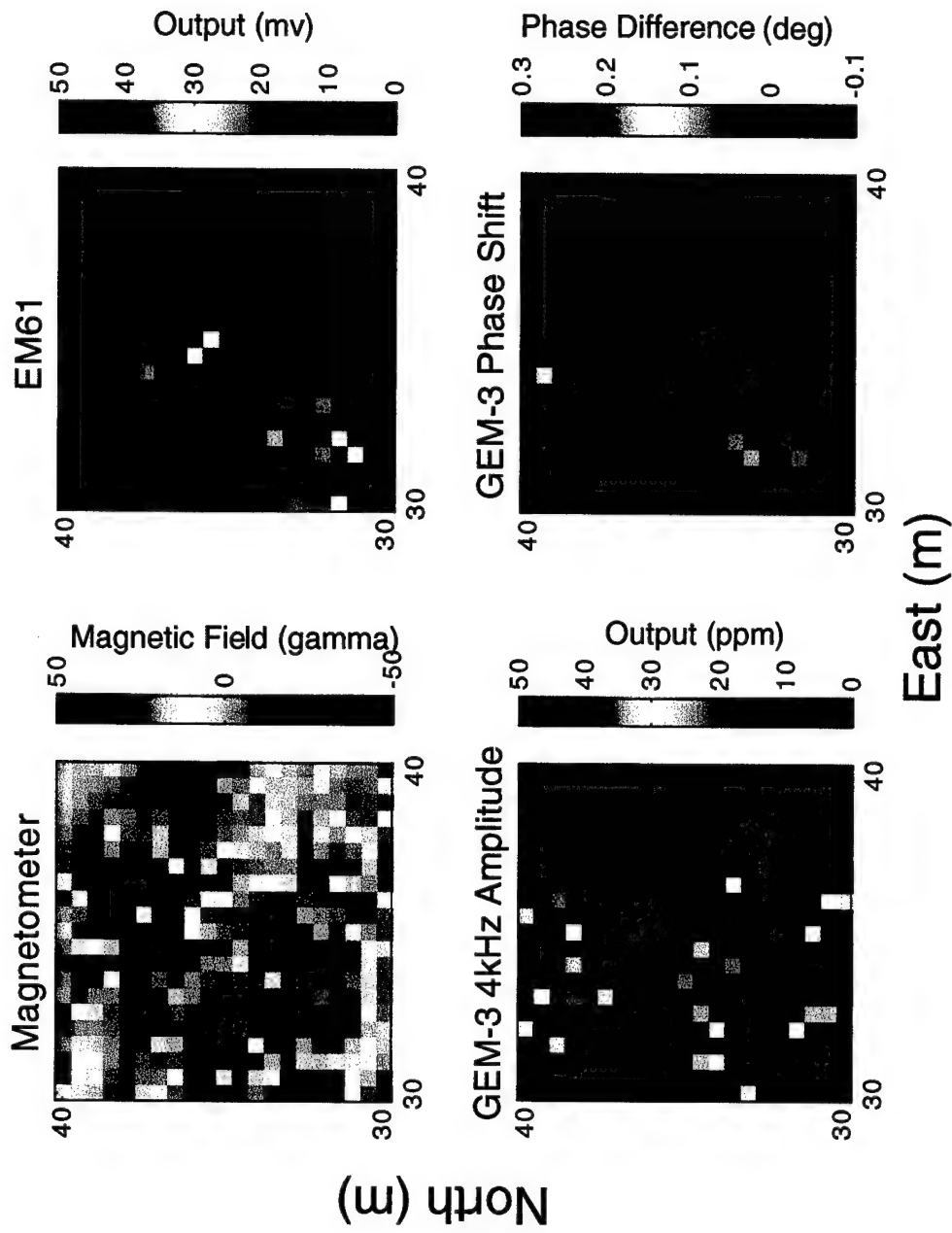
[35E, 5N]

A-12



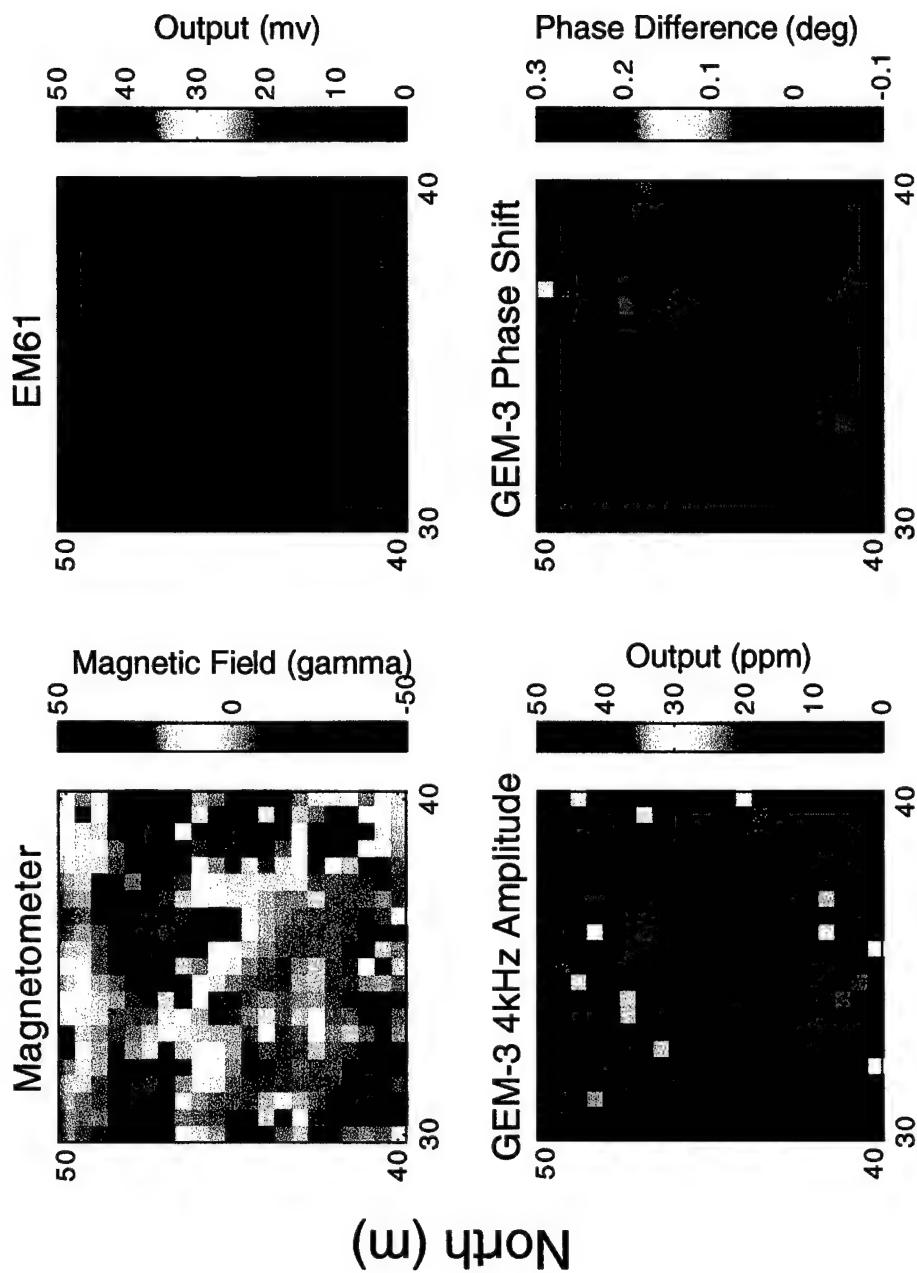
[35E,25N]

A-14



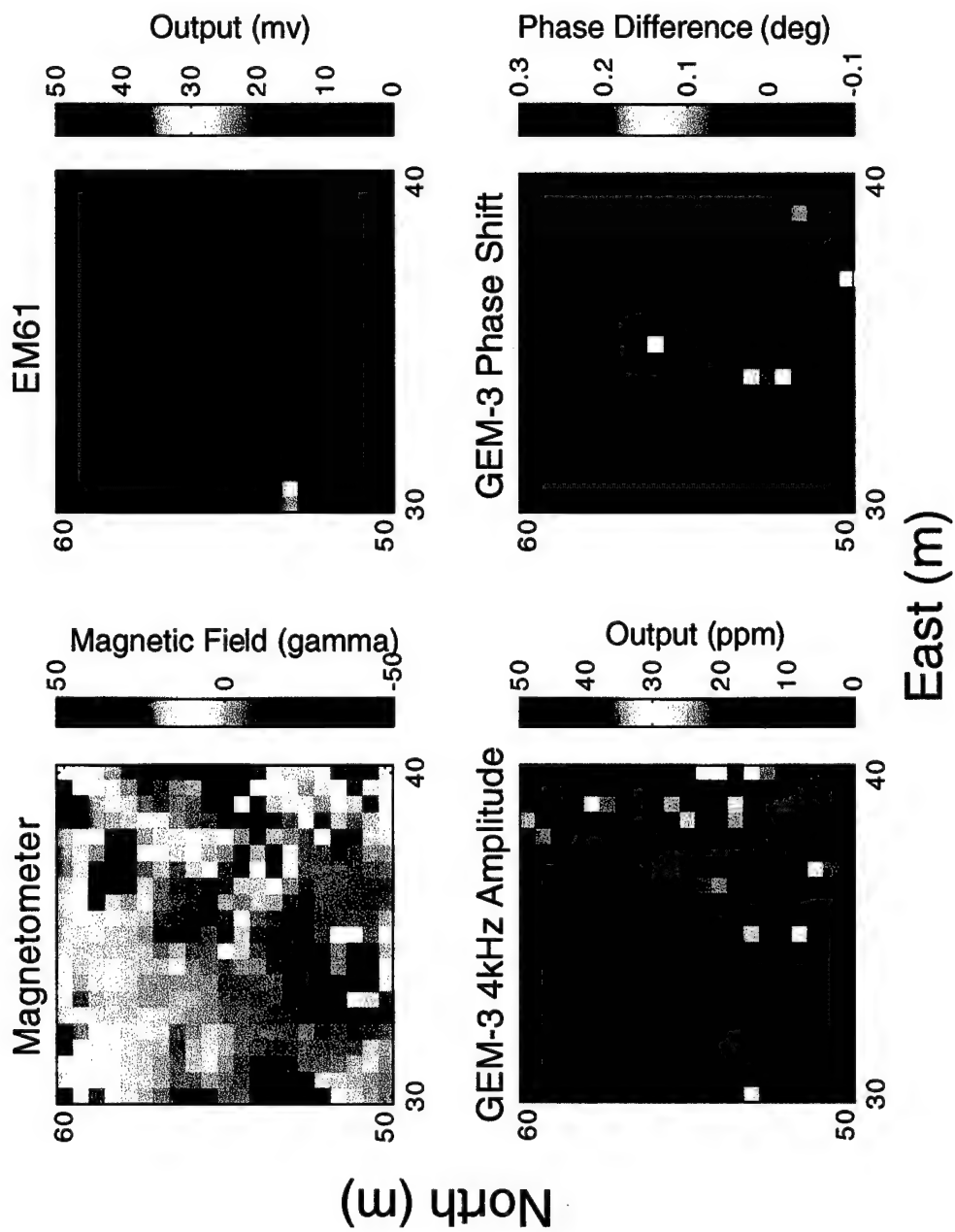
[35E,35N]

A-15



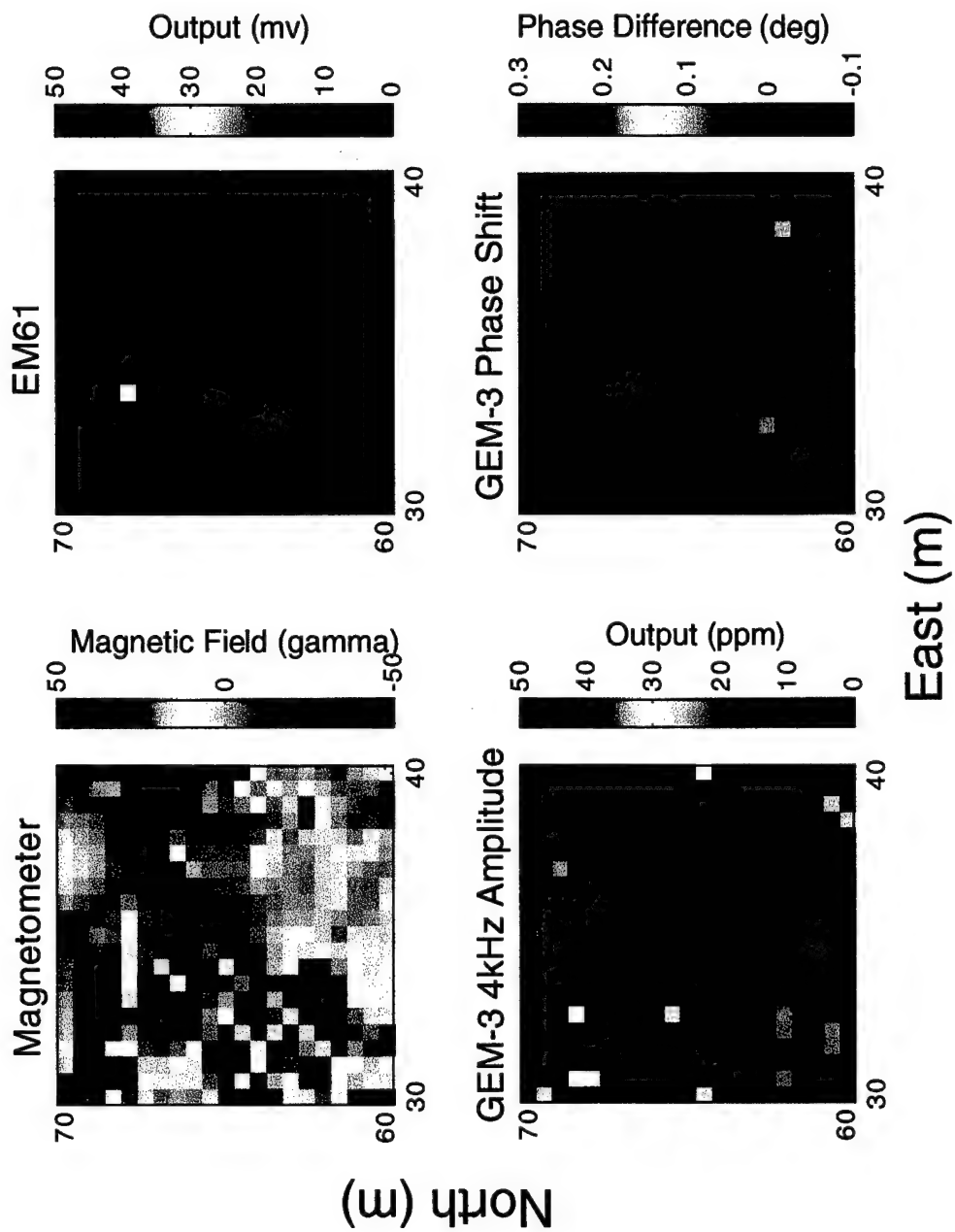
[35E,45N]

A-16



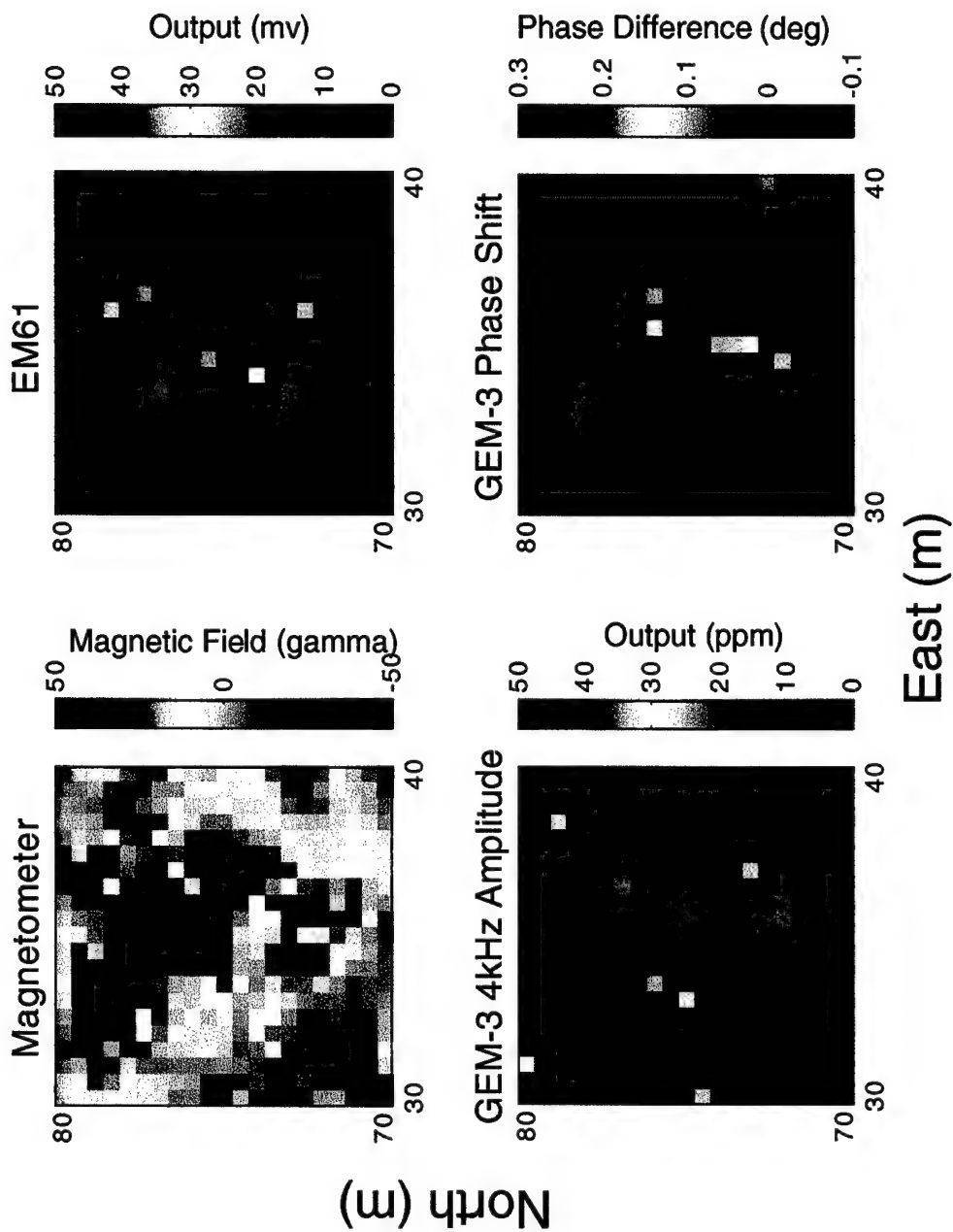
[35E,55N]

A-17



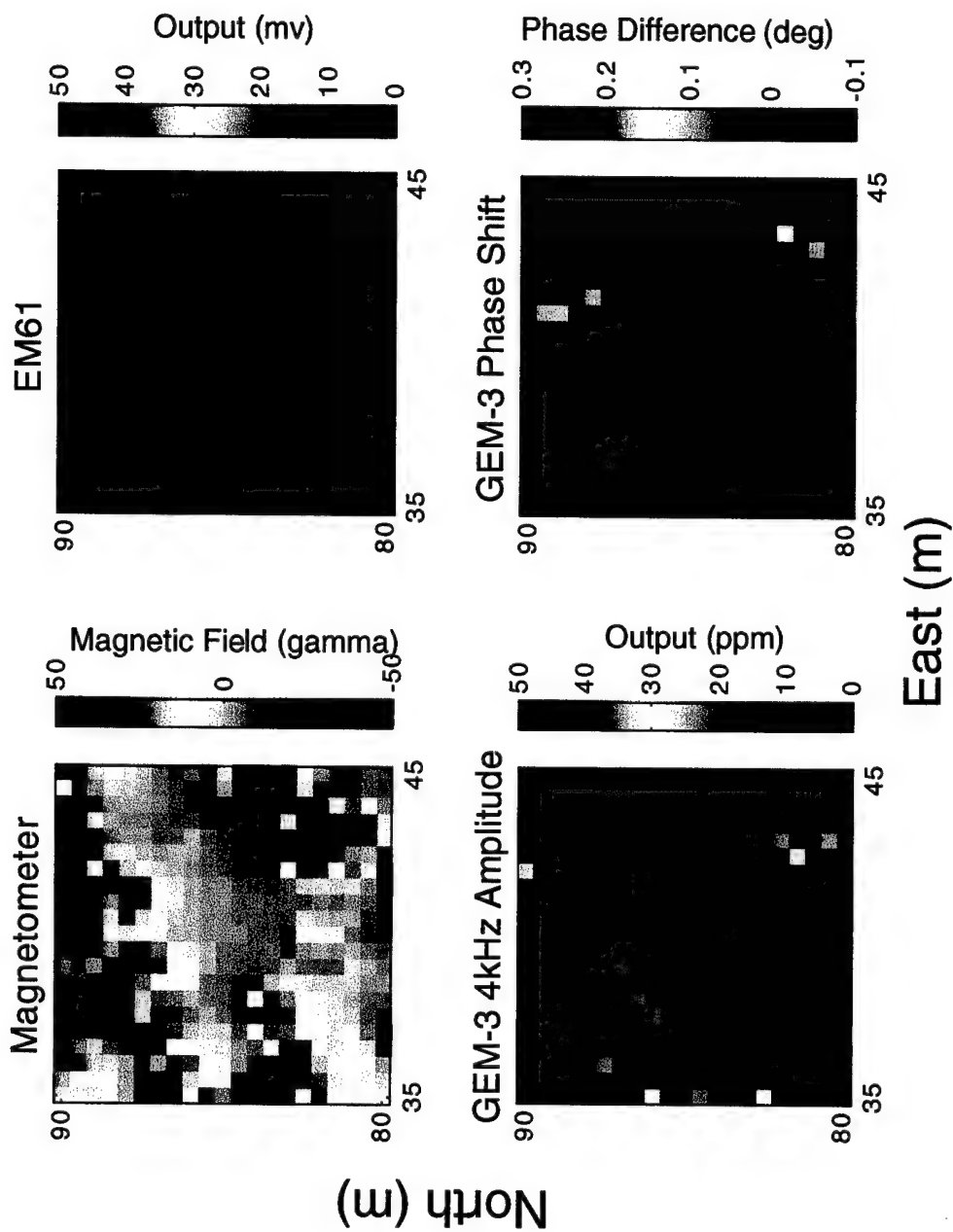
[35E, 65N]

A-18



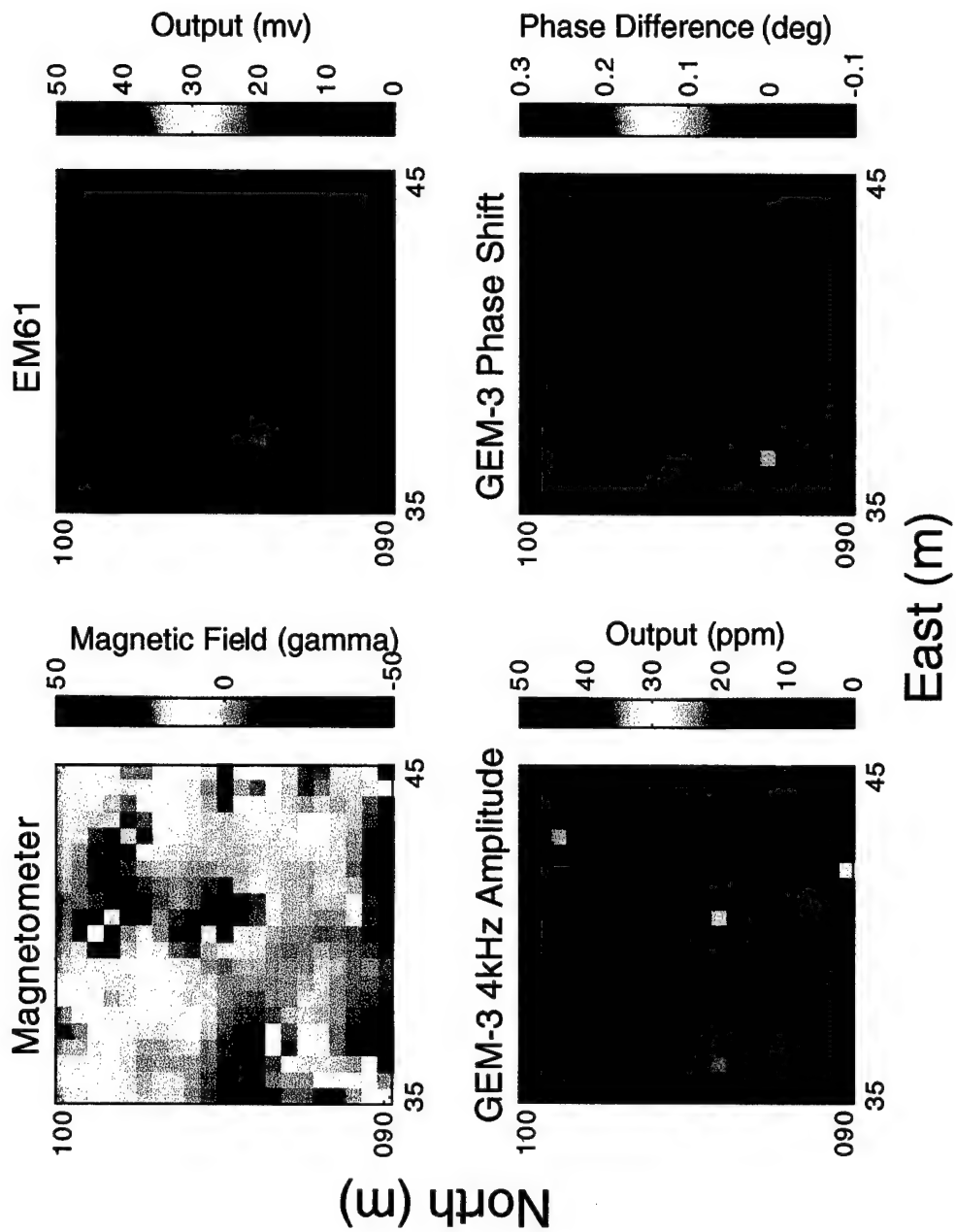
[35E,75N]

A-19



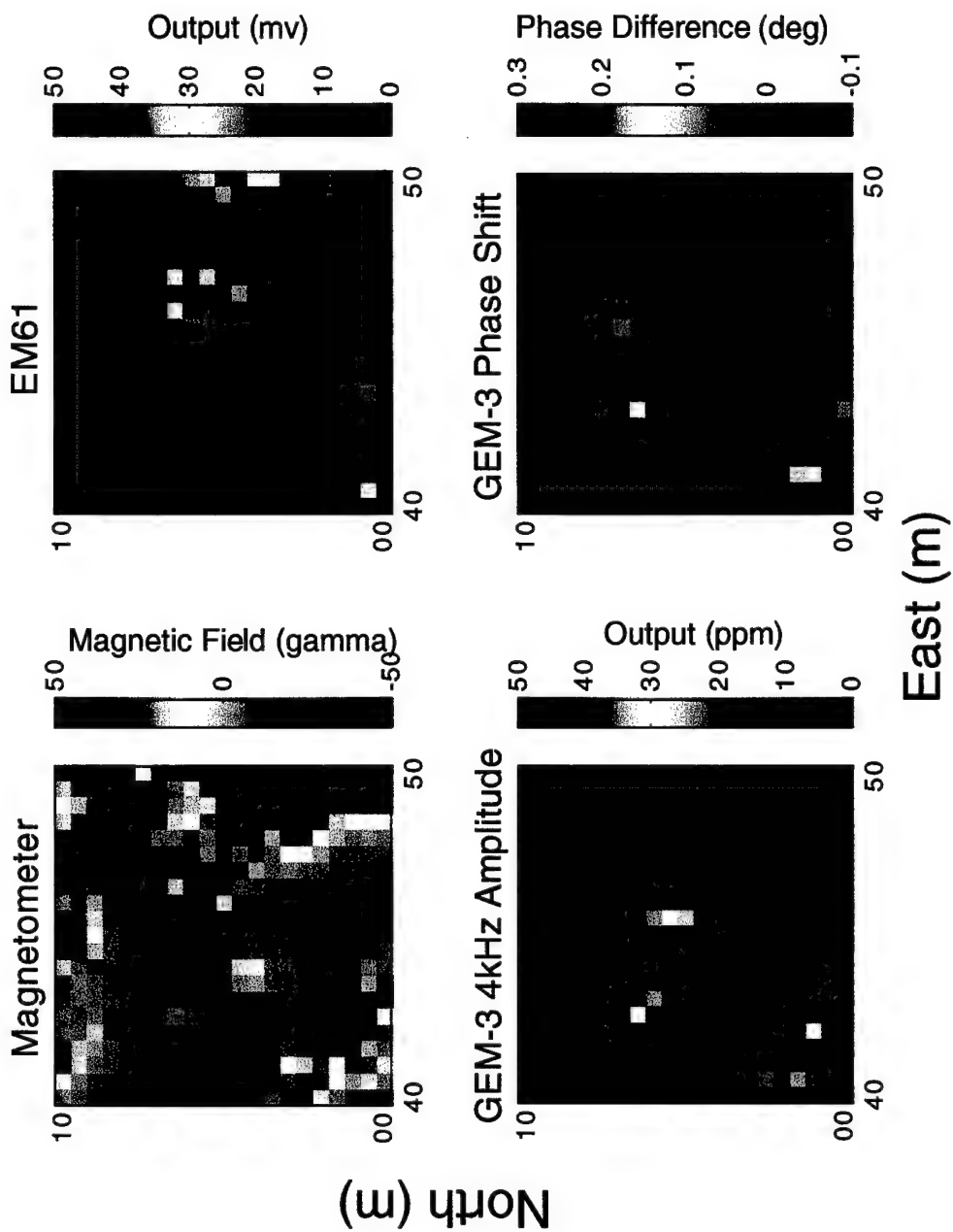
[40E,85N]

A-20



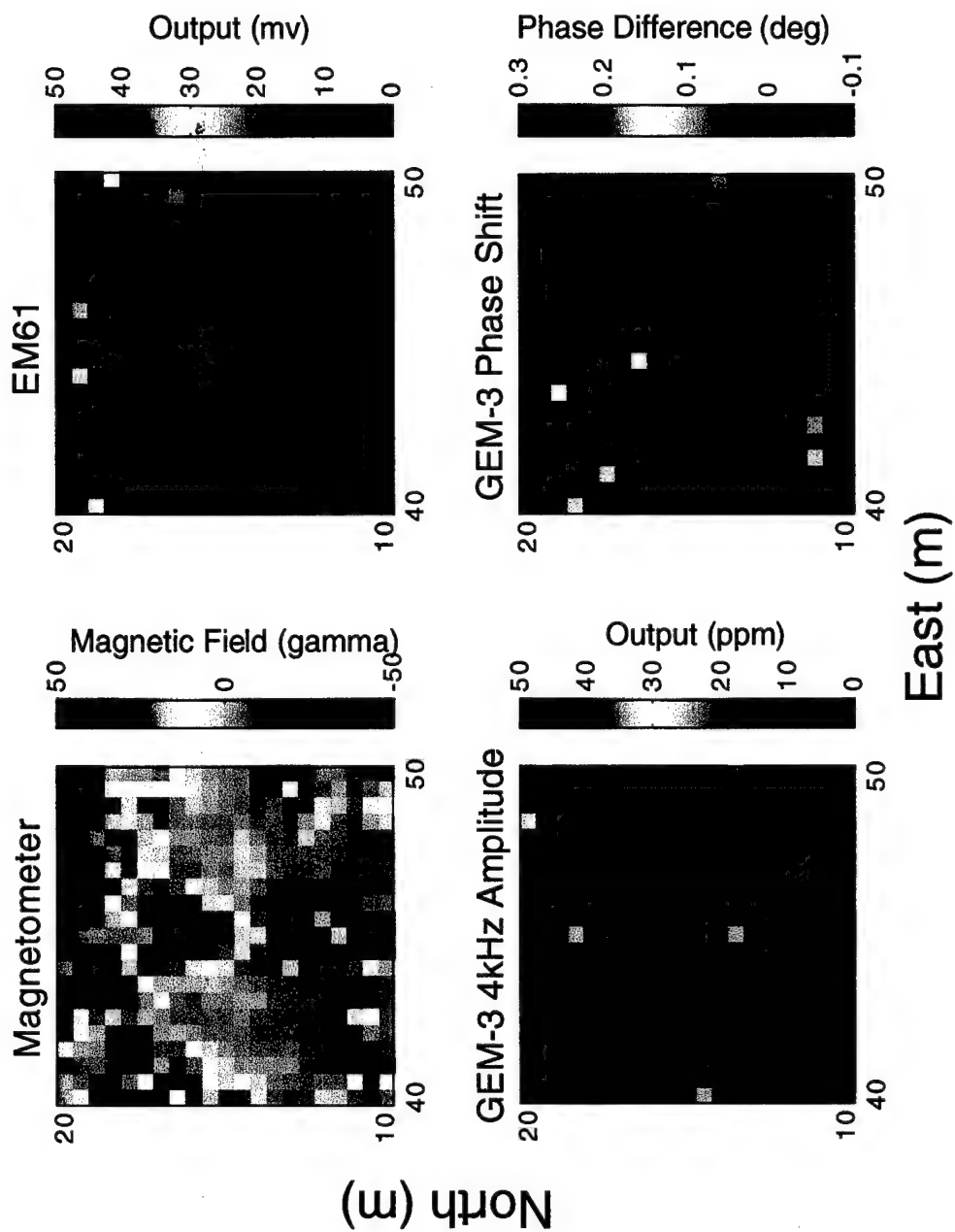
[40E, 65N]

A-21



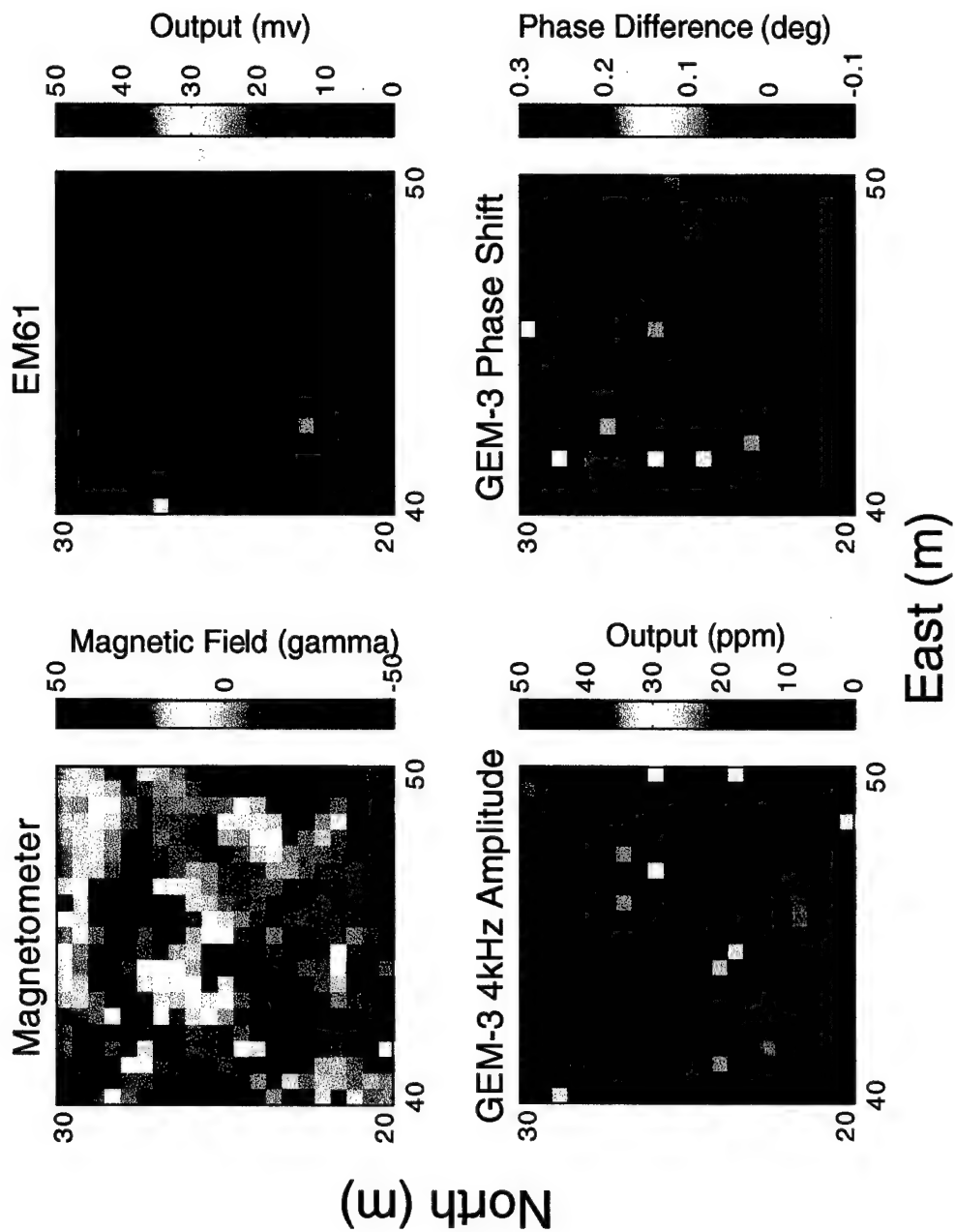
[45E, 5N]

A-22



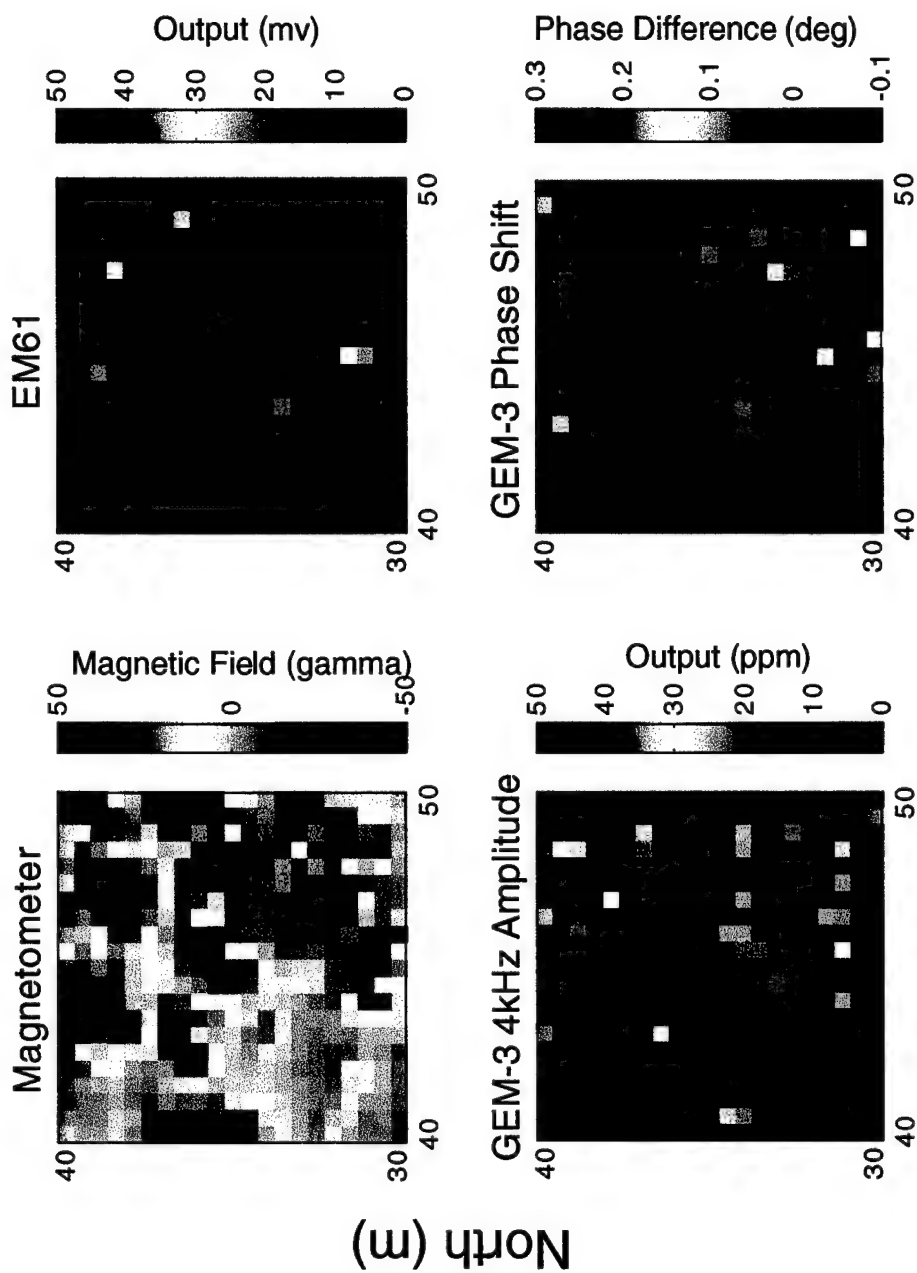
[45E, 15N]

A-23



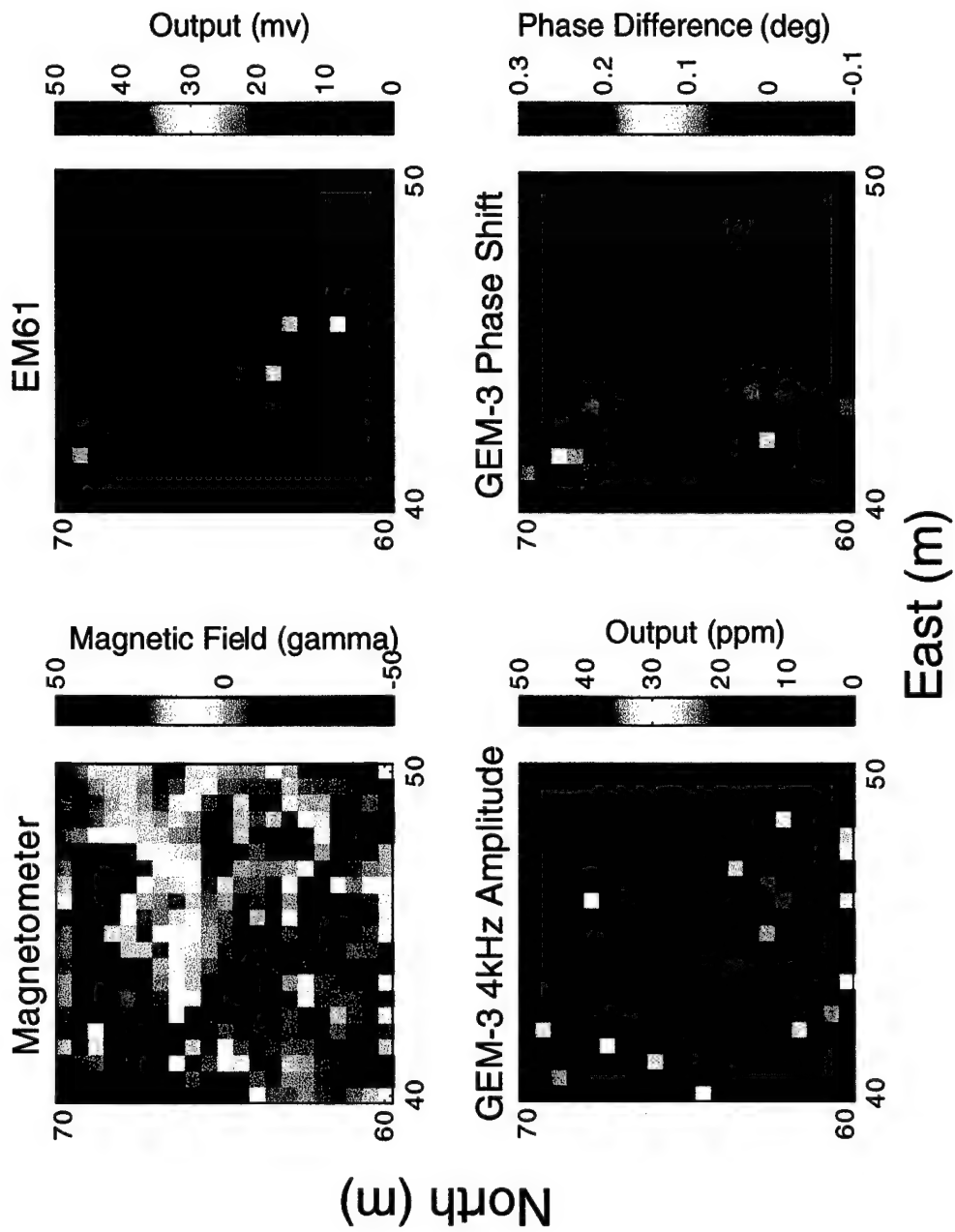
[45E,25N]

A-24



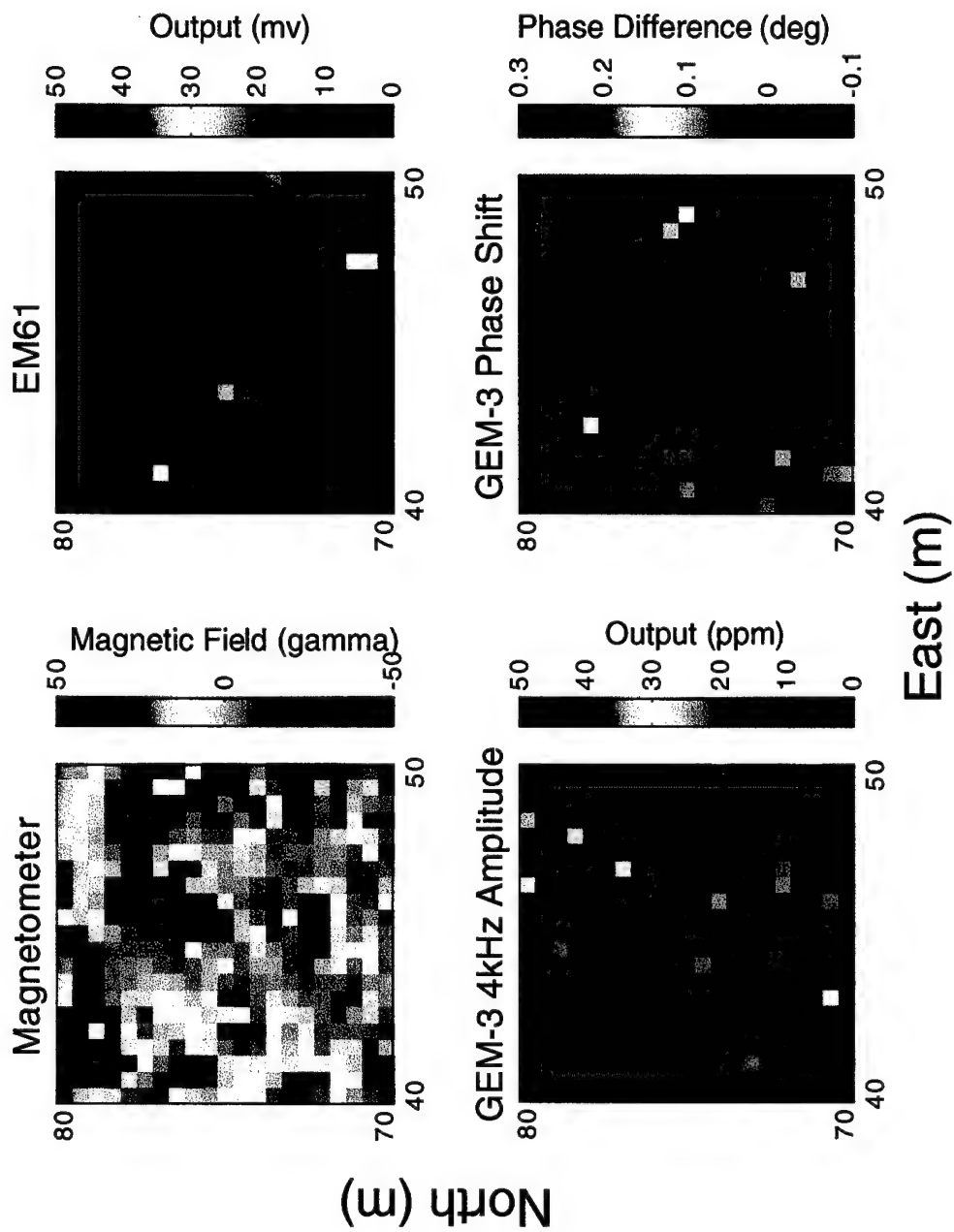
[45E,35N]

A-25



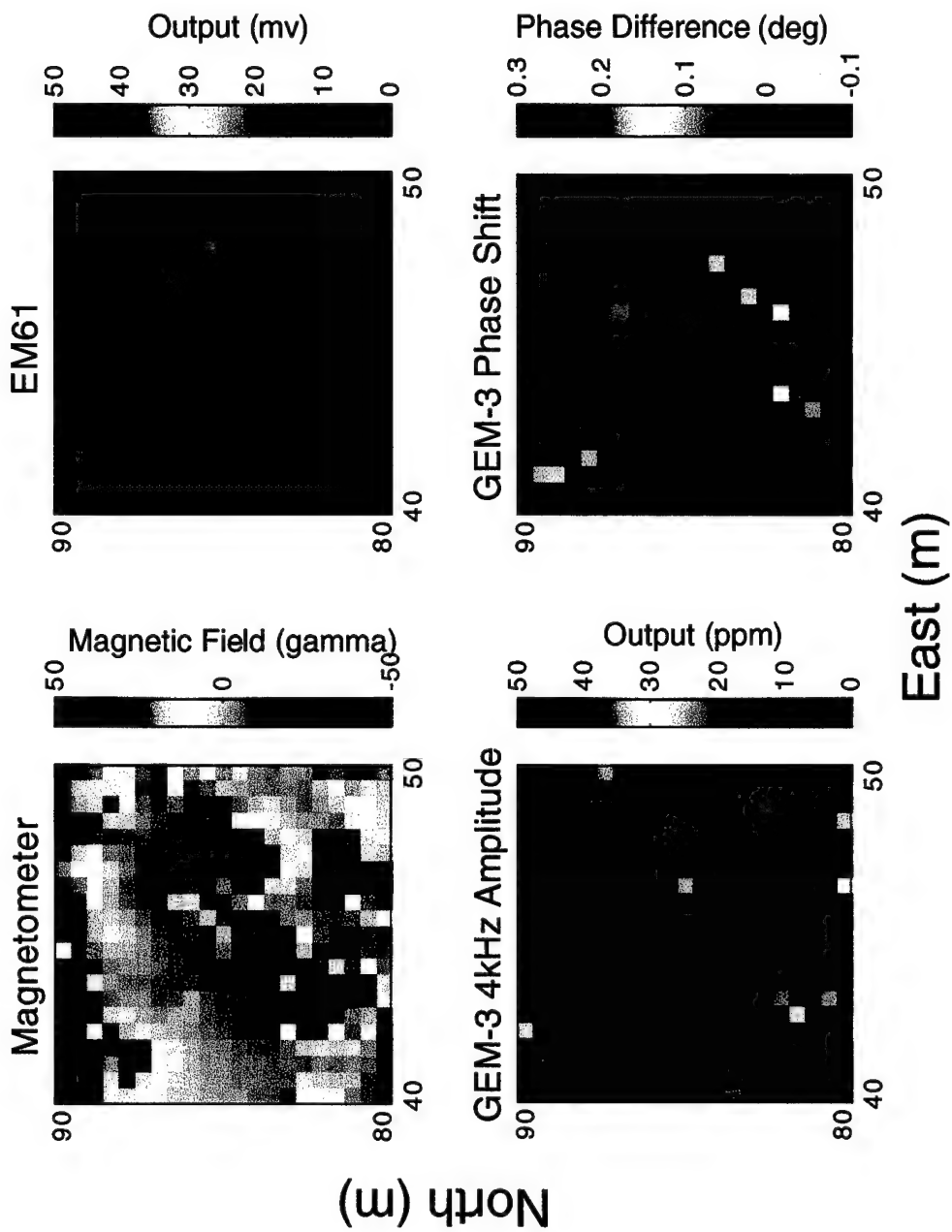
[45E,65N]

A-28



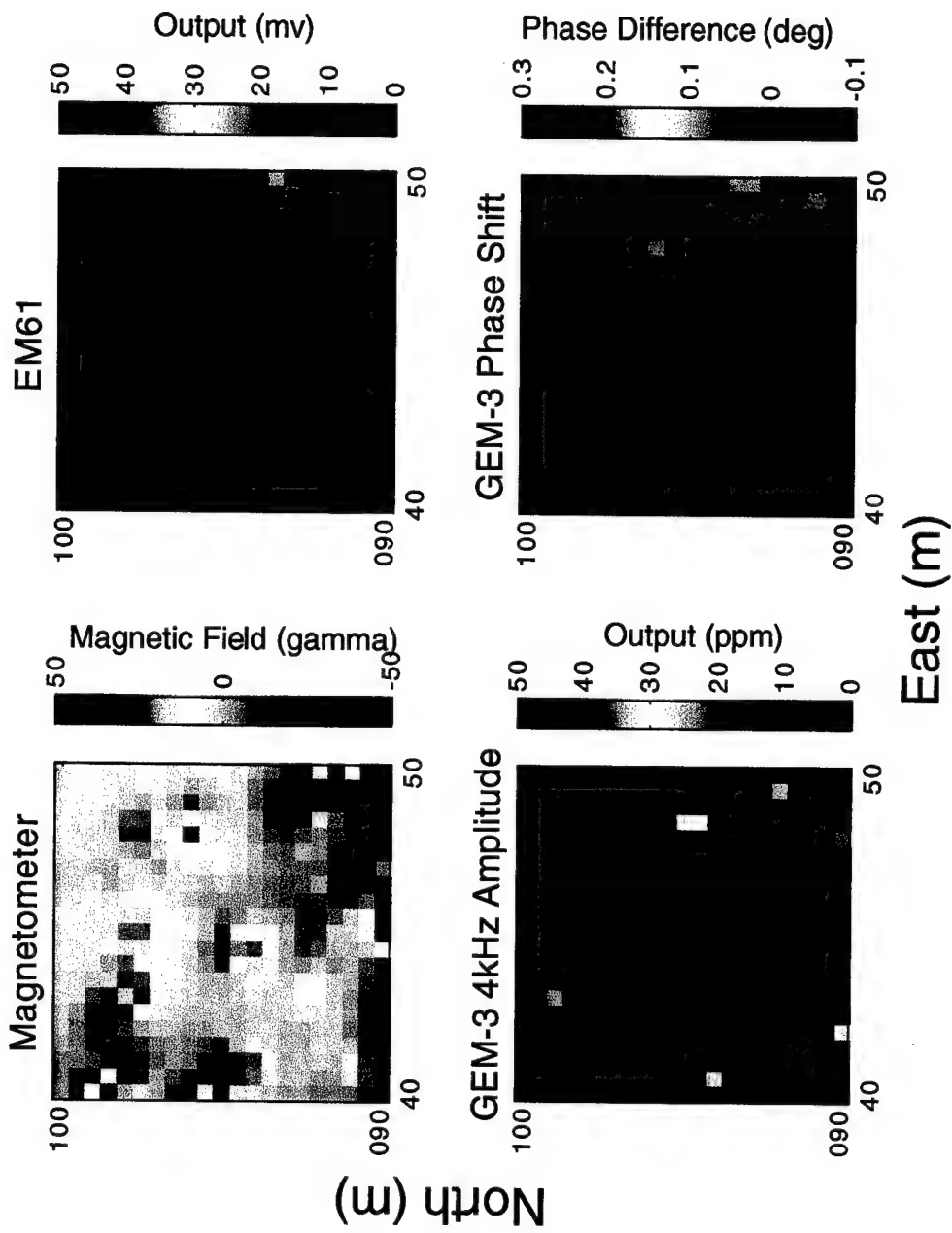
[45E, 75N]

A-29



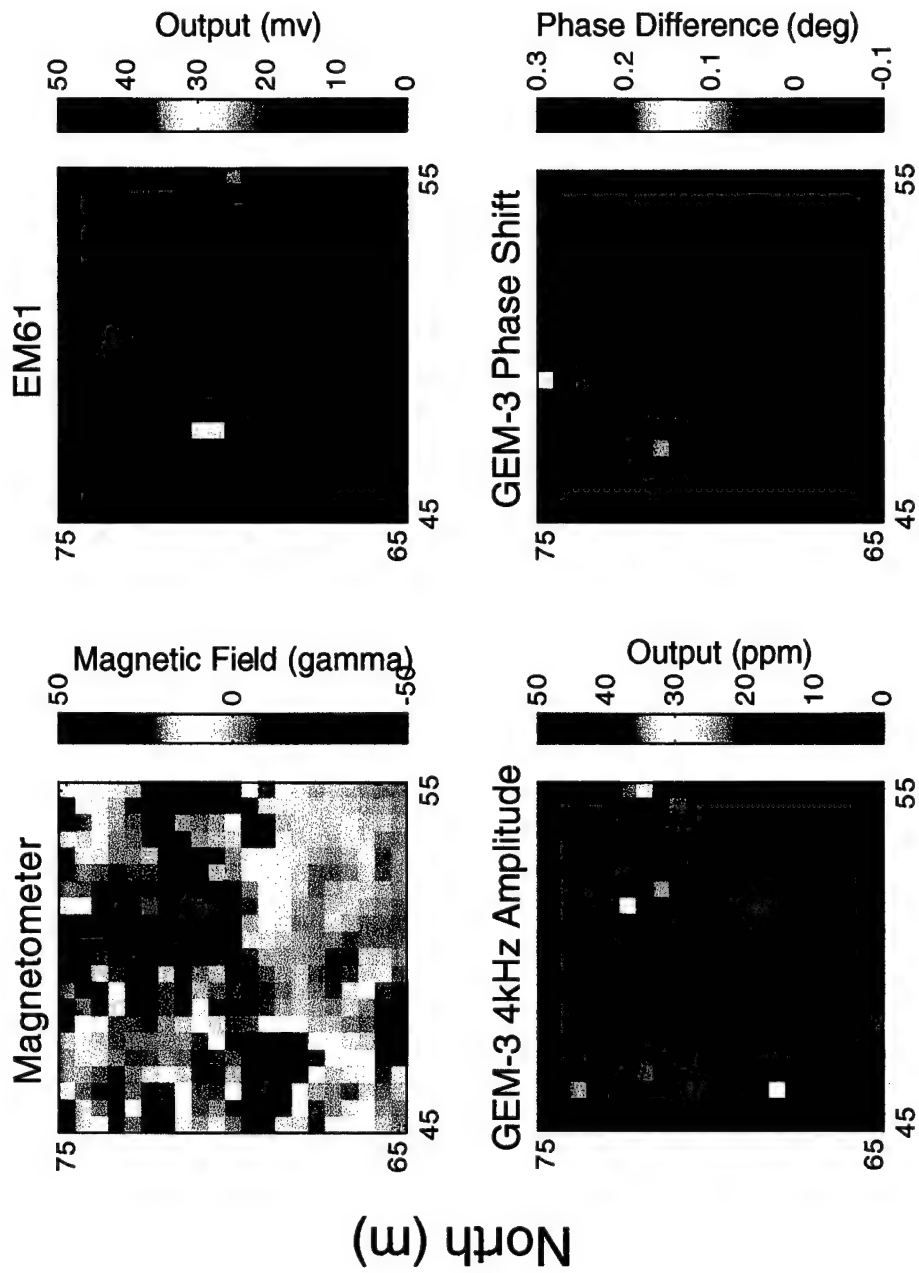
[45E,85N]

A-30



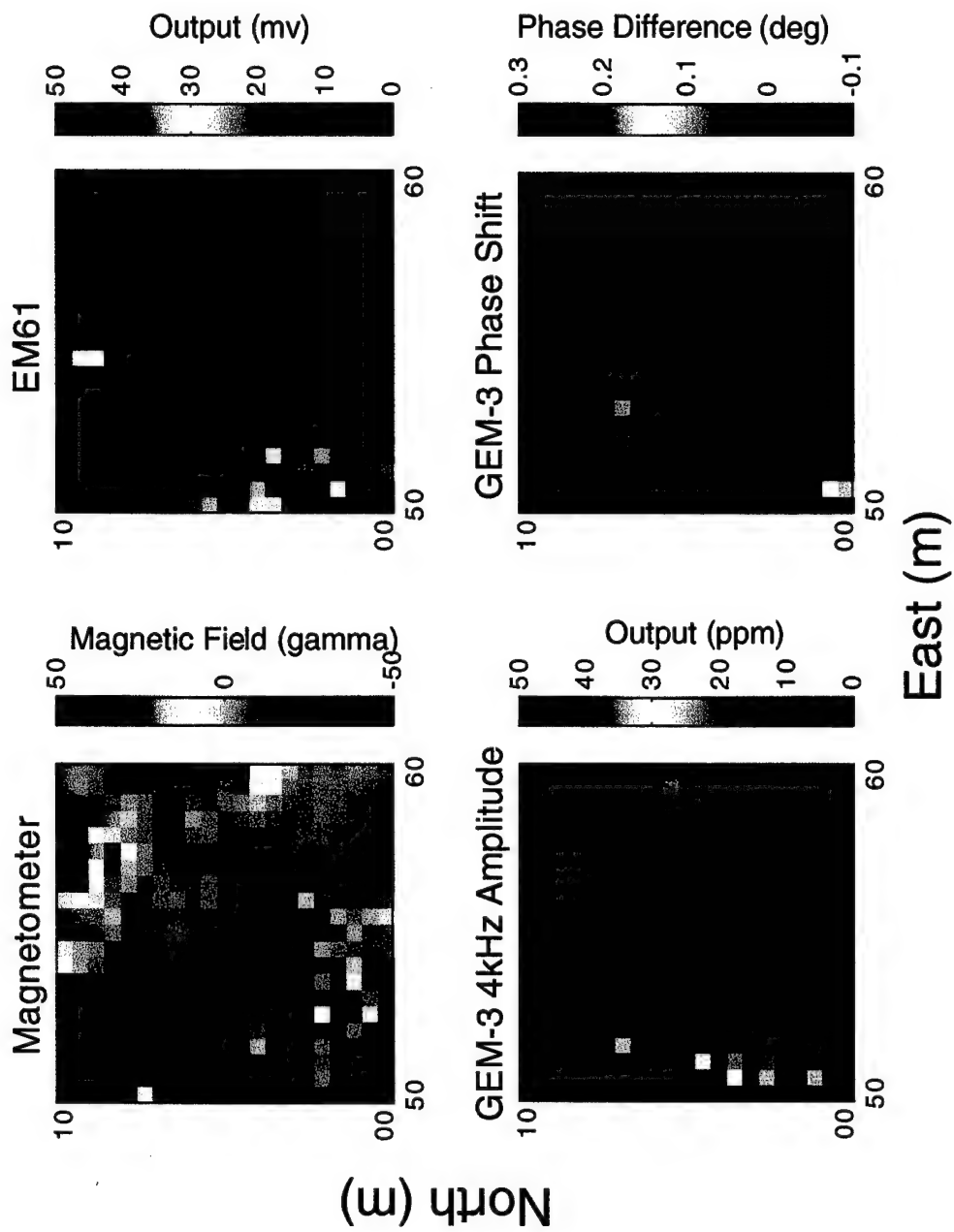
[45E,95N]

A-32



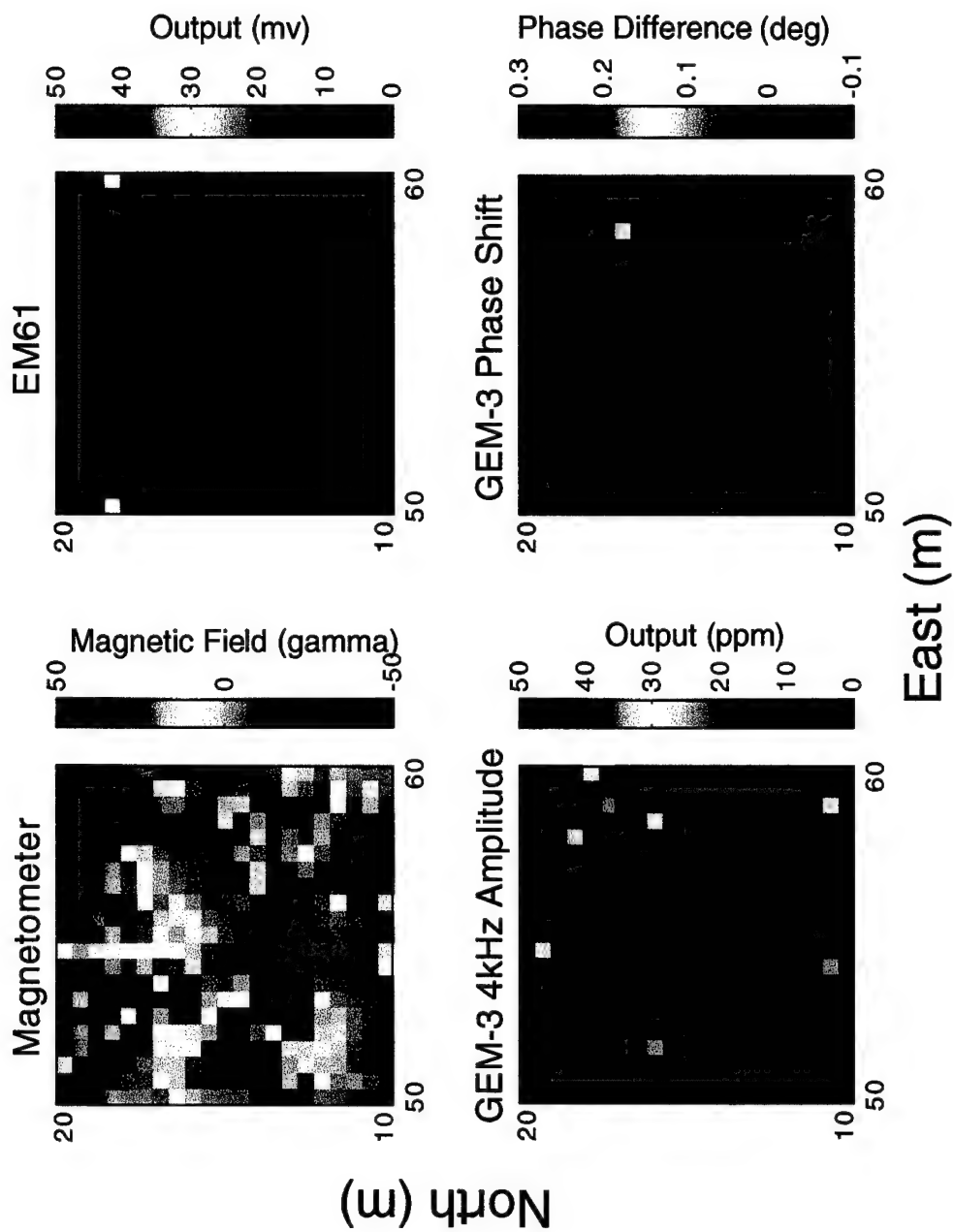
[50E, 70N]

A-33



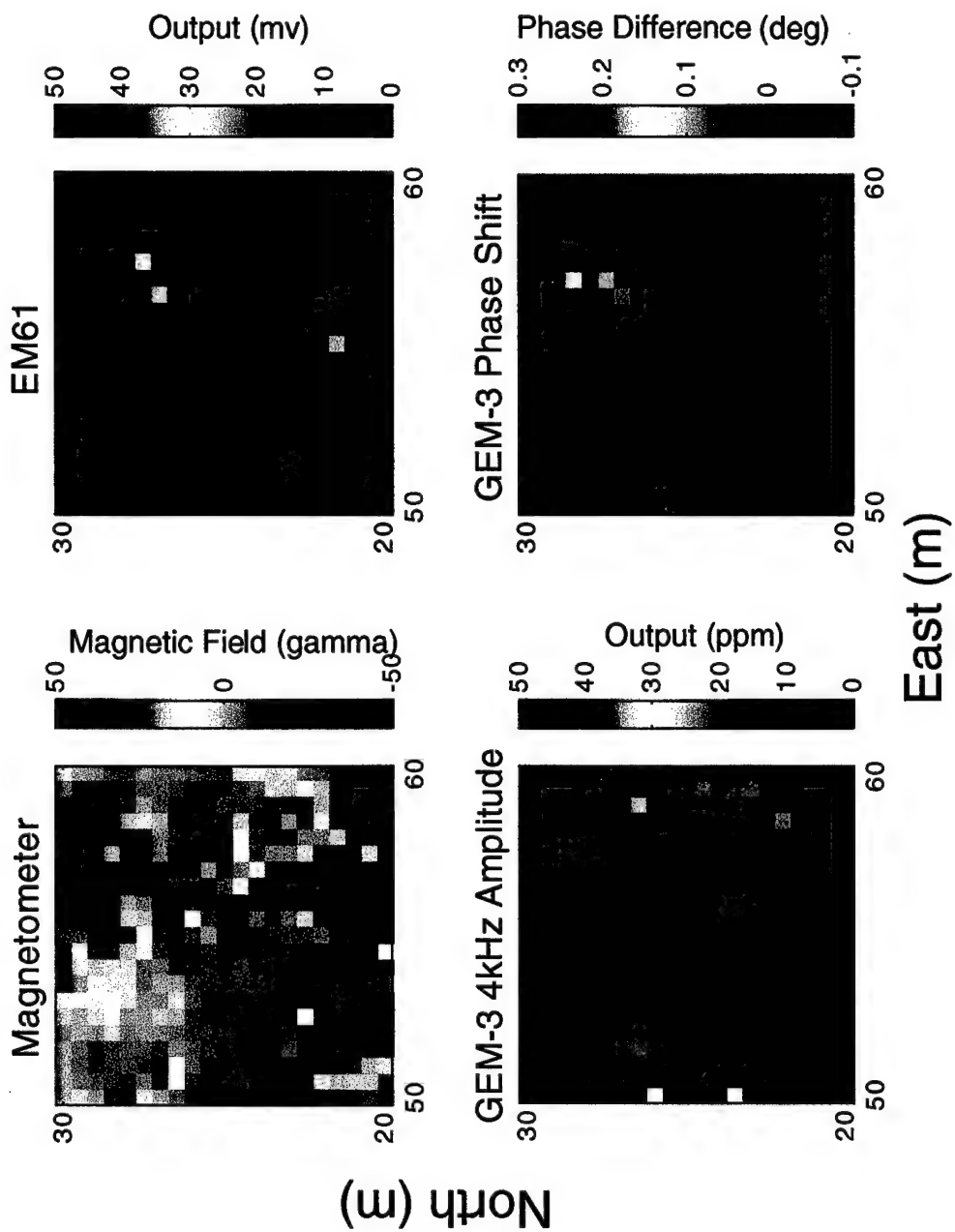
[55E,5N]

A-34



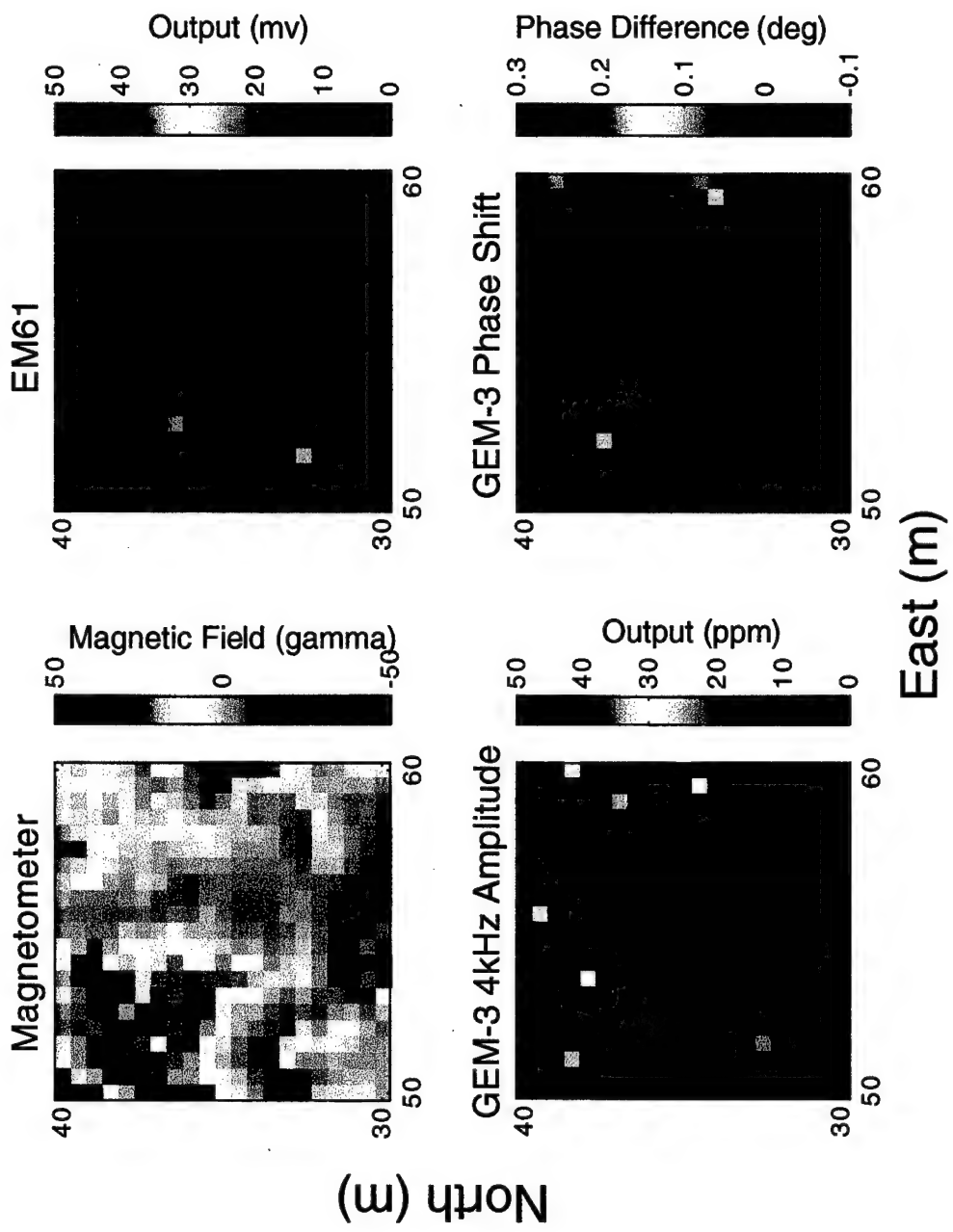
[55E, 15N]

A-35



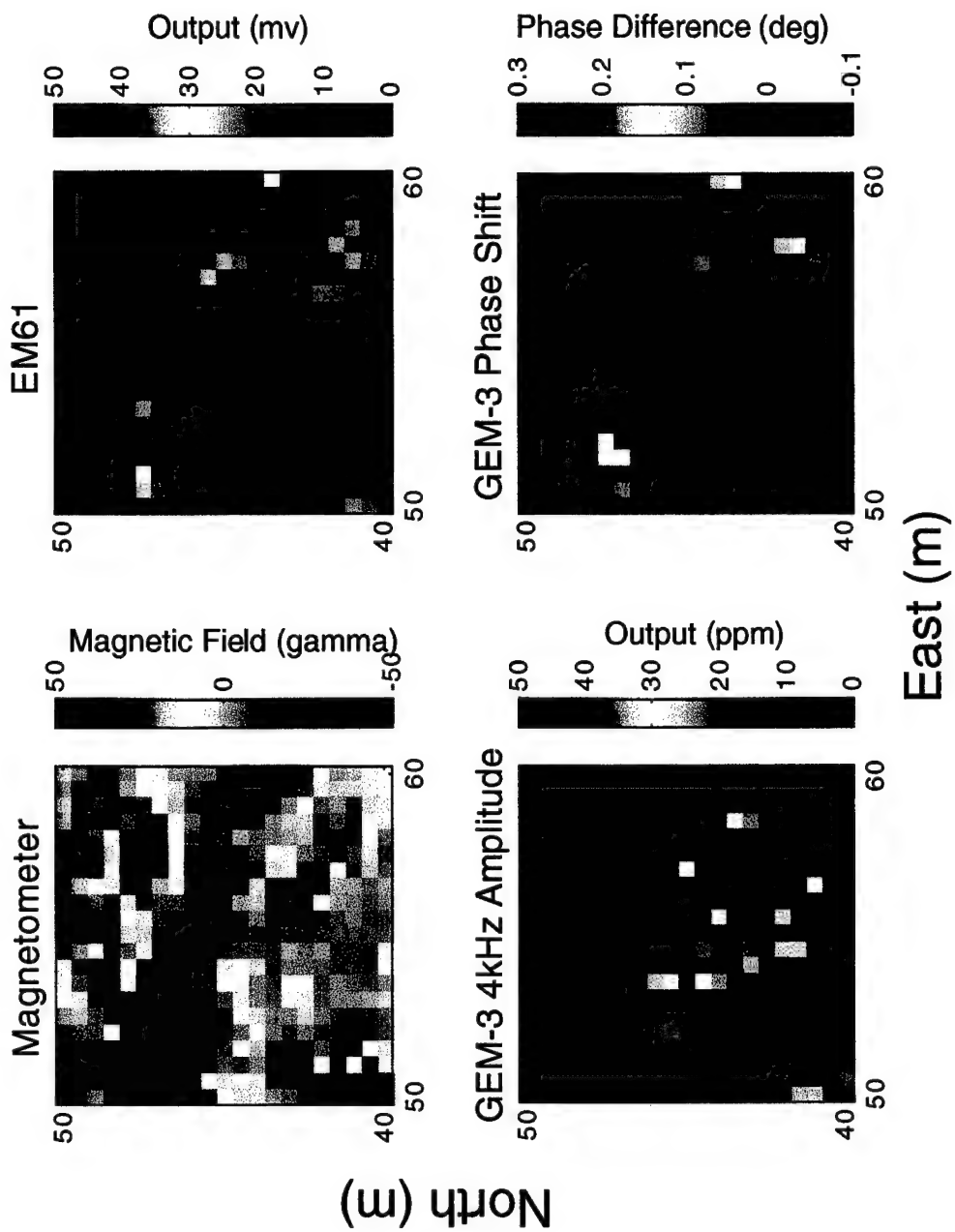
[55E,25N]

A-36



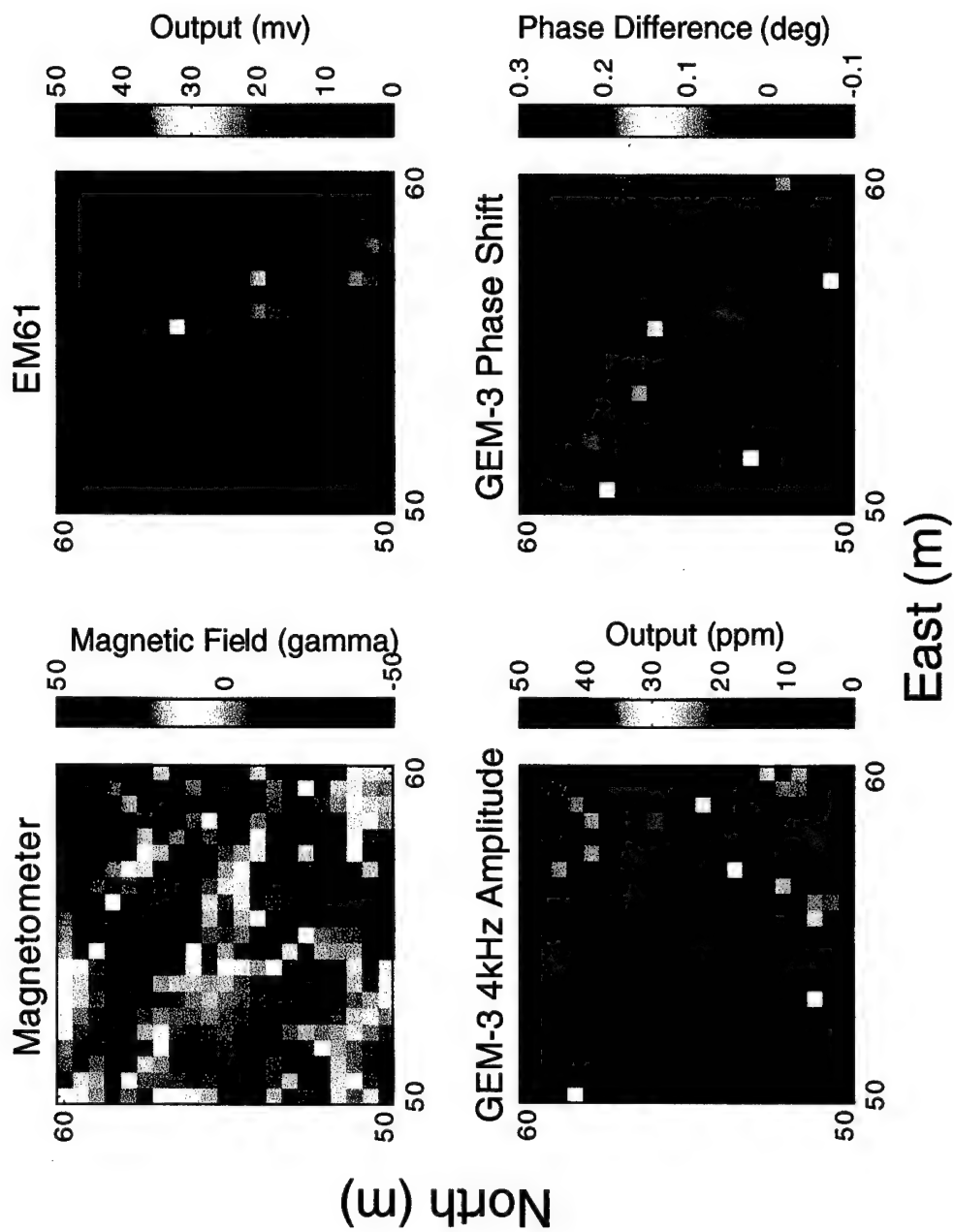
[55E,35N]

A-37



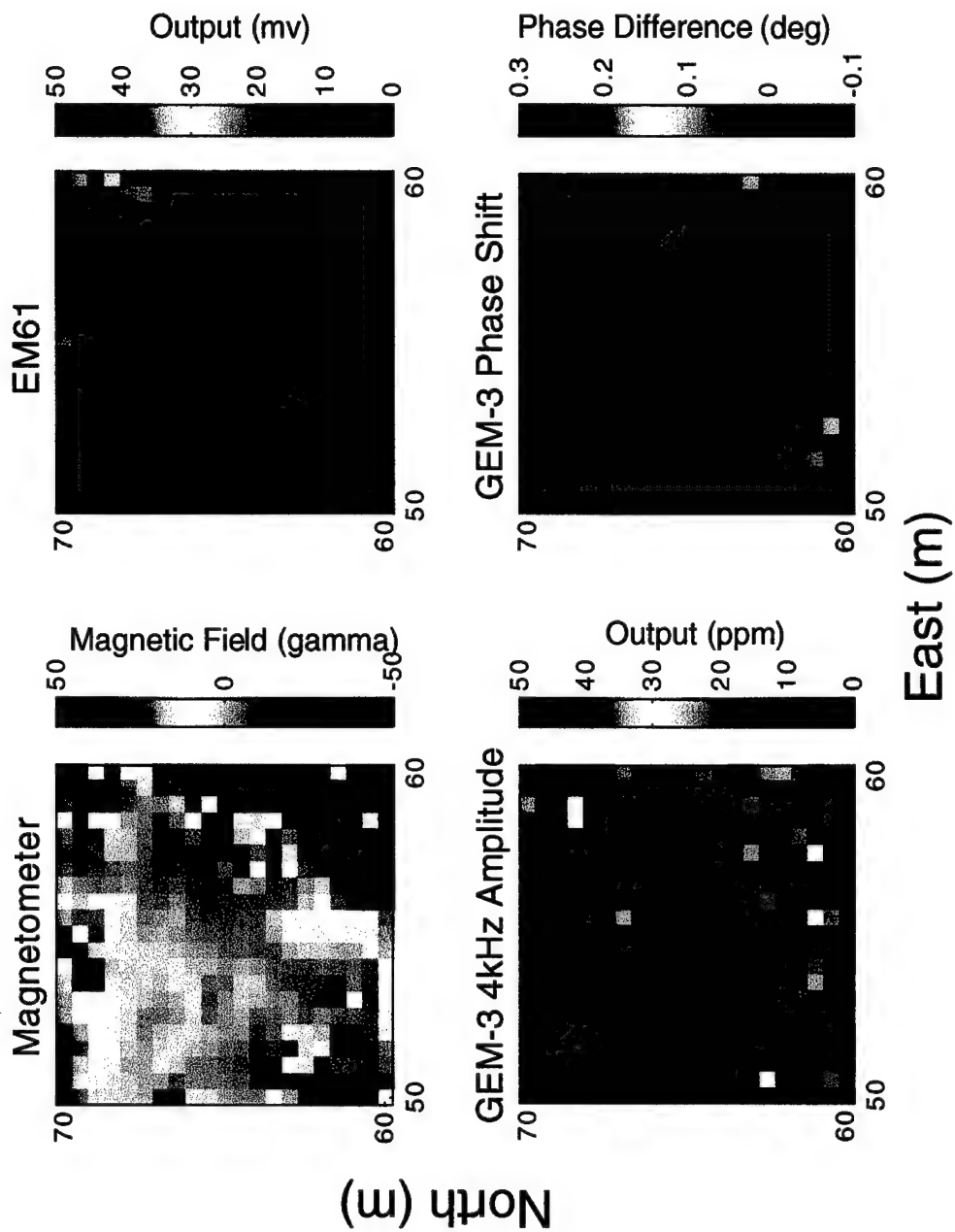
[55E, 45N]

A-38



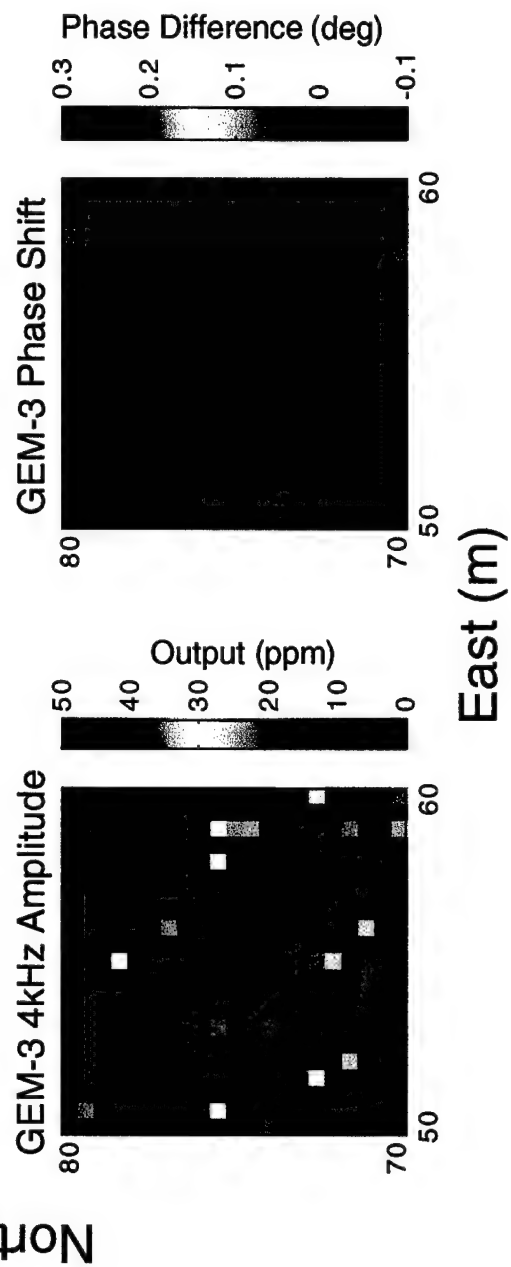
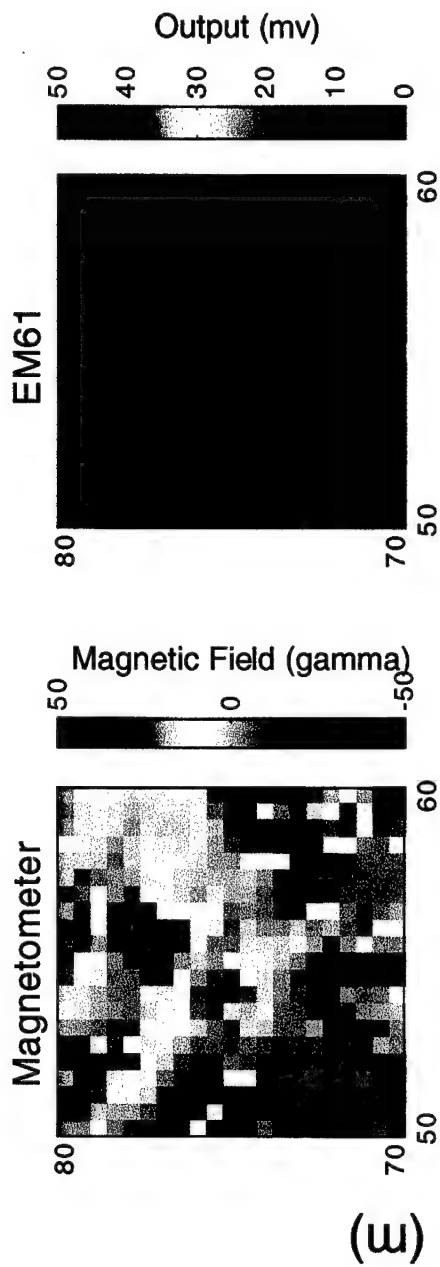
[55E,55N]

A-39



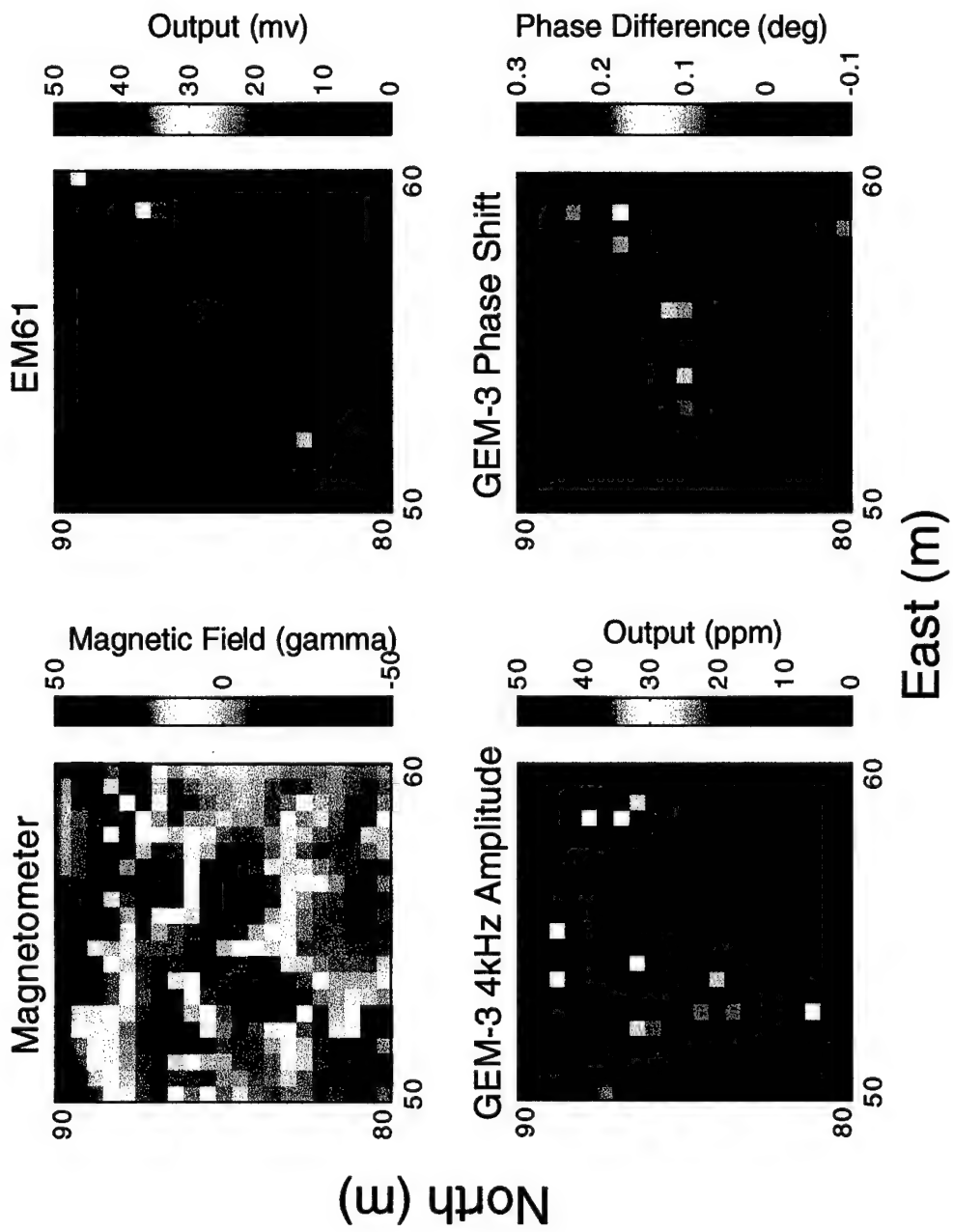
[55E, 65N]

A-40



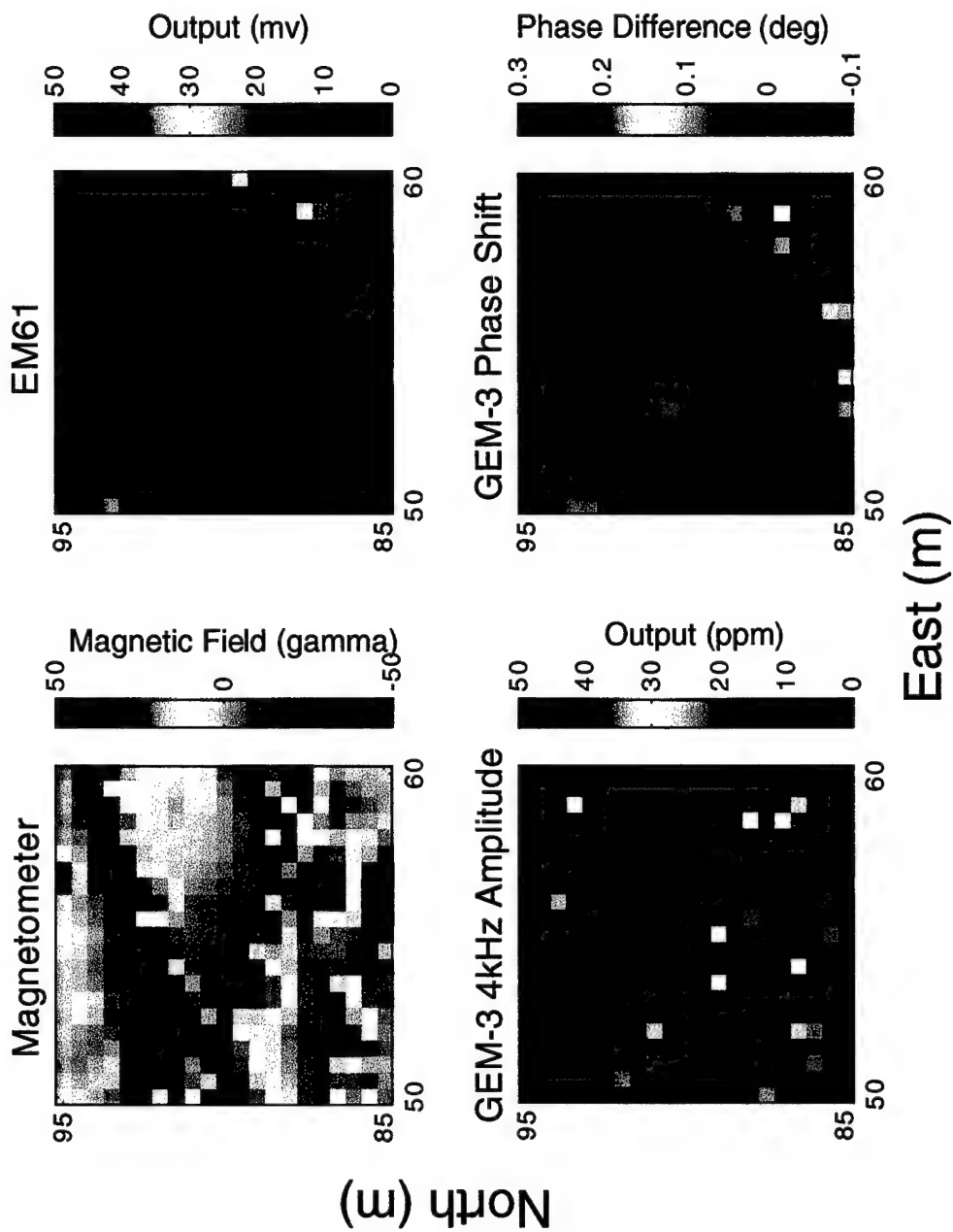
[55E, 75N]

A-41



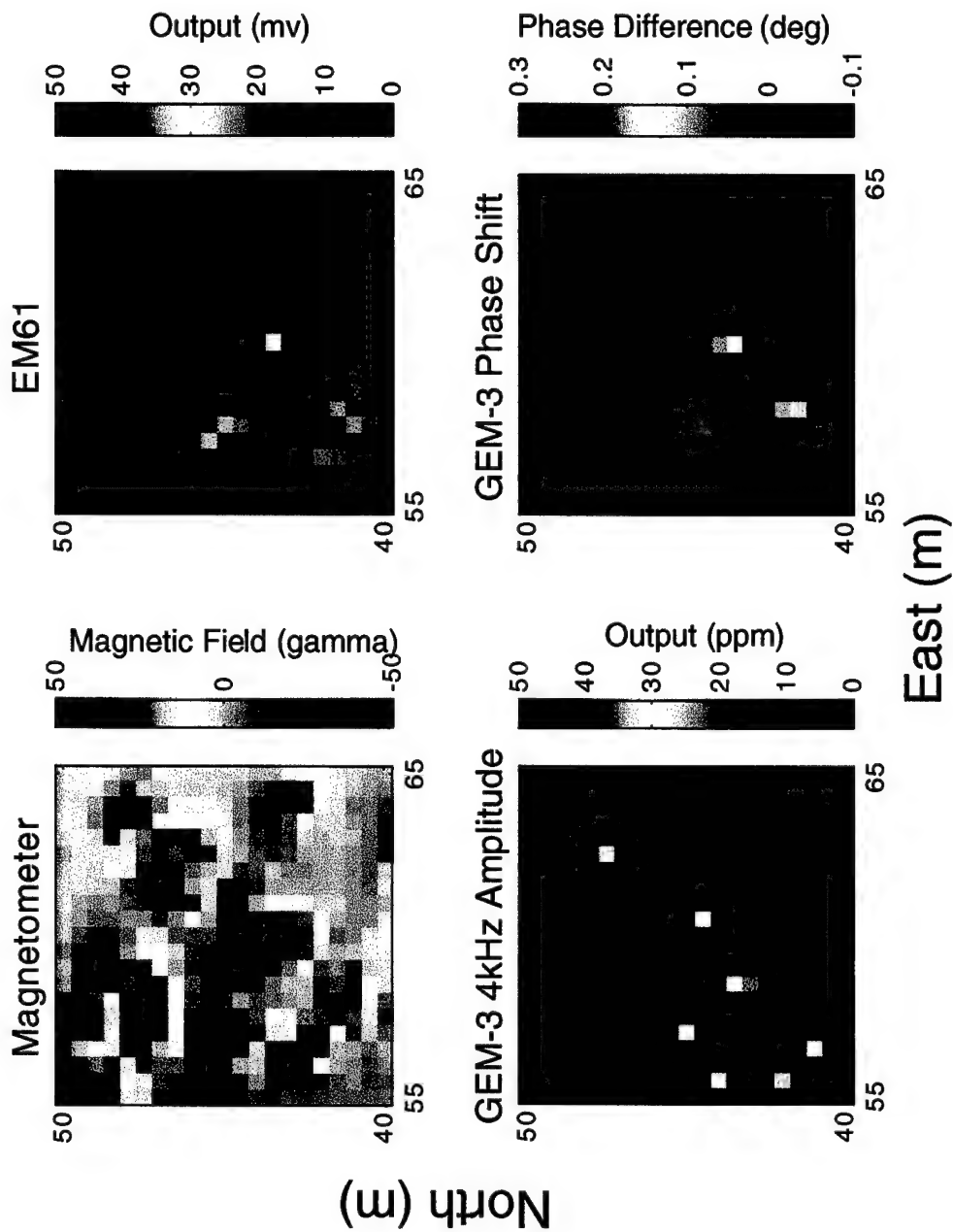
[55E,85N]

A-42



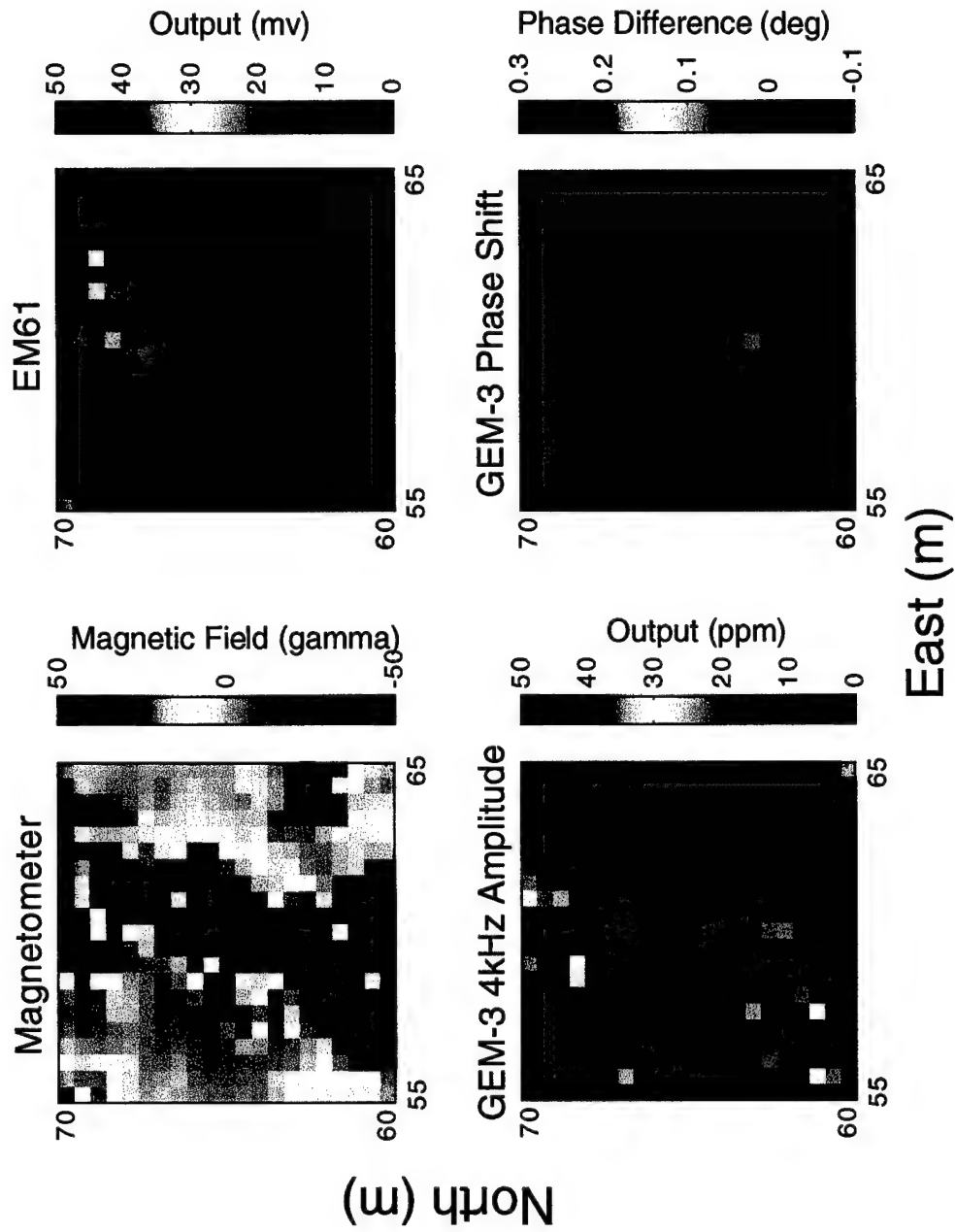
[55E,90N]

A-43



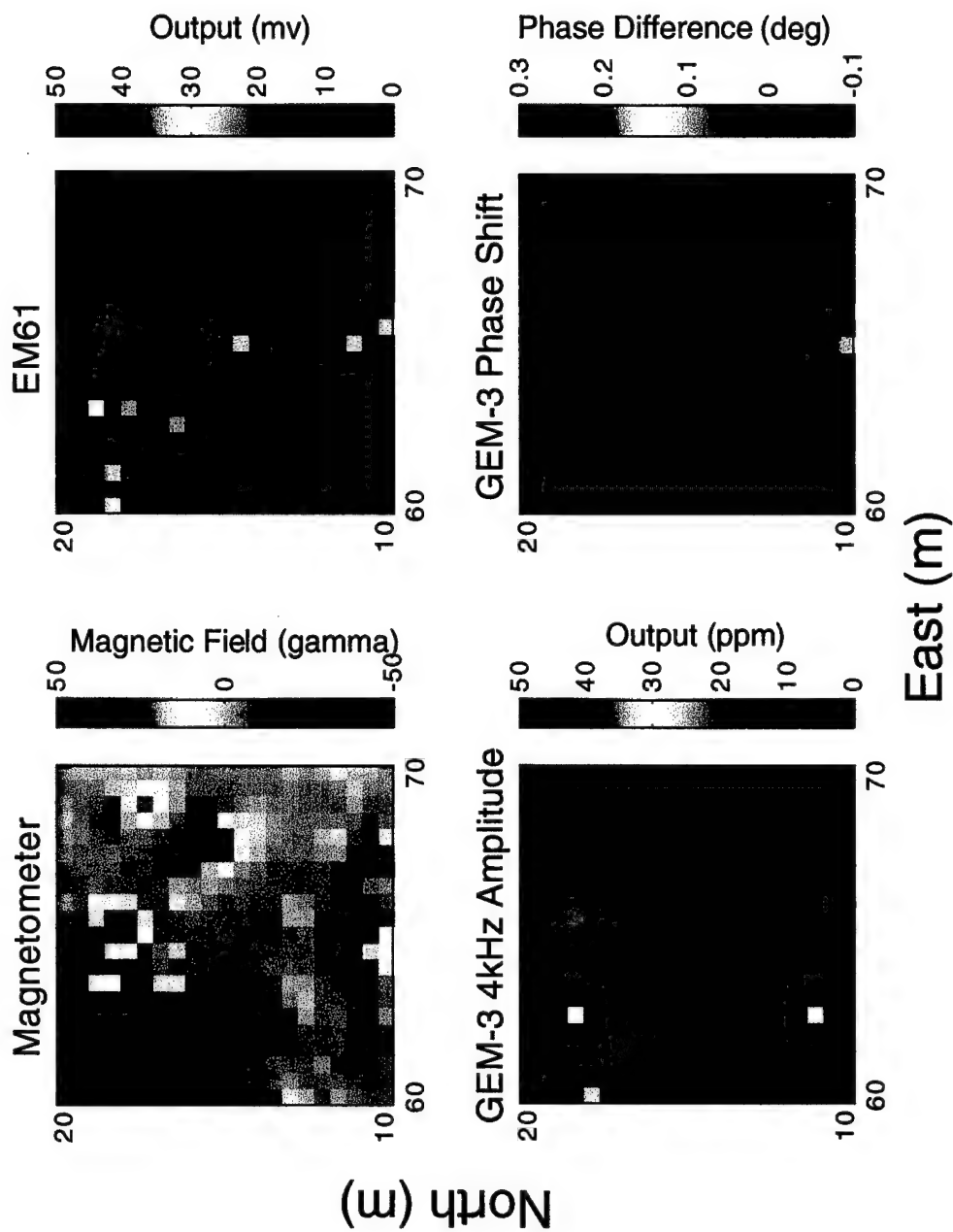
[60E,45N]

A-44



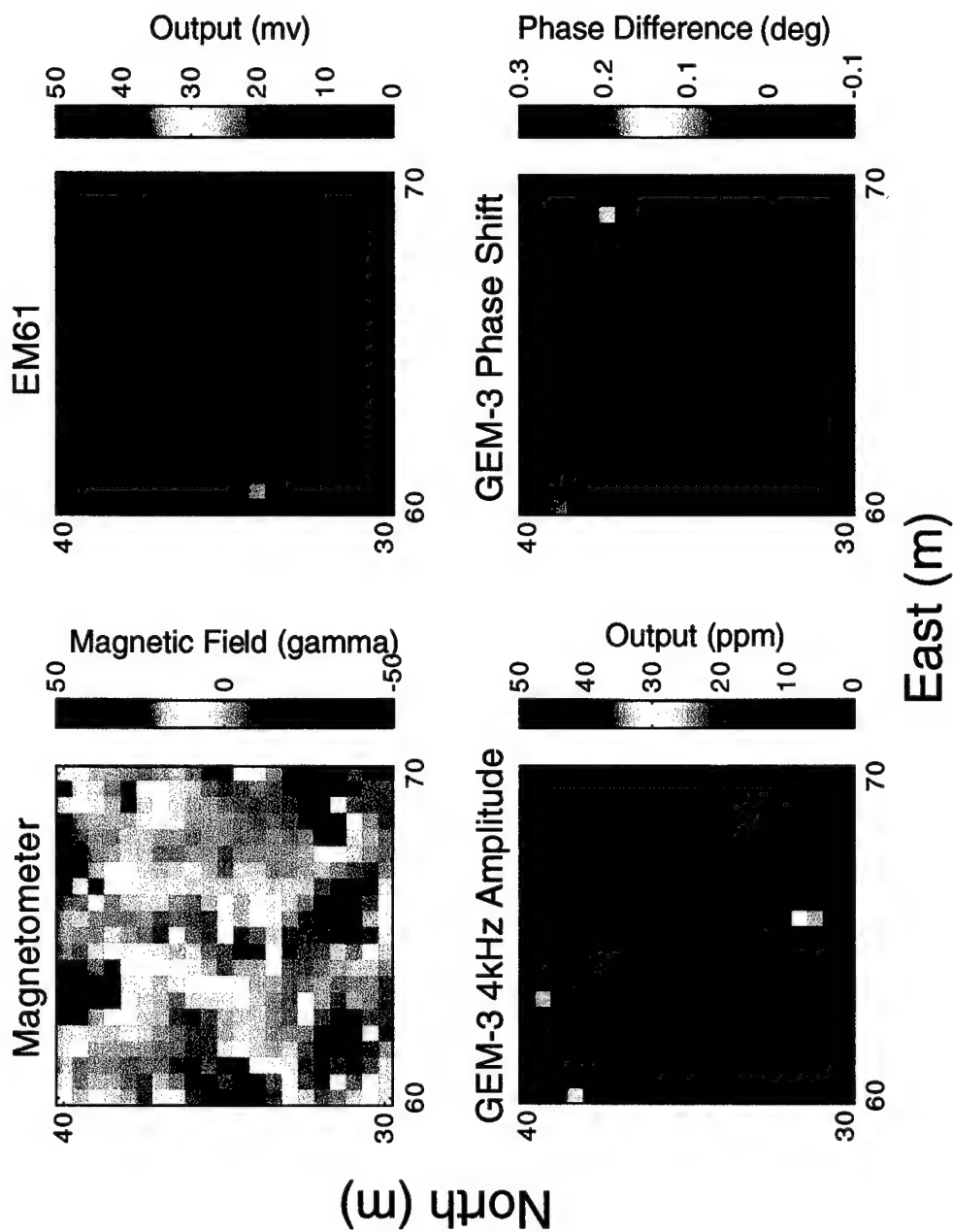
[60E, 65N]

A-45



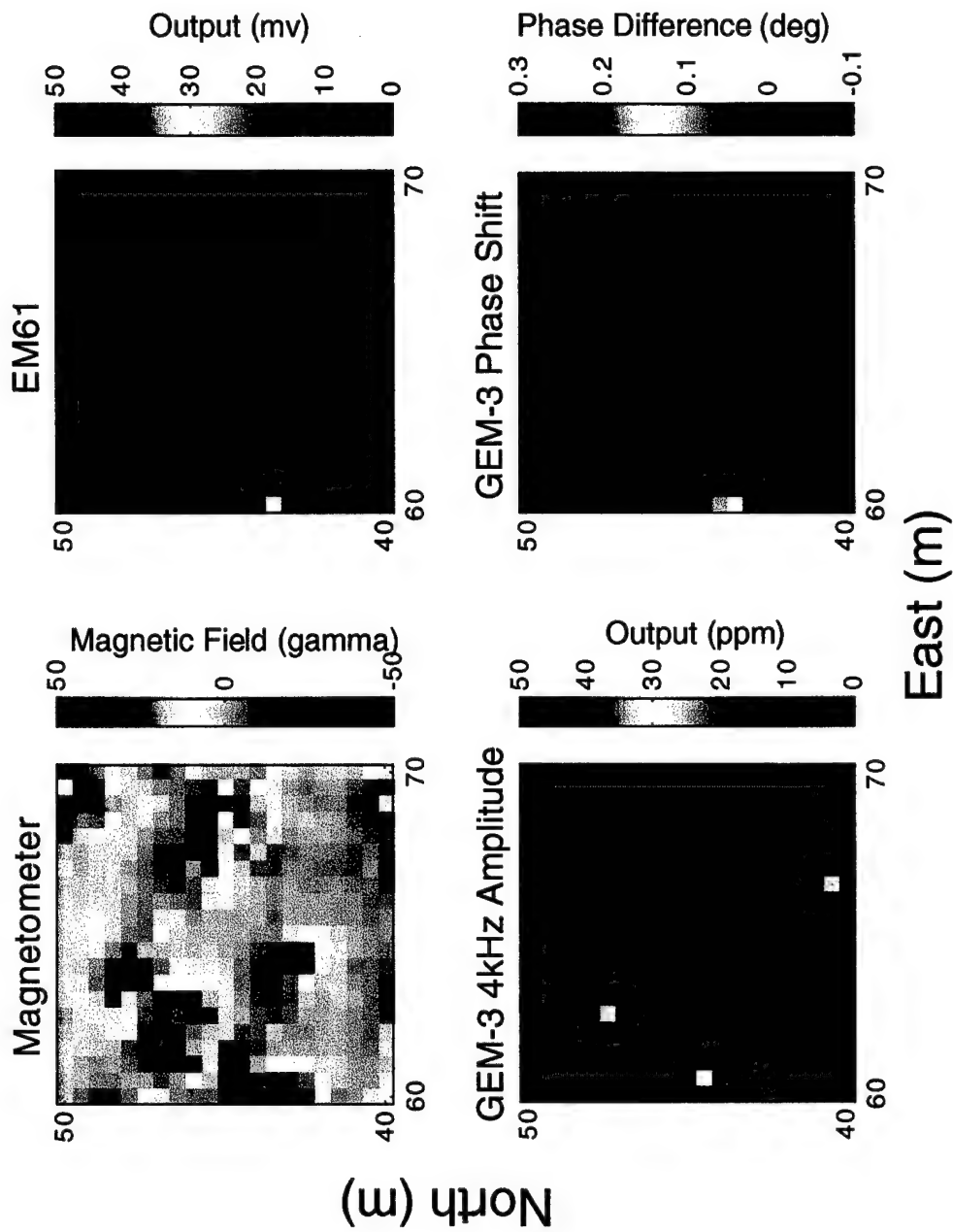
[65E, 15N]

A-46



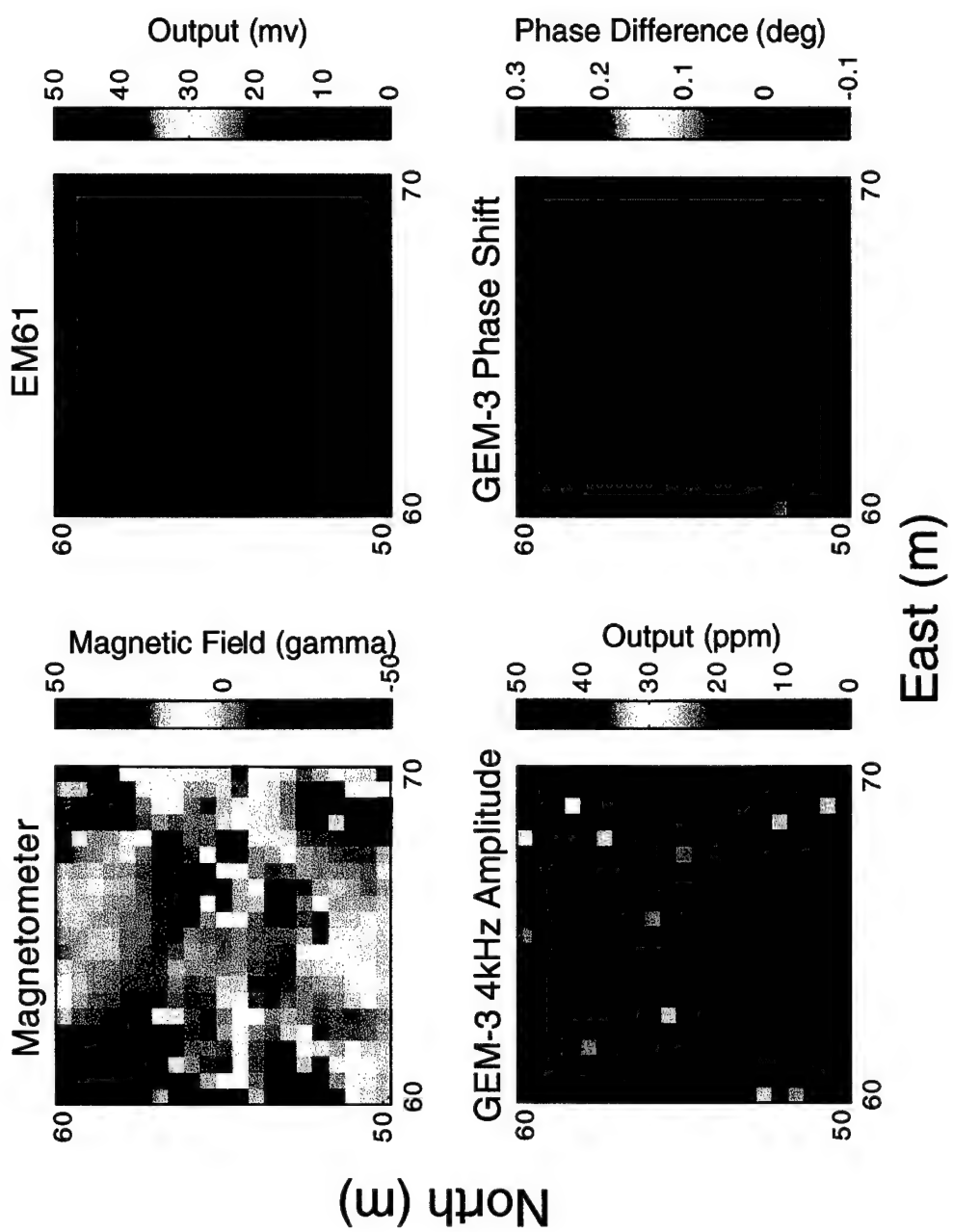
[65E,35N]

A-47



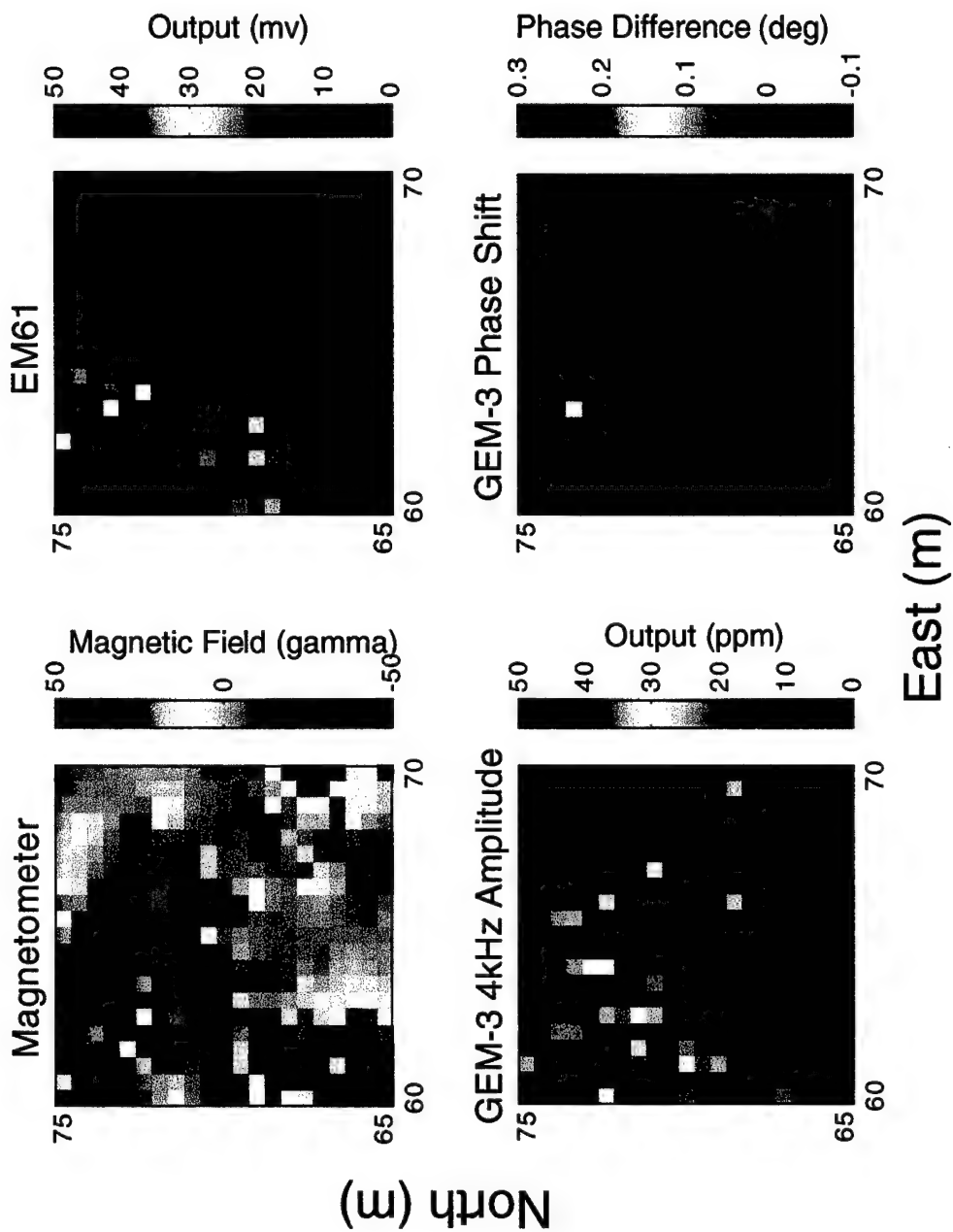
[65E, 45N]

A-48



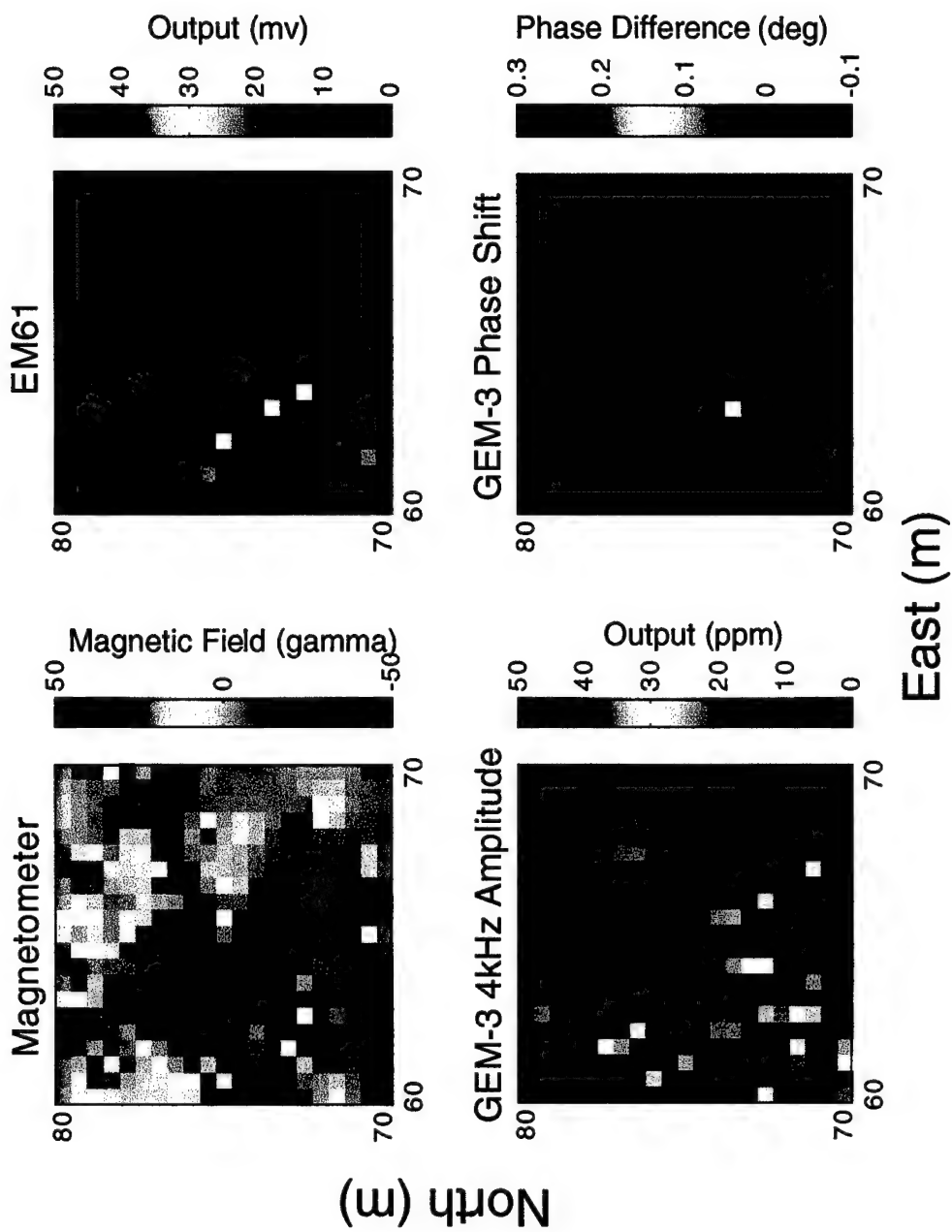
[65E,55N]

A-49



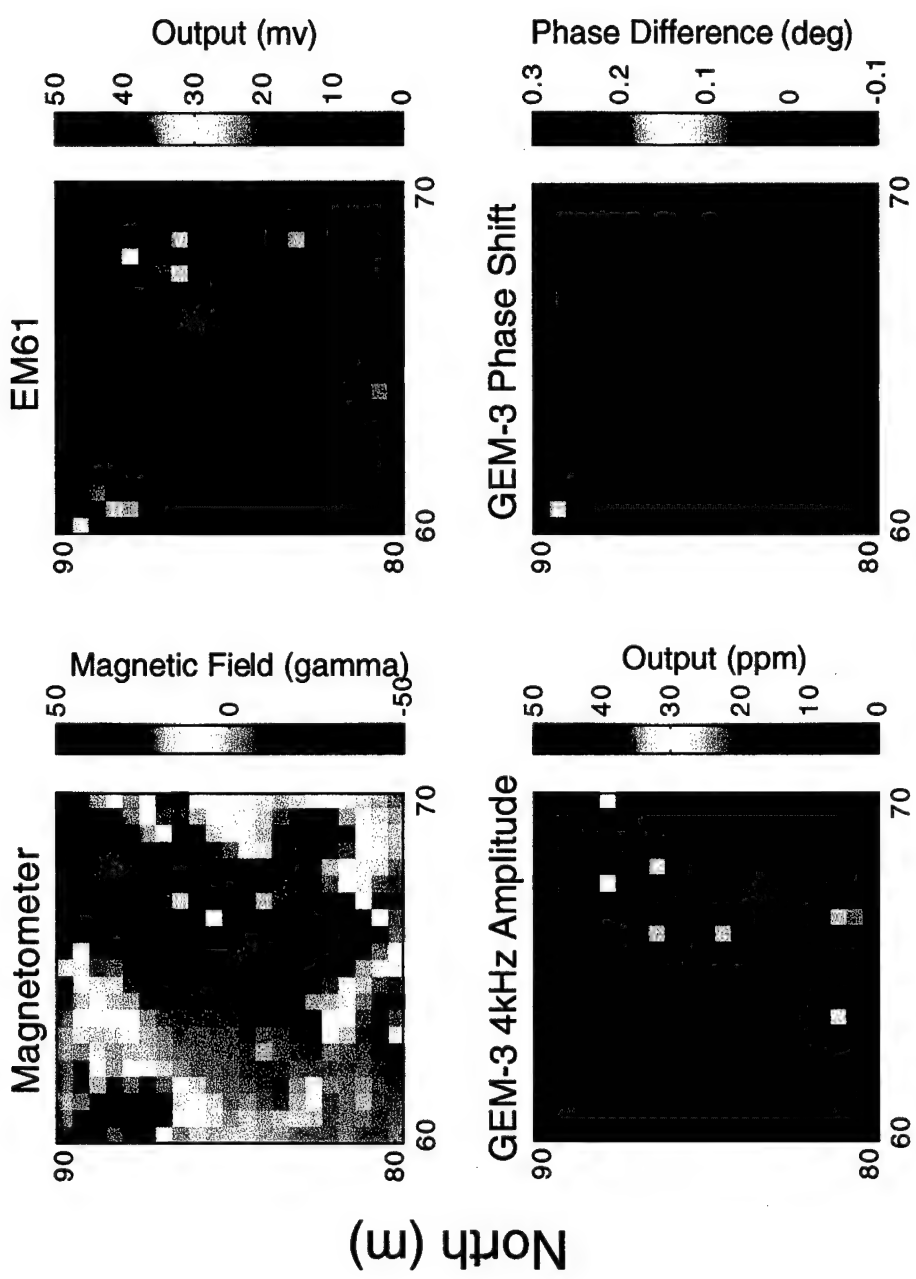
[65E, 70N]

A-50



[65E715N]

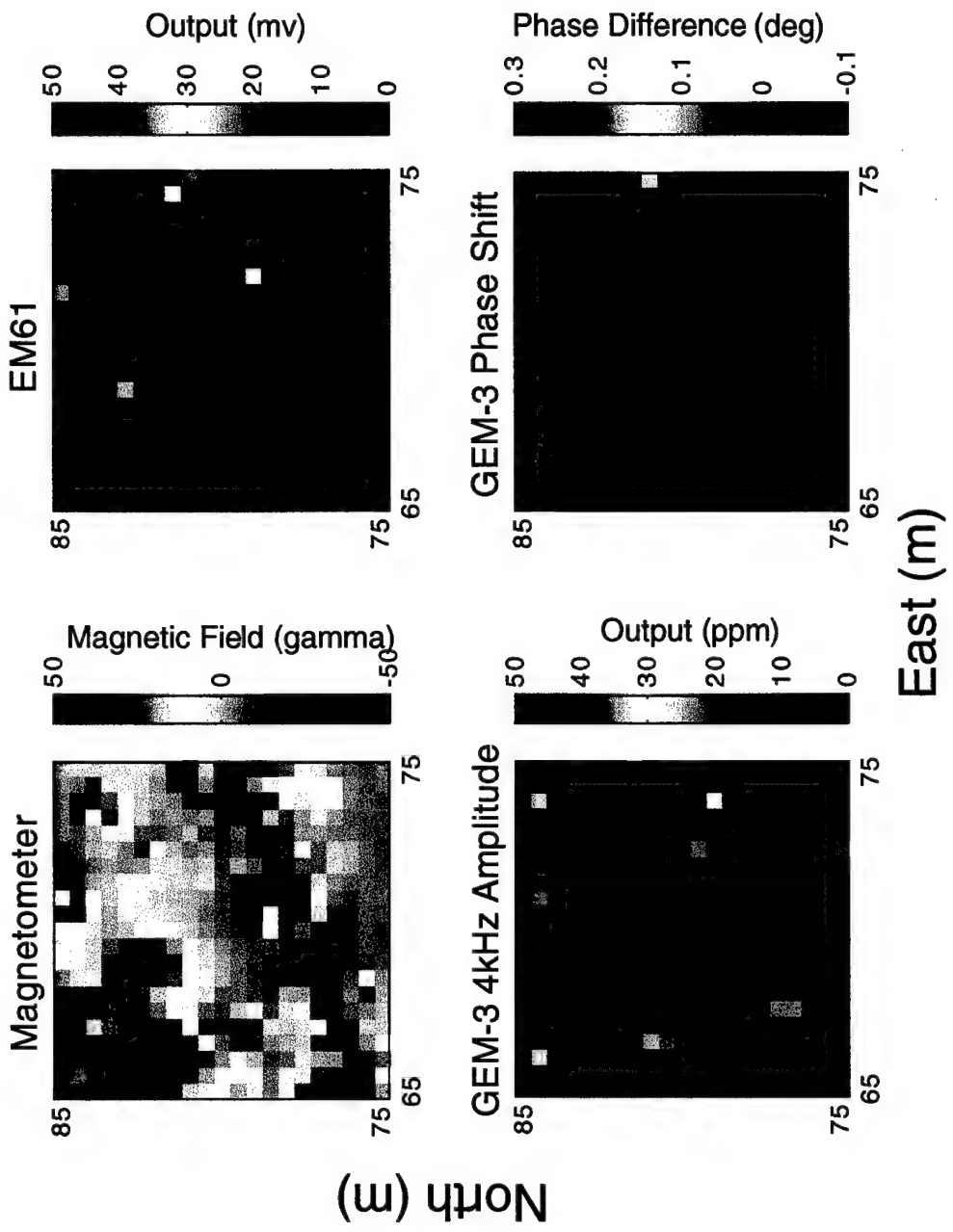
A-51



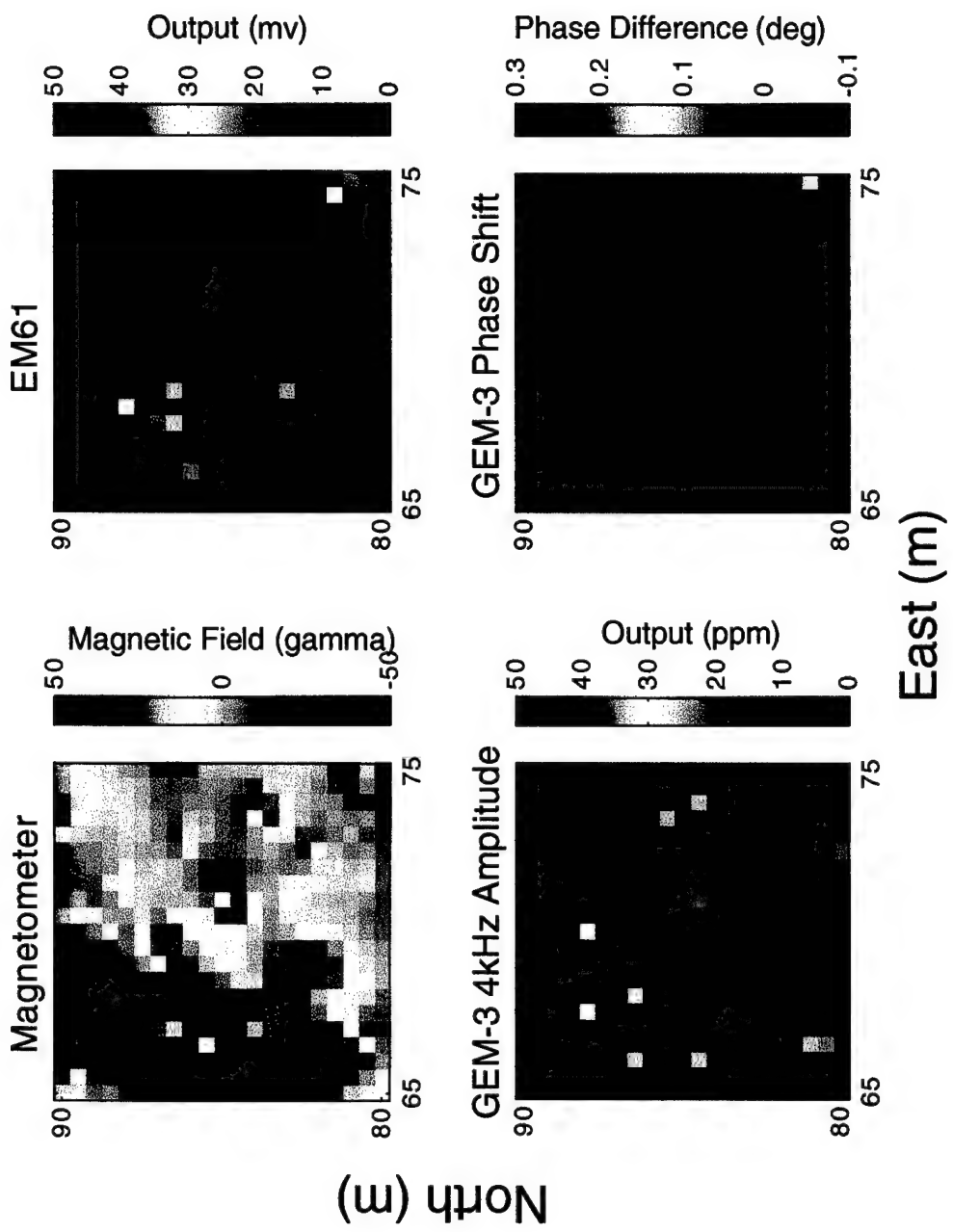
East (m)

[65E,85N]

A-52

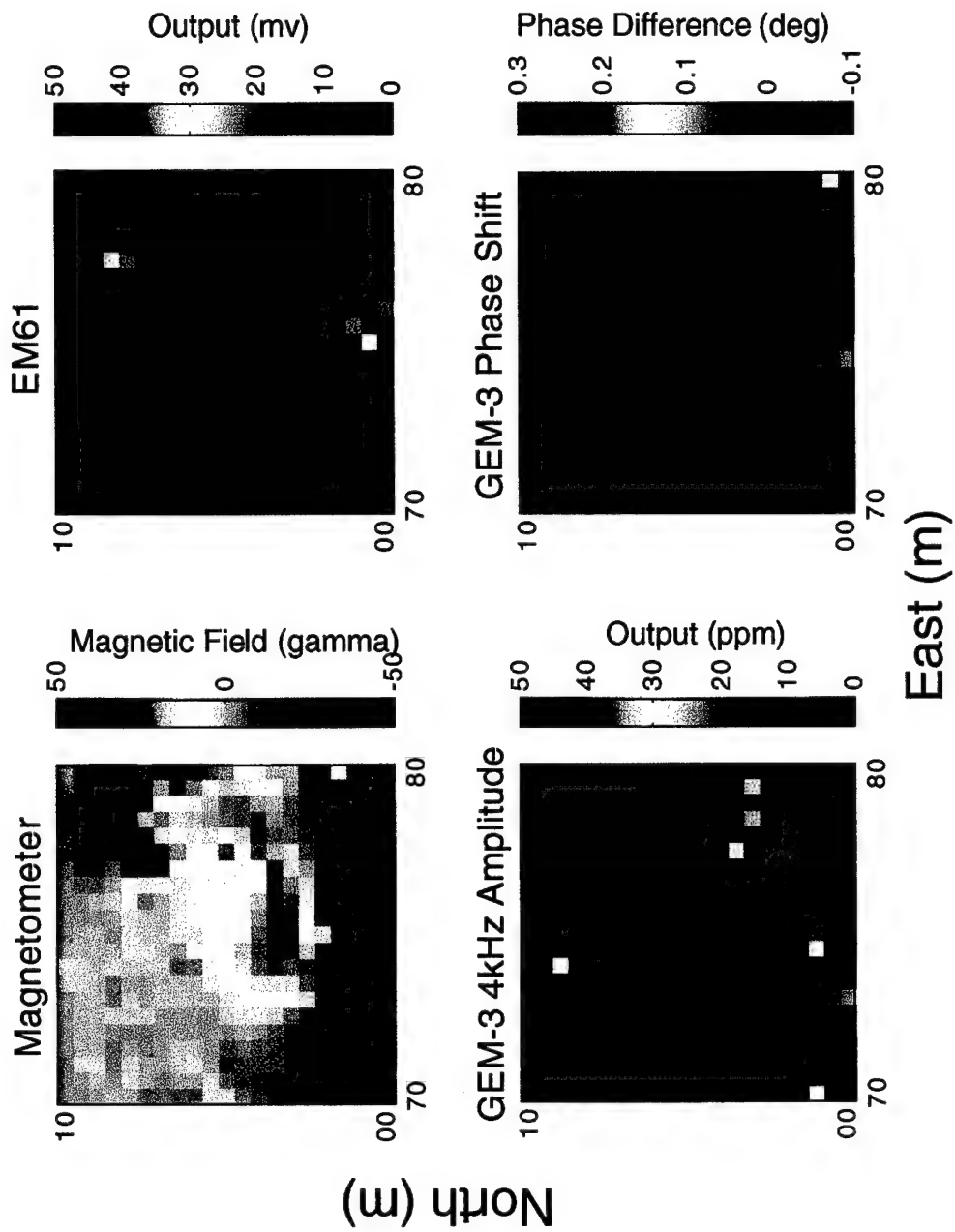


[70E,80N]
A-53



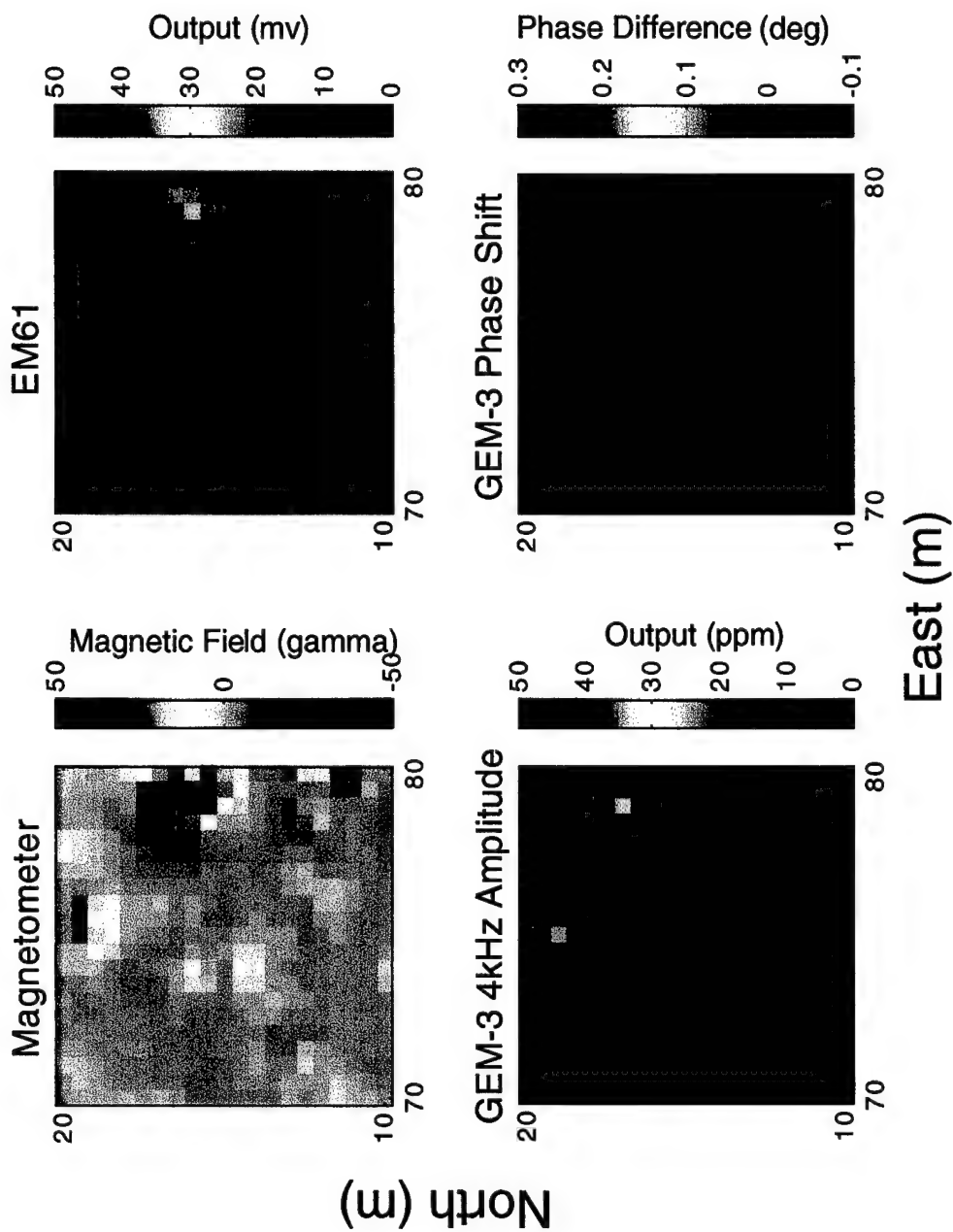
[70E, 85N]

A-54



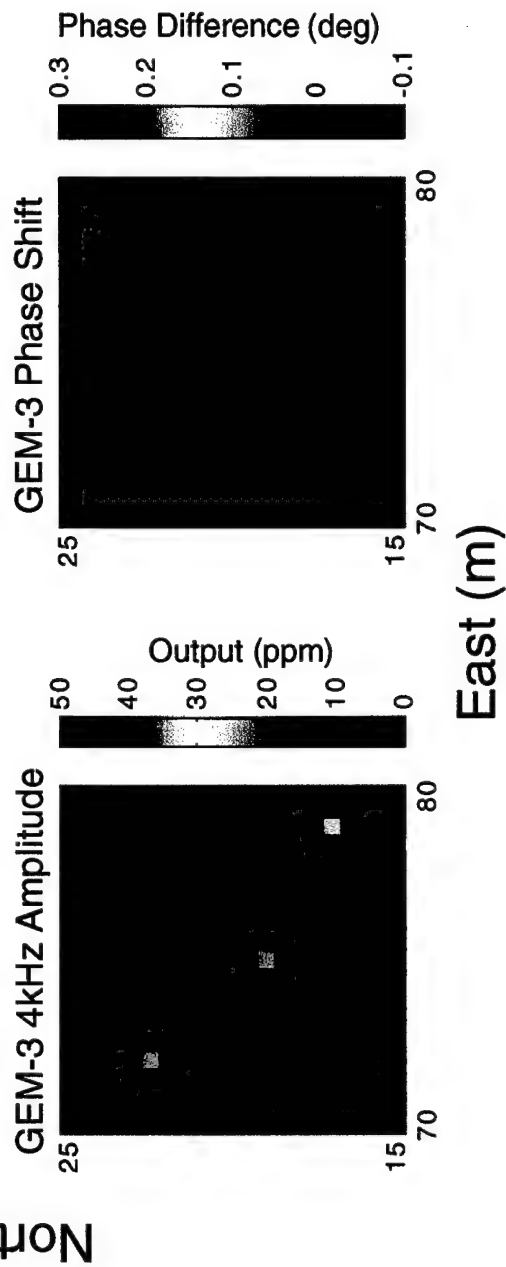
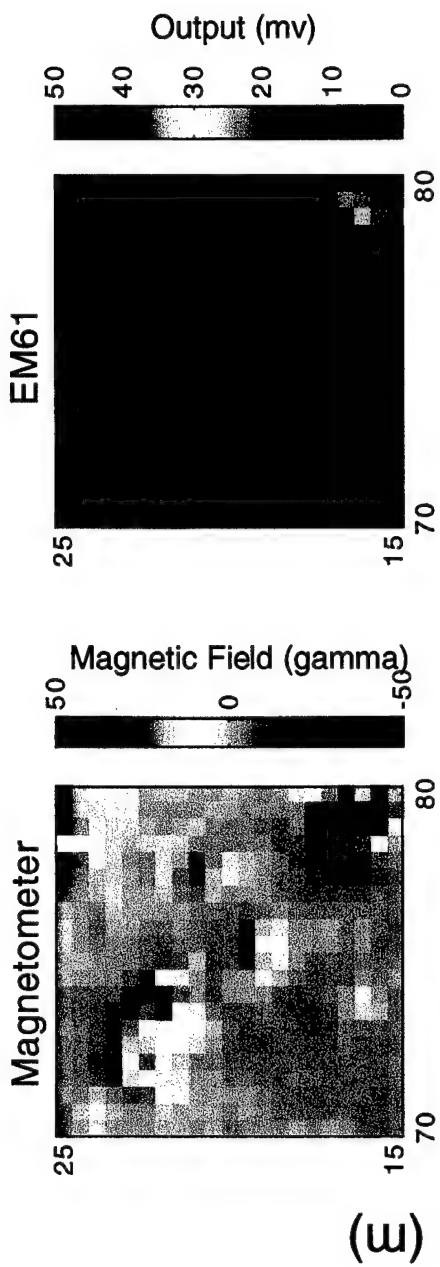
[75E,5N]

A-55



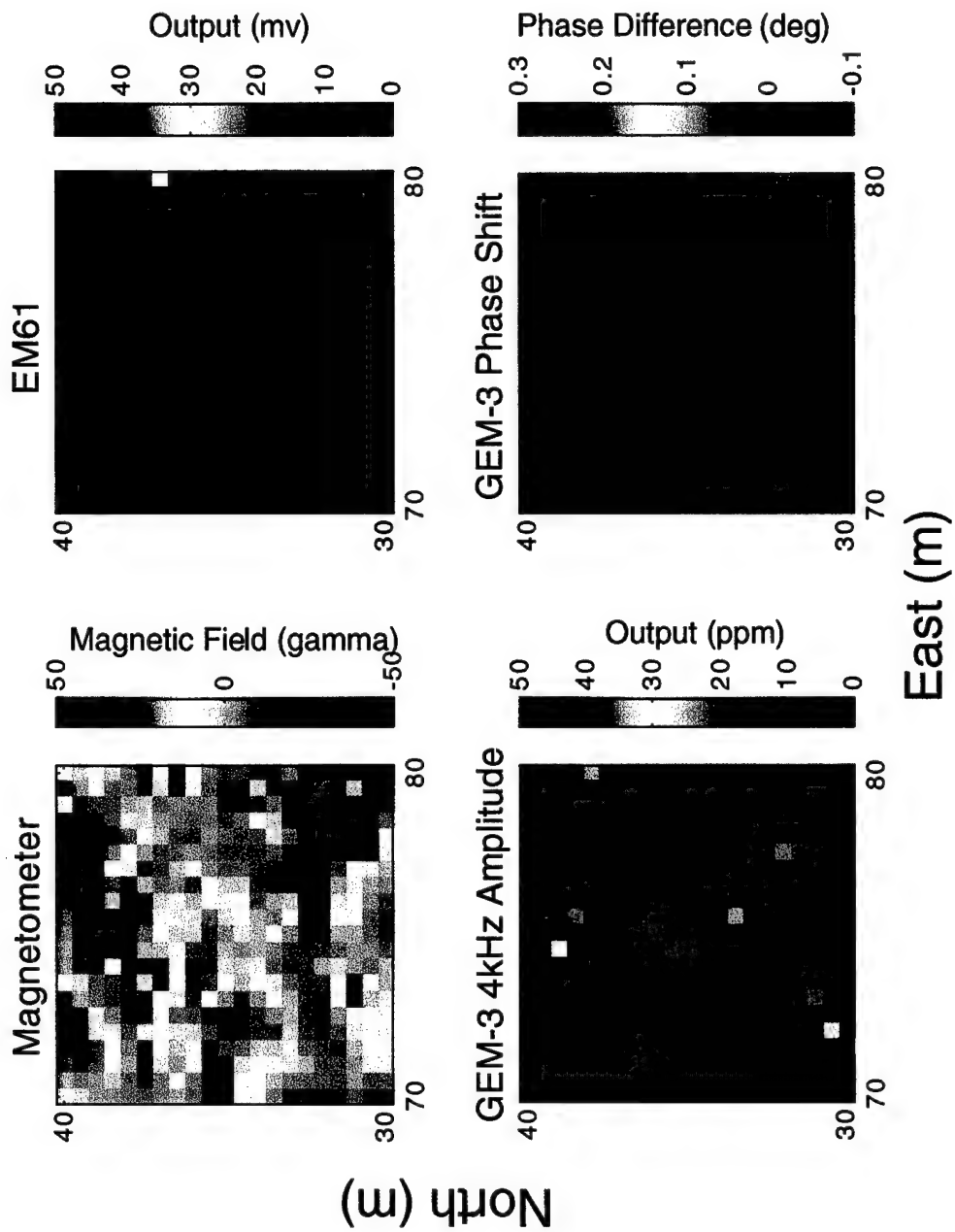
[75E, 15N]

A-56



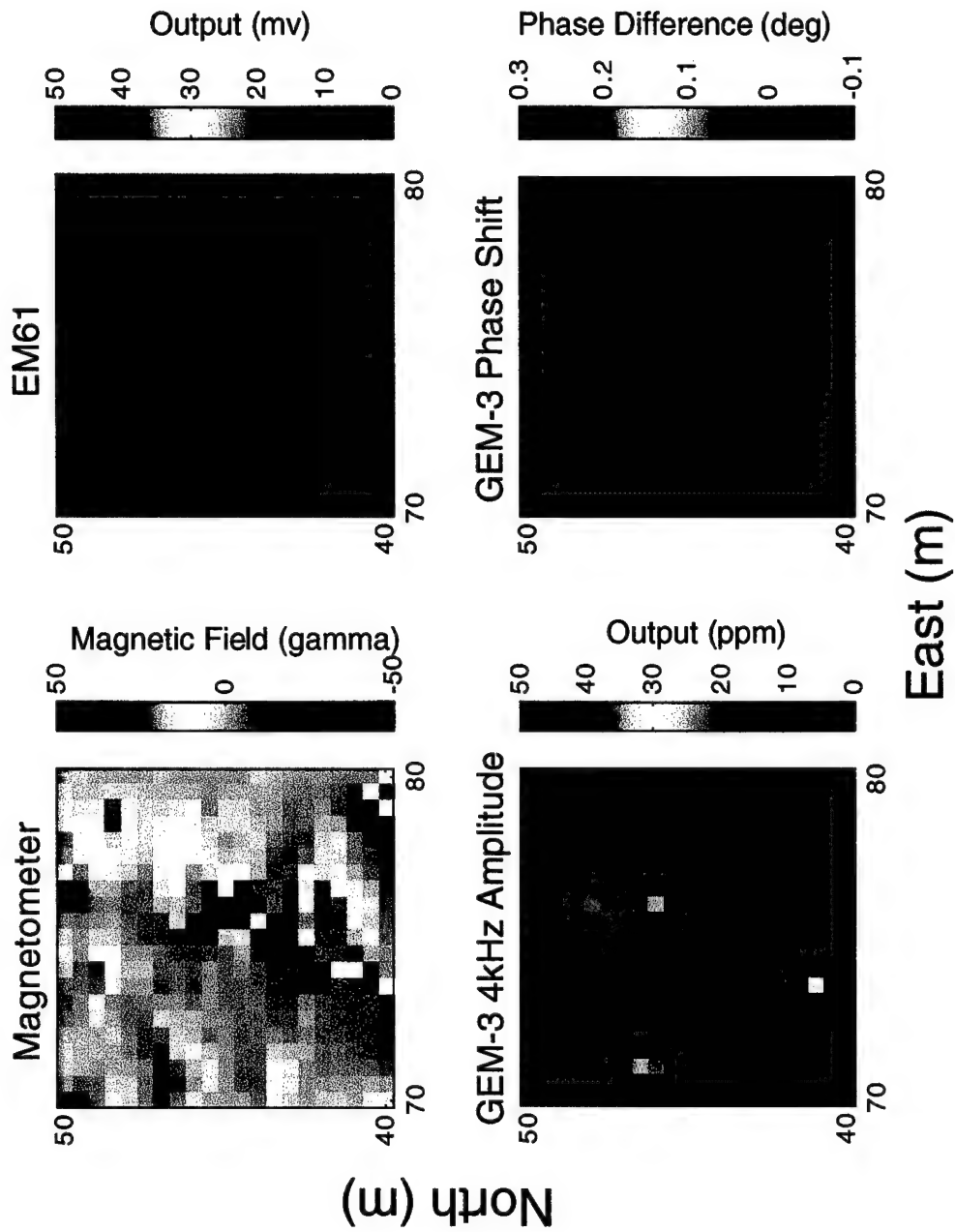
[75E,20N]

A-57



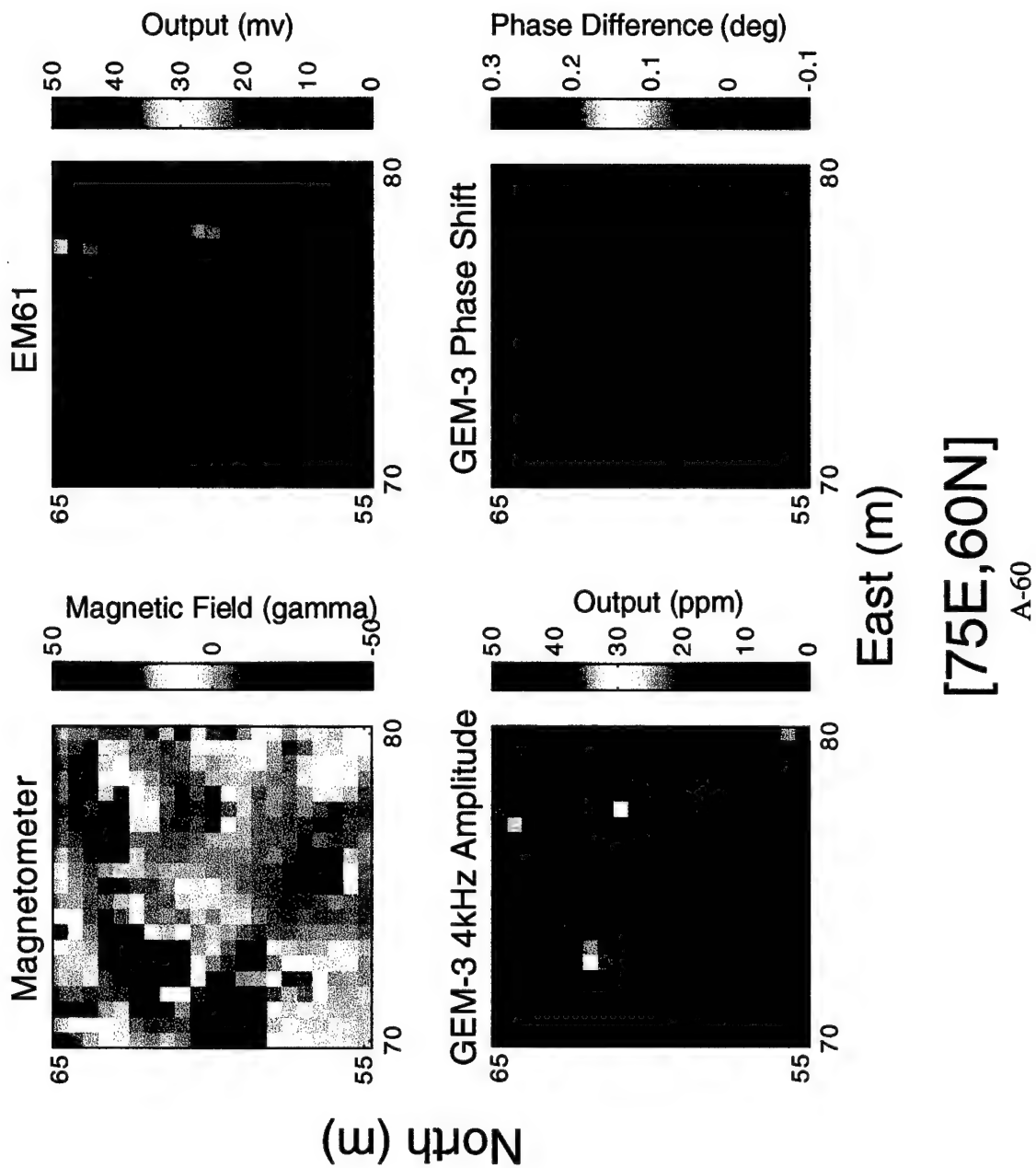
[75E,35N]

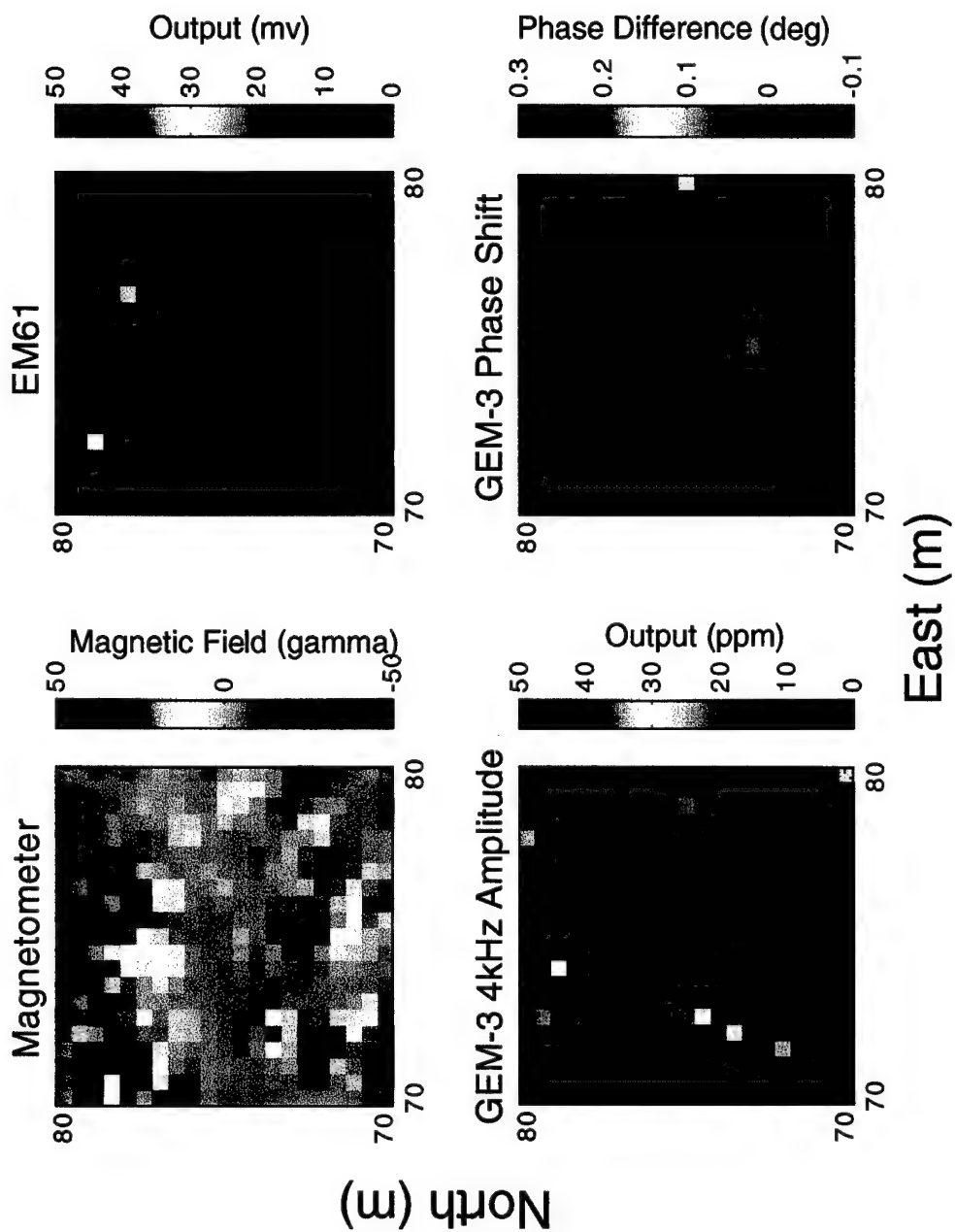
A-58



[75E, 45N]

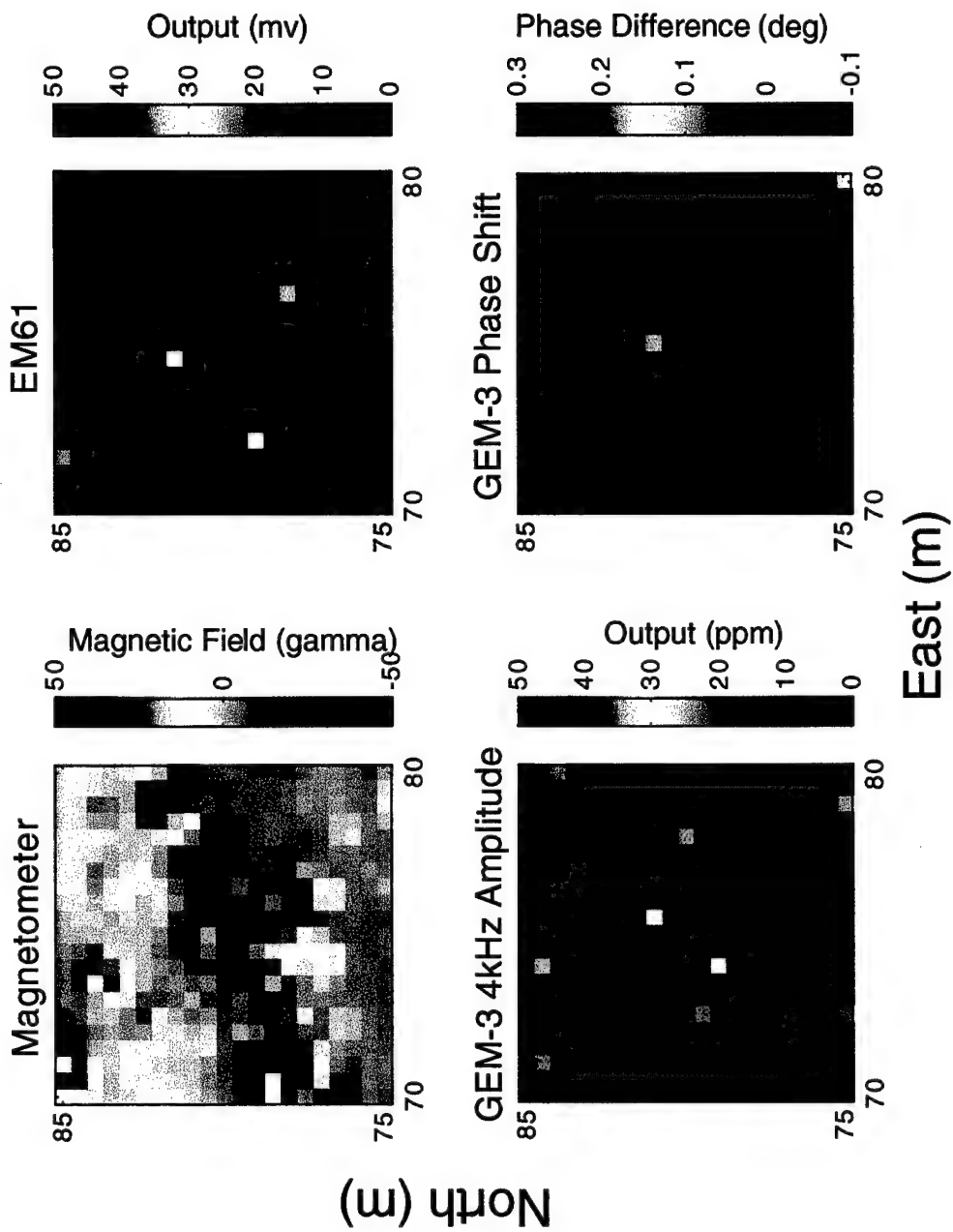
A-59





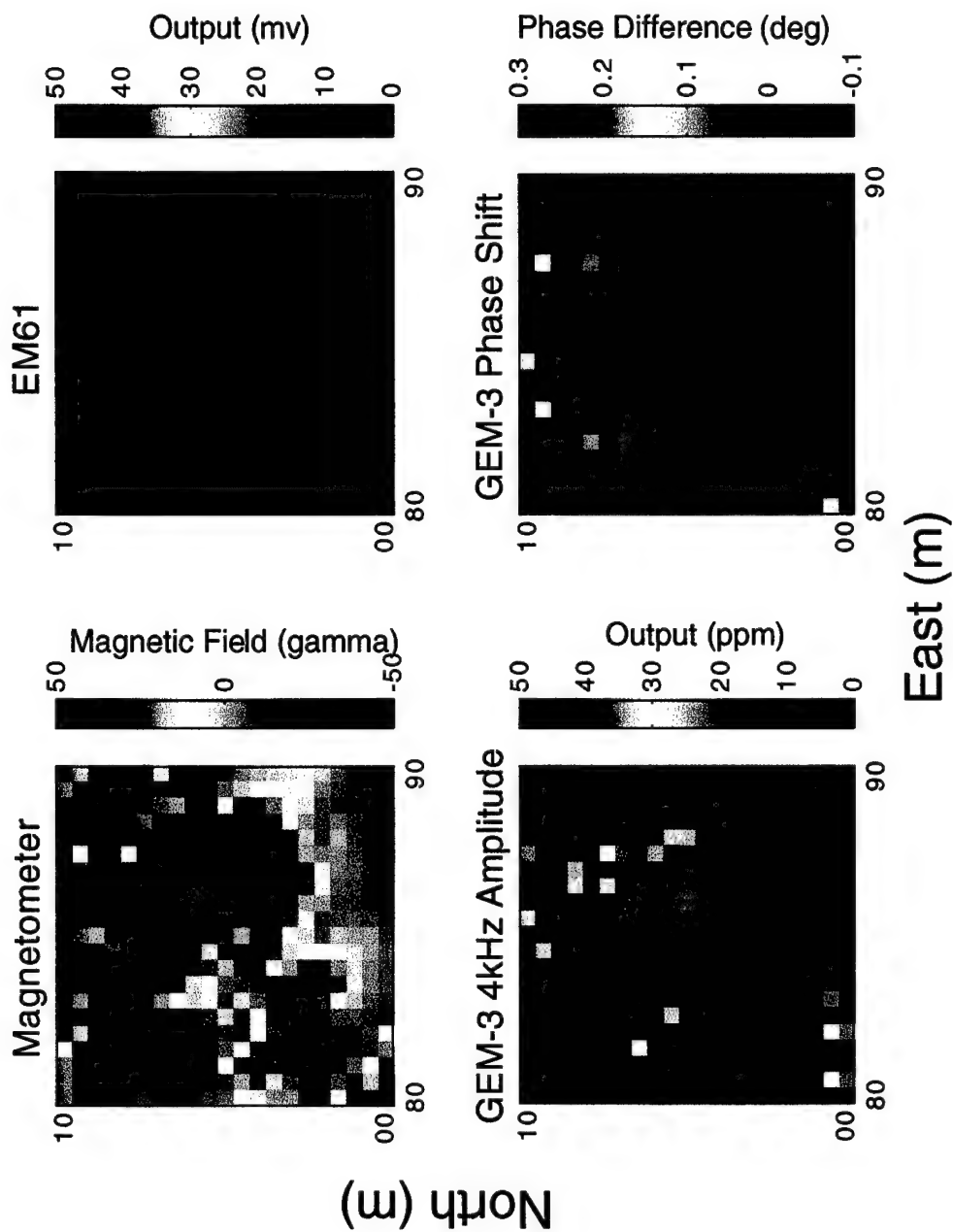
[75E, 75N]

A-61



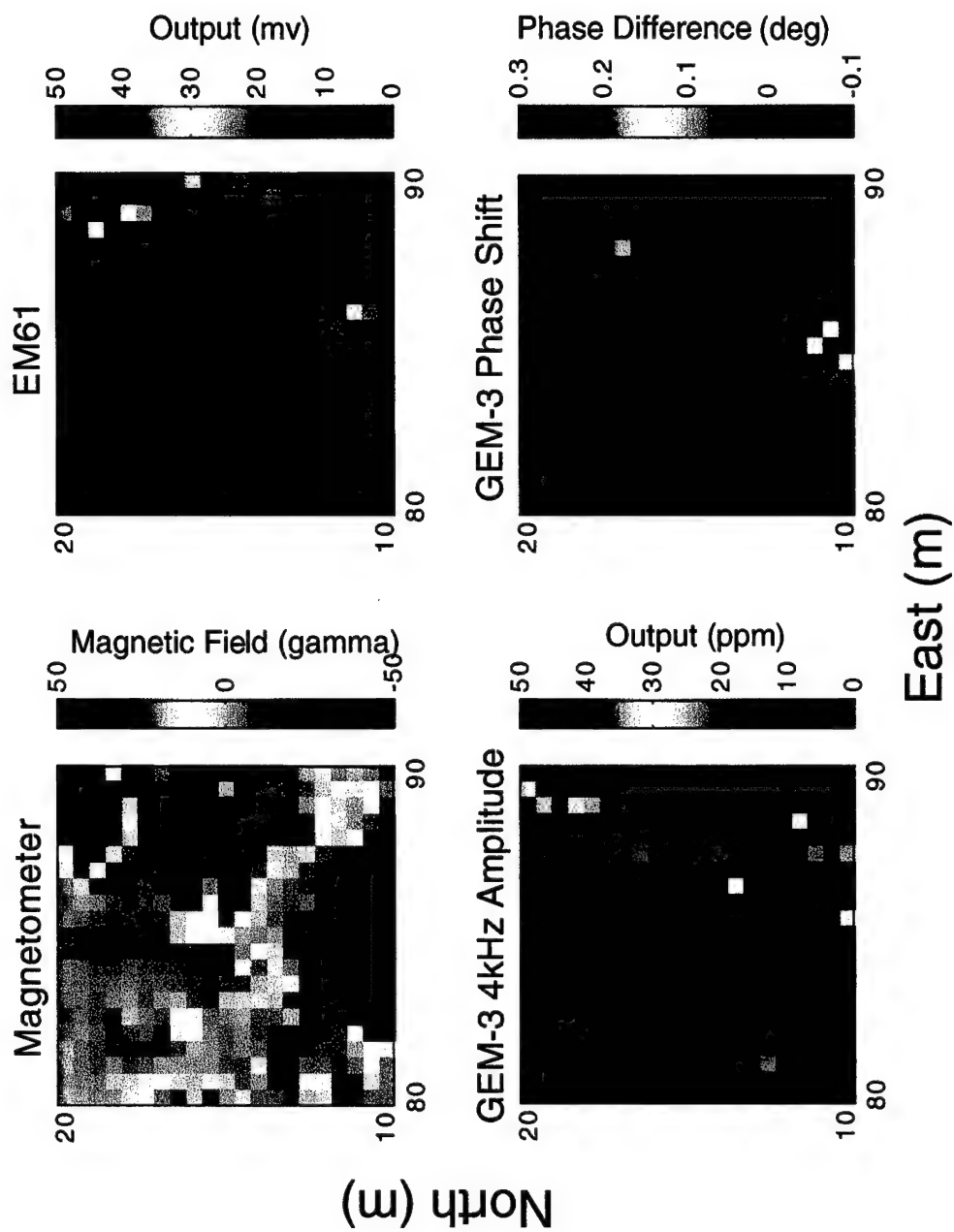
[75E,80N]

A-62



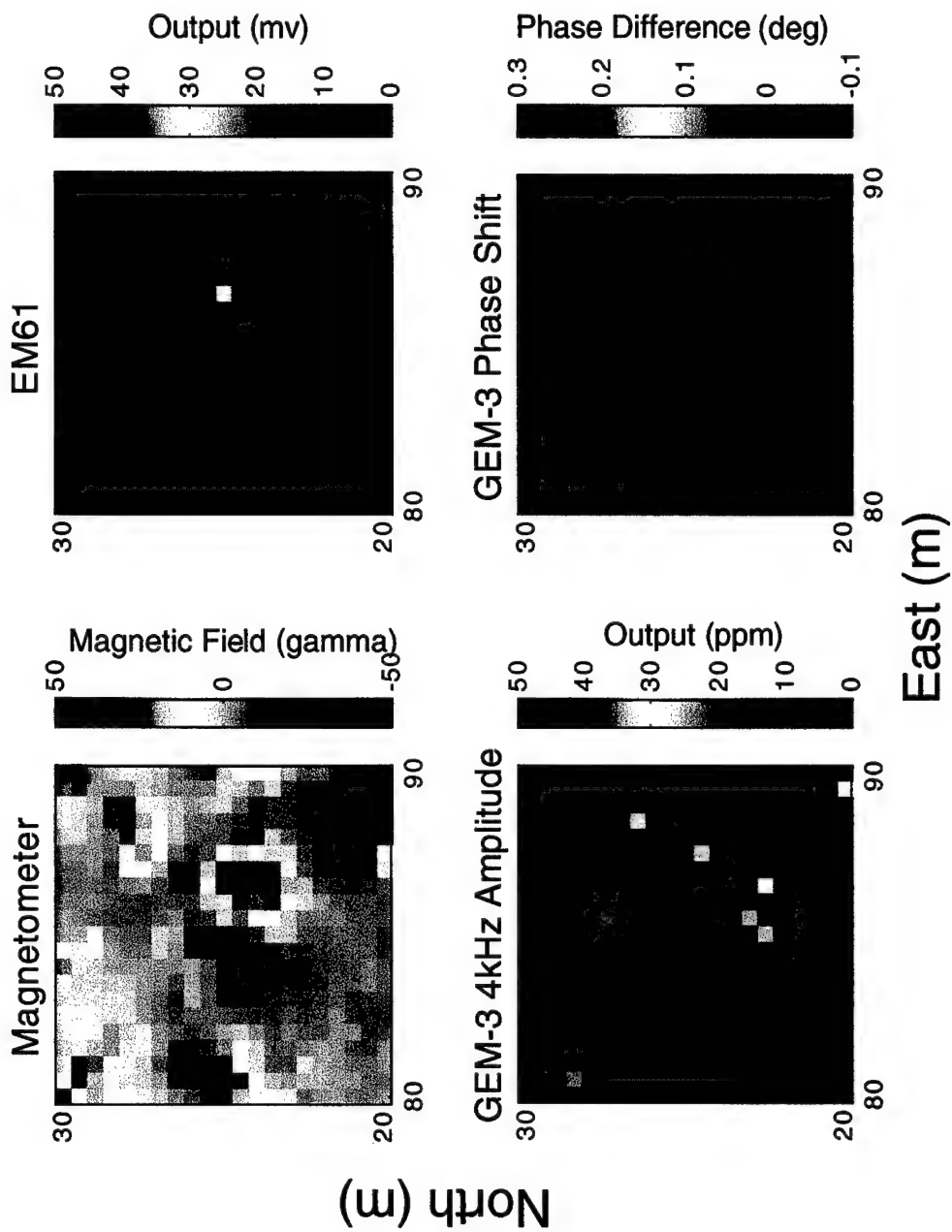
[85E,5N]

A-63



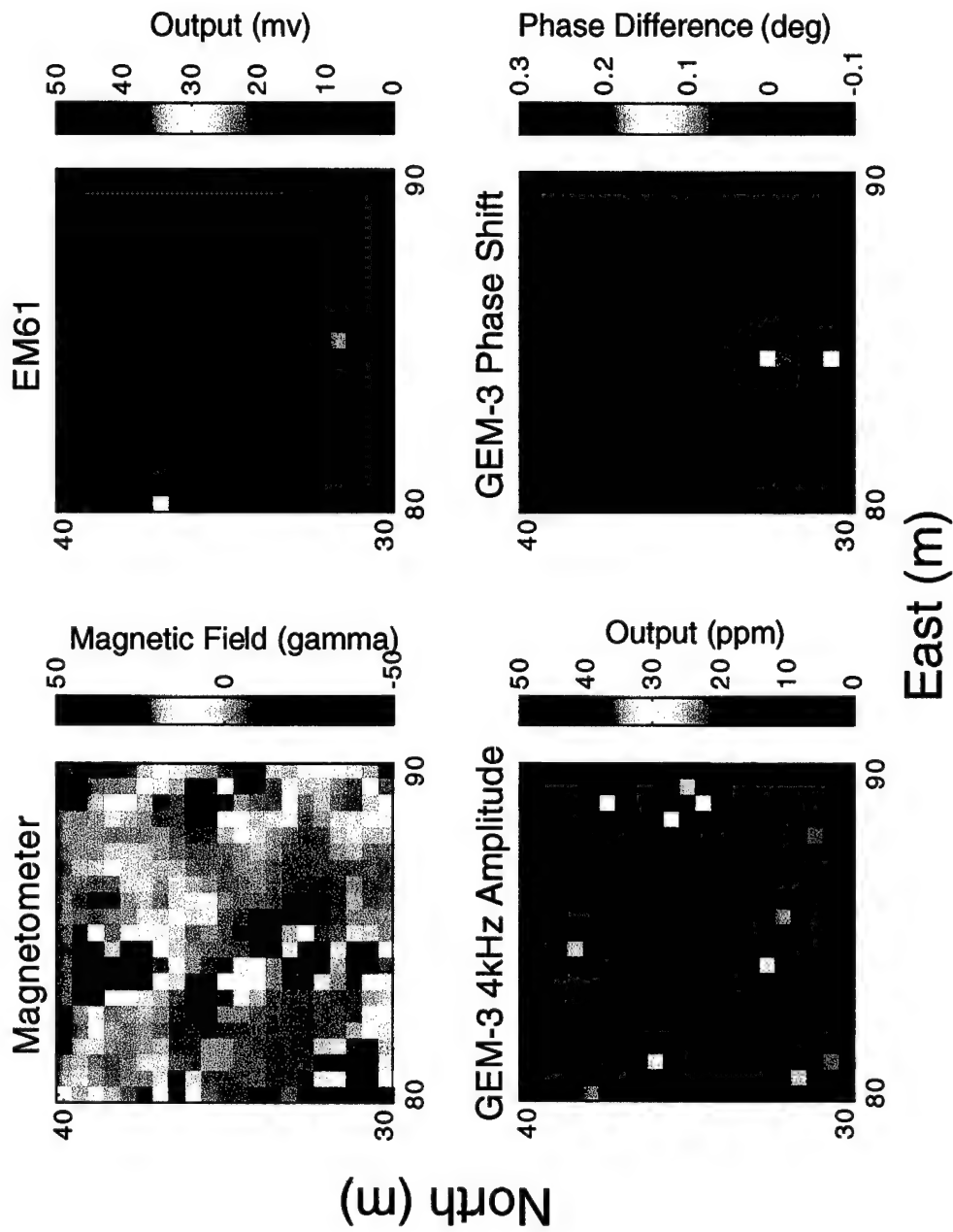
[85E, 15N]

A-64



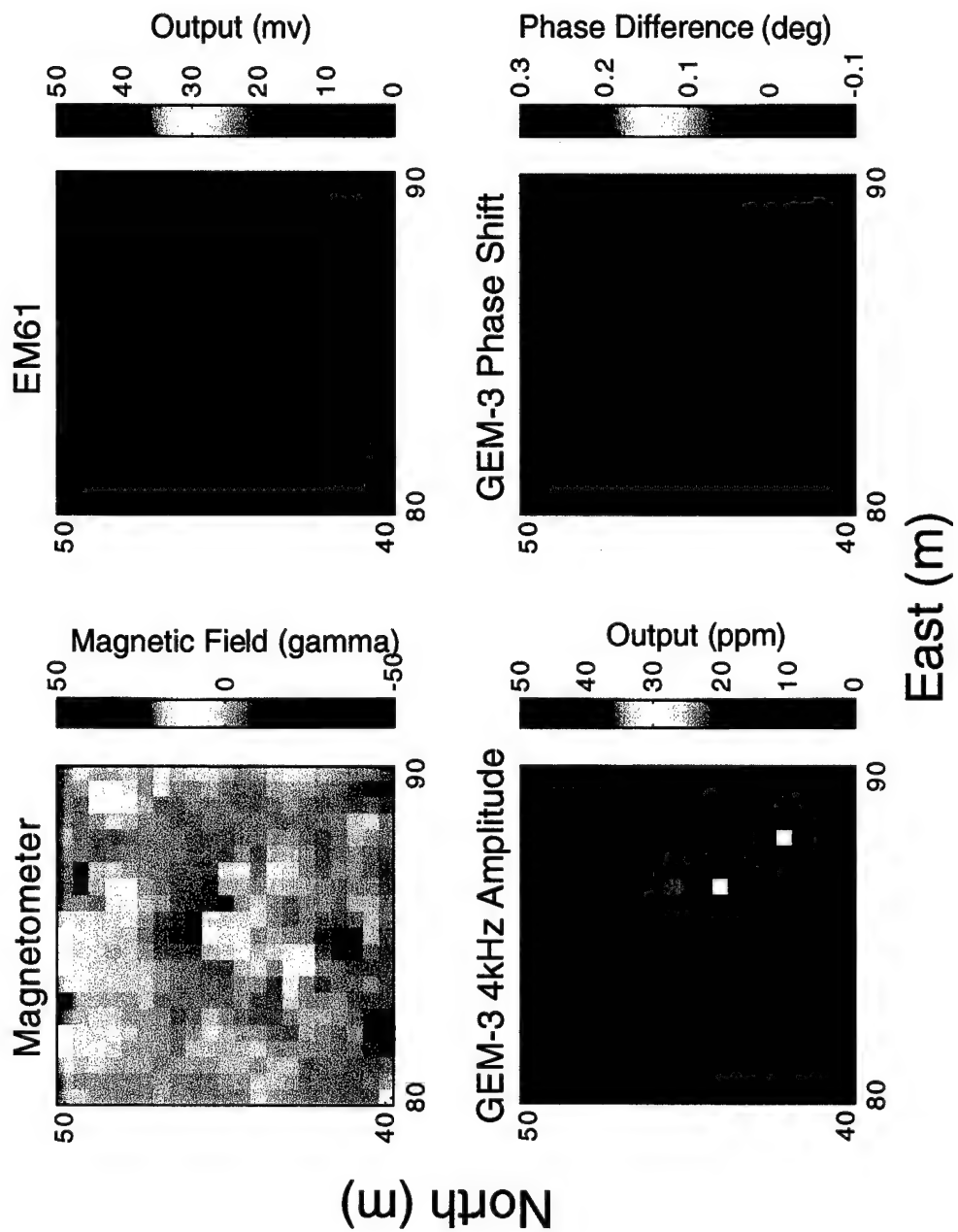
[85E,25N]

A-65



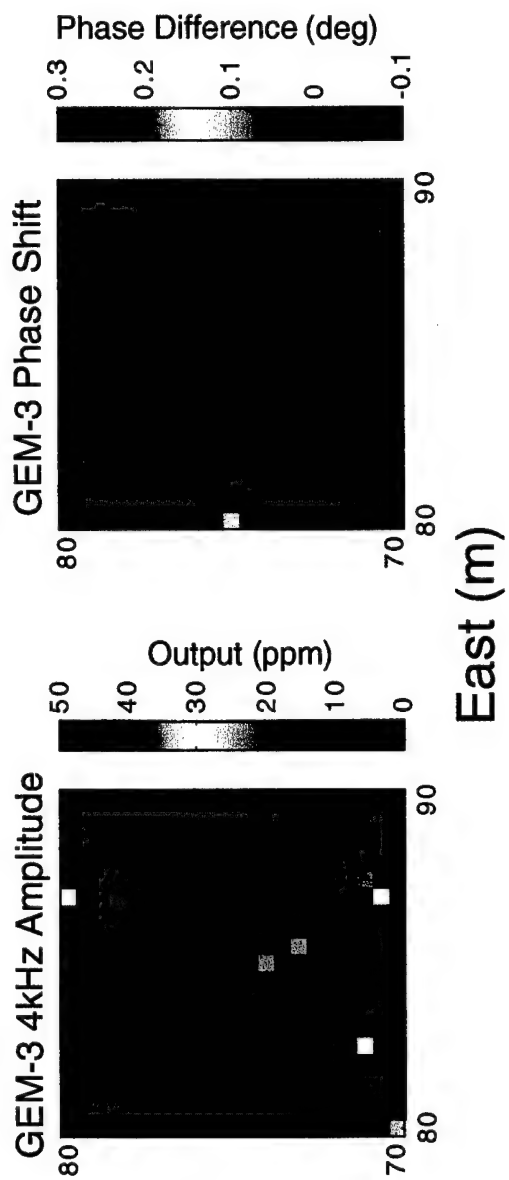
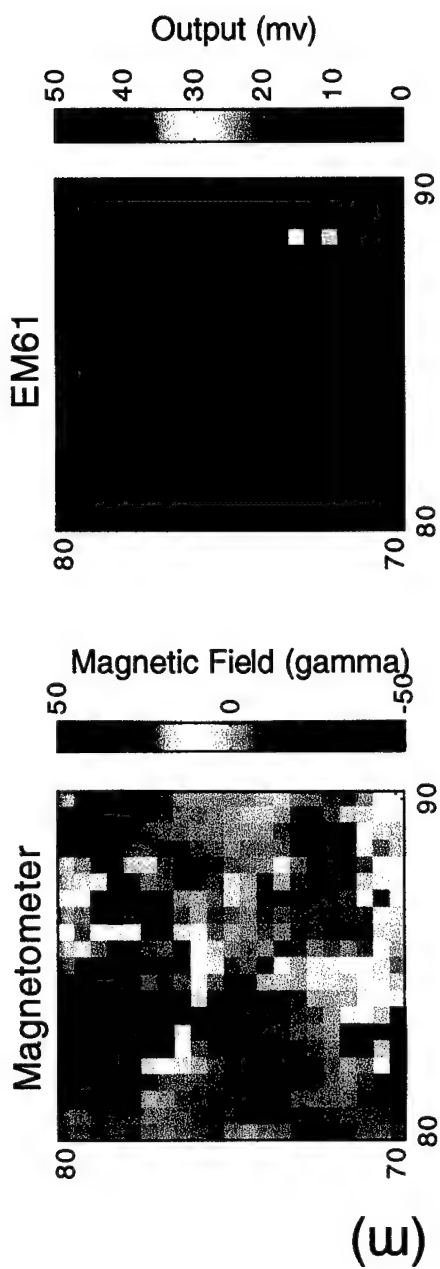
[85E,35N]

A-66



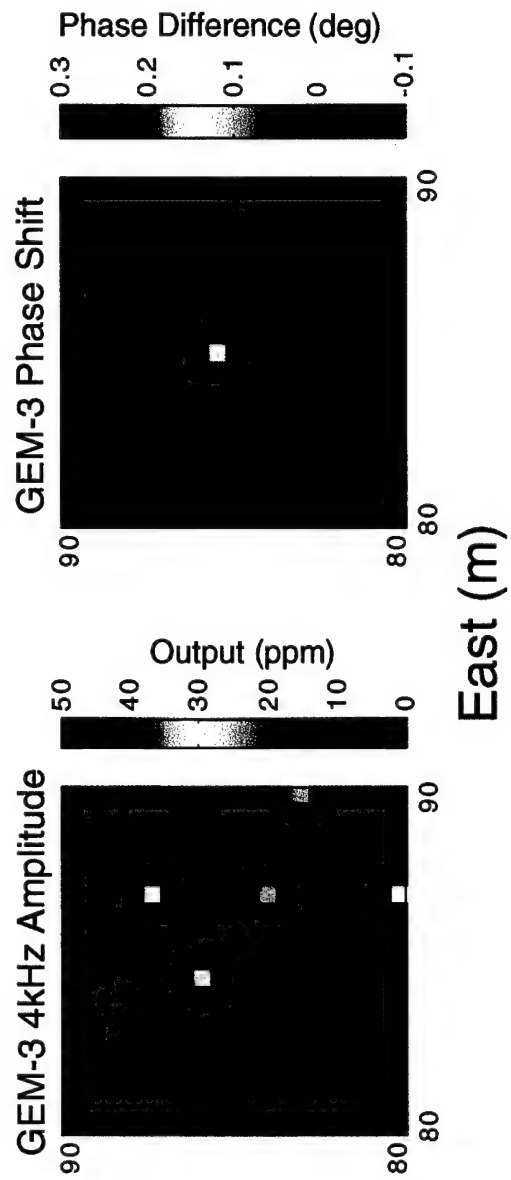
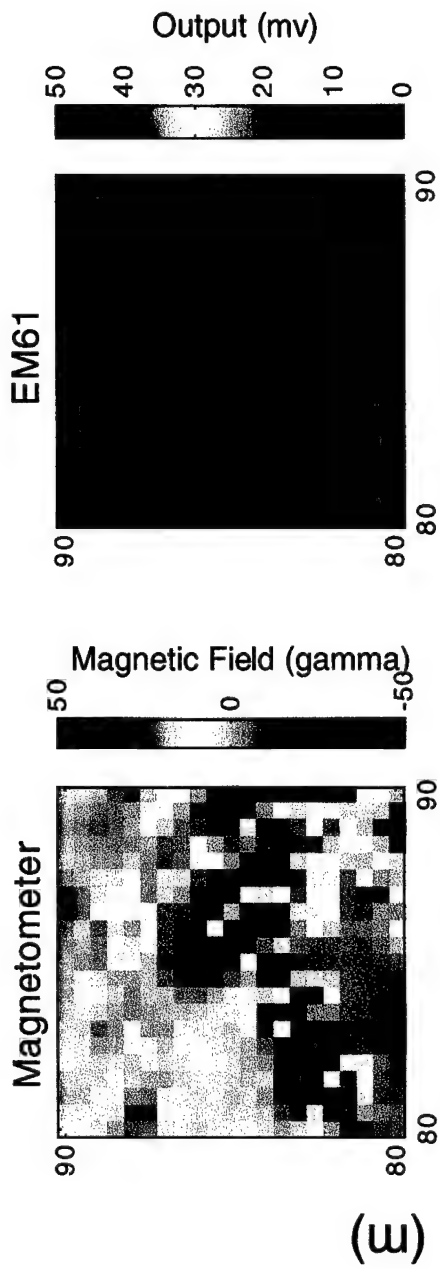
[85E,45N]

A-67



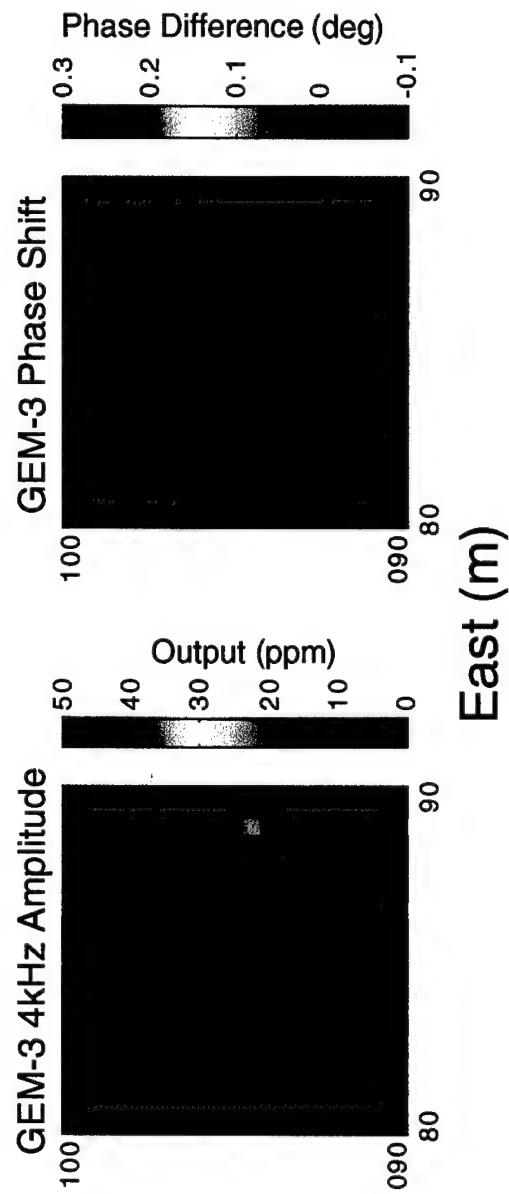
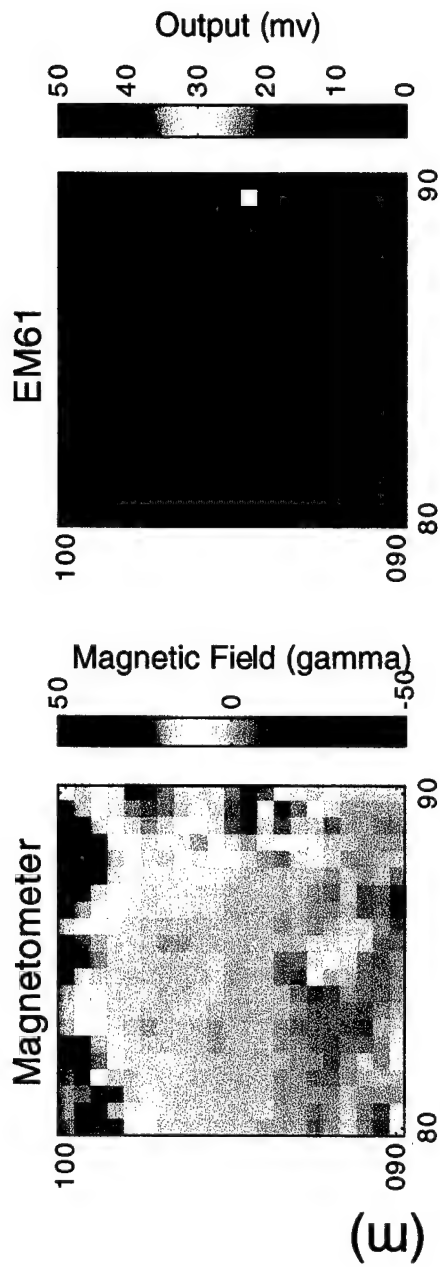
[85E, 75N]

A-68



[85E,85N]

A-69



[85E,95N]

A-70

APPENDIX B

DEPTH ESTIMATION FROM MAGNETIC DATA USING FULL- WIDTH HALF-MAXIMUM METHOD

APPENDIX B

DEPTH ESTIMATION FOR MAGNETIC DATA USING FULL- WIDTH HALF-MAXIMUM METHOD

The analysis of the magnetic data collected by Geometrics, Inc., was used to identify potential locations for excavation. To help guide the excavation process, it was necessary to develop an estimate of the depth of the source of the magnetic anomaly. A full dipole-fitting routine that could be used to determine the location and depth of the magnetic anomaly was not available at IDA. Thus, to estimate the depth of the source of the magnetic anomalies, we used a simple full-width half-maximum (FWHM) method. This method assumes that the depth of the source of the magnetic anomaly is equal to the FWHM of the measured magnetic signature. Here, the depth is the distance from the sensor to the center of volume of the source. To convert this to the actual depth, the sensor height above ground must be subtracted from the measured FWHM. In this appendix we will refer to depth as the distance between the magnetometer and the source of the anomaly (i.e., not actual depth). Although this technique provides a quick estimate of the depth, contributions from magnetic moments of higher order than the dipole moment, line-to-line navigation errors, and the data spatial density can affect the accuracy of the estimate. These error sources are discussed below.

DIPOLE MOMENT FWHM

The FWHM of the magnetic signature of a pure magnetic dipole is very nearly equal to the depth of the dipole. This can be shown in the simple case of a magnetic dipole oriented in the z -direction and measured in the x - y plane using a full-field magnetometer. In this case, the signature of the dipole can be written as

$$H = \frac{3Mz^2}{(\rho^2 + z^2)^{5/2}} - \frac{M}{(\rho^2 + z^2)^{3/2}}$$

where M is the magnitude of the dipole moment and ρ is a point on the x - y plane. For a fixed depth z from the measurement plane, the maximum of the magnetic field is at $\rho = 0$. The FWHM is equal to twice ρ_{Hm} at the point where the magnetic field is half the maximum value of the magnetic field. Thus, the half-maximum field is

$$H_{1/2} = \frac{3M}{z^3} \left\{ \frac{1}{1+\zeta^2} \right\}^{5/2} - \frac{M}{Z^2} \left\{ \frac{1}{1+\zeta^2} \right\}^{3/2}$$

where ζ is the dimensionless quantity ρ_{Hm}/z . Since the half-maximum is also equal to $H_{\max}/2$, this expression can be reduced to

$$3 \left\{ \frac{1}{1+\zeta^2} \right\}^{5/2} - \left\{ \frac{1}{1+\zeta^2} \right\}^{3/2} = 1$$

Solving for ζ yields a single real root with a value of 0.501. Thus, the FWHM is $1.02 \times z$.

For the case where the dipole is oriented along the geomagnetic field, it is easier to work with the magnetic field image. Figure B-1 is the magnetic signature of a dipole aligned with the geomagnetic field as measured at FP20.

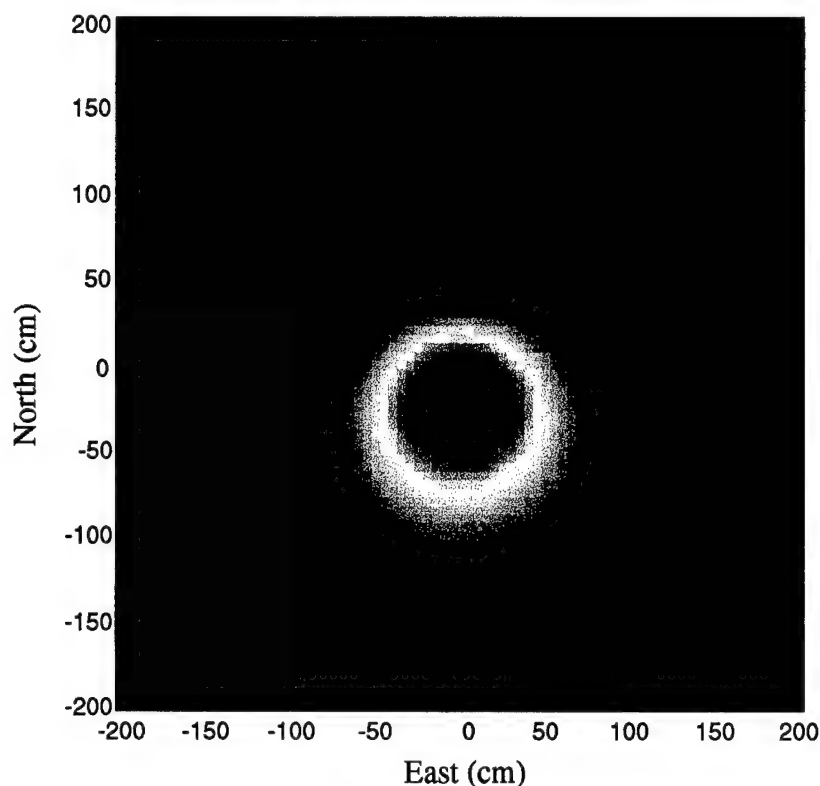


Figure B-1. Image of the Magnitude of the Magnetic Signature of a Dipole at 1-m Depth in the Geomagnetic Field

By measuring the FWHM of a slice of the image through the maximum, the depth is estimated to be 1.0 m (see Figure B-2).

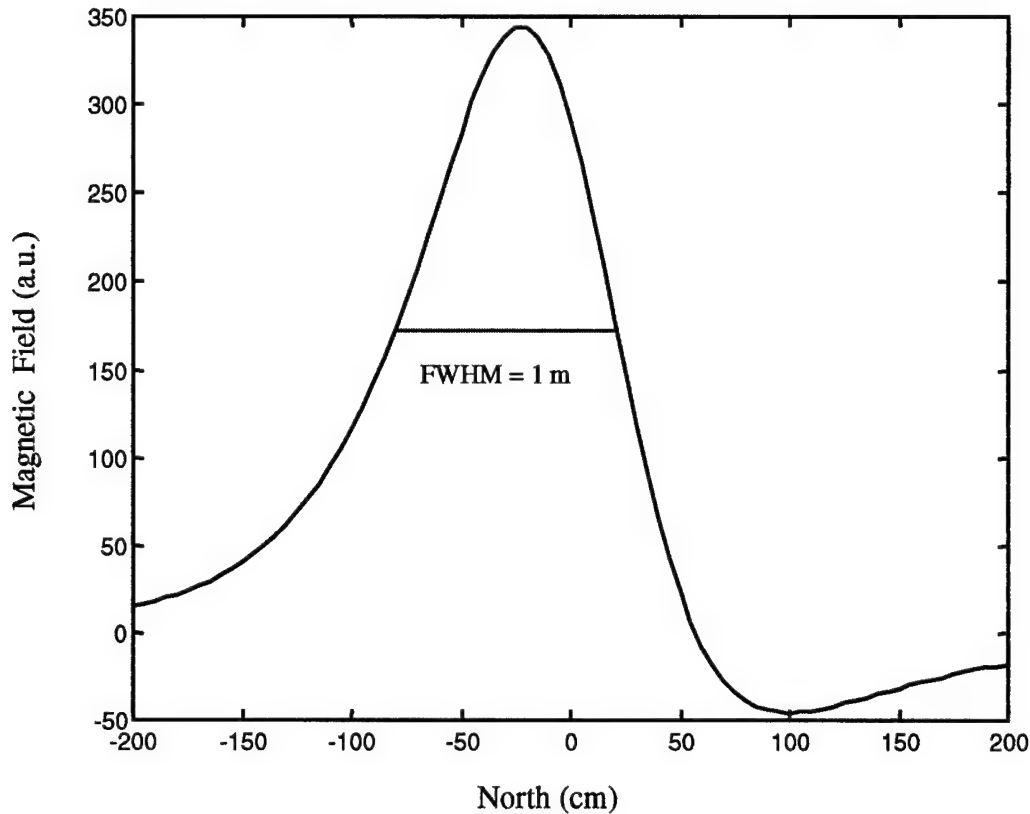


Figure B-2. The Magnitude of the Magnetic Field for a Dipole at 1-m Depth Showing the FWHM Value

ERRORS IN THE FWHM ESTIMATION

There are several sources of errors in the use of the FWHM to estimate the depth of the source of a magnetic anomaly. For example, the presence of magnetic moments higher than the dipole moment in the measured signature can produce estimation errors. These higher moments tend to widen the FWHM. For ordnance, which should have a small quadrupole moment (Altshuler, 1996), the FWHM depth estimate is still relatively robust. But for shallow objects that have a moderate measurable quadrupole, such as some clutter, the effect can be significant. The effect of the quadrupole moment can be seen in Figure B-3. Here, a source with a strong quadrupole moment is present 0.60 m below the sensor measurement plane. Measuring the FWHM in both the north-south and east-west directions results in estimates of the depth of 1.15 m and 1.0 m, respectively

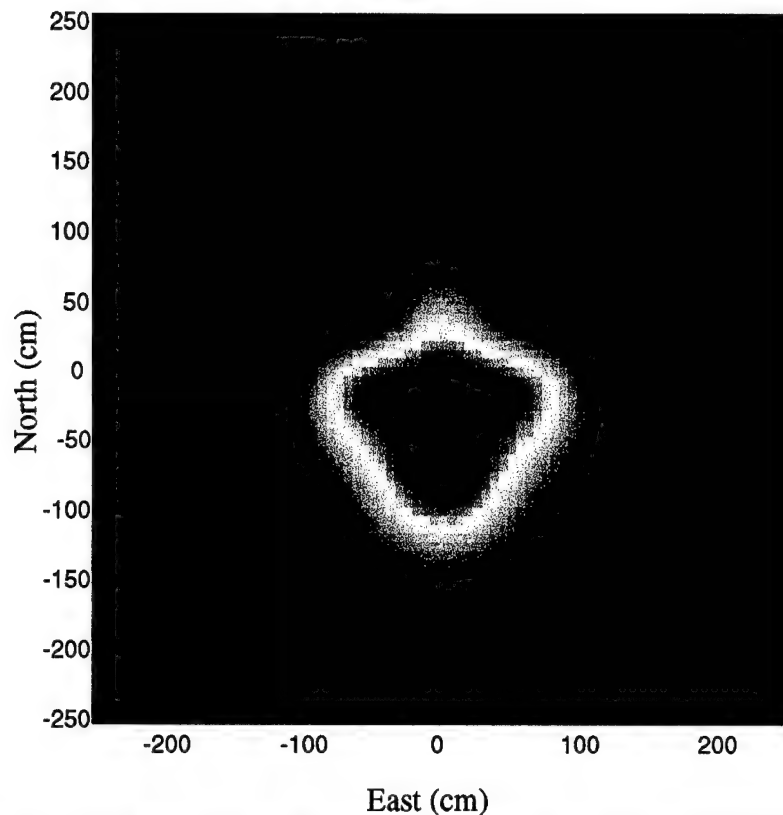


Figure B-3. The Magnitude of the Magnetic Signature from a Magnetic Source with a Strong Quadrupole Moment at a Distance of 0.60 m from the Measurement Plane

(see Figure B-4). This results in respective errors of 66 and 92 percent in the actual depth. Other quick methods used to estimate the FWHM, such as image-processing techniques, result in similar error.

Additional sources of error, such as line-to-line navigation errors (see Appendix C), complicate estimates of the FWHM. Navigation errors coupled with low spatial sampling rates for the magnetic data (12 cm in the north-south direction and 50 cm in the east-west direction) and the presence of large amounts of clutter close to the object of interest also contribute to FWHM estimation errors.

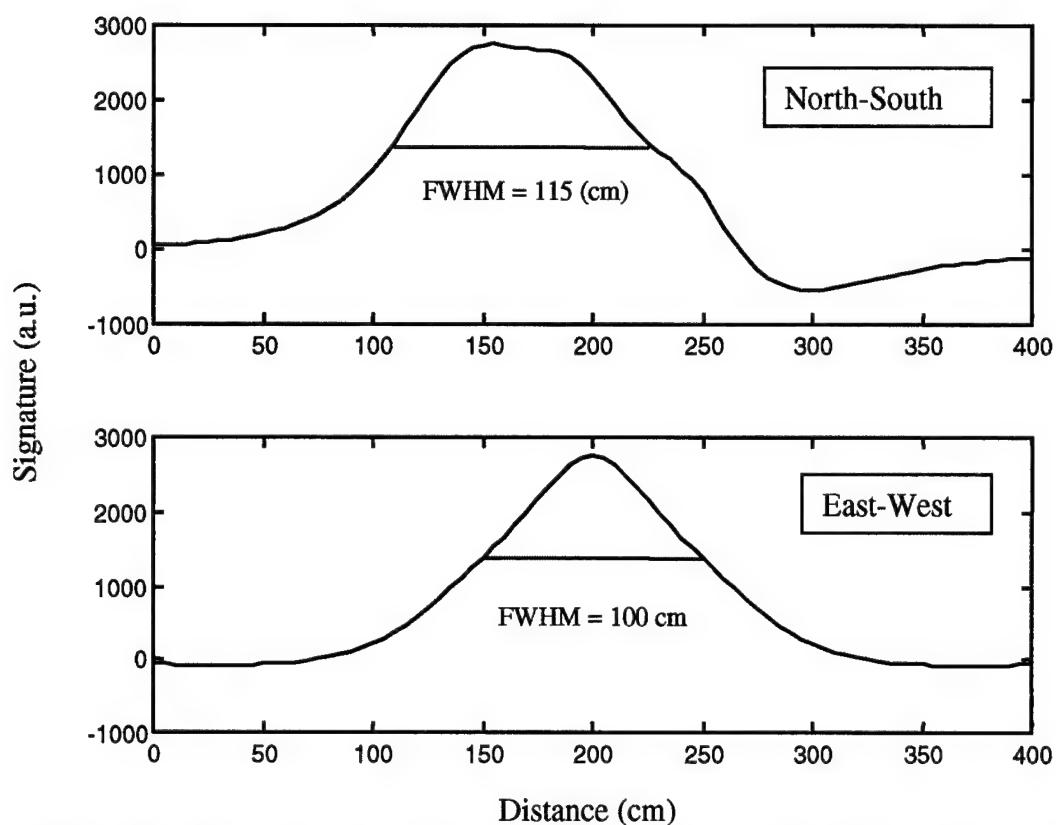


Figure B-4 . Magnitude of the Magnetic Field for a Source with a Strong Quadrupole at 0.6-m Depth Showing the FWHM Value of 1.15 m in the North-South Direction and 1.0 m in the East-West Direction

APPENDIX C

PARSONS AND GEOMETRICS LOCATION DATA ANALYSES

APPENDIX C

PARSONS AND GEOMETRICS LOCATION DATA ANALYSES

In this appendix we discuss the location accuracy of the Parsons EM61 0.5-m EMI data and the Geometrics G-858 magnetometer data. We did not perform a detailed analysis of the location accuracy of the Geophex GEM-3 data because it was very poor.

A. PARSONS LOCATION ACCURACY

Figure C-1 shows the EM61 0.5-m upper coil response due to the presence of OB160, a metal bar approximately 4 m long. A black bar representing OB160 is superimposed on the figure. Notice the line-to-line response misalignment resulting from location errors correlated to the direction of travel.

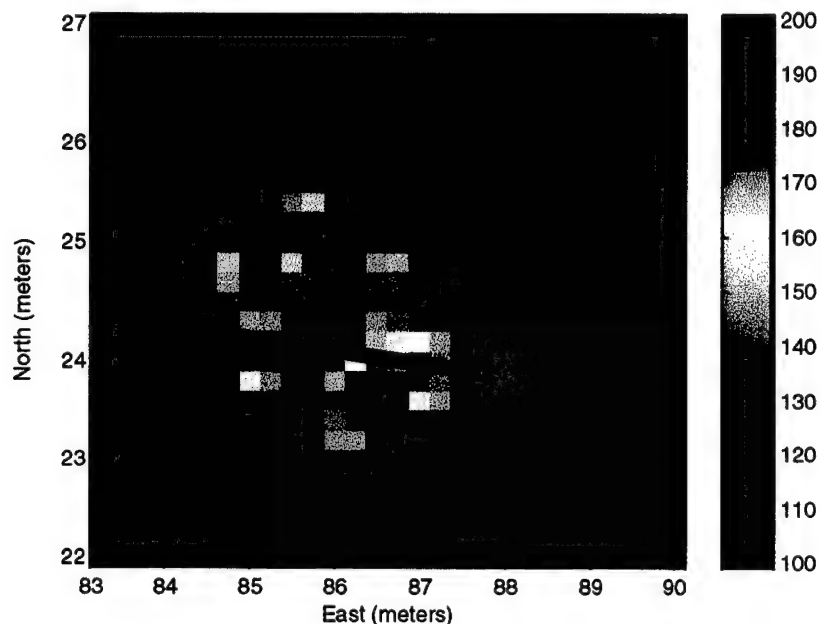


Figure C-1. Parsons Raw EM61 Upper Coil Response to OB160

B. PARSONS NAVIGATION SYSTEM

Parsons uses a tick wheel to trigger its data logger, so the number of sensor responses collected is equal to the number of ticks. Parsons computes the north positions

corresponding to a sensor reading by dividing the length traveled by the number of ticks less one recorded over that length:

$$\Delta N = L/(\text{\#ticks}-1),$$

where $L = 100$ m. Successive north positions are then computed using the formula

$$N_{i+1} = N_i + \Delta N, \quad i = 1, \dots, \text{\#ticks}-1.$$

The east position corresponding to a given north-south traversal of the site is held constant based on the 0.5-m line-to-line spacing that was marked using survey tapes on the north and south sides of the site. Thus, deviations from navigating the imaginary straight lines connecting cones at opposite ends of the site are not accounted for in the Parsons EM61 sensor data. Table C-1 is a sample of a Parsons EM61 data file.

Table C-1. Sample File for Parsons EM61 Sensor Data

Time	East	North	Coil 1	Coil 2
2751.36	122.0	0.00	294.56	-189.0
2751.95	122.0	0.21	293.25	-189.0
2752.14	122.0	0.42	293.25	-189.0
2752.38	122.0	0.63	293.44	-189.0
2752.61	122.0	0.85	293.81	-189.0

For Parsons EM61 data, there are basically four sources of location error:

Parallax

Tick-Wheel Offset

Meandering

Sensor Delay

We discuss each in turn.

1. Parallax Errors

Parallax errors of approximately ± 10 cm in the direction of travel and ± 5 cm in the cross-track direction occur at the beginning and end of 0.5-m lines. These errors are the result of visually lining up the sensor with the 0-m and 100-m cones located at the northern and southern ends of the site.

2. Tick-Wheel Offset Errors

The data-logger triggers located on the tick-wheel are separated by approximately 20 cm along the diameter of the wheel. Thus, when the sensor system begins its motion forward from a stationary start, the first data point is not collected until the tick-wheel is triggered, with a resultant location error of 0 to +20 cm in the direction of travel. When the sensor systems comes to rest at the end of the line, the error is -20 to 0 cm for the last point collected. Thus, errors due to tick-wheel offset vary as a function of distance traveled in the north-south direction. Parallax and tick-wheel offset errors are not accounted for in the raw data file (see Table C-1, where the starting north position is 0.00 m).

3. Meandering

A third source of location error is due to navigational deviations from a straight path; that is, differences in the actual length traveled are also due to east-west meandering. These errors are evident from the number of ticks recorded for each east line. For the 0.5-m lines extending from east 84-m to east 88-m, Table C-2 shows the number of ticks recorded by the data logger.

Table C-2. Number of Ticks for East 84 m to East 88 m

East	#Ticks
84.0 m	510
84.5 m	511
85.0 m	511
85.5 m	513
86.0 m	510
86.5 m	511
87.0 m	510
87.5 m	511
88.0 m	509

The difference between the maximum of 513 ticks at east 85.5-m and the minimum of 509 ticks at east 88.0-m is 80 cm, given the 20-cm tick spacing. Dividing 80 cm by the approximate number of ticks for a given line results in an error of 0.16 cm in the north-south direction due to meandering. The error in the east-west direction due to meandering is estimated to be ± 0.25 m.

4. Sensor Delay

The last source of location error is due to what Parsons describes as a response delay. In Parsons' Backgrounds Report, the line-to-line shifts in anomalies are attributed to a "...slight delay between the voltage induced in the receiver coil and the associated response measured by the data logger." Parsons estimates the delay to be between 0.25 and 0.5 s. At advance rates of approximately 1.3 m/s, this translates to offsets in north position of 32.5 to 65.0 cm. Ignoring the other sources of location error, we would expect this delay to be manifested as a constant offset in the north-south direction across the entire site. The argument might also be made that sensor electronics drift might cause the delay to drift as the site is traversed, but even so, line-to-line offsets should be approximately equal. This hypothesis can be tested in lines containing known objects by comparing the difference between the location of sensor response maximums and the corresponding objects' surveyed location for a given line and for adjacent lines. Figure C-2 shows the upper coil sensor response of Parsons EM61 at FP20 at east 85.0 m. The difference in north between the surveyed location of OB160 and the sensor maximum as computed using an interpolating quadratic is 0.424 m, as indicated on the figure.

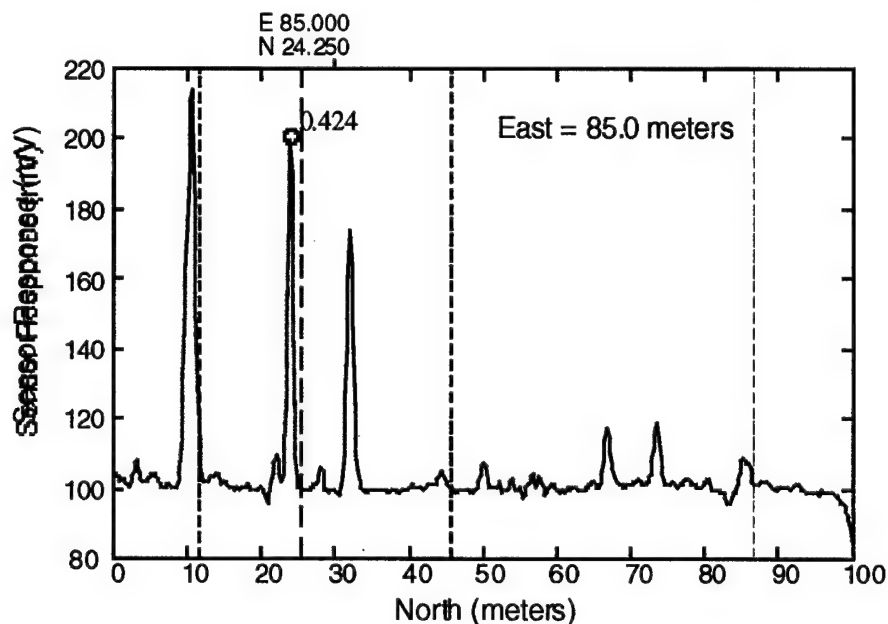


Figure C-2. Parsons EM61 Upper Coil Response at FP20,
East 85.0 m

The same computation was made for the other east lines in the vicinity of OB160, and the results are tabulated in Table C-3. The minimum difference between the sensor maximum as computed using a quadratic interpolating polynomial and the surveyed north position was 0.189 m at east 87.0 m, and the maximum was 0.656 m at east 85.5 m.

**Table C-3. Differences Between Surveyed North Position
and Sensor Maximum for OB160**

Surveyed East (m)	Surveyed North (m)	Difference (m)
84.0	24.365	0.574
84.5	24.307	0.366
85.0	24.250	0.424
85.5	24.192	0.656
86.0	24.135	0.379
86.5	24.077	0.551
87.0	24.019	0.189
87.5	23.962	0.551
88.0	23.904	0.339
	Mean	0.448
	Standard Deviation	0.146

Table C-3 indicates that line-to-line misalignments of sensor maximums with surveyed anomalies will persist even if an attempt is made to preprocess the data by shifting the north positions by some prescribed amount. To show this, we made successive transformations of the raw EM61 data by shifting the north positions by multiples of 0.125 m (remember that the sign of the north offset changes depending on the direction of travel). Figure C-3 shows the result for north offset values of 0.25, 0.50, 0.75, and 1.00 m. As expected, OB160, represented by the black bar, never becomes aligned with the sensor data. As the maximum sensor value for a given east line moves toward the correct surveyed position, an adjacent sensor maximum moves away from the correct surveyed position.

C. INTERACTIVE ALGORITHM FOR IMPROVING LOCATION ACCURACY

From Figure C-3, we conclude that the sources of location error combine in such a way as to prevent a simple north offset correction. We now propose an alternative method for correcting for the location errors in the north-south direction. This new technique uses an interactive computer program to match sensor responses of known objects to correct for offset errors in the north position. The algorithm relies on surveyed object positions uniformly distributed in the east-west direction. It suggests that a more careful excavation be done at the remaining clutter sites to provide a comprehensive database of surveyed objects.

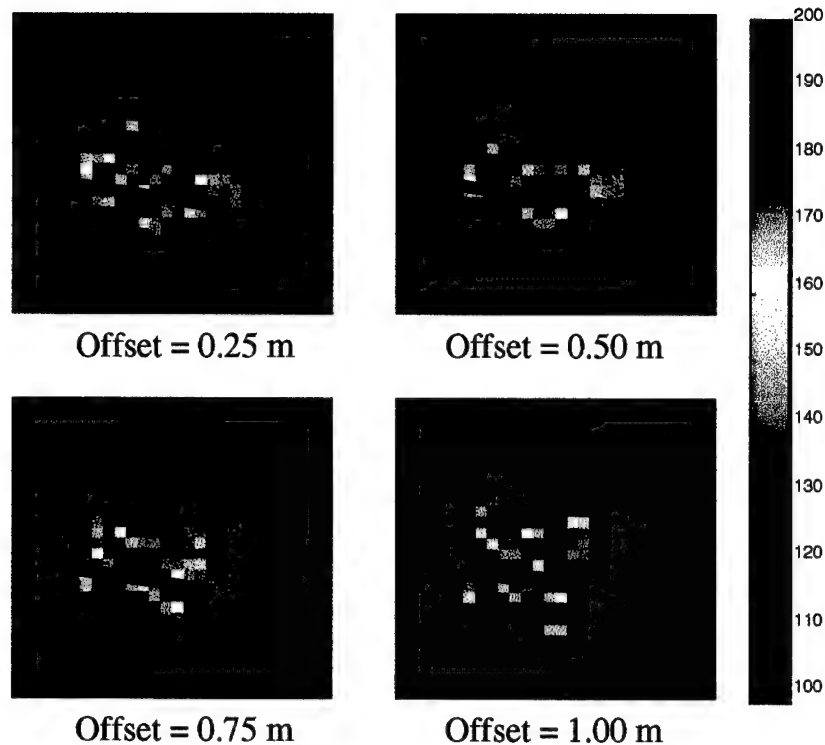


Figure C-3. Results of Using a Constant North Offset to Account for Line-to-Line Misalignments

The interactive program reads in a Parsons' data file corresponding to a single traversal of the site at a particular east coordinate. A plot of the response of the upper coil as a function of north position is made, as shown in Figure C-2. The surveyed positions of objects within 2 m of the current data line with respect to the east-west direction are shown in the form of red vertical dashed lines. This enables the user to associate coil response maximums to corresponding surveyed anomaly positions. The user can immediately observe trends such as a nearly constant offset in north position or the presence of interfering clutter items.

The user is then presented with a set of hash-marks which can be used to select points on the plot. The idea is to select targets that are well defined in this space. By well defined, we mean spatially separated from nearby anomalies that may be caused by other targets or clutter items, and whose associated peak is proximate and has a magnitude above the noise floor. Once the user has visually determined which objects are well defined, they are selected by positioning the cursor on the dashed line corresponding to the object and clicking the left mouse button. A click of the right mouse button ends this procedure and the differences in north position between the surveyed locations of the objects and the location of the associated maximum sensor responses are computed and displayed

on the plot. An average north offset is computed as well as the standard deviation of the offsets. The user is then given the option of continuing with the fusion process or selecting a different set of well-defined objects. Once a set of well-defined objects has been chosen, new north positions are computed for each sensor response by constraining the location of the user-selected anomalies to their corresponding surveyed object locations and by compressing or expanding the points between selected anomalies.

This technique was applied for the region surrounding OB160 and the result is shown in Figure C-4. Notice that the sensor data is more aligned with the surveyed object than for the case when the data was simply shifted in the north-south direction (see Figure C-3).

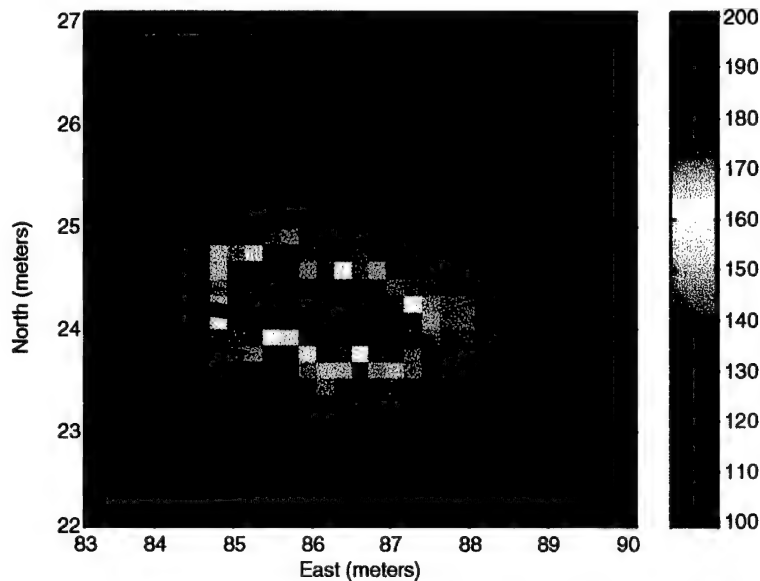


Figure C-4. Result of Interactive Correction Algorithm for OB160

The technique of matching sensor response maximums with corresponding target locations minimizes the location errors caused by parallax, tick-wheel navigation, mean-dering, and sensor delay. The degree to which the location error is minimized is correlated with the number of surveyed anomalies for a given east line. The more well-defined targets per east line there are, the more the location error in the north-south direction can be reduced.

A sort by east position of the digging list for Firing Point 20 reveals any gaps that may be problematic when fusing the entire site. The greatest gap in east position where

no items were surveyed is 3.5 m, located between east 19.4 m and east 23.0 m. For the most part, though, the gaps in east between items is less than 1 m.

The success of the algorithm relies on surveyed target and clutter items uniformly distributed in the east-west direction of each site. Regions containing distinct clutter items that have not been surveyed cannot be chosen by the user during the interactive portion of the algorithm. The algorithm need not be applied to lines that are void of targets or clutter. As an example, at the Seabee and Turkey Creek sites there are many adjacent east-west lines that contain little to no sensor response above the noise floor. Determining the correct positions for each of the associated sensor responses along these lines is unnecessary since subsequent data analysis will not change in a significant measurable manner. One would be simply sliding a response consisting entirely of noise in the north-south direction.

D. GEOMETRICS LOCATION ACCURACY

We now turn to the G-858 magnetometer surveys conducted by Geometrics. In particular, we focus on the sensors located 0.5 m above the ground and separated by 0.5 m in the cross-track direction at Firing Point 20. First, we describe the navigation system. Then, we identify three sources of location error—parallax, meandering, and variable velocity—and discuss them in turn.

1. Geometrics Navigation System

Line-to-line scans were conducted at 1-m intervals, leading to east-west resolution of 0.5 m. An internal clock triggered the collection of magnetometer readings every 10th of a second. Advancing at a rate of approximately 1.1 m/s leads to a north-south resolution of 0.11 m. Figure C-5 shows the 0.5-m magnetometer response due to the presence of OB160. Notice the absence of line-to-line response misalignments compared to the EM61 response to the same object. Extended objects are manifested as dipole signatures in the magnetometer data. Identifying the center of a dipole signature in the data is more difficult than for the monopole case, where the sensor maximum can be aligned with the surveyed center of the object.

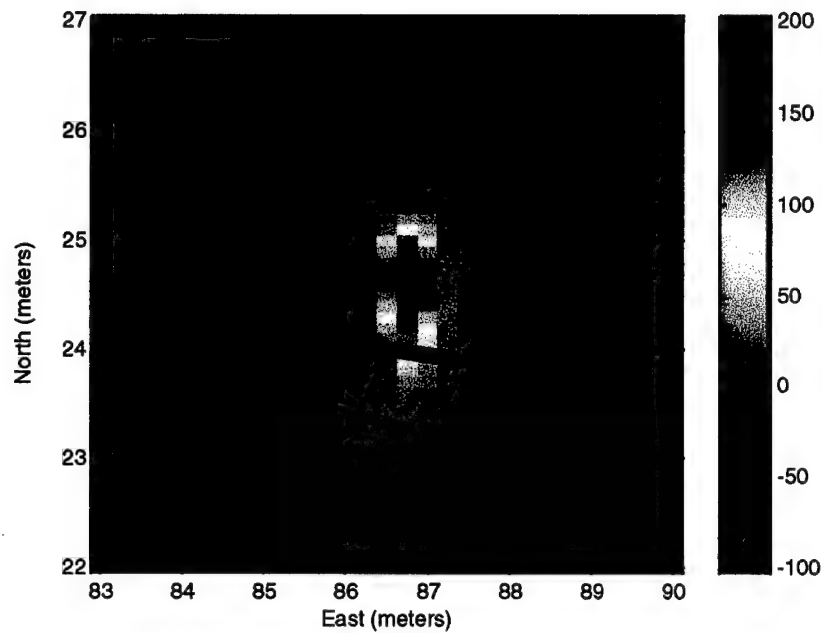


Figure C-5. Geometrics G-858 Magnetometer Data at FP20 - OB160

We choose to use the response induced by some of the M12 landmines discovered in the center region at FP20 to investigate Geometrics location accuracy. Figure C-6 shows the response to OB3, an M12 located at 59.883 m east, 43.867 m north, with the location of the mine superimposed as a black circle.

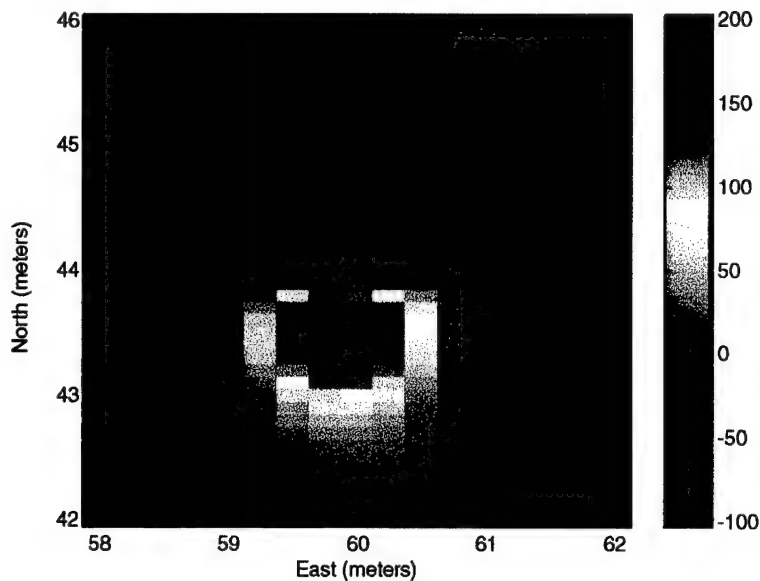


Figure C-6. Geometrics G-858 Magnetometer Data at FP20 - OB3 (M12)

As with OB160, no line-to-line misalignments of the sensor data are noticeable. Based on the response for OB160 and OB3, Geometrics' location accuracy appears to be better than the location accuracy of Parsons' EM61. Geometrics used the same method as Parsons did for assigning an east position for a given traversal of the site and used fiducials inserted during the data collection process to subsequently compute north positions. At Fort A.P. Hill, fiducials at 0, 50, and 100 m were used; at Fort Carson, fiducials were inserted at 0, 25, 50, 75, and 100 m. When the center of the magnetometer array passed over one of the fiducial points as marked by a cone, a pickle switch was pressed, thereby inserting a mark in the data stream indicating the position of the sensors at that time. A clock operating at 10 Hz triggered the sensors to collect data. North positions were then computed in the same manner as for Parsons using the formula

$$N_{i+1} = N_i + \Delta N, \quad i = 1, \dots, \text{\#ticks}-1$$

where $\Delta N = L/(\text{\#ticks}-1)$. Unlike Parsons, though, $L = 50$ m and the number of sensor responses recorded is equal to the number collected for the given 50-m interval.

2. Parallax

Parallax errors occur when fiducial points are inserted into the data. (Geometrics did not use a tick-wheel and Geometrics made no mention of a response delay in their magnetometer array). The operator activates a switch when the sensor passes one of the fiducials. We estimate this error to be ± 20 cm in the direction of travel and ± 10 cm in the cross-track direction, or twice the magnitude of Parsons' parallax errors. The error is this large because the Geometrics magnetometer array is moving when the sensor head is visually lined up with the cone; the Parsons system is not.

3. Meandering

Errors due to meandering apply to the Geometrics data as they did for the Parsons data. The error is greatest in the east-west direction and is estimated to be between ± 0.25 m, while in the north-south direction the error due to meandering is a fraction of a centimeter. A third type of error relating to the variable rate of advance of the magnetometer array over the site is discussed later.

4. Visualization of Data

Since location errors which are positive in the direction of travel are absent from Geometrics data, the line-to-line shift of data which was used in the Parsons data set to localize extended sensor responses will not improve the Geometrics responses. Figure

C-7 shows the sensor response due to OB3 after shifting the data in the north-south direction by 0.125 m.

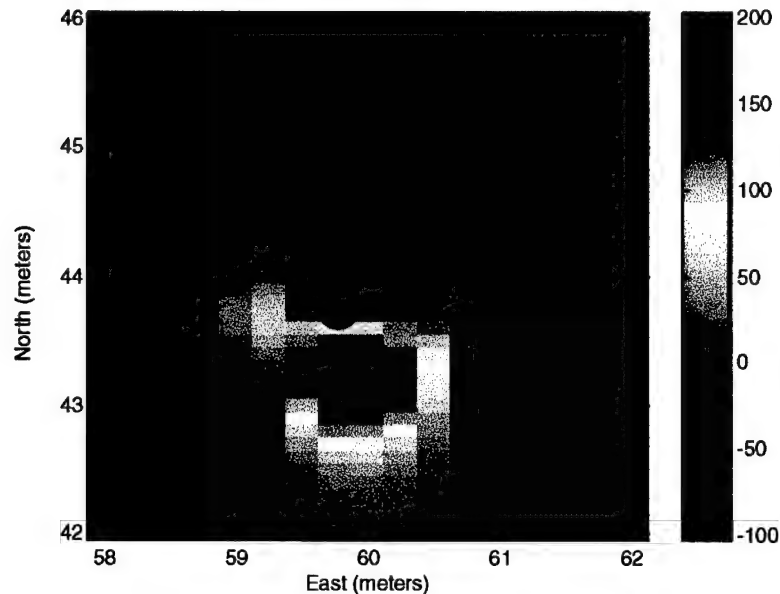


**Figure C-7. Geometrics G-858 Magnetometer Data at FP20 - OB3;
Offset = 0.25 m**

Notice that the dipole breaks up when the data is shifted by this relatively small amount, but that the change is not uniform. That is, the left side of the dipole has clearly become misaligned with the remainder of the dipole, but the center portion of the dipole remains unchanged from Figure C-6. The right side of the dipole also seems to shift away from the center, but is less noticeable.

To better visualize the effects of line-to-line shifts in the data, we interpolate the data to create denser images in the vicinity of anomalies. The effect of this interpolation is to accentuate nonuniformities in the response shapes in order to identify those anomalies which are more localized than others. Note that in Figures C-1 through C-7 the resolution in both the east-west and north-south direction is greater than for the original raw data. Interpolation using approximately twice the density of points in each direction was done so that the resultant color images would be more visually pleasing, without introducing any artificial phenomenon into the data. In fact, when the raw data consisting of 0.5-m resolution in the east-west direction and ~0.1-m resolution in the north-south direction is presented, the images are blocky, and it is difficult to make out dipoles and to separate anomalies from one another. Figure C-8 shows OB49, an M12 located at East 50.593 m,

North 73.219 m, for the case where the offset is 0.0 m and 0.25 m for the coarse raw data and the higher density interpolated data.

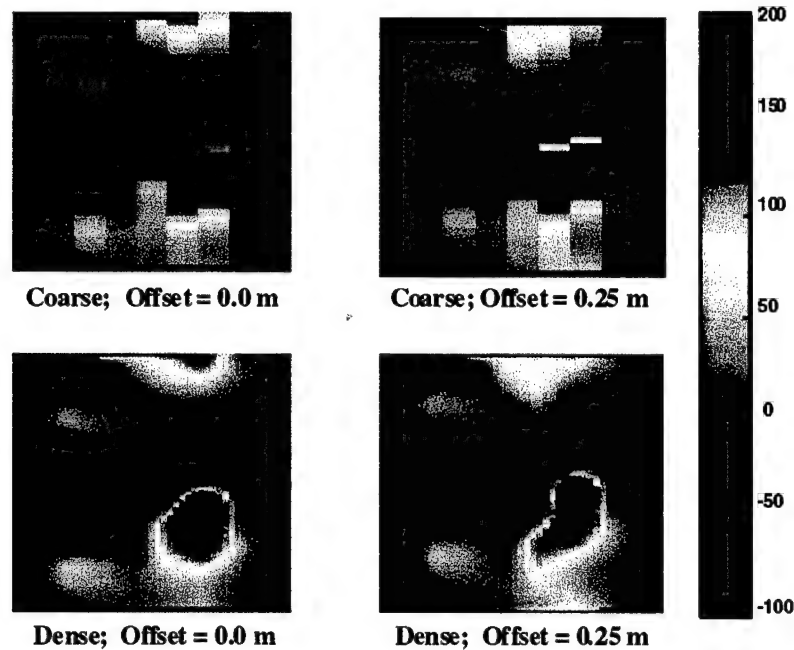


Figure C-8. Geometrics G-858 Magnetometer Data at FP20 - OB49

Note that for the raw data it is both difficult to see the dipole signature and to notice the effect of shifting the data on the structure signature. This contrasts with the higher density data, where the dipole signature is easily recognized, and shifting the data by 0.25 m clearly results in a misshapen signature. In this case, we found that shifting the data decreases the location accuracy.

5. Dipole Fits of Data

Another means to assess location accuracy is to do dipole fits of the data surrounding known anomalies. The location of the dipole can be computed and compared to the known location of the objects using the surveyed positions from the digging data. In addition, a measure of how well the data fit a dipole model can be used as a measure of location accuracy for spatially separated anomalies. We first compare the results of the dipole fit using different mesh densities to understand the dependence of the various fitting parameters on data density. Table C-4 shows the results of the dipole fit for OB3 (see Figure C-6).

Table C-4. Results of Dipole Fits for OB3—Raw and Variable Interpolations

	Raw	Linear Coarse Interpolation	Linear Fine Interpolation	Cubic Fine Interpolation
East	59.952 m	59.930 m	59.934 m	59.935 m
North	43.809 m	43.834 m	43.820 m	43.817 m
Depth	0.213 m	0.286 m	0.265 m	0.241 m
Inclination	16.38 deg	12.62 deg	14.71 deg	14.92 deg
Declination	100.31 deg	99.98 deg	100.63 deg	100.31 deg
Size	0.117 m	0.122 m	0.121 m	0.120 m
Fit	0.9514	0.9492	0.9487	0.9544

For the linear *coarse* interpolation, the number of samples is approximately equal to the number of raw samples. For the linear and cubic *fine* interpolation, the number of samples is five times the number of raw samples in each dimension. Notice that the greatest variation occurs for the depth and inclination parameters. Defining the variation in parameters as the standard deviation divided by the mean, we find that the parameters east, north, declination, and fit vary by 1 percent, while the parameter size varies by less than 2 percent. The fitting parameters of depth and inclination vary by 10 percent. We conclude that the addition of sample points using interpolation does not introduce error into the dipole fitting routines, and may even improve the accuracy of the method based on the fit parameter.

The reason for increasing the number of sample points before using the dipole fitting routines is so that the sample points corresponding to a given anomaly can be extracted by graphical means. It has been shown that increasing the density of the image allows for easier identification of anomalies. Given the ability to extract data from an image by drawing a polygon around an anomaly, we have shown that increasing the density of points in the image aids the extraction process without introducing errors in the dipole fitting procedures. Figure C-9 illustrates this point for a region where there are several anomalies located in the same proximity.

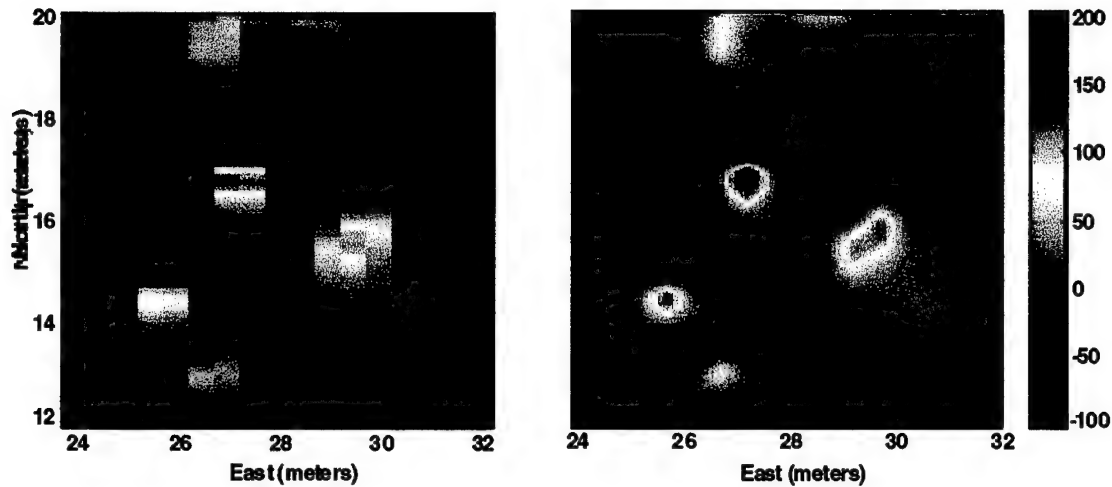


Figure C-9. Effects of Interpolation on Geometrics G-858 Magnetometer Data at FP20

We now return to the idea of using the dipole fit results to evaluate the utility of shifting the data in the north-south direction for the purpose of improving location accuracy. The effect of shifting the line-to-line responses centered on OB3 was shown in Figure C-7 and Figure C-8. To quantify the effect, we compare the dipole fitting parameters as a function of positional offset in the direction of travel. Table C-5 shows the results for the case when offset is equal to 0.0, 0.125, and 0.25 m.

Table C-5. Results of Dipole Fits for OB3 (M12)—Raw and Shifted Data

	Offset 0.0 m	Offset 0.125 m	Offset 0.25 m
East	59.935 m	59.967 m	60.006 m
North	43.817 m	43.711 m	43.577 m
Depth	0.241 m	0.246 m	0.239 m
Inclination	14.92 deg	15.50 deg	17.94 deg
Declination	100.31 deg	96.14 deg	93.14 deg
Size	0.120 m	0.119 m	0.117 m
Fit	0.9544	0.9214	0.8649

The surveyed position of OB3 is East 59.883 m, North 43.867 m. For increasing offset, the difference between the surveyed position and the dipole center computed using the dipole fitting routines increases. A fit parameter is computed as the two-dimensional correlation coefficient between the actual raw data and the dipole-fitted data. The fit

parameter decreases with increasing offset, indicating that the more the data is shifted, the less dipole-like the anomaly becomes. This method of localizing sensor responses, which worked well for the Parsons EM61, data does not improve the location accuracy of the Geometrics magnetometer data. This is not unexpected when one compares Figures 1 and 2, which show the full site images of FP20 using the 0.5-m Geometrics G-858 magnetometer and the Parsons EM61 induction coil, respectively. None of the line-to-line misalignments which are clearly visible in the EM61 image appear in the magnetometer image.

6. Variable Velocity Error

Variable velocity errors are due to fluctuations in the rate of advance which are unaccounted for in the raw data. These errors are not present in the Parsons data set since the tick-wheel method of data collection allows for variable velocity. Figure C-10 shows the velocity profile for Parsons EM61 for both the raw data and the laser tracker.

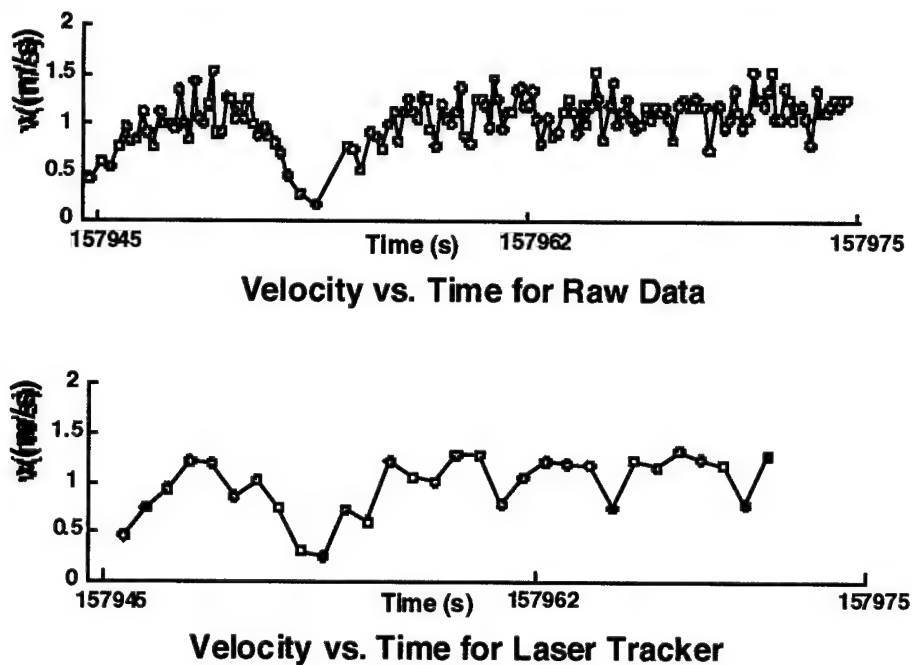


Figure C-10. Parsons EM61 Velocity Profiles

The drop-outs in the laser-tracker velocities, indicated by red circles, occur because the laser tracker failed to record the fractional portion of the second. While traversing this particular line, the Parsons sensor suite slowed down for a short duration. This is evident in both the raw and laser-tracker velocity profiles. To compute the velocities using the raw data, constant lengths are divided by variable time durations as given by the Parsons clock. Thus, any time the contractors slowed down while traversing the site, the

tick-wheel method of data collection captured this phenomena in the raw data, as verified with the associated laser-tracker file. This is in contrast to Geometrics' method of data collection where fluctuations in the rate of advance during data collection are not accurately reflected in the raw data and are not recoverable. Table C-6 shows a sample of a Geometrics raw data file. Notice both the time (T) and north (Y) differences are constant.

Table C-6. Geometrics G-858 Raw Data File at FP20

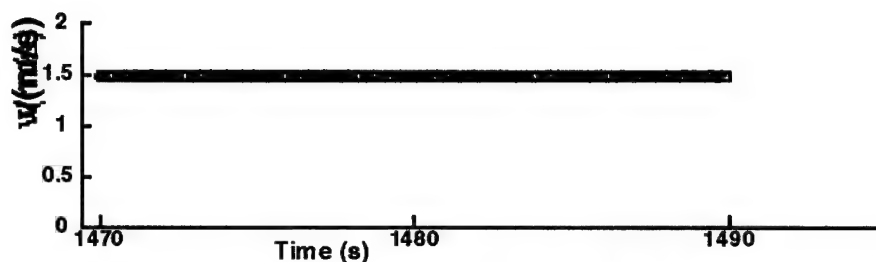
T	X	Y	M1	M2	COG	MRAW1	MRAW2	MREF
0.0	108.0	0.000	-83.625	-51.432	90	53388.388	53420.581	53475.406
0.1	108.0	0.145	-76.452	-42.543	90	53395.561	53429.470	53475.406
0.2	108.0	0.290	-68.862	-30.346	90	53403.152	53441.668	53475.407
0.3	108.0	0.435	-58.088	-8.636	90	53413.926	53463.378	53475.407
0.4	108.0	0.580	-43.481	24.990	90	53428.173	53497.004	53475.407

Figure C-11 shows the Geometrics velocity profiles for the raw data and the laser-tracker data. The velocities as given by the raw data are constant because they are derived by constant lengths divided by constant time durations. (Recall that an internal clock operating at 10 Hz triggered the system to collect a sample.) Ignoring the dropouts in the laser-tracker velocity profile, we compute the variable velocity error as the standard deviation of the mean of the remaining points. For a representative sample of lines across FP 20 the error is approximately 5 cm.

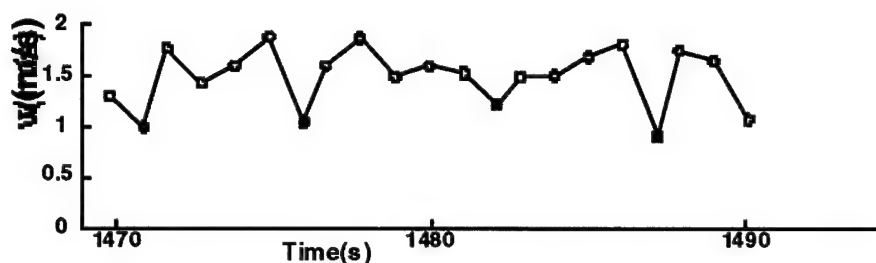
During the data collection process, Geometrics personnel attempted to maintain a constant rate of advance. Instances of poor location are most likely due to large fluctuations in rate of advance. For instance, if the contractors slowed down considerably, the subsequent computation of ΔN for that line would be inaccurate since the number of samples would be artificially large. An extreme case would occur if the system stopped, with samples being collected at 10 Hz over the same part of the ground. After accelerating to finish the line, the number of samples would be on average high, and the subsequent computation of N_i would not reflect that the sensor had stopped.

7. Enumeration of Errors

The apparent differences in location error for the Parsons EM61 and Geometrics G-858 systems can be explained by tabulating the size and direction of the errors for both systems, as shown in Table C-7.



Velocity vs. Time for Raw Data



Velocity vs. Time for Laser Tracker

Figure C-11. Geometrics G-858 Velocity Profiles

Table C-7. Location Errors for Parsons EM61 and Geometrics G-858

	Parsons North-South Error	Geometrics North-South Error	Parsons East-West Error	Geometrics East-West Error
Parallax	± 10 cm	± 20 cm	± 5 cm	± 10 cm
Tick-Wheel Offset	0 cm to +20 cm (beginning of lines) -20 cm to 0 cm (end of lines)	-	-	-
Meandering	<1 cm	<1 cm	±25 cm	±25 cm
Sensor Delay	+32 cm to +65 cm	-	-	-
Variable Velocity	-	±5 cm	-	-
Total Error	+22 cm to +95 cm (beginning of lines) +2 cm to +75 cm (end of lines)	±25 cm	±30 cm	±35 cm

If the sensor delay error that Parsons discusses in their final report is ignored, the total error for Parsons EM61 system at the beginning of lines is estimated to be -10 cm to +30 cm. No instances were observed where an offset in the negative direction improved location accuracy. We attribute the location errors in the Parsons and Geometrics data

sets to the errors discussed here, where the magnitude of the error in the north-south direction is +2 cm to +95 cm for Parsons and ± 25 cm for Geometrics. The magnitude of the total error in the east-west direction is ± 30 cm for Parsons and ± 35 cm for Geometrics.

APPENDIX D

SUMMARY OF EXCAVATION AND OBJECT INFORMATION

APPENDIX D

SUMMARY OF EXCAVATION AND OBJECT INFORMATION

NOTES: A total of 101 holes were excavated, resulting in 203 objects: 12 M12 inert training mines, 1 M16 inert landmine, and 1 metal-cased AT mine rusted beyond recognition. All object dimensions are estimates of the spatial extent. Most objects have irregular shapes, making more precise measurements difficult. The M12 landmine is 7 cm thick and 32 cm in diameter. Many depths are listed as "just under roots," which is 8–10 cm below the surface. If two hole dimensions are given, the hole is elliptical, and one dimension is the approximate diameter of the hole. An object is described as AI if it is not rusted. If there are many small items in a hole, the location is surveyed at the approximate center of the objects. Some objects are listed as a piece of an old mine sign, based on similarity to OB-155. The code TCTBO indicates that the object is too close to a larger object for the signature to be analyzed as a separate object.

Object ID	Size Bin	Excavation ID	Easting (m)	Northing (m)	Hole Diameter	Depth	Description
EX07P	Unknown		59.897	43.876			
EX109C	cable	EX-109	84.842	83.903			white cable
EX118C	cable		56.062	92.951	40 cm		white cable bundle; black cable
EX124C	cable		73.834	79.589			white cable bundle
EX128P	medium	EX-128	59.088	61.196	1.4 m × 1.95 m	77 cm	lots of metal fragments, rust spots, blue stuff, all small pieces; possible impact spot
EX157P	no metal	EX-157	67.638	36.511	1 m	8 cm	empty hole
EX172P	deep/ordnance-like	EX-172	51.228	3.518			55-gal drum, surveyed pt. not exactly where drum was

Object ID	Size Bin	Excavation ID	Easting (m)	Northing (m)	Hole Diameter	Depth	Description
EX30P	no metal	EX-30	32.301	23.542	1.2 m x 1 m	13 cm	concrete block, hole abandoned
EX63C	cable	EX-63	25.662	64.289		40 cm	white cable bundle; 2 photos, one little east of second w/all white cables
OB1A	medium	EX-1	77.735	7.944	40 cm	just under roots	wadded-up piece of metal, approx. 40 cm x 20 cm; 2 M16 rounds
OB1B	medium	EX-1	77.882	8.237			
OB2	big object	EX-17	82.206	7.341			1/2 of a differential (big)
OB3	M12	EX-7	59.883	43.867	89 cm	29 cm to bottom, 11 cm to top	M12 metallic AT training mine
OB4	M12	EX-5	56.774	28.259	57 cm	10 cm to top, 26 cm to bottom	M12 training mine
OB5	big metal plate	EX-2	52.898	18.054	75 cm	just under roots	square sheet metal, 40 cm x 37 cm, center 1.1 kg
OB6A	TCTBO	EX-2	52.747	17.909		just under roots	banding, .2 kg, 4 cm x 40 cm bent
OB6B	TCTBO	EX-2	52.867	18.306			
OB6C	TCTBO	EX-2	52.881	18.219			
OB7A	TCTBO	EX-2	52.681	18.193		just under roots	wire, very light
OB7B	TCTBO	EX-2	52.731	18.344			
OB7C	TCTBO	EX-2	52.97	18.108			
OB8A	large	EX-18	85.308	11.469		just under roots	1.5" metal pipe, 288 cm long
OB8B	large	EX-18	83.996	10.31			
OB8C	large	EX-18	83.001	9.809			
OB9	TCTBO	EX-18	83.2	10.147		just under roots	wadded-up piece of metal, 16 cm x 13 cm, 1.1 kg, filled w/ dirt
OB10A	TCTBO	EX-18	83.926	10.174		just under roots	piece of Al banding 20 cm x 4 cm, .1 kg
OB10B	TCTBO	EX-18	83.936	9.968			

Object ID	Size Bin	Excavation ID	Easting (m)	Northing (m)	Hole Diameter	Depth	Description
OB11A	TCTBO	EX-17	82.066	7.476			Al banding, 39 cm x 4 cm
OB11B	TCTBO	EX-17	82.212	7.141			
OB12A	TCTBO	EX-17	82.428	7.641			metal banding, 52 cm x 4 cm
OB12B	TCTBO	EX-17	81.897	7.523			
OB13A	TCTBO	EX-17	82.282	7.722			Al banding, 43 cm x 4 cm
OB13B	TCTBO	EX-17	82.504	7.331			
OB14A	TCTBO	EX-17	82.428	7.52			metal banding, 45 cm x 4 cm
OB14B	TCTBO	EX-17	82.341	7.045			
OB15	TCTBO	EX-17	81.868	6.9			Al banding, 11 cm x 4 cm
OB16A	large	EX-17	81.487	8.187			angle iron, 1.5" wide (use survey pts to est. length)
OB16B	large	EX-17	81.173	7.351			
OB16C	large	EX-17	81.675	6.954			
OB16D	large	EX-17	82.149	7.158			
OB19A	medium	EX-116	51.582	90.716	57 cm	8 cm	scrap metal, approx. extent = 20 cm x 40 cm
OB19B	medium	EX-116	51.759	91.099			
OB19C	medium	EX-116	51.862	90.876			
OB20	small	EX-117	53.624	92.503	70 cm x 43 cm	11 cm	wadded-up scrap metal, probably moved prior to survey, medium size
OB21	TCTBO	EX-117	53.624	92.503		directly beneath OB20	piece of wire, same as in hole EX-118 but only one strand
OB22	TCTBO	EX-118	56.049	92.949	40 cm	just under roots	wire, 13 strands, white and black
OB23A	medium	EX-72	71.663	78.523		just under roots	piece of metal, 45 cm long (various widths not exceeding 10 cm)

Object ID	Size Bin	Excavation ID	Easting (m)	Northing (m)	Hole Diameter	Depth	Description
OB23B	medium	EX-72	71.22	78.435			
OB24	cable	EX-72	71.694	78.621	65 cm x 30 cm	just under roots	M16 training rounds
OB25	cable	EX-72	72.078	79.604		just under roots	M16 training rounds
OB26	cable	EX-72	71.998	79.818		just under roots	M16 training rounds
OB27	cable	EX-72	72.097	79.972		just under roots	M16 training rounds
OB28	cable	EX-72	72.243	80.147		just under roots	M16 training rounds
OB29	cable	EX-72	72.17	80.236		just under roots	M16 training rounds
OB30	cable	EX-72	72.233	80.358		just under roots	M16 training rounds
OB31	cable	EX-124	73.017	79.305	27 cm	11 cm	hinge
OB32	cable	EX-124	73.995	78.972	35 cm	18 cm	scrap metal, 14 cm x 5 cm
OB33	small	EX-124	74.073	79.171	25 cm	just under roots	reinforced box corner, 8 cm x 3 cm
OB34	cable	EX-124	73.179	78.509	25 cm	16 cm	8 cm x 3.5 cm
OB35	cable	EX-124	74.933	80.035	25 cm	15 cm	soda can?
OB36	medium	EX-124	74.652	81.089			gas can, 1 gal, 29 cm x 22 cm
OB37A	medium	EX-124	75.776	80.612	30 cm x 25 cm	17 cm	metal banding, 57 cm x 4 cm
OB37B	medium	EX-124	75.958	80.176			
OB38	small	EX-124	77.955	80.683	50 cm	24 cm	piece of corroded metal, 8 cm x 4 cm, blue stuff
OB39	small	EX-124	81.107	82.244	35 cm	just under roots	piece of metal, 11 cm x 7 cm
OB40A	small	EX-124	81.517	82.962	33 cm	just under roots	coat hanger
OB40B	small	EX-124	81.663	82.609			
OB41	small	EX-124	83.34	83.748	39 cm	11 cm	piece of metal, 11 cm x 3 cm

Object ID	Size Bin	Excavation ID	Easting (m)	Northing (m)	Hole Diameter	Depth	Description
OB42	small	EX-109	84.864	85.613	30 cm	just under roots	link off 20mm clip , helicopter fired, 8 cm x 4 cm
OB43A	small-medium	EX-109	85.281	85.684	30 cm	just under roots	metal banding 4 cm, bent two segments = 17 cm and 24 cm
OB43B	small-medium	EX-109	85.153	85.915			
OB43C	small-medium	EX-109	85.098	85.753			
OB44	small	EX-109	85.107	87.01	40 cm	8 cm	piece of corroded metal, 14 cm x 2.5 cm
OB45	TCTBO	EX-129	62.656	73.821	10 cm x 48 cm	just under grass roots	metal banding, 48 cm x 4 cm
OB46	medium	EX-112	88.621	71.807	60 cm x 57 cm	just under roots	round piece of metal, part of a can, 27 cm x 25 cm
OB47A	medium	EX-107	68.322	86.946	95 cm x 55 cm	just under roots	metal banding 4 cm, bent two segments = 36 cm and 40 cm
OB47B	medium	EX-107	68.072	87.208			
OB47C	medium	EX-107	67.651	87.041			
OB48	M12	EX-105	62.662	73.812			M12
OB49	M12	EX-16	50.593	73.219	51 cm x 60 cm	just under roots	M12
OB50A	medium	EX-121	46.945	71.383		just under roots	metal banding, 45 cm x 4 cm
OB50B	medium	EX-121	47.349	71.191			
OB51A	medium	EX-121	47.018	70.553		just under roots	metal banding, 45 cm x 4 cm
OB51B	medium	EX-121	47.457	70.678			
OB52A	medium	EX-121	45.687	69.458		18 cm	metal banding, 4 cm x 43 cm
OB52B	medium	EX-121	46.149	69.418			
OB53	small	EX-121	46.585	69.473		14 cm	Al circular piece, 12.5 diameter
OB54	TCTBO	EX-121	46.429	68.602			metal fragment?, 15 cm x 2 cm

Object ID	Size Bin	Excavation ID	Easting (m)	Northing (m)	Hole Diameter	Depth	Description
OB55	TCTBO	EX-61	43.847	63.194		10 cm	metal 11 cm x 2 cm + piece of old mine sign
OB56A	medium	EX-61	43.115	62.814		8 cm	metal banding, 48 cm x 4 cm
OB56B	medium	EX-61	43.613	62.893			
OB57	big metal plate	EX-26	45.458	61.962		just under roots	piece of sheet metal, 48 cm x 20 cm
OB58A	medium	EX-8	42.492	56.248	approx. target size	just under roots	metal banding 4 cm, bent two segments = 24 cm and 28 cm
OB58B	medium	EX-8	42.567	55.983			
OB58C	medium	EX-8	42.796	56.034			
OB59	small	EX-8	41.397	55.74		12 cm	hollow circular object, metal, 5 cm diameter
OB60A	medium	EX-8	40.589	56.485	approx. target size	just under roots	metal banding, 43 cm x 4 cm
OB60B	medium	EX-8	40.563	56.061			
OB61A	medium	EX-25	41.864	51.927	approx. target size	just under roots	metal banding, 47 cm x 4 cm
OB61B	medium	EX-25	41.876	51.429			
OB62	medium	EX-98	41.645	46.451	50 cm	23 cm	M16 landmine
OB63	M12	EX-6	28.057	43.339	50 cm	8 cm to top, 20 cm to bottom	M12, driven over/flattened, 5 cm in height
OB64	TCTBO	EX-6	29.053	44.142	50 cm	just under roots	sheet metal, 17 cm x 7 cm
OB65A	medium	EX-130	22.965	35.72		just under roots	metal banding, 50 cm x 4 cm
OB65B	medium	EX-130	23.434	35.689			
OB66	deep/ordnance-like	EX-14	35.588	20.893	40 cm	just under roots	benchmark, 106 mm round straight down in cement
OB67A	medium	EX-33	28.133	20.515	50 cm	just under roots	metal banding, 46 cm x 4 cm

Object ID	Size Bin	Excavation ID	Easting (m)	Northing (m)	Hole Diameter	Depth	Description
OB67B	medium	EX-33	28.437	20.145			
OB68	big metal plate	EX-55	27.226	16.789	35 cm	just under roots	metal circular object, approx. 1 cm thick, 34 cm diameter
OB69A	medium	EX-104	25.466	14.85		just under roots	metal banding, 37 cm x 4 cm
OB69B	medium	EX-104	25.611	14.491			
OB70	medium	EX-29	45.672	27.353	50 cm	18 cm	very old rusted metallic AT mine w/a handle
OB71A	medium	EX-9	55.391	57.635		just under roots	irregularly shaped piece of metal, approx. extent 45 cm x 7 cm
OB71B	medium	EX-9	55.301	57.183			
OB72	small	EX-51	59.616	67.897		just under roots	thick wire, 15 cm x 16 cm
OB73	in a cluster	EX-51	59.933	68.213		just under roots	chunk of metal, 23 cm x 11 cm
OB74	TCTBO	EX-51	59.163	68.893		12 cm	chunk of Al, 9 cm x 3 cm
OB75	TCTBO	EX-51	60.013	68.639		18 cm	blue metal, 10 cm x 5 cm
OB76	medium	EX-51	60.078	69.004		just under roots	metal car part, 15 cm x 7 cm
OB77	M12	EX-11	61.897	70.139		8 cm top	M12
OB78A	small-medium	EX-77	40.887	89.01		11 cm	piece of metal, 22 cm x 7 cm
OB78B	small-medium	EX-77	40.892	88.805			
OB79	small	EX-100	43.586	81.904	20 cm x 40 cm	just under roots, 37 cm	tail fin assembly, Al, 13 cm x 8 cm, moved prior to survey to dig below
OB80A	medium	EX-100	43.414	81.444	20 cm x 40 cm	just under roots	metal banding, 46 cm x 4 cm
OB80B	medium	EX-100	43.901	81.512			
OB81A	TCTBO	EX-126	19.422	81.322		just under roots	metal banding, 59 cm x 2 cm + piece of an old mine sign?
OB81B	TCTBO	EX-126	18.939	81.049			

Object ID	Size Bin	Excavation ID	Easting (m)	Northing (m)	Hole Diameter	Depth	Description
OB82	small	EX-126	18.998	81.355		just under roots	metal scrap, 17 cm x 2.5 cm
OB83	TCTBO	EX-120	27.497	72.394		16 cm	chunk of metal, 11 cm x 7 cm
OB84A	medium	EX-120	26.824	72.588		just under roots	metal banding 4 cm, bent two segments = 20 cm and 20 cm
OB84B	medium	EX-120	26.776	72.769			
OB84C	medium	EX-120	26.561	72.755			
OB85	big metal plate	EX-63	27.168	68.744		18 cm	thick metal slab, 45 cm x 30 cm
OB86A	medium	EX-63	27.367	67.077		just under roots	metal banding, 50 cm x 4 cm
OB86B	medium	EX-63	27.029	66.723			
OB87	TCTBO	EX-40	28.489	38.847		16 cm	metal rebar?, 10 cm long
OB88A	medium	EX-40	28.122	39.047		16 cm	metal banding, 44 cm x 4 cm
OB88B	medium	EX-40	28.411	38.784			
OB89A	TCTBO	EX-40	27.984	39.065		16 cm	metal banding, 46 cm x 4 cm
OB89B	TCTBO	EX-40	28.298	38.7			
OB90	small	EX-40	28.134	38.611		16 cm	metal chunk, 11 cm x 4 cm
OB91A	medium	EX-96	23.781	15.663		just under roots	metal banding, 38 cm x 4 cm
OB91B	medium	EX-96	23.731	15.271			
OB100A	deep/ordnance-like	EX-127	88.573	8.01		65 cm	Big metal piece, flattened, tree branches also found in the hole
OB100B	deep/ordnance-like	EX-127	88.105	7.756			
OB100C	deep/ordnance-like	EX-127	87.82	6.987			
OB101A	medium	EX-93	57.151	9.234		just under roots	metal banding, 32 cm x 4 cm
OB101B	medium	EX-93	57.17	8.905			

Object ID	Size Bin	Excavation ID	Easting (m)	Northing (m)	Hole Diameter	Depth	Description
OB102	small	EX-62	55.169	8.557		15 cm	hollow circular piece of metal, 8 cm diameter
OB103	small	EX-62	55.204	8.918		10 cm	metal scrap, 10 cm x 1 cm
OB104	M12	EX-3	59.228	18.009		11.5 cm	M12
OB105A	deep/ordnance-like	EX-3	62.281	18.8		25 cm at deepest, just under roots	fuel tank?, 67 cm x 24 cm, lies N-S
OB105B	deep/ordnance-like	EX-3	62.139	18.423			
OB105C	deep/ordnance-like	EX-3	62.074	17.809			
OB106A	small	EX-94	53.932	30.024		just under roots	47 cm long (mine sign?)
OB106B	small	EX-94	54.058	30.48			
OB107	small	EX-66	51.997	34.519		12 cm	Al foil, 20 cm x 15 cm
OB108	small	EX-66	51.856	35.297		just under roots	metal clump, 6 cm diameter
OB109A	TCTBO	EX-99	57.75	41.17		just under roots	crumpled wire, 34 cm long
OB109B	TCTBO	EX-99	58.12	41.15			
OB110A	medium	EX-99	57.61	41.31		just under roots	metal banding 4 cm, bent, two segments = 45 cm and 38 cm
OB110B	medium	EX-99	58.09	41.33			
OB110C	medium	EX-99	58.27	41.04			
OB111A	medium	EX-86	57.021	45.054		just under roots	metal banding, 36 cm x 4 cm; golf ball
OB111B	medium	EX-86	57.077	45.431			
OB-112A	TCTBO	EX-16	51.2	72.96		just under roots	piece of an old minefield sign, 37 cm
OB-112B	TCTBO	EX-16	50.95	72.67			
OB113	M12	EX-123	53.069	84.399		8 cm to top	M12
OB114	small	EX-121	47.59	68.978		8 cm	metal banding, 12 cm x 3 cm

Object ID	Size Bin	Excavation ID	Easting (m)	Northing (m)	Hole Diameter	Depth	Description
OB115A	medium	EX-106	60.509	88.861		just under roots	metal banding, 47 cm x 8 cm (two 4-cm pieces side by side)
OB115B	medium	EX-106	60.164	89.186			
OB116	small	EX-106	61.597	87.894		just under roots	metal clump, 6 cm diameter
OB117A	large	EX-88	50.998	47.677		8.5 cm	metal fence post, 1.5 m long; not all in photo
OB117B	large	EX-88	52.509	47.271			
OB118A	medium	EX-70	51.296	61.534		just under roots	metal banding, 45 cm x 4 cm
OB118B	medium	EX-70	50.87	61.759			
OB119	M12	EX-10	36.183	77.13	10 cm		M12
OB120	medium	EX-10	35.188	76.59		just under roots	metal wad, 43 cm x 30 cm
OB121A	close to M12	EX-10	34.75	76.782		just under roots	metal fragment, 23 cm x 3 cm
OB121B	close to M13	EX-10	34.751	76.539			
OB122A	medium-large	EX-63	25.444	64.472		17 cm	metal banding, 52 cm x 8 cm
OB122B	medium-large	EX-63	25.905	64.671			
OB123	small	EX-122	36.202	58.33		just under roots	piece of old mine sign, 16 cm long
OB124	small	EX-122	36.501	58.351		just under roots	irregularly shaped piece of metal, 16 cm ²
OB125	small	EX-122	37.664	57.745		just under roots	chunk of metal, 9 cm x 7 cm
OB126A	small	EX-122	38.218	58.306		just under roots	gasket like piece of metal, 16 cm approx. diameter
OB126B	small	EX-122	38.054	58.269			
OB127A	small-medium	EX-75	39.333	49.296		just under roots	metal banding, wadded around its side, 22 cm long, 4 cm wide
OB127B	small-medium	EX-75	39.51	49.473			
OB128A	medium	EX-97	23.324	7.838		just under roots	metal banding, 65 cm x 4 cm

Object ID	Size Bin	Excavation ID	Easting (m)	Northing (m)	Hole Diameter	Depth	Description
OB128B	medium	EX-97	23.043	7.236			
OB129	small	EX-119	24.996	7.293			metal banding, folded into a triangle, 16-cm sides and 14-cm base
OB130	big metal plate	EX-12	32.076	1.206		20 cm	thick circular plate, N side shallowest, 34 cm in diameter
OB131	small	EX-12	31.086	3.133		just under roots	metal can, 8 cm x 8 cm
OB132	small	EX-12	31.364	2.991		just under roots	metal clump, 7 cm x 5 cm
OB133A	medium	EX-101	37.23	2.432			metal banding, 4 cm, bent, two segments = 37 cm and 35 cm
OB133B	medium	EX-101	37.001	2.155			
OB133C	medium	EX-101	36.726	2.455			
OB134	big metal plate	EX-64	39.674	1.436		10 cm	Al plate, 34 cm in diameter
OB135	small	EX-4	38.155	16.111		16 cm	metal chunk, 21 cm x 6 cm x 6 cm
OB136A	medium	EX-4	39.057	16.057		13 cm	metal banding, 45 x 4 cm
OB136B	medium	EX-4	38.626	16.092			
OB137A	large	EX-4	37.356	17.246		10 cm	fence post, 1.4 m x 10 cm
OB137B	large	EX-4	38.052	18.333			
OB138	big metal plate	EX-4	39.827	17.769		10 cm	metal plate w/Al threads (4), 33 cm in diameter
OB139	TCTBO	EX-4	37.939	17.399		just under roots	Al banding, 13 cm x 4 cm
OB140A	TCTBO	EX-4	39.437	18.255		just under roots	metal banding, 33 x 4 cm
OB140B	TCTBO	EX-4	39.676	17.945			
OB141	medium	EX-146	42.036	22.624		just under roots	angle iron, wadded up badly, 46 cm x 22 cm
OB142A	small	EX-115	50.956	26.372		just under roots	piece of metal, 20 cm x 7 cm

Object ID	Size Bin	Excavation ID	Easting (m)	Northing (m)	Hole Diameter	Depth	Description
OB142B	small	EX-115	51.153	26.287			
OB143A	small-medium	EX-158	63.82	43.337		just under roots	old mine sign in poor shape
OB143B	small-medium	EX-158	64.031	42.981			
OB144A	small-medium	EX-155	65.548	31.177		just under roots	metal banding, 44 cm x 4 cm
OB144B	small-medium	EX-155	65.19	30.894			
OB145A	small	EX-156	67.574	30.883		just under roots	tent stake stuck in ground, 30 cm, 4 cm across top
OB145B	small	EX-156	67.887	30.922			
OB146	small	EX-157	69.028	37.743		just under roots	metal banding, 18 cm x 10 cm
OB147A	small	EX-151	70.084	43.524		just under roots	nails
OB147B	small	EX-151	70.694	43.242			
OB148	tiny	EX-150	69.763	46.091		9 cm	tiny metal object, 1-2 cm ²
OB149	small	EX-160	74.029	47.58		just under roots	metal banding, 10 cm x 4 cm
OB150A	medium	EX-161	76.023	45.275		just under roots	metal banding, 44 cm x 4 cm
OB150B	medium	EX-161	75.862	45.689			
OB151A	small	EX-140	76.202	41.839		14 cm	metal banding?, thicker than usual, 19 cm x 4 cm
OB151B	small	EX-140	76.373	41.945			
OB152	small-medium	EX-165	85.139	45.391		just under roots	metal chain, coiled up, 10 cm x 8 cm
OB153A	small	EX-165	85.23	45.001		just under roots	Al banding, 14 cm x 4 cm
OB153B	small	EX-165	85.031	44.9			
OB154A	small-medium	EX-165	85.891	44.558		just under roots	Al banding, 20 cm x 4 cm
OB154B	small-medium	EX-165	85.698	44.458			

Object ID	Size Bin	Excavation ID	Easting (m)	Northing (m)	Hole Diameter	Depth	Description
OB155	medium	EX-91	83.834	38.623		just under roots	sheet metal + homemade mine sign, 30 cm x 25 cm piece; sign 48 cm; post, 13 cm x 10 cm; 3rd piece 9 cm x 9 cm
OB156	medium	EX-113	84.481	32.582	69 cm		metal pieces, banding, wire, Al banding
OB157A	medium	EX-113	85.35	32.042		just under roots	Al banding, 57 cm
OB157B	medium	EX-113	84.962	32.494			
OB158A	small	EX-113	84.962	32.34			metal piece, 26 cm x 8 cm
OB158B	medium	EX-113	84.867	32.568			
OB159	small	EX-149	75.275	37.014		just under roots	metal object, 12 x 6 cm
OB160A	large	EX-42	84.181	24.344		just under roots	metal banding, 3.4 m x 4 cm, E-W, not all in photo
OB160B	large	EX-42	87.522	23.959			
OB161A	small	EX-164	69.114	18.571		just under roots	piece of rusty wire, 37 cm long
OB161B	small	EX-164	68.722	18.665			
OB162	tiny	EX-159	74.99	17.602			spent shell M16?
OB163	small	EX-159	86.478	39.304		just under roots	old mine sign in bad condition, 32 cm long
OB164	TCTBO	EX-170	33.093	51.472		11 cm	7.62 blank cartridge from a M60 machine gun
OB165	TCTBO	EX-170	33.384	51.203		just under roots	doughnut-shaped piece of metal, 13 cm diameter
OB166	M12	EX-170	33.951	51.561		16.5 cm at high end, 21.5 cm at the low end	M12
OB167	tiny	EX-114	57.892	14.444		just under roots	small piece of metal, 9 cm x 2 cm
OB168	M12	EX-171	50.634	0.68		just under roots	M12, rusted, sand interior
OB169	M12	EX-15	58.889	55.257		just under roots	M12 and piece of an old minefield sign

Object ID	Size Bin	Excavation ID	Easting (m)	Northing (m)	Hole Diameter	Depth	Description
OB170A	medium	EX-143	70.82	59.512		just under roots	metal banding, 45 x 4 cm
OB170B	medium	EX-143	70.791	59.962			
OB171	small	EX-143	70.673	59.32		just under roots	piece of metal, 15 cm x 4 cm
OB172A	medium	EX-142	72.623	62.736		just under roots	piece of metal banding, 43 cm x 4 cm
OB172B	medium	EX-142	72.652	62.271			
OB173	tiny	EX-144	67.85	67.789		just under roots	metal scraps, 12.5 cm x 1.5 cm
OB174	small	EX-144	67.569	67.929		just under roots	metal scraps, 14 cm x 2.5 cm
OB175	tiny	EX-144	67.494	67.909		just under roots	metal scraps, 10 cm x 1 cm
OB176	tiny	EX-144	67.614	67.604		just under roots	metal scraps, 3 cm x 2 cm; 2 nails
OB177	small	EX-144	67.578	67.414		just under roots	metal scraps, metal thicker, 7 cm x 6.5 cm
OB178A	medium	EX-162	74.917	73.123		just under roots	metal banding, 36 cm x 4 cm; and metal scrap, 23 cm x 3.5 cm
OB178B	medium	EX-162	75.176	72.928			
OB179	small	EX-72	72.234	79.78		just under roots	metal banding, 9 cm x 2 cm
OB180	tiny	EX-72	70.635	79.664		just under roots	M16 round
OB181A	small	EX-142	71.877	62.391			very old mine sign, 47 cm
OB181B	small	EX-142	72.121	62.038			
OB182A	small-medium	EX-110	82.299	87.745		just under roots	piece of metal, reinforced corner of a box, 29 cm square
OB182B	small-medium	EX-110	82.458	87.565			
OB183	small	EX-110	82.545	87.97			piece of metal, reinforced corner of a box, 17 cm square
OB184	small	EX-163	84.873	91.194		9 cm	metal banding, 10 cm x 3 cm
OB185A	small	EX-163	84.901	92.743		just under roots	coat hanger, 30 cm x 12 cm
OB185B	small	EX-163	84.613	92.703			

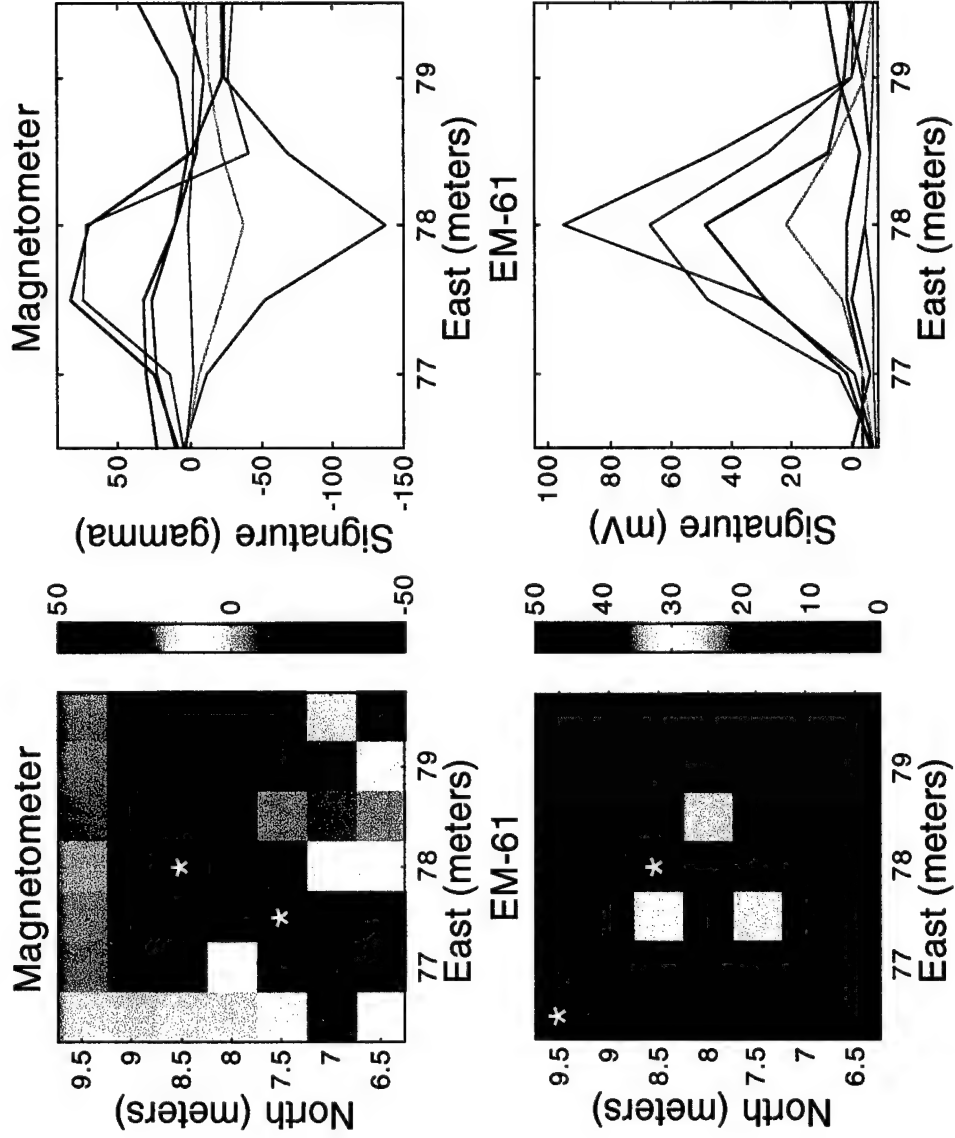
Object ID	Size Bin	Excavation ID	Easting (m)	Northing (m)	Hole Diameter	Depth	Description
OB186	small	EX-108	88.834	93.742		11 cm-16 cm (inclined, extreme depths)	metal, 11 cm x 1 cm x 1 cm
OB187	small	EX-108	90.318	93.152		17 cm	sheet metal, 13.5 x 8 cm
OB188	small	EX-111	83.649	78.692		10 cm	metal scrap, 10 cm x 2 cm
OB189	small	EX-111	83.36	78.103		10 cm	metal scrap, 6 cm x 2 cm
OB190A	medium	EX-148	78.297	31.59		just under roots	metal scrap, .5m long, 16 cm wide
OB190B	medium	EX-148	77.869	31.84			
OB191A	medium	EX-148	78.8	31.844		just under roots	metal banding, 43 cm x 4 cm
OB191B	medium	EX-148	78.984	31.448			
OB192A	medium	EX-154	61.565	31.492		just under roots	metal banding, 48 cm x 4 cm
OB192B	medium	EX-154	61.302	31.07			
OB193A	medium	EX-147	47.115	32.501		just under roots	metal banding, 46 cm x 4 cm
OB193B	medium	EX-147	47.186	32.065			
OB194	medium	EX-23	44.038	39.469		18 cm	metal banding, 35 cm x 4 cm; can 13 cm in length; spent shell
OB195A	medium	EX-23	43.808	40.026		just under roots	Al banding, 50 cm x 4 cm
OB195B	medium	EX-23	43.479	39.96			
OB195C	medium	EX-23	43.419	39.661			
OB196A	small-medium	EX-102	35.007	8.958		just under roots	metal banding, 28 cm x 4 cm
OB196B	small-medium	EX-102	35.189	8.694			
OB197A	medium	EX-24	46.11	49.77		just under roots	metal banding, 45 cm x 4 cm
OB197B	medium	EX-24	46.14	49.25			
OB198A	medium	EX-24	46.52	49.05		just under roots	metal banding, 45 cm x 4 cm
OB198B	medium	EX-24	46.81	49.34			

Object ID	Size Bin	Excavation ID	Easting (m)	Northing (m)	Hole Diameter	Depth	Description
OB198C	medium	EX-24	46.74	49.46			
OB199	tiny	EX-125A	59.7	64.37		10 cm	piece of metal, 8 cm x 2 cm
OB200	tiny	EX-162	75.96	72.07		just under roots	piece of metal, 7 cm x 13 cm
OB201	tiny	EX-145	84.74	77.39		just under roots	piece of metal small ~6 cm x 1 cm
OB202A	medium	EX-50	48.37	54.49		just under roots	metal banding, 42 x 4 cm
OB202B	medium	EX-50	48.61	54.87			

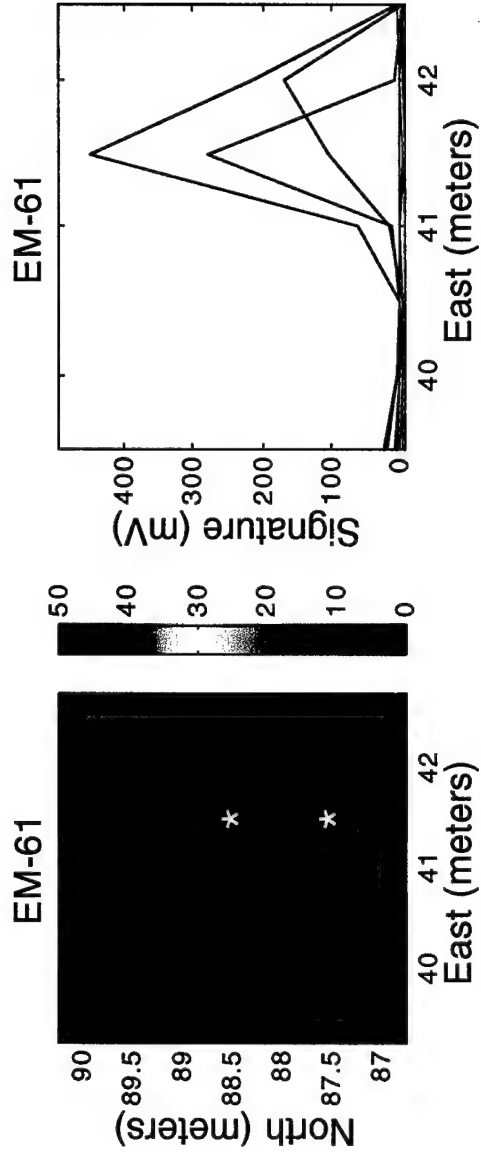
APPENDIX E

DATA IMAGE CATALOG OF PRE-DIG SURVEY DATA

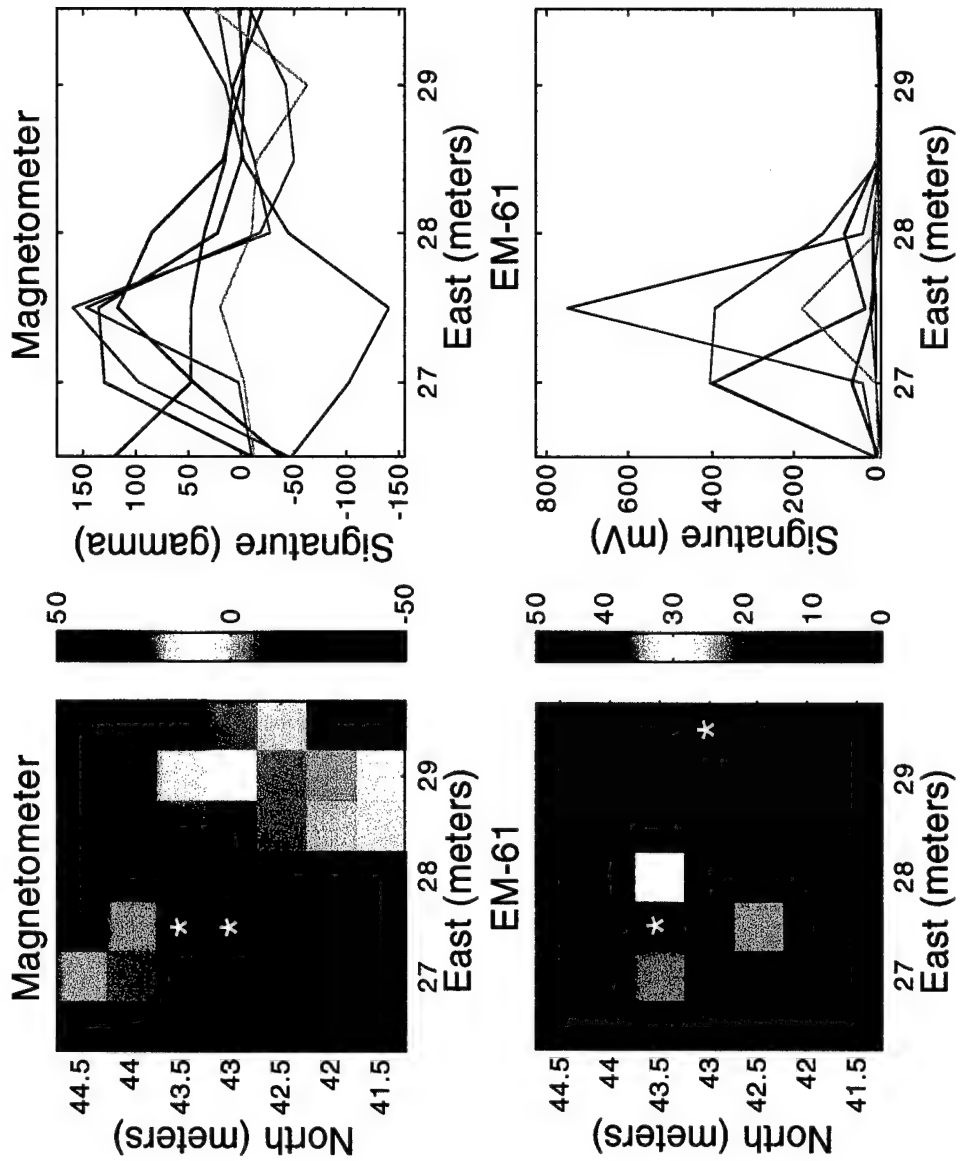
EX-1



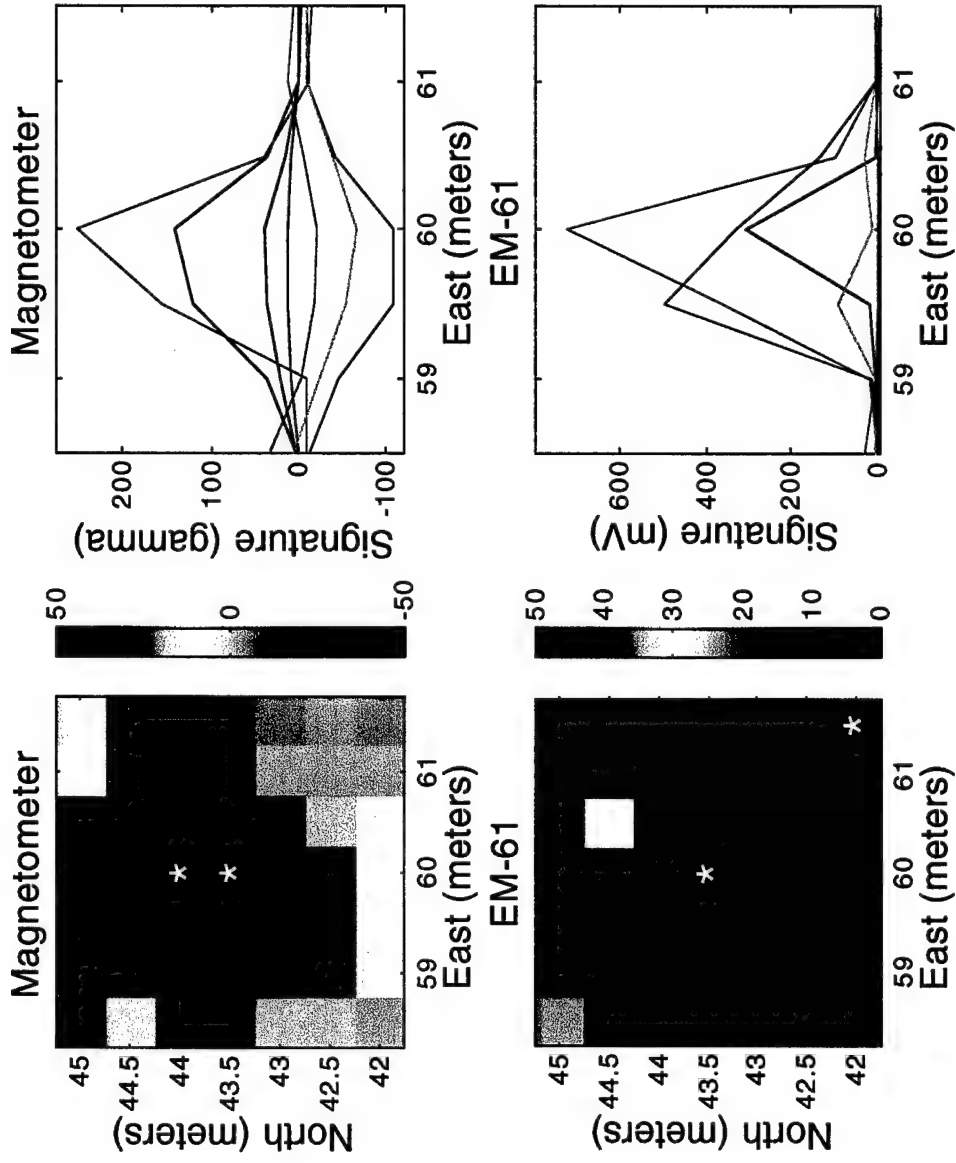
EX-2



EX-6

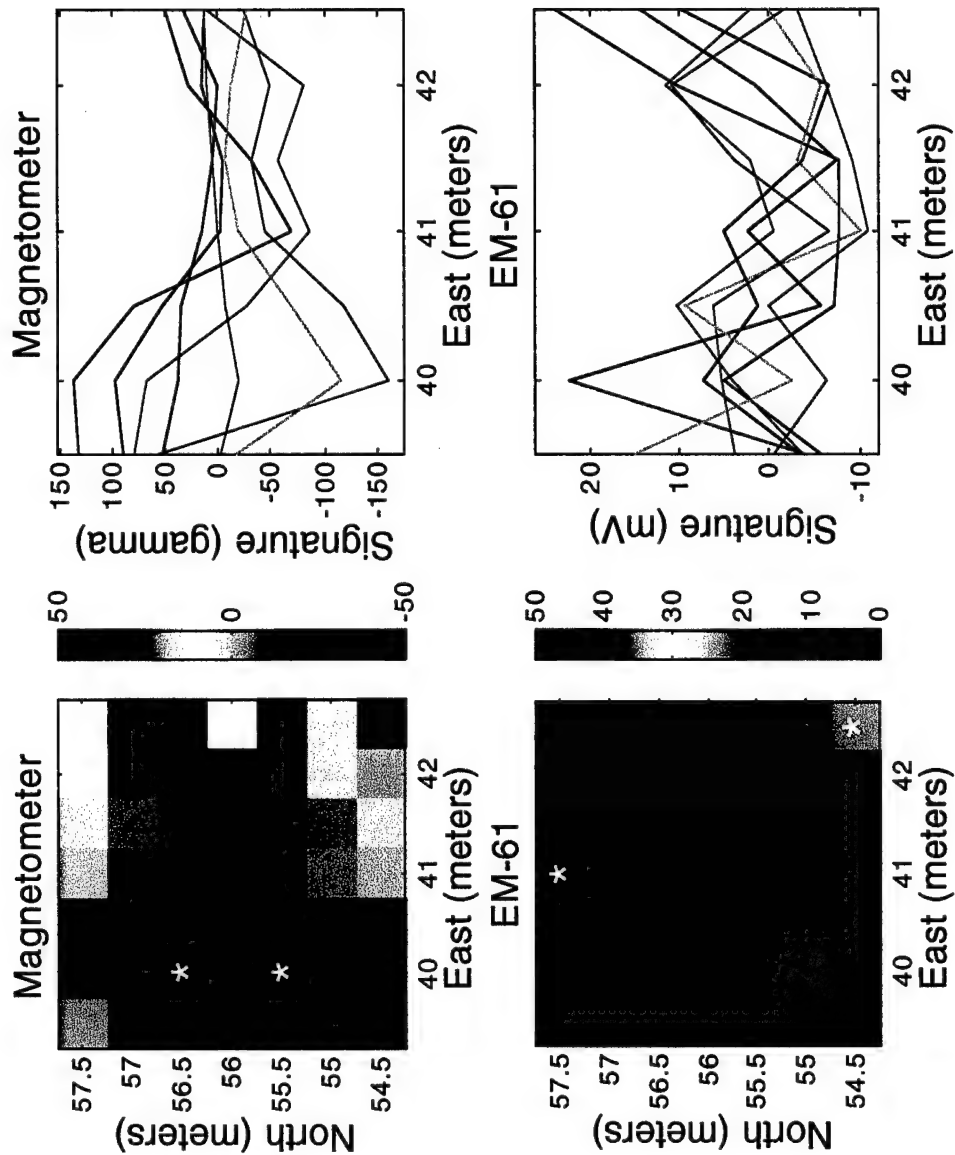


EX-7

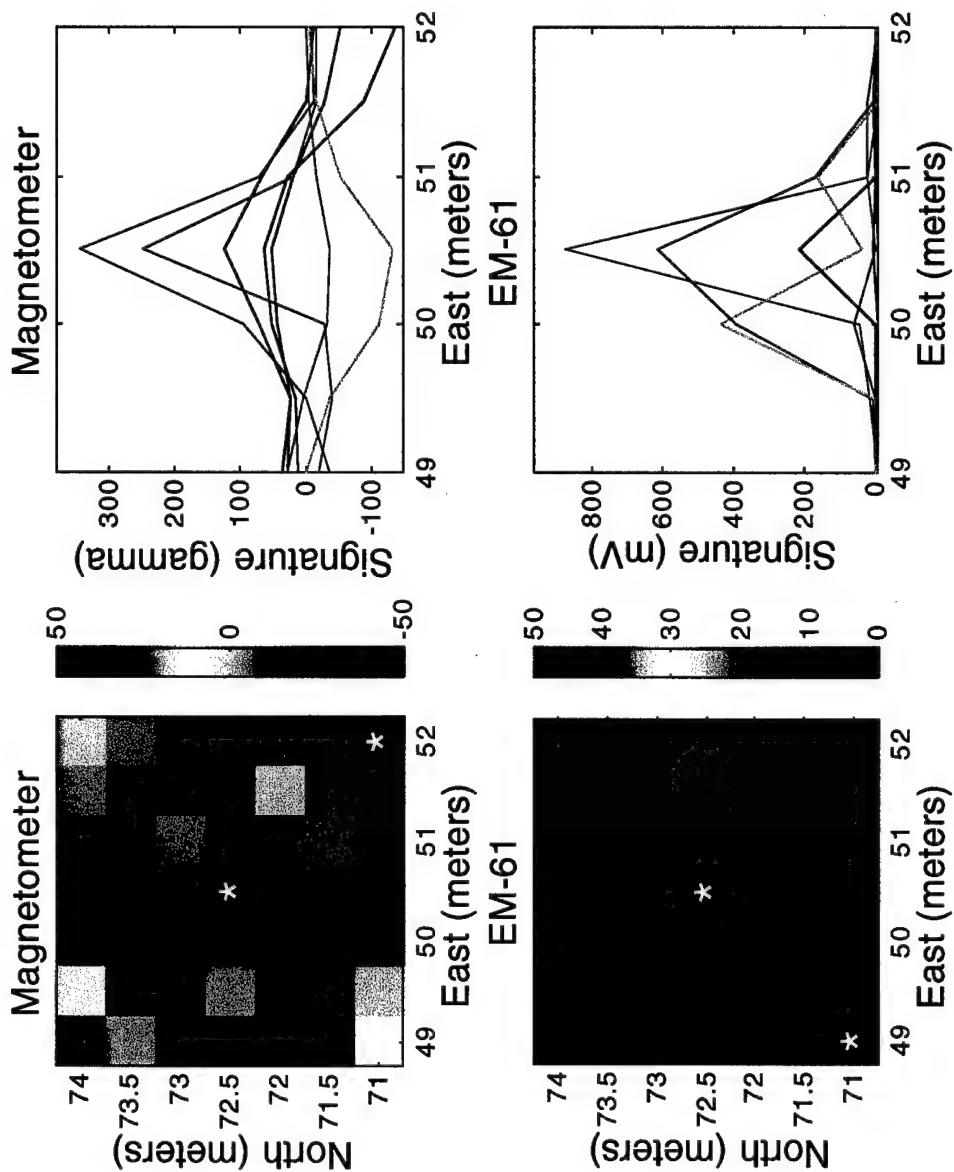


E-6

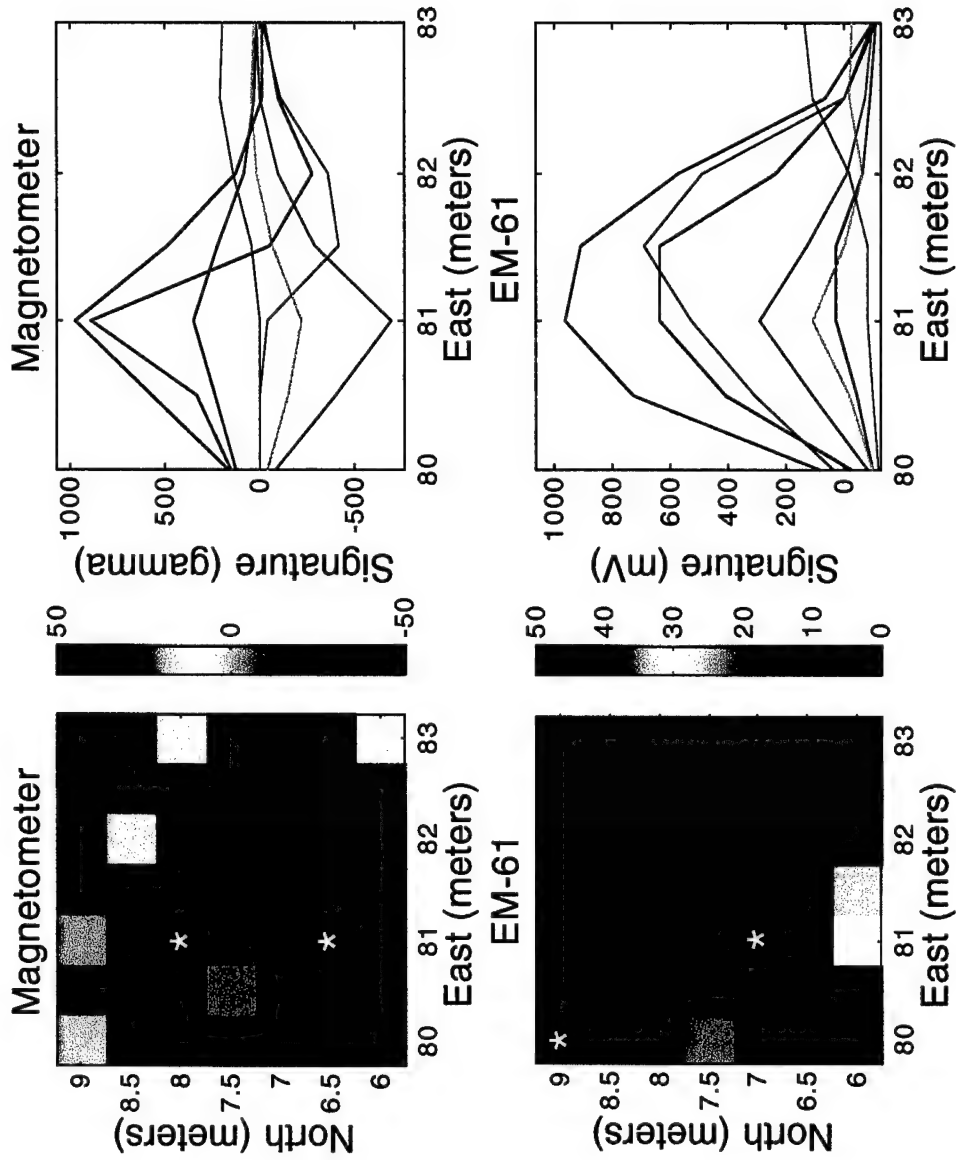
EX-8



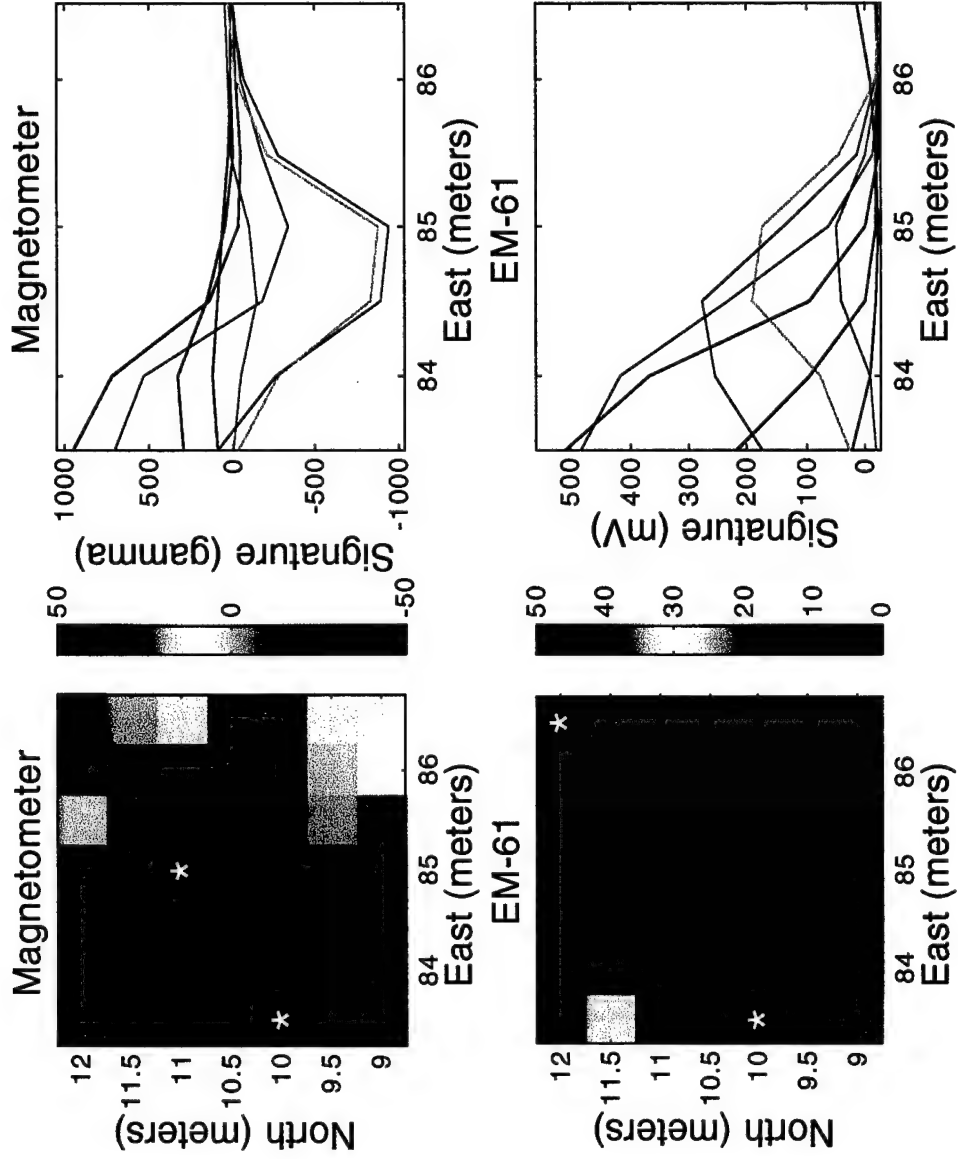
EX-16



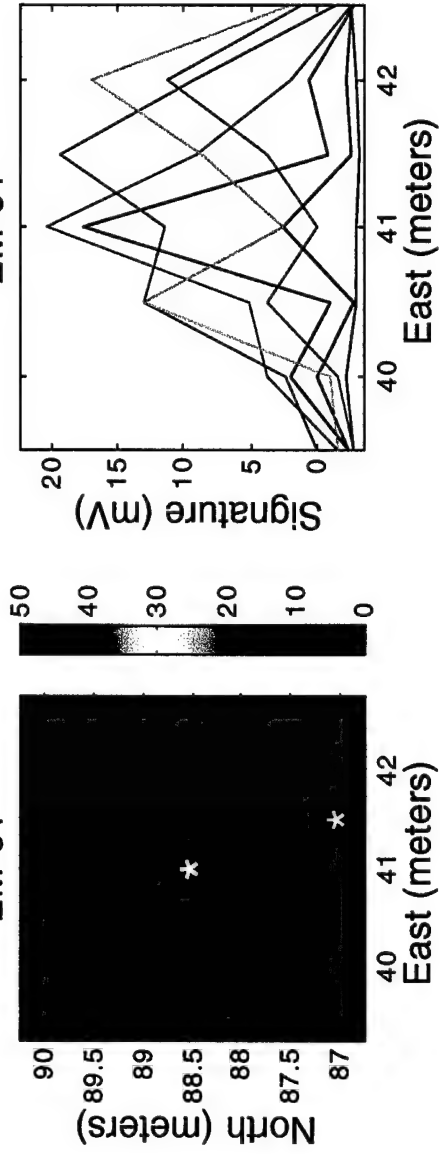
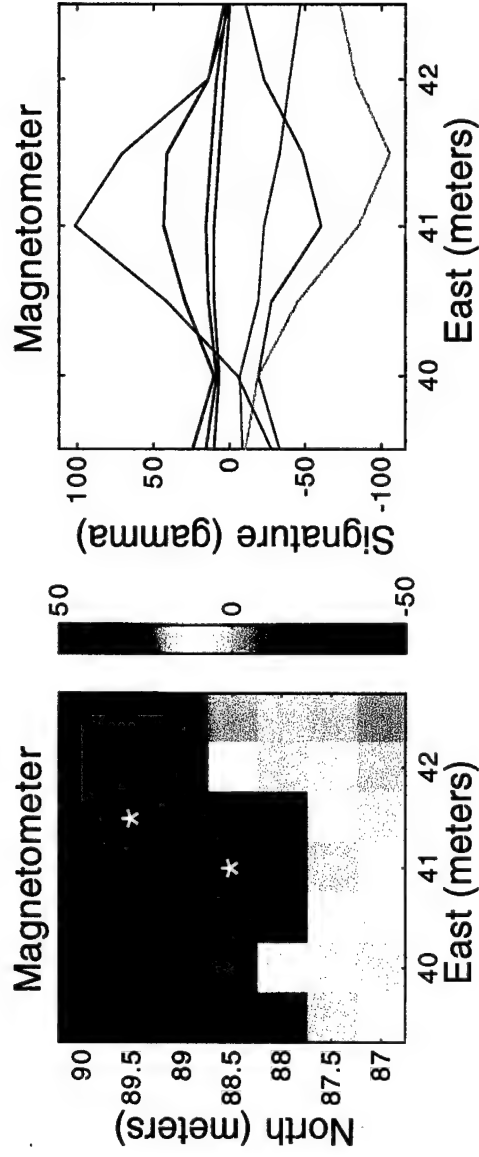
EX-17



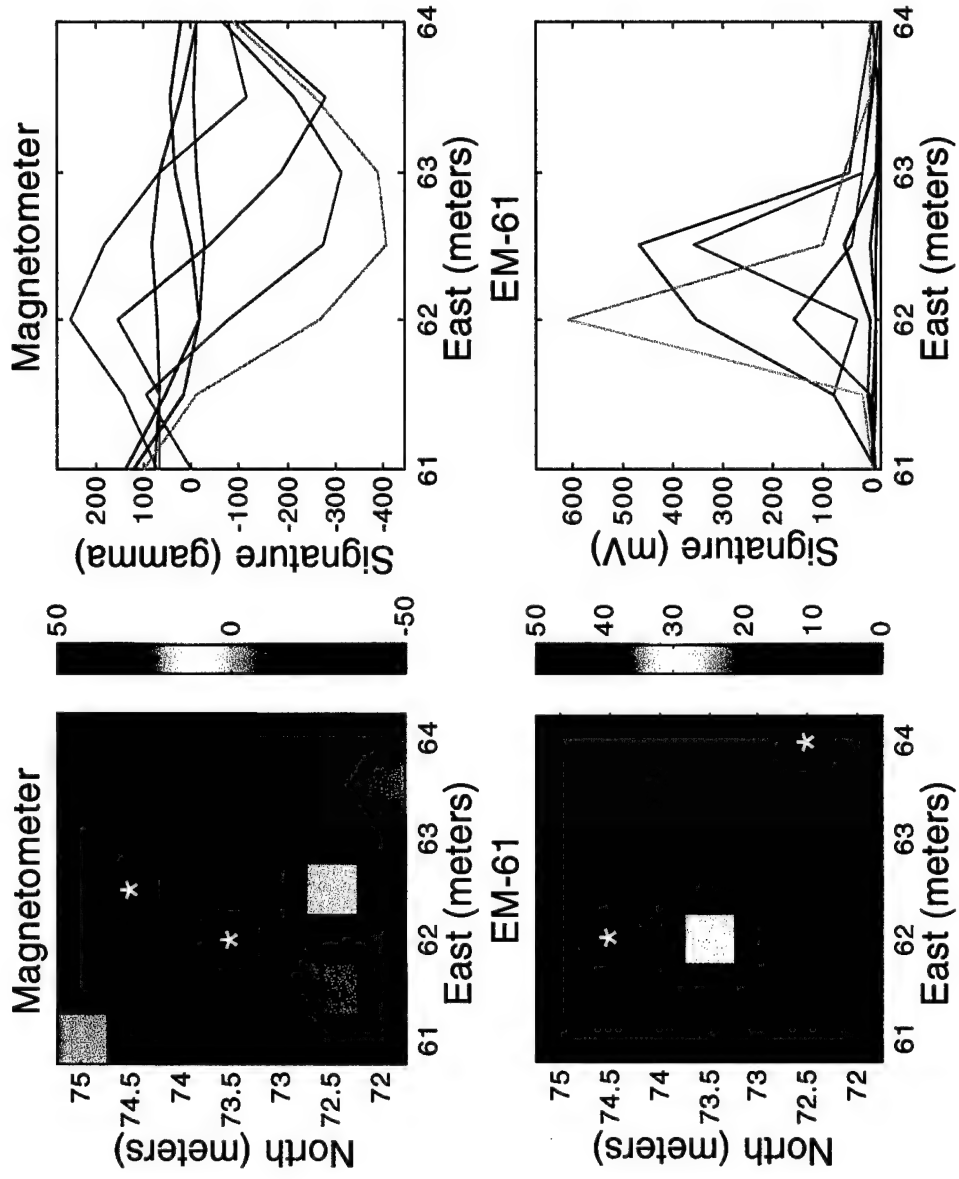
EX-18



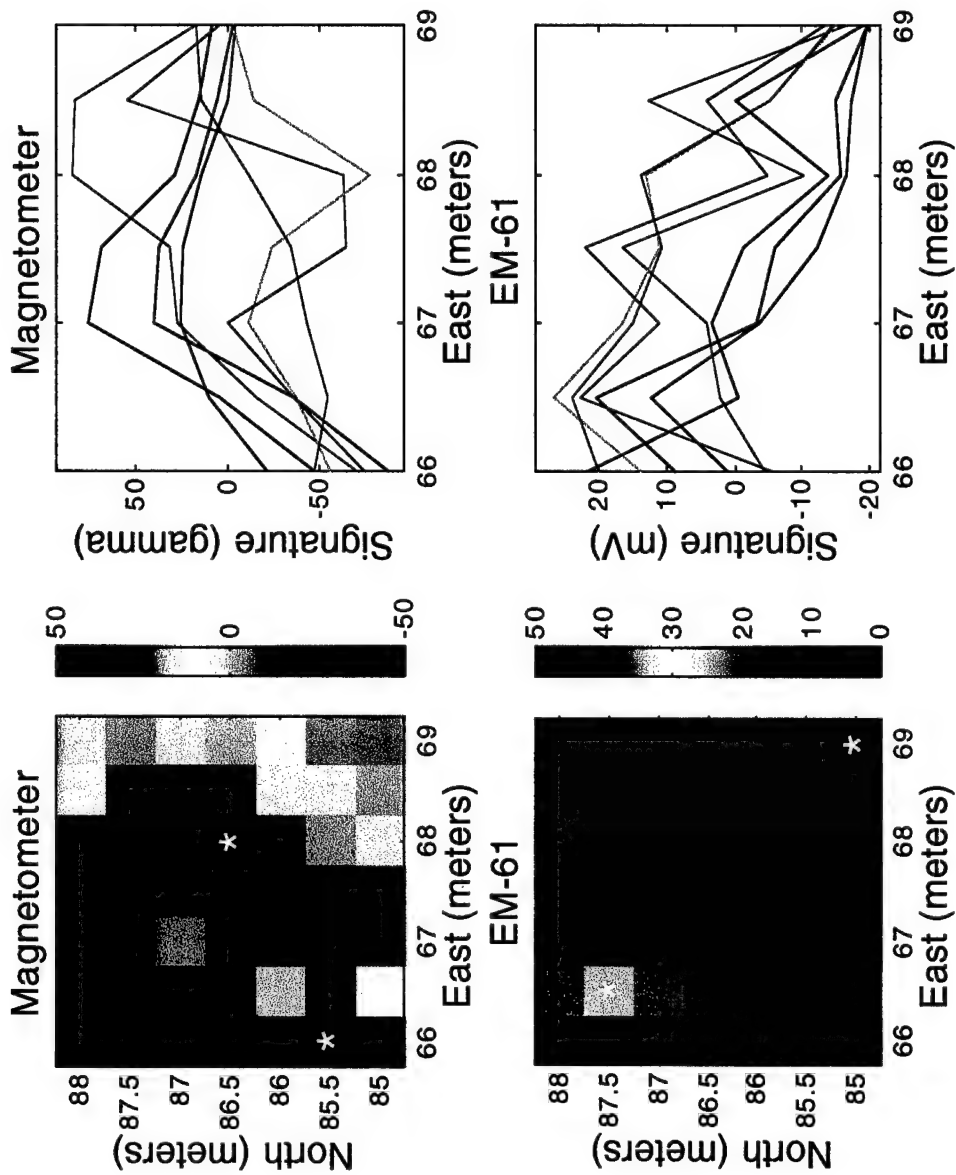
EX-77



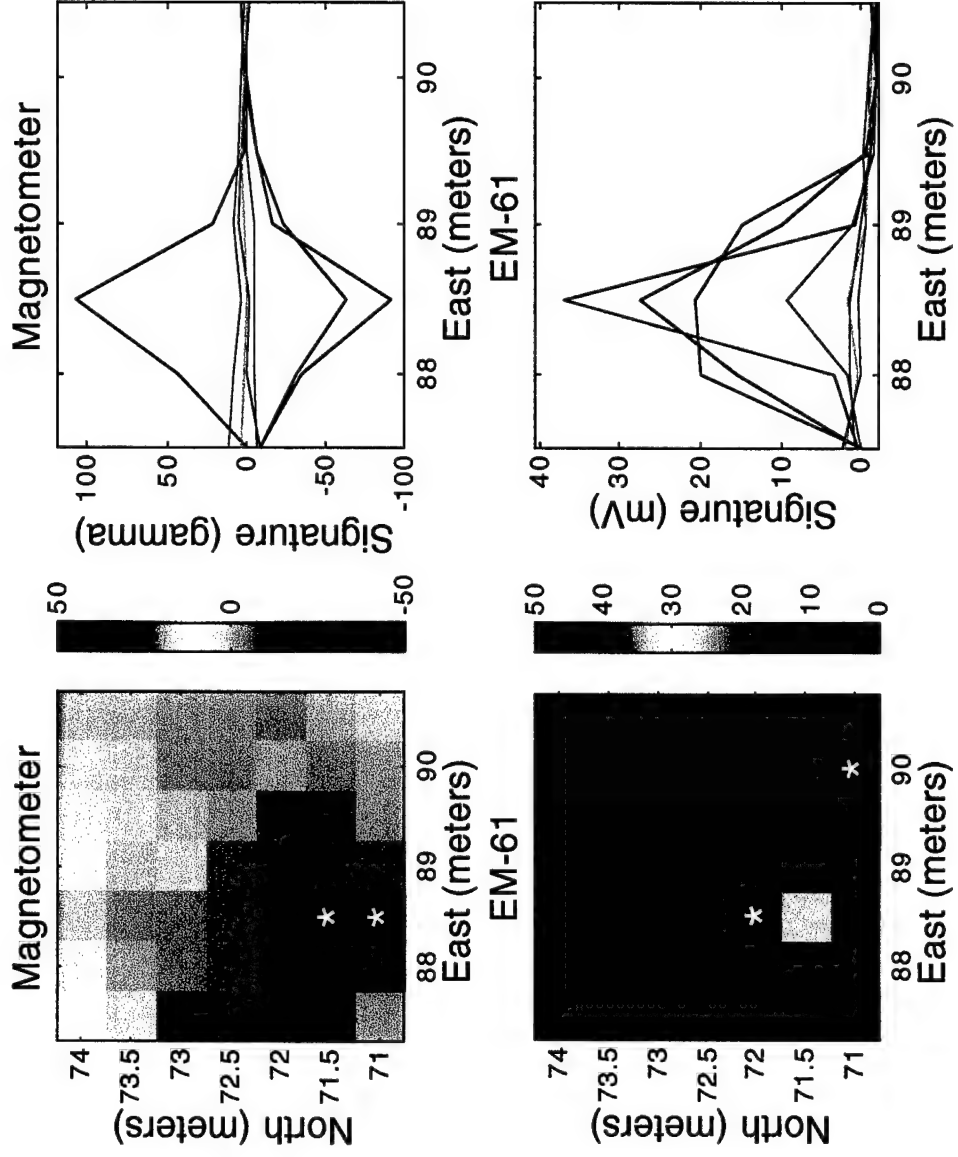
EX-105



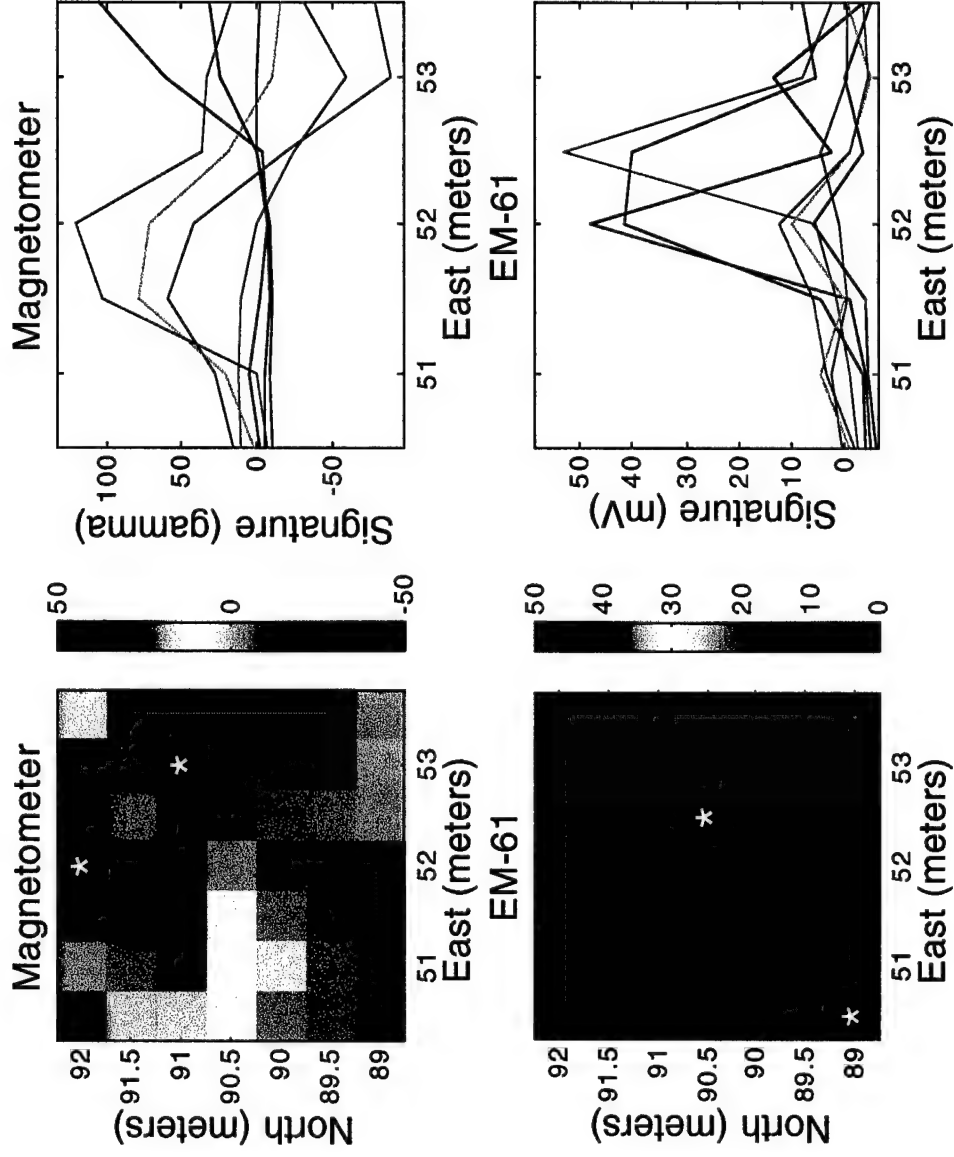
EX-107



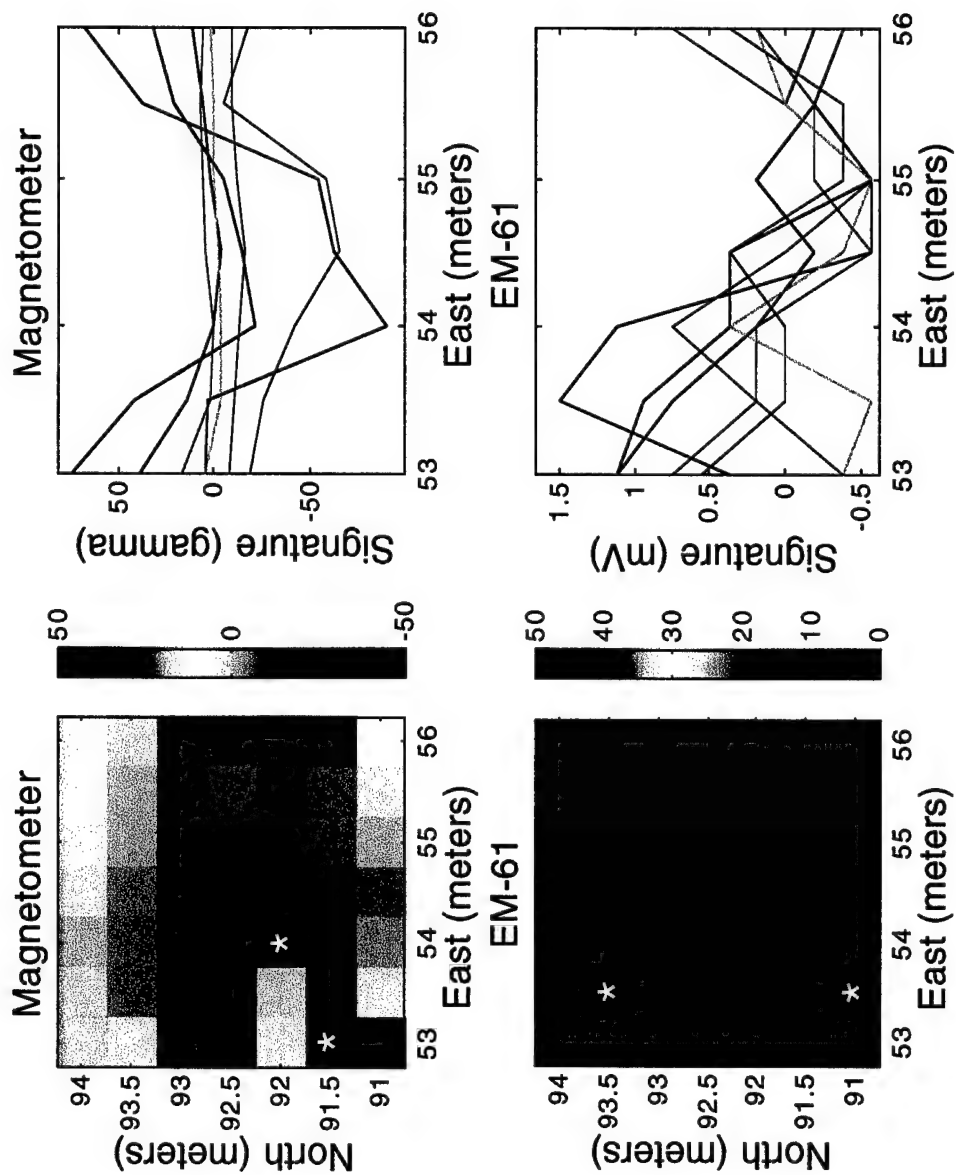
EX-112



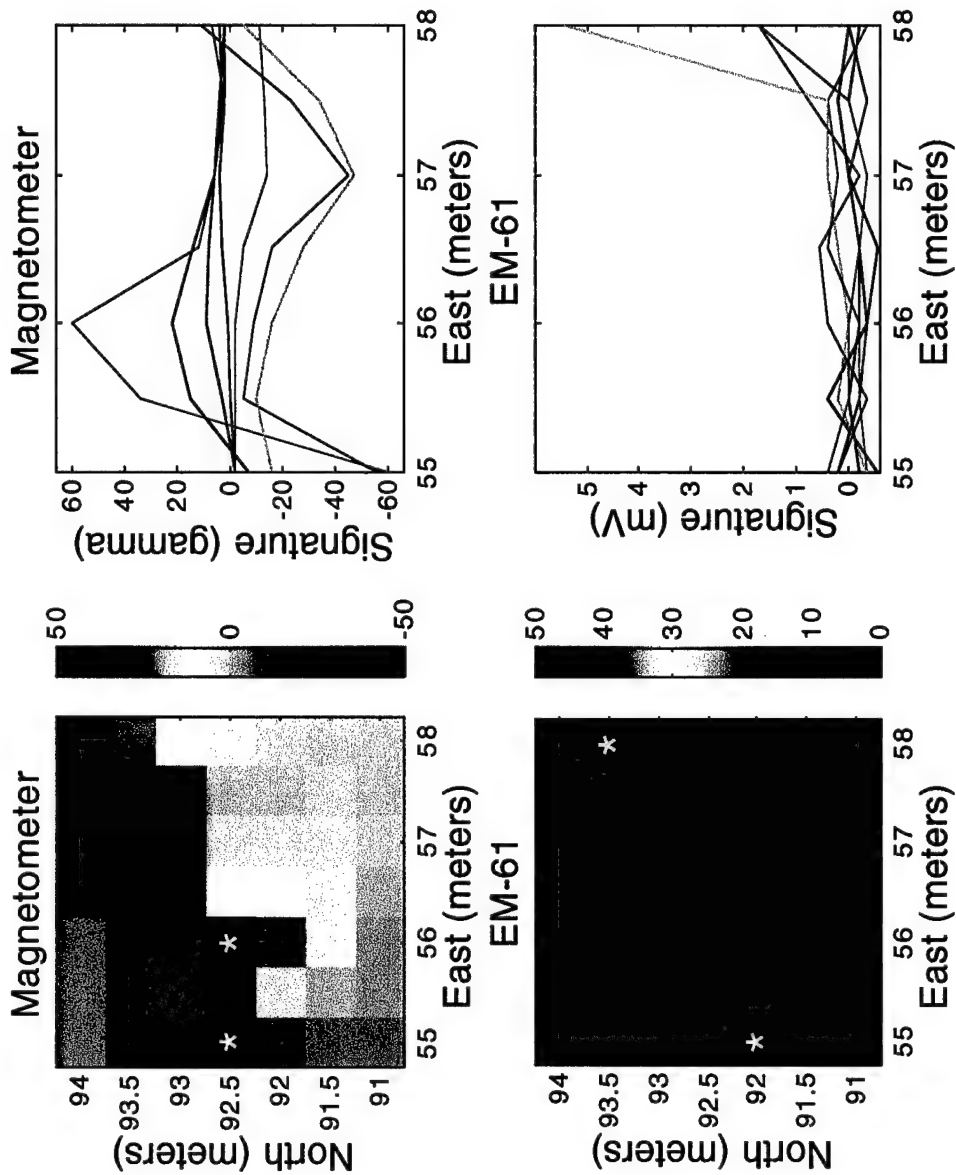
EX-116



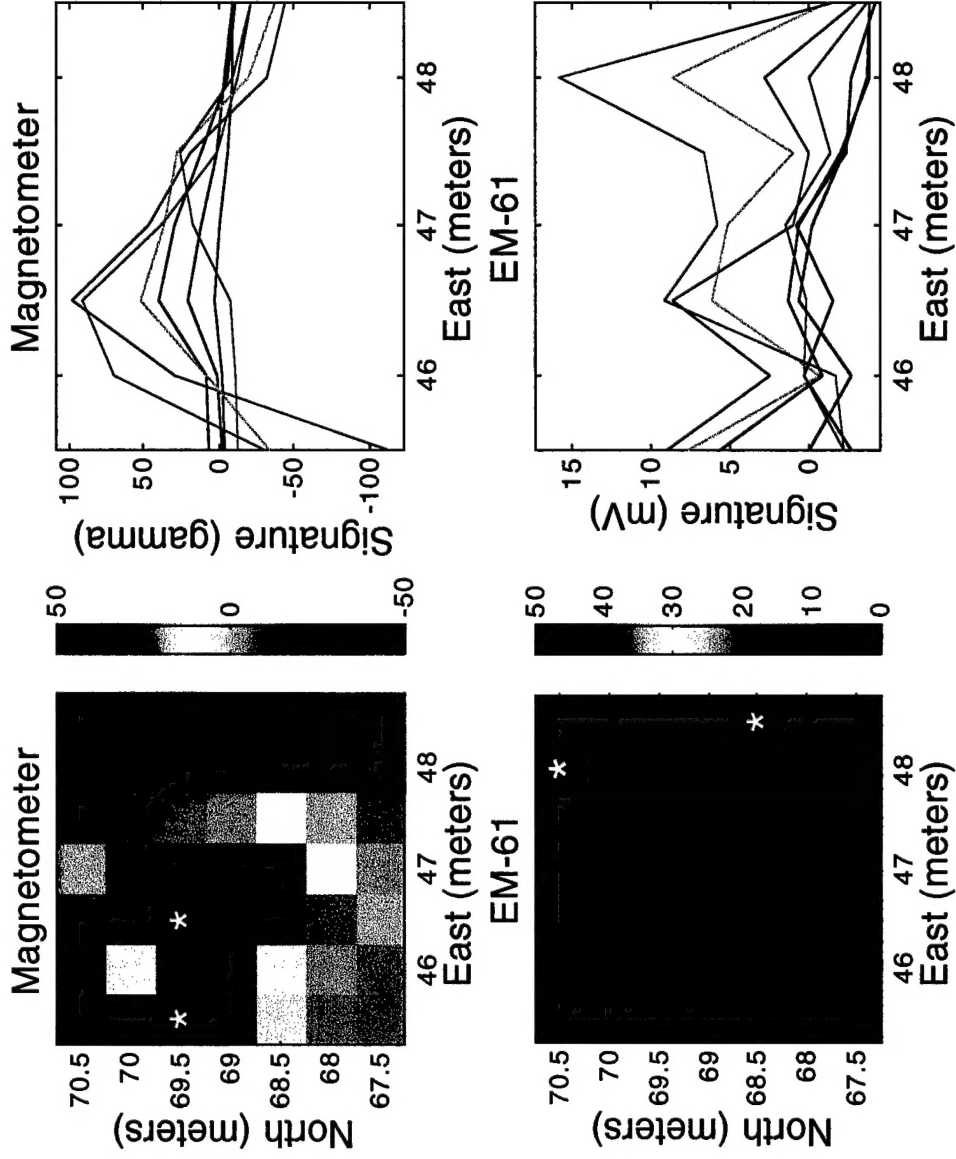
EX-117



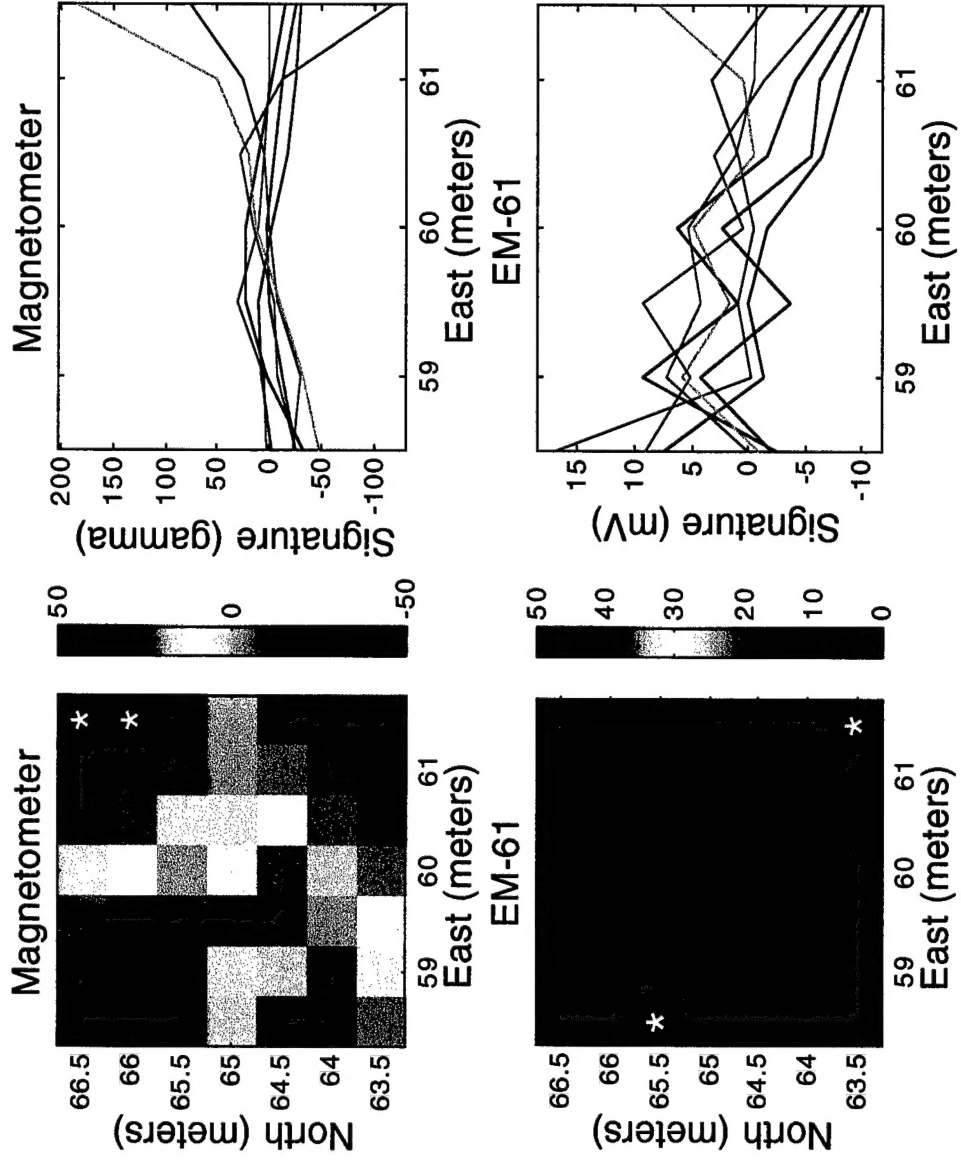
EX-118



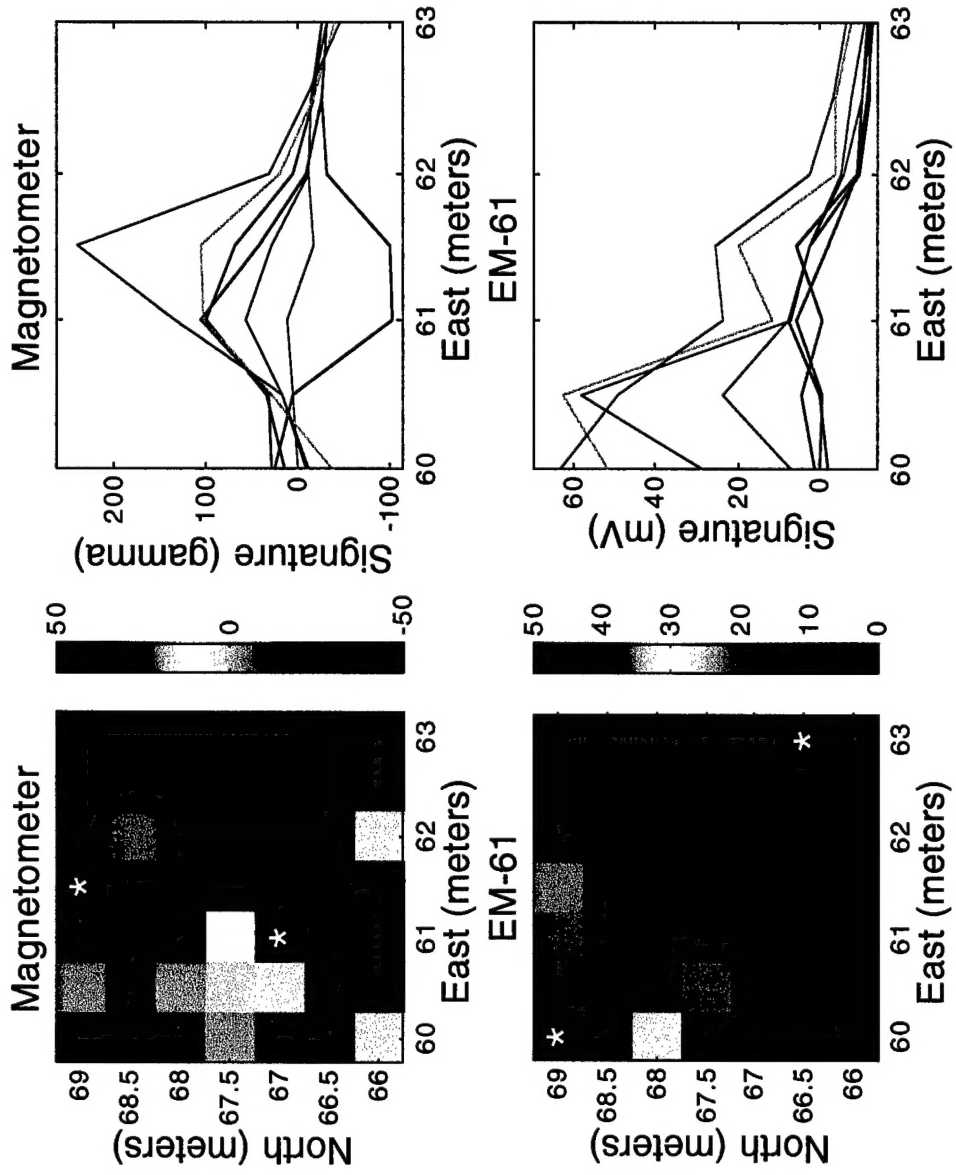
EX-121



EX-125A



EX-125B



EX-126

